Microkinetic Model Development for Methane Oxidation over Palladium Catalysts

Zur Erlangung des akademischen Grades eines
DOKTORS DER INGENIEURWISSENSCHAFTEN
(Dr.-Ing.)

von der KIT-Fakultät für
Chemieingenieurwesen und Verfahrenstechnik
des Karlsruher Instituts für Technologie (KIT)

genehmigte
DISSERTATION
von

Dipl.-Ing. Henning Stotz
aus Leinfelden-Echterdingen

Tag der mündlichen Prüfung:	25.06.2020
Hauptreferent:	Prof. Dr. rer. nat. Olaf Deutschmann
Korreferent:	Prof. Dr.-Ing. Roland Dittmeyer

Abstract

In order to further reduce fossil fuel based CO_2 greenhouse gas emissions in the transportation sector, in addition to other engine related pollutants, such as nitrogen oxides (NO_x), carbon monoxide (CO) and particulate matter (PM), an increased utilization of gas-engine driven cars, trucks and ships in comparison to conventional diesel or gasoline fueled devices, represents a direct measure to achieve this target. Supplementary fuel resources such as synthetic methane, obtained from renewable energy driven power-to-gas technologies, provides another option - in the medium to long term - to even further reduce and ultimately eliminate fossil fuel based CO_2 emission from gas-engines used in the transportation sector as well as for stationary applications.
Typical exhaust gas after-treatment systems of gas-engines use palladium (Pd) based catalysts due to their strong total oxidation activity towards unburned methane which needs to be catalytically converted before released to the environment as its greenhouse gas global warming potential over a 100 year time horizon is ca. 25 times higher than for CO_2. Thus, for optimization and design improvement of the technical and catalytic systems and to support the development process due to various technical configurations, an improved mechanistic and model-based understanding is necessary and builds the foundation for further analysis.
The Pd catalyst system shows a complex behavior depending on the gas-phase composition, temperature and pre-treatment of the catalyst. The reaction kinetics of reduced and oxide phase are different and the Pd particle structure can change during phase transformation, altering the kinetic behaviour. Water as one by-product of the gas-engine, once fed to the catalyst, is able to deteriorate the methane total oxidation activity of the catalyst. Chemically reducing agents such as carbon monoxide (CO) and hydrogen (H_2) can reduce the active oxide phase and thereby lowering the catalyst activity as well. In combination with high temperatures, thermal reduction of the oxide phase may impose additional challenges to maintain the catalyst activity stable.

In this thesis, two detailed microkinetic mechanisms for the oxidation of methane over the reduced and the oxidized phase have been developed in order to obtain

a better model based understanding of this reaction system. The model for the reduced Pd mechanism comprises following features:

- Considers gas-phase species of $CH_4/O_2/CO/CO_2/H_2/H_2O$
- Takes total/partial oxidation, steam reforming and water-gas shift reactions into account
- Energetics are based on semi-empirical UBI-QEP method
- Model is developed for a single active Pd site within the mean field approximation
- Incorporates different methane activation paths depending on the amount of surface oxygen
- Model predicts spatial resolved and ex situ measurements

The features for oxidized PdO(101) mechanism comprises following points:

- Considers gas-phase species of $CH_4/O_2/CO_2/H_2O$
- Incorporates formate surface species as observed by in situ DRIFTS measurements and reactions.
- Takes total oxidation reactions over PdO oxide phase into account
- Energetics are based on density-functional theory (DFT) calculations
- Model is developed as a mean field extension for coordinatively unsaturated (cus) Pd and O sites (two-site mechsanism)
- Incorporates various reaction paths following Mars-van-Krevelen mechanisms
- Mechanism predicts the water inhibition effect
- Model predicts thermal light-off cycling measurements

To the end, both mechanisms were combined with a degree of oxidation model (DOM) to incorporate thermal phase transformation effects, as e.g. given during light-out cool down, and to account for the related effect on the change of the catalytic active surface area of the Pd and PdO phases. The DOM and the mechanisms were therefore validated against thermal light-off/-out cycling experiments.

Zusammenfassung

Der Einsatz von Erdgasmotoren für Anwendungen im Schiffs-, Lkw- und Pkw-Verkehr, stellt im Vergleich zu konventionellen Diesel- oder Benzinmotoren eine direkte Maßnahme dar, um die verkehrsbedingten CO_2-Emissionen, sowie Stickoxid (NO_x), Kohlenmonoxid (CO) und Feinstaub (PM) Belastungen weiter zu senken. Synthetisches Methan, das unter Verwendung erneuerbarer Energien im Power-To-Gas Verfahren erzeugt wird, stellt eine erweiterte Option dar, damit die Ziele, die CO_2-Emissionen, im Verkehrsbereich und bei stationären Anwendungen, zu reduzieren, sowie mittel bis langfristig vollständig zu eliminieren, erreicht werden.
Typische für Erdgasmotoren eingesetzte Katalystoren verwenden Palladium (Pd) basierte Beschichtungen zur vollständigen Oxidation von Methan. Diese sind aufgrund ihrer hohen Methan Aktivität in der Lage, motorseitig unverbranntes Methan katalytisch zu konvertieren. Dies ist notwendig, weil Methan über einen Zeithorizont von 100 Jahren ein Globales Erderwärmungs Potential (GWP) von über 25 aufweist und damit als starkes Treibhausgas gilt. Ein deutlich verbessertes mechanistisches und modellbasiertes Verständnis dieser am Katalysator ablaufenden Prozesse ist deshalb insbesondere im Hinblick auf die zu erzielende System-Optimierung und Verbesserung, als auch zur Unterstützung des Entwicklungprozesses solcher katalytischen Systeme von großer Relevanz.
Das Pd-Katalysator-System zeigt dabei ein äußertst komplexes Verhalten, das sowohl von der Zusammensetzung der Gasphase, der Temperatur als auch von der Vorbehandlung des Katalysators beeinflusst wird. Die Reaktionskinetik der oxidierten Pd-Phase (PdO) unterscheidet sich dabei grundlegend von der reduzierten Pd-Phase. Zusätzliche Änderungen der Pd-Partikelstruktur können während einer Phasenumwandlung ebenso auftreten. Eine damit einhergehende Veränderung spiegelt sich im Reaktionsverhalten wider. Wasser, das sich bei der Verbrennung im Erdgasmotor bildet und folglich als Nebenprodukt über den Abgasstrang in den Katalysator gelangt, wirkt sich negativ auf den Methanumsatz aus. Im Abgas auftretende Reduktionsmittel, CO und H_2, sind in der Lage, die katalytisch sehr aktive PdO-Phase chemisch zu reduzieren und so die Aktivität zu mindern. Eine zusätzliche Herausforderung zur Aufrechterhaltung einer stabilen Katalysatoraktivität stellt die in Verbindung mit hohen Temperaturen eintretende thermische Reduktion der PdO-Phase dar.

Im Rahmen der vorliegenden Arbeit wurden zwei detaillierte Reaktions Mechanismen entwickelt. Der Mechanismus für die Pd-Phase umfaßt dabei folgende Merkmale:

- Beinhaltet folgende Gasphasen Spezies: $CH_4/O_2/CO/CO_2/H_2/H_2O$
- Berücksichtigt Total-/Partialoxidation von Methan, Wasserdampf Reformierung und Wasser-Gas-Shift Reaktionen
- Energetische Berechnungen mit semi-empirischer UBI-QEP-Methode
- Eine aktive Pd-Oberflächenspezies; Mean Field Näherung
- Verschiedene Methan Aktivierungspfade in Abhängigkeit der Sauerstoff Oberflächenbedeckung
- Voraussage ortsaufgelöster Konzentrationsprofile

Die Besonderheiten des PdO-Mechanismus zeichnen sich durch folgenden Punkte aus:

- Beinhaltet folgende Gasphasen Spezies: $CH_4/O_2/CO_2/H_2O$
- Format-Oberflächenspezies; bestätigt durch in-situ DRIFTS
- Berücksichtigt Total-Oxidation von Methan
- Energetische Parameter basieren auf DFT–Rechnungen
- Modellentwicklung als Mean Field Erweiterung für zwei koordinativ ungesättigte (cus) Pd- und O-Adsorptionszentren
- Reaktionspfade gemäß Mars-van-Krevelen Mechanismus
- Vorhersage des Wasser-Inhibierungseffektes
- Voraussage von Light-off Verläufen

Beide Mechanismen wurden mittels eines Oxidationsgrad abhängigen Ansatzes verknüpft, um so den Effekt der temperaturabhängigen Phasenumwandlung auf die Kinetik zu berücksichtigen. Eine zusätzliche Validierung des Oxidationsgrad abhängigen Ansatzes in Kombination mit den Mechanismen erfolgte dabei anhand von zyklischen Light-off und Light-out Experimenten.

Executive Summary[1]

The usage of methane or natural gas (NG) as a supplementary fuel resource, driven by the enhanced production of shale gas, as well as the flexible availability from a range of other, both renewable- and fossil-fuel-based sources such as bio-gas, power-to-gas (PTG) and methane hydrates, has a profound effect on related industrial applications [3]. In particular, stationary applications for the production of combined heat and power, gas-turbines, and also mobile applications such as natural-gas-fueled cars, trucks or ships benefit from this trend, as decreasing costs for NG favor the economical viability. NG-fueled devices generally have lower CO_2 emissions compared with their gasoline- or diesel-fueled counterparts, due to the higher hydrogen:carbon ratio of methane, which is the main constituent of NG at about 90 % by volume. However, since methane is also a potent greenhouse gas exposing a global warming potential to the environment which is ca. 25 times higher than that of CO_2 [4], necessitating an efficient, durable and clean exhaust gas emission control system in order to also fulfill upcoming stringent hydrocarbon (HC) emission regulations and to eliminate methane slip from those natural-gas driven lean-burn engines. Such exhaust gas abatement systems are typically build on palladium-based catalysts because they have been proven to be good oxidation catalysts for the purpose of catalytic oxidization of methane.

Accordingly, the focus of this work is an improved model based understanding of the detailed kinetics of the catalytic oxidation of methane (partial and total) over the palladium catalyst system, which is essential to improve and optimize catalytic emission control systems as well as the efficiency of those microreactors. This objective was achieved in a systematic way by studying the different kinetic behaviors of the methane oxidation reaction over the palladium catalyst system at catalyst reducing (Pd) and oxidizing (PdO) conditions and thereof developing for each catalyst phase detailed kinetic mechanisms within the mean-field approach.

[1] Parts of this summary have been taken from [1] H. Stotz, L. Maier and O. Deutschmann, *Top. Catal.*, 60 (2017) 83–109 and from [2] H. Stotz, L. Maier, A. Boubnov, A. T. Gremminger, J.-D. Grunwaldt and O. Deutschmann, *J. Catal.*, 370 (2019) 152–175.

Methane oxidation over Palladium

This thesis aims to be comprehensive in the sense that a variety of experimental tools, theoretical methods and literature information were systematically used and combined to obtain an overall understanding and the necessary information needed for the development of these kinetic models. Finally, both mechanisms were additionally validated against experimental light-off cycling results covering both oxidizing and thermally reducing conditions.

Detailed kinetic model for Pd at catalyst reducing conditions

A kinetic modeling study on methane oxidation over reduced Pd for various fuel-rich conditions around the stoichiometric point of the partial oxidation reaction at high temperatures (900 – 1100 K) is presented. A thermodynamically consistent detailed surface reaction mechanism is developed within the mean field approximation. The proposed kinetic model consists of 27 reversible elementary-step based reactions including 7 gas-phase species and 15 surface intermediates. Three different methane activation paths are implemented, comprising pyrolytic C-H bond dissociation steps, oxygen-assisted and dual-oxygen-assisted CH_4 activation. In situ experimental measurements in a quasi-autothermally operated flow reactor, using the capillary sampling technique, were performed for model evaluation. The provided experimental data includes spatially resolved temperature and concentration profiles within a single catalytic channel of a Pd/Al_2O_3-coated monolith. Supplementary numerical simulations based on literature data for fuel-lean and fuel-rich conditions at high temperatures extend the model's capability to predict a wide range of different experimental conditions.

Influence of C/O-ratio on spatial resolved profiles

A schematic of the experimental measurement configuration and the results of the recorded spatial resolved gas-phase and wall temperature profiles for the different investigated C/O-ratios are depicted in Fig. 1. Especially, for C/O-ratios smaller one, excessive heat is released by the reaction and leads to a pronounced hot spot formation with strong temperature gradients between gas-phase and catalyst wall near the entrance region of the channel. Increasing the C/O-ratio instead, leads to less exothermic behavior because methane is mainly converted

due to partial oxidation. The measured wall temperature profiles are used as boundary condition for the model simulations of the reactive channel flow with the developed surface mechanism for the reduced phase of Pd.

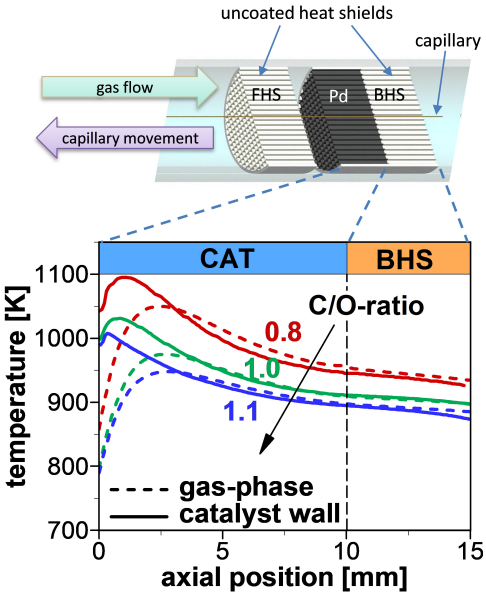

Figure 1: Experimental gas-phase temperature and catalyst wall temperature profiles along the channel axis at three different inlet C/O-ratios, 4 SLPM (0.220 Nm^3/h) and N_2-dilution of 80 vol.-%. Data for temperature profiles at C/O = 1.0 adapted from Diehm et al. [5]. Figure adapted from Stotz et al. [1].

Spatial resolved concentration profiles and model validation

Measured concentration profiles are shown in Fig. 2 and compared to the simulated results using the developed mechanism for the Pd phase. The results show that oxygen is rapidly consumed and depleted within the first 1.5 mm to

2 mm of the channel. Three different reaction zones are identified based on the appearance of reaction products:

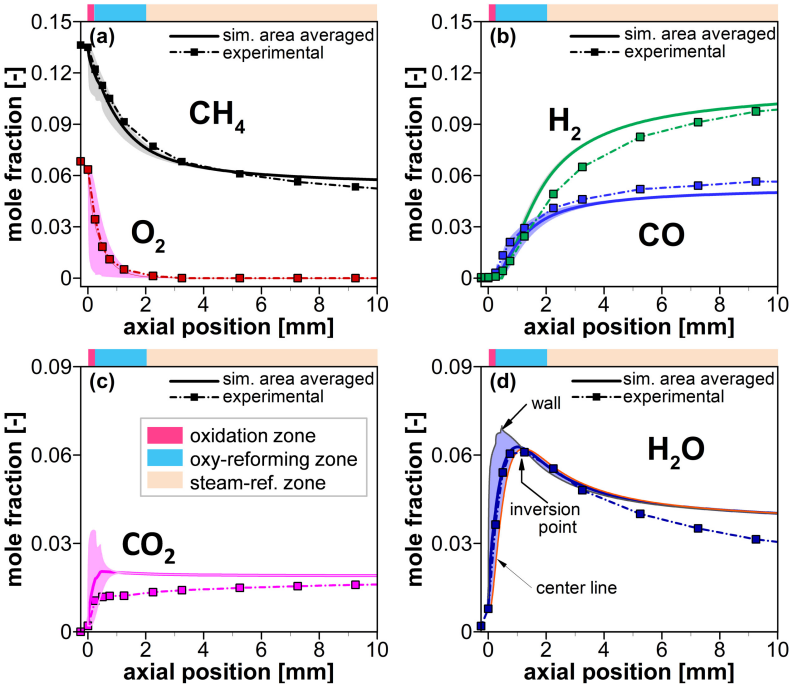

Figure 2: Concentration profiles for (a) reactants CH_4 and O_2, (b) partial oxidation products CO and H_2 and (c) total oxidation products CO_2 and (d) H_2O. Inlet conditions as fed: C/O-ratio = 1.1 at 4 SLPM and N_2-dilution of 80 vol.-%. Adapted from Stotz et al. [1].

- **Oxidation zone (0-0.25 mm):** Formation of total oxidation products CO_2 and H_2O are favored. Partial oxidation products are not found.

- **Oxy-reforming zone (0.25-2 mm):** Combined total and partial oxidation together with steam reforming takes place. Both total oxidation (CO_2, H_2O) and partial oxidation (CO, H_2) products form.

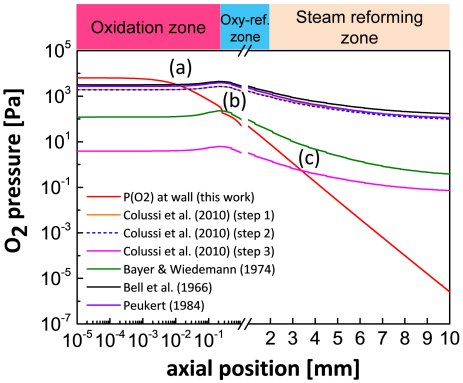

Figure 3: Simulated O_2 channel profile (red solid line). Inlet conditions as fed: C/O-ratio = 1.1 at 4 SLPM and N_2-dilution = 80 vol.-%. Calculated O_2 profiles (other lines) for PdO decomposition onset, based on measured wall temperatures and according to equilibrium data from Colussi et al. [6], Peukert [7], Bayer and Wiedemann [8] and Bell et al. [9]. Adapted from Stotz et al. [1].

- **Steam reforming zone (2-10 mm):** Methane is primarily converted via steam reforming. Water decreases while nearly no further increase in CO_2 is observed. Water-gas-shift plays only a minor role.

The developed multi-step surface reaction kinetics for the reduced Pd phase predicts all features of the experimental spatially-resolved species profiles.

Thermodynamic Analysis on possible PdO formation

Since inflowing gases cool down the catalyst wall at the entrance region of the catalyst channel, the hot spot formation may not lead to temperatures high enough to thermally reduce the Pd particles on the alumina surface, at the given inlet oxygen chemical potential. This would affect the kinetics and would also lead to model inconsistencies due to the formation of PdO oxide phases which was not intended at this stage.

The thermodynamic possibility for PdO decomposition was investigated by evaluating a modified Van't Hoff plot as shown in Fig. 3 for different equilibrium PdO decomposition steps [6–9] together with the simulation based oxygen partial pressure profile. The results indicate that the total oxidation activity cannot be unequivocally excluded nor attributed to either Pd or PdO at the channel entrance section. More precise investigations are needed to characterize in situ the channel entrance point with respect to its oxidation state.

Microkinetic model for PdO at catalyst oxidizing conditions

A two-site mean field extended microkinetic model was developed based on DFT data [10] to investigate the methane oxidation reaction over PdO(101) for environmental applications at atmospheric to moderate pressures, fuel-lean and low-temperature model exhaust gas conditions. The mechanism includes various carbonaceous pathways for methane oxidation together with lattice oxygen vacancy formation via Mars-van-Krevelen steps (cf. Fig. 4). The mechanism was compared with catalytic light-off curves (573 - 823 K) on a Pd/Al_2O_3 coated on monolith for $CH_4/O_2/H_2O/N_2$ mixtures with 1000 ppm CH_4, 10 vol.-% O_2 at varying H_2O feed concentration (0-12 vol.-%) and pressure (1 - 4 bar). The mechanism was demonstrated to quantitatively reproduce experimental light-off curves for dry and wet feeds and capture the water inhibition phenomena, when catalyst deactivation and/or particle size dependent kinetic effects are taken into account. A degree of rate control analysis reveals dissociative H_2O adsorption via hydrogen abstraction over Pd_{cus}-O_{cus} site-pairs as the major rate controlling step during light-off. Supplementary in situ DRIFTS investigations analyzed for dry and wet reactive gas-mixtures containing different types of C_1-fuels, namely methane, methanol and formic acid were conducted to identify surface species during catalytic methane oxidation and hydroxide formation.

Influence of PdO formation on metal dispersion

Metal dispersions of the investigated Pd/Al_2O_3 catalyst were experimentally determined in the reduced state of the catalyst as shown in Fig. 5. Additional corrections for the oxide phase using appropriately developed correlations on volume expansion and estimations on particle fracturing, indicate that the structural changes on the particle level between Pd and PdO phase, and resulting deviations need to be considered for the model based kinetic simulations under fuel-lean conditions when the active phase of palladium is present in oxidized form.

Influence of water concentration and metal dispersion on catalytic light-off curves as well as mechanistic consequences

Figure 6 shows experimental light-off curves at different water concentrations, in comparison to the simulation results of the PdO mechanism for reduced metal and metal oxide corrected dispersions. The better predictability in the low

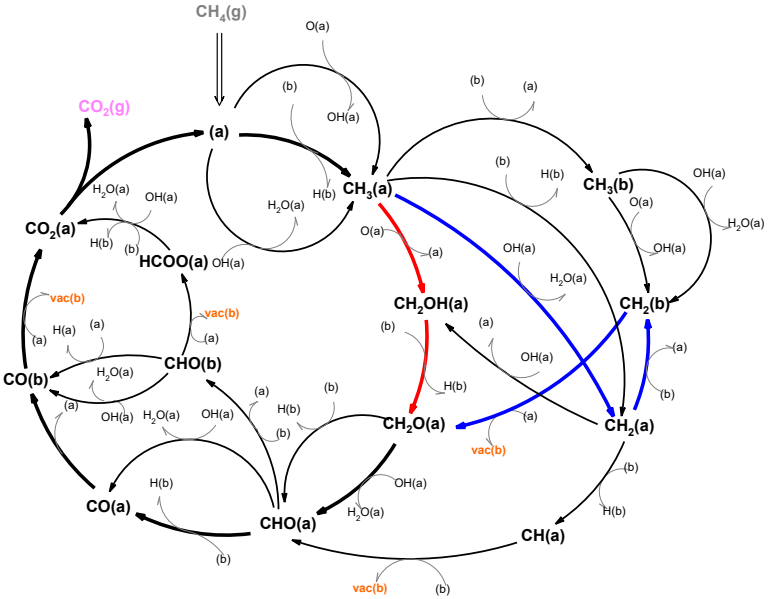

Figure 4: Schematic of the considered C_1-pathways containing carbonaceous CH_xO_y intermediates. *Red arrows*: indicate the preferential reaction pathway at dry conditions before light-off (low temperature path). *Blue arrows*: preferential reaction path after light-off at dry and mainly during wet conditions (high temperature path). *Black bold arrows*: common preferential reaction pathway. Adapted from Stotz et al. [2].

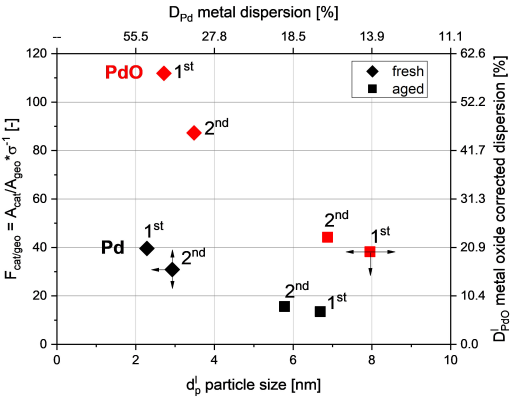

Figure 5: Metal dispersions and related parametric model input values of $F_{\mathrm{cat/geo}}$ (black symbols = Pd, red symbols = PdO (oxide corrected values)). Measurements determined from CO TPD for fresh state (◆ = fresh) and after the series of light-off experiments (■ = aged). Each measurement consecutively repeated (1^{st} and 2^{nd}). From Stotz et al. [2].

conversion region in case of the dispersion corrected simulation, resembles the experimental light-off curves more closely. The results imply that activity losses caused by immediate water inhibition (light-off shift) and gradual deactivation need to be distinguished, mainly because these two processes appear on a much different time scale. An analysis of the reaction network including analysis of the most abundant intermediates, a reaction path analysis and a degree of rate control sensitivity analysis show that hydroxide formation on coordinatively undersaturated oxygen sites, via $(\mathrm{H})_{\mathrm{O(cus)}}$ species, plays a central role for the immediate water inhibition effect. However, the gradual water deactivation cannot be explained as a consequence of a gradual hydroxide build-up. The DFT based PdO mechanism lags in describing this effect, because neither shape change effects of the PdO particles as function of the gas-phase chemical potentials nor changes related to the active facet during light-off, have been considered in the model. These effects likely contribute to the water deactivation effect.

Influence of the degree of oxidation on conversion during light-off cycling

Figure 7 compares an experimental light-off cycling curve at lean conditions from Groppi et al. [11] with simulated results obtained with both the developed mechanisms incorporating a degree of oxidation model with sectoral Pd to PdO particle growth mode. The processes during cooling the catalyst from high towards low temperatures are summarized below:

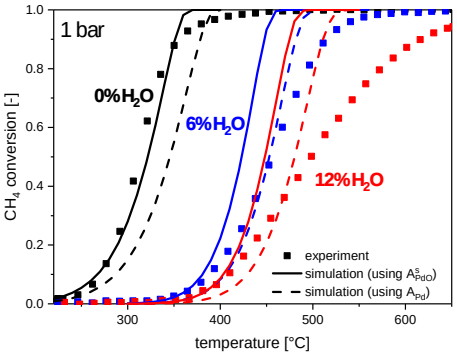

Figure 6: Simulated and experimental light-off curves at different feed conditions: 1000 ppm CH_4, 10 vol.-% O_2, 0-12 vol.-% H_2O, N_2 balance to 1 bar. Simulations at different H_2O feed concentrations, taking into account oxide corrected metal dispersions. Adapted from Stotz et al. [2].

(1) **Thermally reduced Pd:** Above ca. 800 °C the Pd phase of the catalyst is in a thermally reduced state at a particle size of ca. 65 nm. The surface is adequately empty and surface reactions proceed fast, resulting in a high conversion rate for methane oxidation.

(2) **Oxygen passivated Pd surface:** Cooling below 800 °C the surface gets increasingly blocked through strongly adsorbed oxygen species resulting in passivisation of the active sites on the surface and decreasing activity.

(3) **PdO phase formation onset:** Below 600 °C oxygen diffused into the bulk of the Pd particles, leads to the formation of a secondary PdO phase. The formation starts along the grain boundaries leading to a sectoral arrangement of aggregated Pd/PdO particles. Even though the temperature is lowered, activity keeps up rising due to the onset formation of highly active PdO, exposed to the surface.

(4) **Redispersion of aggregated PdO/Pd particles:** Activity keeps up rising upon further decrease in temperature. At the same time PdO/Pd particles start to redisperse due to morphological changes of the particles during oxide phase formation. Thus, contributing to a higher activity, due to a further increase in the catalytic active surface area for PdO.

(5) **Peak activity during cool down:** The regaining activity cycles through its maximum around 450 °C. Nearly all palladium is present as PdO. The particle size shrinks to ca. 25 nm due to redispersion and break-up.

(6) **Activity decrease/light-out:** Finally, activity starts to fall again, since light-out temperature has been reached for the PdO phase. Simultaneously,

particles start to break-up further, leading to particle fragmentation into cauliflower like structures possessing a high catalytic active surface area.

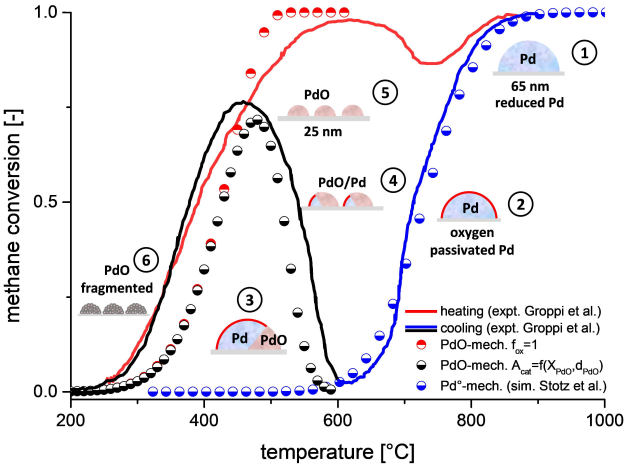

Figure 7: Simulated CH_4 light-off (red symbols) and light-out (black/blue symbols) under fuel-lean conditions (C/O-ratio = 0.125) within an annular reactor configuration. Experimental temperature programmed combustion data for heat-up (red line) and cool-down (blue/black lines). Experimental data adapted from Groppi et al. [11]. Figure adapted from Stotz et al. [2].

Contents

1 Introduction

1.1 Motivation and Importance

The increasing anthropogenic greenhouse gas emissions, in particular carbon dioxide (CO_2), released into the atmosphere over the last century, have caused the onset of climate change which affects the livelihood of humankind and nature. The existing energy system, based primarily on fossil fuels as primary energy carriers, will have to undergo a significant transformation process, in order to stop or decelerate the increase of CO_2 concentrations in the atmosphere. A successful decarbonization of the energy system (Energiewende) will have to affect all relevant energy related sectors responsible for CO_2 emission sources, including mainly industry, transportation, private households, and business, trade and services, respectively. Since, solar and wind energy are expected as one of the main future energy suppliers, replacing fossil fuel based power plants, those produce electricity as primary energy carrier. Due to the nature of these new energy sources, the electric energy supply is volatile. Thus, the aforementioned approach requires that:

- The energy system is sufficiently dimensioned. In case of an oversupply of electricity, the energy can be adequately stored and is ready to use once an under supply/over-demand, due to the absence of wind or solar radiation occurs (energy storage and supply).
- The electric energy can be coupled into all sectors of the energy infrastructure system (sector coupling).

A main challenge arises within the transportation sector where mechanical energy is the main required form of energy in order to drive all sorts of cars, ships or trucks. Electrification of the power train seems to be a primary option for decarbonization of the transportation sector. However, an alternative sector coupling option arises, with the power-to-fuel (P2F) technology (e.g. power-to-gas (P2G), power-to-liquids (P2L)), which enables the production of hydrogen and hydrocarbon based fuels (e.g. H_2, CH_4, Diesel) of high energy density from electricity, produced from renewable energy sources by water splitting

electrolysis into hydrogen and subsequent hydrogenation of CO_2 as obtained from the environment air or other process related waste sources. The P2F technology proves to be beneficial in situations when an oversupply of renewable wind or solar energy is present, as the surplus energy can be conveniently harvested and stored in form of synthetic fuels over long periods of time, instead of decoupling wind mills or solar cell farms from the energy grid in case of an overload. Additionally, the existing transportation infrastructure can be beneficially used to transport and supply the synthetic fuels to the consumers. In this regard, methane seems to be an advantageous supplementary fuel resource, because existing infrastructure and natural gas-fueled devices can be conveniently used and other devices can be (re-)build with less effort to operate based on methane (natural gas). The usage of methane or natural gas (NG) as a supplementary fuel resource, is also driven by the enhanced production of shale gas, and the flexible availability from a range of other, both renewable- and fossil-fuel-based sources such as bio-gas and methane hydrates, and has also a profound effect on related industrial applications [3]. Methane powered gas-engines produce less CO_2 emissions, in comparison to their diesel- or gasoline-fueled counterparts. Thus, even in the case when methane is not CO_2-neutrally obtained, it provides a direct measure to lower the extend of the existing CO_2-emissions as well as pollutants from the transportation sector, by replacing existing diesel or gasoline powered devices.
However, since methane is a potent greenhouse gas exposing a global warming potential (GWP) to the environment which is ca. 25 times higher than that of CO_2 over a 100 year time horizon [4], necessitating an efficient, durable and clean exhaust gas emission control system in order to fulfill upcoming stringent hydrocarbon (HC) emission regulations and to eliminate methane slip from natural-gas driven lean-burn engines [1].

The abatement of methane via catalytic oxidation to achieve full conversion at low temperatures and lean-burn conditions has therefore been studied extensively in the literature [12–17], because it offers environmental advantages as NO_x, particulate matter, SO_x and other unburned hydrocarbon (HC) emissions are greatly reduced as compared with conventional devices [1].

Palladium-based catalysts have proven to be good oxidation catalysts for the purpose of catalytic oxidization of methane. Therefore, the understanding of the detailed kinetics of the catalytic (partial and total) oxidation of methane over the palladium catalyst system is essential to improve and optimize catalytic emission control systems as well as the efficiency of microreactors [1].

The applicability of microkinetic models (MKM) for kinetic model predictions in technical applications is however, difficult to realize. Such models are numerical

demanding for the purpose of e.g. on-board control and diagnostics, and should ideally only capture intrinsic kinetic effects of the corresponding catalyst phase. This lays the ground why many kinetic modelling studies frequently focus on global kinetic modeling, fitted against experimental data to the exact conditions and the specific catalyst, than using microkinetic models [18–22]. However, fitted parameter sets of global kinetic models obscure the physics behind the apparent kinetic behavior of the catalyst. Oftentimes effects of transport, kinetics, support and an altered catalyst structure are lumped into a small pseudo-kinetic parameter set for the global model. For those situations however, when it is relevant to study the interplay between kinetics and e.g. catalyst deactivation through structural changes of the catalyst or other related factors, it may be beneficial to use MKMs as with those it is possible to compare and distinguish contributions from the intrinsic kinetic behavior of the catalyst model with the observed structural and/or deactivation effects seen in experiments [2].

2 Overview - Methane Oxidation and the Palladium System[1]

2.1 Methane Oxidation

Oxidation of methane proceeds differently under fuel-lean or fuel-rich conditions and further consequent reactions of the products with methane are also possible. The different overall reactions and their corresponding reaction enthalpies are shown in Tab. 2.1. The two main oxidation reactions R_{o1} and R_{o2} show distinctive heats of reaction, which is in the case of the total oxidation highly exothermic and comparatively mildly exothermic for the partial oxidation of methane. On the contrary, the steam reforming reactions (R_{o3-4}) represent endothermic conversion routes. The table with the main conversion paths (global reactions) also emphasizes the importance of the water-gas-shift (WGS) reaction when syngas products (H_2 and CO) during partial oxidation form in conjunction with the total oxidation products (H_2O and CO_2).

2.2 The Complex Palladium System

Pd-based catalysts are generally considered to be good oxidation catalysts and have therefore been the focus of interest for catalytical oxidization of methane [23–27]. For this purpose, Pd/Al_2O_3 catalysts have proven to be most active when compared with other monometallic-supported noble metal catalysts [28, 29] under dry reaction conditions.
The topic has been broadly reviewed by a number of authors over the past two

[1] Parts of this chapter and its subsections have been taken from [1] H. Stotz, L. Maier and O. Deutschmann, Methane oxidation over palladium: on the mechanism in fuel-rich mixtures at high temperatures, *Top. Catal.*, 60 (2017) 83–109 and from [2] H. Stotz, L. Maier, A. Boubnov, A. T. Gremminger, J.-D. Grunwaldt and O. Deutschmann, Surface reaction kinetics of methane oxidation over PdO, *J. Catal.*, 370 (2019) 152–175.

Table 2.1: Important net conversion paths during the (autothermal) oxidation of methane. Table adapted from Stotz et al. [1].

#	Reaction	Reaction Enthalpy [kJ/mol]	$\left(\frac{C}{O}\right)_{\text{stoic}}$
	Methane Total Oxidation (CTOX)		
$R_{o,1}$	$CH_4 + 2O_2 \rightleftharpoons CO_2 + 2H_2O$	$\Delta_R H^0_{298\,K} = -880$	0.25
	Methane Partial Oxidation (CPOX)		
$R_{o,2}$	$CH_4 + \frac{1}{2}O_2 \rightleftharpoons CO + 2H_2$	$\Delta_R H^0_{298\,K} = -35.6$	1.0
	Methane Steam Reforming (SR)		
$R_{o,3}$	$CH_4 + H_2O \rightleftharpoons CO + 3H_2$	$\Delta_R H^0_{298\,K} = 205.9$	1.0
$R_{o,4}$	$CH_4 + 2H_2O \rightleftharpoons CO_2 + 4H_2$	$\Delta_R H^0_{298\,K} = 164.7$	0.5
	Water-Gas-Shift (WGS)		
$R_{o,5}$	$CO + H_2O \rightleftharpoons CO_2 + H_2$	$\Delta_R H^0_{298\,K} = -41.2$	1.0

decades [13, 28, 30–34]. Several studies focus on the catalytic activity of Pd for oxidation of other light HCs such as ethane, propane, propene or butane as well as carbon monoxide [14–16, 26, 35] and therein involved changes in the chemical state of Pd depending on the type of the reducer.
However, the complex redox behavior of Pd and the concomitant change in the nature of the active sites under reaction conditions is still not well understood yet. The reversible PdO-Pd-transformation plays the key role and involves changes in the morphology, structure and oxidation state, leading to a distribution of differently oxidized PdO species depending on the pretreatment and history of the reaction conditions to which the catalyst was exposed to [6, 30].

2.2.1 PdO ↔ Pd Interconversion Phenomena

Accordingly, the phase transformation also influences the surface energetic, leading to different binding energies of surface intermediates and activation energy barriers for the reaction steps of the methane oxidation. Many experiments show that PdO is more active than reduced Pd in oxidizing CH_4, as the mechanism itself changes during the course of the phase transformation [36, 37]. It is suggested that the reaction via the oxide phase follows a redox mechanism related to a Mars-van-Krevelen-type mechanism [38], whereas the reaction responsible for oxidizing CH_4 via the reduced phase of Pd seems to be a Langmuir-Hinshelwood mechanism with competitive adsorption of O_2 and CH_4. Zhu and Ribeiro et

al. [24] state that the reaction kinetics on Pd differs from that on PdO, suggesting that the reaction mechanism is different. These examples emphasize the need for separate reaction mechanisms over the reduced Pd and the oxidized PdO phase.

2.2.2 Conversion Hysteresis

The influence of the Pd oxidation state on the conversion activity for the complete oxidation of methane via alumina-supported Pd catalysts has been investigated by analyzing temperature-programmed oxidation and reduction (TPO/TPR) cycles and conducting thermogravimetric analysis (TGA). In this context, Farrauto et al. [39] first reported about the anomalous hysteresis behavior in the rate of CH_4 oxidation upon heating and cooling, caused by the temperature gap between the thermal decomposition temperature of PdO during heating and the Pd re-oxidation temperature during cool down of the reaction. A lower activity was found at higher temperatures during heating and a higher activity at lower temperatures during cool down. Whether the activity recovery stems from a surface area increase and/or the formation of PdO, respectively, has been discussed in the literature [40].

2.2.3 Oscillatory Behavior

The strong exothermicity during the total oxidation of methane can lead to an auto-thermal-reduction of the PdO phase and subsequent self-inhibition of the reaction due to exposure of the less active metallic Pd phase [41]. Once the temperature of the catalyst, in its inactive reduced state, has reached a threshold temperature low enough for the catalyst phase to re-oxidize, the activity increases due to formation of the more active oxidized form and the temperature begins to rise again. This behavior can lead to oscillations in the concentrations of reactants and product species.
Similar observations have also been recorded during the experiments on the spacial resolved measurements in this work (cf. Fig. 2.1), but have not been detailed further as this was not main focus of this thesis.

The identification of the different PdO species during the thermal decomposition has been controversially discussed by Farrauto et al. [39] and McCarty [42]. Investigations by Groppi et al [6, 43] on alumina-supported PdO under different concentrations of oxygen have shown a thermodynamically controlled process

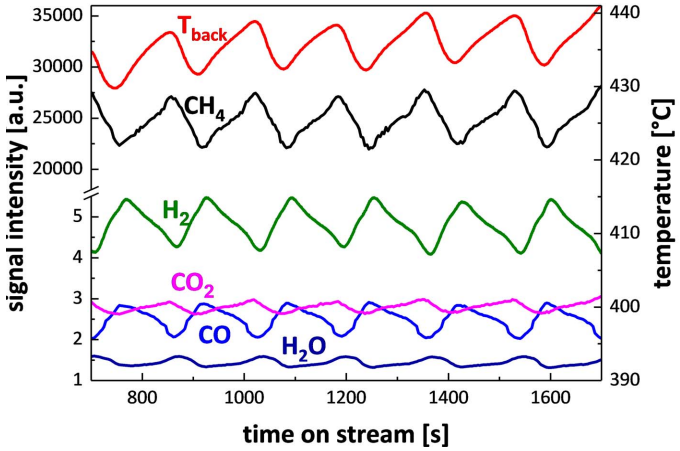

Figure 2.1: Self-oscillatory behavior observed during measurements at the syngas test bench for spatial resolved (SpaciPro) experiments at ITCP. Oscillations started once the N_2-dilution was increased from 80 % to 90 % at a constant C/O feed-ratio (methane to oxygen ratio) of 0.8 and a total volumetric inlet flow rate of 4 SLPM.

which occurs sequentially. Each decomposition step was associated with a corresponding PdO species of different thermal stability. A first low-temperature step has been associated with PdO species interacting with metallic Pd, while a second step at higher temperatures was due to bulk PdO decomposition. A third step at high temperatures was related to PdO, strongly interacting with the support. Chen and coworkers [44] studied systematically the temperature-programmed decomposition of PdO and concluded that the two-step decomposition is a characteristic feature of a certain PdO particle size range. The first decomposition step being initiated at the surface of the PdO particles forming a Pd-shell structure. Chen et al. suggest that based on their data, the metastable core-shell structure causes the delayed second decomposition peak at higher temperatures, due to epitaxial and strain effects of the surrounding Pd-shell with the underlying PdO lattice.

2.3 Overview on the Reduced Palladium Phase

An important aspect when observing Pd catalysts is the order dependence on the reaction rate and the Pd activity towards CH_4 conversion. Different reaction orders have been reported depending on the nature of the active sites and the operating conditions. Ribeiro et al. [37, 45, 46] reports reaction order dependencies on PdO to be $n_{CH_4} \approx 1$, $n_{O_2} \approx 0$ and $n_{H_2O} \approx -1$, following a Mars-van-Krevelen-type mechanism, where the first-order dependency in methane indicates that the C-H bond activation step in CH_4 is rate-limiting and the negative dependence on H_2O points to product inhibition by water.

The situation over the reduced phase of Pd differs from that over PdO and the order dependency is less straightforward, as most studies look at conditions where the oxidized phase of the catalyst is stable. Conditions where the reduced phase of Pd is the only present phase on the surface are not easily examined under reaction conditions. One reason is the facile formation of surface oxides PdO_x under lean conditions and the concomitant appearance of mass-transport limitations and pronounced temperature gradients at elevated temperatures, which complicates kinetic measurements in a differential manner.

For example, Ciuparu et al. [47] observed in a pulse experiment an increase in CH_4 conversion upon switching the reaction mixture at 680 °C from fuel-lean (4 % O_2, 1 % CH_4 in He) to fuel-rich (0 % O_2, 1 % CH_4 in He), concluding consistency with a "-1" reaction order dependence with respect to O_2. Similarly, Lyubovsky et al. [48] found in a flow reactor study at 760 °C with a reaction mixture of varying amounts of oxygen and 3 % CH_4 in N_2, after sufficiently lowering the O_2 pressure

from 8 % to 6 % a sudden increase in methane conversion, concluding PdO decomposed into metallic Pd. Conversely, the reaction orders for the turnover rate of CH_4 with respect to CH_4, O_2 and H_2O at high temperatures (933 K to 1003 K) and fuel lean conditions (C/O-ratios $\sim$ 0.1, $p_{O_2} \sim 3.07$ mbar) have been reported by Ribeiro et al. [24], showing a near first-order rate-dependence in CH_4 ($n_{CH_4} \approx 0.7$) and near zero-order dependence in O_2 and H_2O ($n_{O_2} = -0.1, n_{H_2O} = -0.1$), when the bulk state of a Pd-foil catalyst was found in the metallic state. The authors explain the unusual zero-order dependence in oxygen over reduced Pd by pointing out that the oxygen surface coverage is one monolayer (ML). However, it should be noted here, that despite the reduced state of the Pd bulk, the presence of surface oxides was found through XPS [24], which could give an additional explanation for the zero-order dependence in oxygen.

Under conditions where the reduced state of Pd is stable, the observed first-order methane rate dependency point to the fact that the first C-H bond cleavage during the CH_4 activation process is rate limiting. The zero-order dependence in O_2 at lean conditions gives rise to the assumption that adsorbed oxygen species strongly cover the Pd metal surface. In contrast, during rich conditions when the surface is less saturated with oxygen, competitive adsorption between CH_4 and O_2 can explain the negative first-order oxygen rate dependence. Similarly, Iglesia and coworkers [36, 49] observed different kinetic regimes when comparing the pseudo-first-order rate coefficient $\left(k^{1st}_{CH_4} = \tilde{R}_{CH_4} \cdot (p_{CH_4})^{-1}\right)$ for the methane oxidation reaction at a wide range of different O_2 pressures. The rate constant showed a proportional dependence at low ($<$ 0.2 kPa) and an inversely proportional dependence at higher O_2 pressures (0.2 kPa to 0.4 kPa). Upon further increasing the oxygen chemical potential the rate constant became independent of O_2 pressure. These examples show, that the observed activity of Pd towards CH_4 oxidation during the different regimes changes markedly.

2.4 Overview on the Oxidized Palladium Phase

Under fuel lean conditions and temperatures below 600 °C the catalyst is typically present in its oxidized form. However, supported palladium catalysts have their limitations regarding activation of methane and the manifold aspects that have been observed in this system:

- the impact of the catalyst long term stability onto the catalytic methane oxidation activity has been reported under dry and wet conditions [17, 50–52],

- the Pd oxidation state plays a crucial role for the activity [11, 36, 53],
- the reaction gas-mixture influences the total oxidation activity of the Pd-based catalyst system [54–57] and affects the rate of Pd sintering [58, 59] and aging [60];
- oscillations in the rate of methane oxidation have been observed depending on the oxygen-to-methane feed ratio [41, 61–64],
- the methane oxidation activity and its turnover frequency have been claimed to be a function of the Pd particle size [65, 66],
- the effect of Pd loading for a Pd/SiO_2 catalyst was studied [67] and showed to influence the methane conversion light-off temperature after the catalyst was hydrothermally aged.
- the autoreduction of the PdO phase has been observed at elevated temperatures [39, 68, 69].

A number of other studies have analyzed the influence of the catalyst support and its related oxygen mobility onto the oxidation reaction [47, 52, 70–73] or the role of OH species on the support, impeding the exchange of oxygen between PdO particle and support [50, 74–76].

Scheffler et al. [77, 78] identified from a constrained Wulff polyhedron the PdO(100) surface as the thermodynamically most stable configuration amongst all low-index (1x1) PdO terminations right followed by PdO(101). However, the C-H bond activation barrier in methane over PdO(101) is comparatively lower than on PdO(100) [79, 80]
Other DFT based studies focus on the oxidation process in particular the transition from surface to bulk oxide under oxygen-rich conditions [81]. Seriani et al. show that the PdO(101) surface oxide grown as an overlayer structure onto a Pd(100) film is the most stable orientation of a grown oxide film at any thickness. Jelic et al. [82] points out that based on the work of Lundgren et al. [78] transformation of the surface oxide into a bulk oxide is kinetically limited while the surface oxide seems to be the best model to describe in their case NO oxidation for Pd surfaces. In a DFT study by Hensen et al. [83] shape and stability effects of Pd nanoparticles were analyzed, under various oxygen-rich/lean conditions. For particles $> 5\,\text{nm}$, the calculations show that at high oxygen chemical potentials reduced Pd cubes will expose mainly (100) faces which are in turn stabilized via the formation of a PdO(101) overlayer structure. An experimental in situ high pressure x-ray photoelectron spectroscopy (HPXPS) study on Pd particles in the range of 15 nm to 35 nm supported on SiO_x showed similar ultra thin surface oxides under oxidizing atmospheres upon heating from room temperature to

250 °C [41]. The limiting film thickness of PdO(101) thin film oxides, to achieve the necessary ligand effect responsible for lowering the initial C-H bond dissociation barrier in methane, have also been under investigation [79, 80]. Accordingly, a few multiple layers of PdO(101) are already effective in decreasing the barrier significantly.

Aforementioned results have led several groups to study kinetics and energetic interactions on PdO(101) regarding methane [84–86] and alkane [85, 87] activation, H_2O [88], NO [89] and CO adsorption [90–92].

3 Approach and Objectives[1]

The objective of this work focuses on the development of the surface reaction kinetics for the catalytic partial and total oxidation of methane, under conditions where either reduced palladium or oxidized palladium is the prevalent stable catalyst phase. Palladium-based catalysts are typically used in technical exhaust gas abatement systems for natural gas (NG) driven engines of stationary and mobile systems due to their prominent total oxidation activity towards methane. In this context, an improved experimental and model based understanding on the kinetics of the methane oxidation reaction over palladium-based catalysts is crucial, in particular to improve technical applications. A fundamental understanding of the reaction mechanism is also important, in order to describe the complex behavior of the Pd catalyst in this system.

Since, the nature of active phases of the palladium catalyst structure is complex, as has already briefly outlined in the preceding chaper 2, this work approaches the problem systematically in a 2-folded way by considering different kinetic schemes for each phase at a first glance. In a second step, after separate development and validation of the kinetic schemes over their single respective phases (cf. chapters 5.2 and 5.3), a combined model validation is performed with experimental data for thermal light-off cycling (cf. chapter 6.3), considering interphase transformation between reduced and oxide phase.

This work aims to be comprehensive on the subject in the sense that a broad range of different experimental and theoretical methods are used in conjunction with information gathered from already existing studies (cf. Fig. 3.1), in order to complement missing pieces needed and to characterize the model catalyst system adequately, obtaining the necessary information for the development of the mechanisms, the required input data for simulation and finally their validation. The different relevant aspects of the reaction system are highlighted in the preceding chapters.

[1] Parts of this chapter have been taken from [1] H. Stotz, L. Maier and O. Deutschmann, Methane oxidation over palladium: on the mechanism in fuel-rich mixtures at high temperatures, *Top. Catal.*, 60 (2017) 83–109 and from [2] H. Stotz, L. Maier,

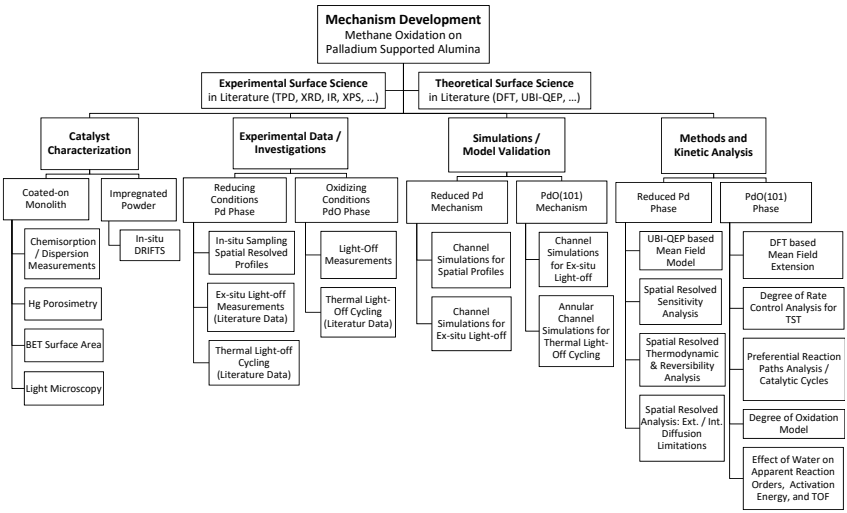

Figure 3.1: Overview on the building blocks used in this thesis for the development of the reaction mechanisms.

The developed surface reaction mechanism for the reduced phase of Pd is evaluated by comparison of simulated species profiles in a catalyst channel with experimentally obtained axially resolved species concentration profiles. This, e.g. was done by applying the in situ sampling technique within a commercial Pd/Al_2O_3-coated cordierite honeycomb monolith, operated under quasi-autothermal conditions. The development of the mean-field kinetic scheme was achived iteratively by applying semi-empirical methods such as UBI-QEP for the energetic barriers and binding energies of the steps and species, respectively. Additionally, where necessary for bridging the gap of model accuracy, experimental and first-principle DFT derived data on considered species and steps were taken into account.
Additionally, a mean-field extended MKM was developed based on first-principles density functional theory (DFT) data for PdO(101) [10]. This mechanism was also tested with the objective to study whether the mean-field extension can sufficiently mimic relevant kinetic aspects for the methane oxidation over the oxide-phase. The proposed model considers the presence of various sites on the PdO surface. The model also attempts to account for the changes in particle size during thermal light-off cycling and the metal-oxide interconversion during cool down, addressing the dynamic and the structural transition during light-off. A combination of approaches including microkinetic modelling, light-off studies and in situ diffuse reflectance-fourier transform infrared spectroscopy (DRIFTS), are used to identify the mechanism behind the methane oxidation reaction over the PdO surface. A central aspect of this part of the work is the water inhibitory effect [55] and the resulting deactivation, as seen during the catalytic light-off, including involved changes in dispersion, the preferred reaction pathways, apparent activation energies and reaction orders. The influence of pressure on the kinetics and deactivation of the catalyst with respect to the microkinetic model is also discussed. Alongside with the MKM results, supplementary in situ DRIFTS results of different reactive gas-mixtures containing various types of C_1-compounds (methane, methanol and formic acid) are analyzed regarding active surface intermediates, participating in the mechanism.

A. Boubnov, A. T. Gremminger, J.-D. Grunwaldt and O. Deutschmann, Surface reaction kinetics of methane oxidation over PdO, *J. Catal.*, 370 (2019) 152–175.

4 Experimental Investigations[1][2]

This chapter presents an overview on the experiments, the setups used for conducting the experiments, including measurement procedures, catalyst pretreatments and investigated reaction and operating conditions. The catalysts used in this work and its characterization is also examined. Finally, experimental results are presented and discussed.

4.1 Catalysts and Characterization

4.1.1 Palladium on Alumina Powder Catalyst

The Pd/Al_2O_3 catalyst (Pd loading 2.4%) for the DRIFTS experiments was previously prepared at ITCP by incipient wetness impregnation of γ-Al_2O_3 with a basic aqueous solution of tetraamminepalladium(II) nitrate, dried and calcined at 600 °C. Characterization of the catalyst by XRD, TEM and XAS has revealed that fully oxidized PdO particles of around 5 nm are well-dispersed on the surface of γ-Al_2O_3 [93]. The in-house prepared sample powder has been characterized by DRIFTS measurements. The catalyst powder used for the measurements was present in a sieve fraction of 125 µm to 250 µm.

[1] Parts of this chapter and its subsections have been taken from [1] H. Stotz, L. Maier and O. Deutschmann, Methane oxidation over palladium: on the mechanism in fuel-rich mixtures at high temperatures, *Top. Catal.*, 60 (2017) 83–109 and from [2] H. Stotz, L. Maier, A. Boubnov, A. T. Gremminger, J.-D. Grunwaldt and O. Deutschmann, Surface reaction kinetics of methane oxidation over PdO, *J. Catal.*, 370 (2019) 152–175.

[2] Experimental work conducted at ITCP for the purpose of this thesis were supported by A. Boubnov (DRIFTS characterization and powder catalyst preparation), A. Gremminger (light-off measurements), K. Schäfer (CO chemisorption measurements), C. Antinori and A. Ünal (spatial resolved profiles), I. Zellner (light microscopy). Experiments conducted elsewhere at KIT and subject to this thesis were supported by A. Burcea (CVT, Hg-porosimetry) and T. Bergfeld (IAM-WET, elemental analysis).

4.1.2 Palladium on Alumina Coated on Monolith Catalyst

The catalyst studied for spacial resolved measurements and light-off activity tests is a washcoated cordierite honeycomb monolith of 600 cpsi, with a Pd loading of 30 g/ft^3 dispersed in Al_2O_3. The catalyst was provided by the catalyst manufacturer Umicore AG & Co. KG. The complete set of catalyst parameters is given in Tab. 4.1. The same catalyst has been used by the group in a previous study on methane oxidation over the reduced phase of Pd [5]. The Pd metal dispersion on the coated monolith, as given from the earlier study was equal to $\sim 23\,\%$, and was determined from CO chemisorption measurements. Thus, the same value was assumed to be given for the herein conducted spatial resolved measurements on the reduced phase of Pd. Values for the light-off experiments on the oxidized phase of Pd were determined separately. Dispersions for both experiments are summarized in Tab. 4.3 while geometric dimensions of the monoliths are summarized in Tab. 4.2.

CO Chemisorption Measurements

The overall Pd metal dispersion of the monolithic sample was estimated using temperature programmed desorption (TPD) of CO under continuous flow of 500 mL/min on an in-house built setup [94]. The sample was placed in a tubular quartz glass reactor. Prior to the measurements, the catalysts were pre-treated in air for 15 min at 400 °C, followed by a reduction in 4 % H_2/N_2 at 400 °C for 30 min. Subsequently, the reactor was rapidly cooled down to room temperature under N_2 flow. After saturating the catalyst with 1 % CO/N_2 for 1 hour, weakly adsorbed CO was removed by purging the reactor with pure N_2 for 45 min. TPD in a N_2 flow was performed by linearly ramping the temperature at 20 K/min up to 550 °C. Gas concentrations of CO and CO_2 evolved during TPD, were monitored by an NDIR detector (BINOS1000). For determining a principal value of the Pd metal dispersion (D_{Pd}), a CO:Pd adsorption stoichiometry of $\alpha_{\mathrm{Pd}} = 1:1$ was assumed [70, 95, 96]. Calculations are based on

$$D_{\mathrm{Pd}} = \alpha_{\mathrm{Pd}} \cdot \int x(t) \cdot dt \cdot \dot{V} \cdot \left(\frac{p}{RT}\right) \cdot \left(\frac{M_{\mathrm{Pd}}}{L_{\mathrm{Pd}} \cdot V_{\mathrm{cat}}}\right) \tag{4.1}$$

with, x the evolved mole fraction during TPD, $\dot{V}$ the volumetric flow rate of the sampled gas stream, $P = 1.013\,\mathrm{bar}$, $T = 291.15\,\mathrm{K}$, R the universal gas constant, $M_{\mathrm{Pd}} = 106.42\,\mathrm{g/mol}$, the molecular weight of Pd, L_{Pd} the Pd catalyst loading with respect to the monolithic catalyst sample volume, V_{cat}. The average palladium particle size and the related catalytic active surface area

Table 4.1: Catalyst parameters of the Pd/Al_2O_3 monolith assuming a square channel geometry. Table adapted from Stotz et al. [1].

Parameter	Symbol	Value	Unit
Cells per square inch	N_{cpsi}	600†	[1/in^2]
Wall thickness	δ_{s}	109.22†	[μm]
Washcoat loading	L_{wc}	100†	[g/L]
Washcoat density	ρ_{wc}	1400†	[g/L]
Average washcoat thickness	δ_{wc}	20.7‡	[μm]
Cell size of monolith	s	1037	[μm]
Open width of square channel	a	886*	[μm]
Pd loading	L_{Pd}	1.06†	[g/L]
Mean porosity (macropores)	ϵ_{M}	0.299§	[-]
Mean porosity (mesopores)	ϵ_{m}	0.207§	[-]
Mean pore diameter (macropores)	$d_{\mathrm{p,M}}$	1.5§	[μm]
Mean pore diameter (mesopores)	$d_{\mathrm{p,m}}$	10§	[nm]
Tortuosity	τ	3$^{\diamond}$	[-]
BET surface area	S_{BET}	29$^{\perp}$	[m^2/g$_{\mathrm{monolith}}$]
Surface site density of Pd	Γ_{Pd}	2.09×10^{-9}	[mol/cm^2]

† Value provided by catalyst manufacturer UMICORE.
‡ Value was determined from LMI.
* Value was calculated with Eq. (5.19).
§ Value was determined from Hg-Porosimetry.
$^{\diamond}$ Estimate.
$^{\perp}$ Value communicated by A. Gremminger as determined from N_2 chemisorption with the monolith sample.

Table 4.2: Geometry parameters of the Pd/Al_2O_3 monoliths.

Parameter	Symbol	Spacial Profiles	Light-off Expts.
Length of monolith	L	10 mm	50 mm
Diameter of monolith	D	18.5 mm	20 mm
Number of channels	N_{ch}	250	292
Geometric surface area	$A_{\mathrm{geo,ch}}$	31.4 mm^2	157.1 mm^2

of the pre-reduced catalyst for a single channel have been determined based on the hemispherical particle assumption [97] with $d_{\mathrm{p,Pd}}$ given in [nm] and the measured metal dispersion D_{Pd}:

$$d_{\mathrm{p,Pd}} = \left(6 \cdot \frac{v_{\mathrm{m}}}{a_{\mathrm{m}}}\right) \cdot \frac{1}{D_{\mathrm{Pd}}} \tag{4.2}$$

$$= \frac{1.11}{D_{\mathrm{Pd}}} \tag{4.3}$$

$$A_{\mathrm{Pd}} = \frac{D_{\mathrm{Pd}} L_{\mathrm{Pd}}}{M_{\mathrm{Pd}} \Gamma_{\mathrm{Pd}}} \cdot \frac{V_{\mathrm{cat}}}{N_{\mathrm{ch}}} \tag{4.4}$$

Where v_m =14.7 Å^3/atom, is the molar volume of the face centered cubic (fcc) bulk crystal structure of reduced Pd and a_m =7.93 Å^2/atom, is the unit surface area of the Pd(111) facet [97], N_{ch}, is the number of channels of the monolith sample and Γ_{Pd} =2.09 × 10^{-9} mol/cm^2, the averaged surface site density of the reduced Pd phase [97].

Table 4.3: Pd metal dispersion measured by CO-TPD and PdO metal oxide corrected dispersions assuming preserved hemispherical particle shape upon complete stoichiometric oxidation. Table adapted from Stotz et al. [2].

Catalyst State	D_{Pd} [%]	$d^{\mathrm{l}}_{\mathrm{Pd}}$ [nm]	D_{PdO} [%]	$d^{\mathrm{l}}_{\mathrm{PdO}}$ [nm]
cf. [5]	23	4.8	28	5.7
Fresh, 1$^{\mathrm{st}}$ TPD	48.6	2.3	58	2.7
Fresh, 2$^{\mathrm{nd}}$ TPD	37.9	2.9	46	3.5
Aged, 1$^{\mathrm{st}}$ TPD	16.6	6.7	20	8.0
Aged, 2$^{\mathrm{nd}}$ TPD	19.2	5.8	23	6.9

Hg Porosimetry

Hg intrusion porosimetry has been used to obtain information on the washcoat pore size and porosity (cf. Fig. 4.1). Intrusion curves for the washcoated Pd/Al_2O_3 monolith catalyst were determined (Autopore III 9420, from Micrometrics) at the Institute of Chemical Process Engineering (CVT) at KIT.
Macro- and mesopore volumes (porosities) have been evaluated according the IUPAC classification of pore sizes:

micropores:	$d < 2\,\text{nm}$
mesopores:	$2\,\text{nm} < d < 50\,\text{nm}$
macropores:	$50\,\text{nm} < d$

Macro- and mesopore sizes (pore diameter) were determined from the peak height of the intrusion curve within the corresponding IUPAC size ranges.

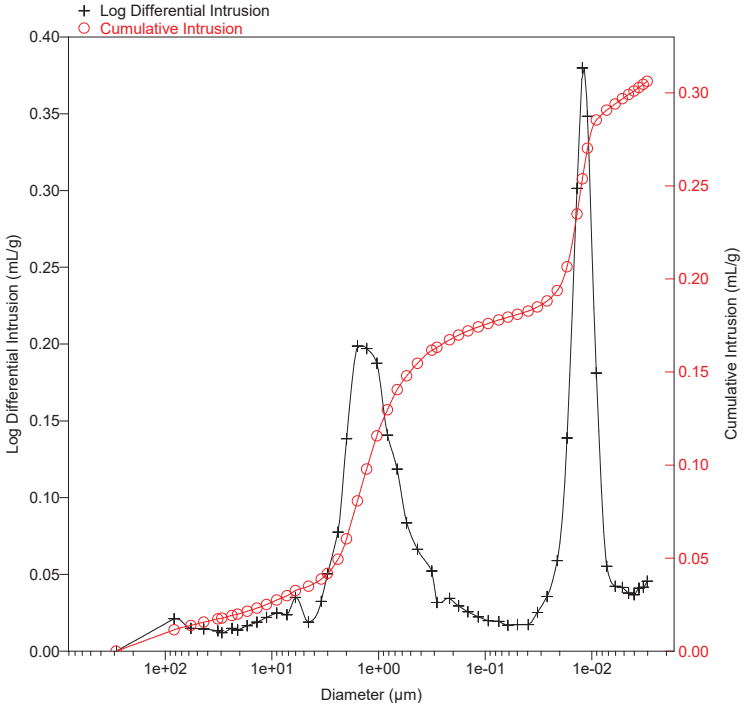

Figure 4.1: Intrusion curves as measured from Hg-Intrusion Porosimetry of the washcoated Pd/Al_2O_3 monolith catalyst. Weight specific values refer to the catalyst sample weight of 0.4485 g. The measurements were performed after the catalyst was regenerated in air.

Elemental Analysis

The monolith catalyst was further tested for impurities at the "Institut für Angewandte Materialien - Angewandte Werkstoffphysik (IAM-AWP), Chemische Analytik" at KIT. Elements tested within the elemental analysis were: Pd, Pt, Rh, Ce and Zr. The corresponding concentrations found are presented in Tab. 4.4. Amongst the elements tested for no significant impurities besides the expected Pd phase were found.

Table 4.4: Elemental Analysis of the washcoated Pd/Al_2O_3 catalyst.

Element	Quantification limit [wt.-%]	concentration [wt.-%]	standard deviation [wt.-%]
Zr	0.0002	0.0061	0.0001
Rh	0.001	< 0.001	
Pd	0.004	0.220	0.005
Ce	0.002	< 0.002	
Pt	0.0004	< 0.0004	

Light Microscopy Images

Additional light-microscopy images at different magnifications have been taken in order to visualize the nonuniform situation of the washcoat thickness within the catalyst channels (cf. Fig. 4.2).

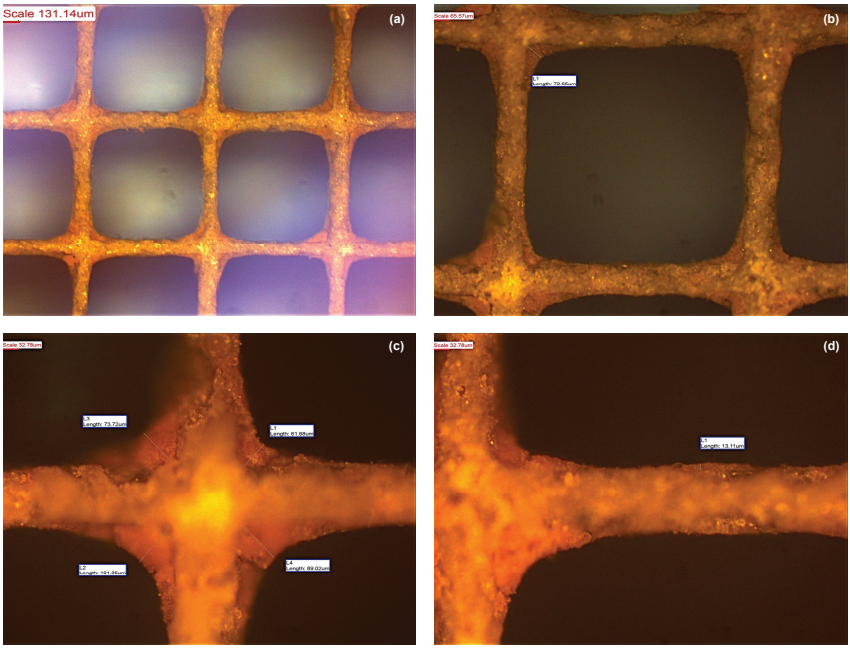

Figure 4.2: Light microscopy images of the washcoated Pd/Al_2O_3 monolith catalyst at different magnifications: (a) 25x, (b) 50x, δ_{wc} at corner: 73 nm, (c) 100x, δ_{wc} at corners: 61 nm, 73 nm, 89 nm and 101 nm, (d) 100x, δ_{wc} at edge 13 nm.

4.2 Experimental Setup

4.2.1 Setup for In Situ DRIFTS Measurements

DRIFTS spectra were recorded on a Bruker VERTEX 70 spectrometer equipped with diffuse-reflectance optics (Praying Mantis, Harrick) and an in situ cell (Harrick) for heating in a gas flow. The catalyst sample powder was placed in the sample cup (6 mm diameter and 3 mm depth) and the cell was closed with a dome cover with KBr windows. The gas passed the sample from the top of the cup and exited through a wire mesh at the bottom. Gases (Air Liquide, purity 5.0) were dosed using mass flow controllers and mixed before being directed to the cell. Liquid components (methanol and formic acid) were dosed via saturators by bubbling a portion of the gas flow through it. The gas composition at the exit of the cell was analyzed by mass spectrometry. For the wet reaction mixture, water was dosed via a heated bubble column saturator.

4.2.2 Setup for Light-off Measurements

An in-house built laboratory test bench was used for activity measurements on a Pd/Al_2O_3 catalyst with $30\,g/ft^3$ noble metal loading and 600 cpsi. The monolithic sample with $D = 20\,mm$ in diameter and $L = 50\,mm$ length was placed inside of a plug-flow reactor made from coated stainless steel and fixed with quartz glass wool. Heating was realized by an electrical furnace and temperature was controlled by a Eurotherm 2208 controller with two radially-centered K-type thermocouples placed 3 mm in front and behind the catalyst. The gas mixture was fed by Bronkhorst MFCs and the reaction products were monitored by a FT-IR spectrometer (Multigas 2030, MKS).

4.2.3 Setup for Spatial Resolved Profile Measurements

Spatial resolved experimental measurements were used for evaluating the mechanism. This was accomplished with a lab-scale flow reactor setup, equipped with a movable capillary for sampling gas compositions at various axial locations inside of a catalytic channel of the monolith.
The reactor consisted of a quartz tube positioned in an oven for heating and thermal insulation of the catalyst as well as to provide the initial heat to ignite the reaction. The insertion probe sampling technique, a minimally invasive in situ technique, and the experimental setup used in this study have been

previously described in detail [98].
The monolith ($D = 19\,\text{mm}$, $L = 10\,\text{mm}$) was wrapped in a ceramic fiber sheet in order to avoid bypassing of gases and positioned in the quartz tube ($ID = 20\,\text{mm}$). To minimize heat losses, due to thermal radiation and to create a uniform flow field, uncoated cordierite monoliths were placed as heat shields, with a gap of ca. 5 mm in front (FHS, 600 cpsi, $D = 19\,\text{mm}$, $L = 10\,\text{mm}$), and next to the catalyst downstream, as back heat shield (BHS, 600 cpsi, $\varnothing\,19\,\text{mm}$, $L = 10\,\text{mm}$), respectively.

Similar or related techniques have been applied by a number of other research groups to gather in situ information on the catalytic behavior in various types of lab-scale reactor systems. For example in monoliths [99–101], foam catalysts [102, 103], packed beds [104–106] and over catalytic plates [107, 108] using the insertion probe sampling technique. Further studies have employed in situ Raman spectroscopy and laser-induced fluorescence over foils [109], catalytic plates [110–113] in order to obtain in situ information on the gas-phase concentration profiles, respectively.

4.3 Measurement Procedure

4.3.1 Procedure for In Situ DRIFTS Measurements

DRIFTS spectra were acquired in reflectance mode ($R = I_r/I_0$) and converted according the Kubelka-Munk function, $f_{KM}(R) = \frac{1}{2} \cdot \frac{(1-R)^2}{R}$. Background spectra were taken in air at 550 °C, 450 °C, 350 °C and 250 °C, starting from the highest temperature and cooling in between. The catalyst was heated to 550 °C, the first reaction mixture (methane and oxygen) was dosed and spectra were acquired at the same four temperatures in the same order, followed by a bake-out. The procedure was repeated with the other two reaction mixtures (methanol and oxygen, formic acid and oxygen). The series of experiments was repeated for the same reaction mixtures with the same procedure but adding additional water to the mixture for obtaining wet conditions.

4.3.2 Procedure for Light-off Measurements on PdO

The light-off consisted of heating from 225 °C to 650 °C and consecutive cooling to 225 °C with a ramp rate of 3 K/min. Experiments were performed in the order of increasing water concentrations. Each experiment was first performed at 1 bar and then repeated at 4 bar total pressure, except for the case of 6 % water which was only tested at 1 bar. Prior to each run of catalytic light-offs the catalyst was subjected to a pretreatment procedure as explained in section 4.4.2.

4.3.3 Procedure for Spatial Resolved Measurements on Pd

The gas composition at various axial positions inside a centered channel of the monolith was sucked out at a volumetric flow rate of 2 ml/min (corresponding to ca. 12.5 % of the total volumetric flow rate at SATP of a single channel) by means of a capillary (OD 170 µm, ID 100 µm, and sequentially transferred to the gas analytics. Gas-phase species concentrations for CO, CO_2, CH_4 and H_2O were analyzed using a FT-IR analyzer (MKS Multigas 2030), O_2 and H_2 have been analyzed separately with IMR- and EI-MS (V&F, AirSense and HSense), respectively. Atom balances for carbon and oxygen close within $\sim\pm$ 5 %, while balances for hydrogen are within the range of $\sim\pm$ 10 % accurate. Axial wall- and gas-temperature profiles were recorded using an optical-fiber with

a 45°-polish-angle, connected to an infrared (IR) pyrometer (OD 245 µm) and a thermocouple (K-type, ∅ 250 µm), each inserted into a fused silica capillary (OD 630 µm, ID 570 µm) for protection purposes. Both wall- and gas-phase temperatures were measured separately by inserting the fused silica capillary in the same center channel as for the measurement of the concentration profiles. All in situ profile measurements were conducted from the start of the rear part of the catalytic channel downstream and then continued by stepwise moving upstream. At least three concentration samples were collected at each axial location investigated before the capillary was moved further upstream. In between collecting samples at the same axial position a waiting time of 5 min., and between collecting from different axial positions a 10 min. relaxation time was followed, in order to obtain steady-state values.

4.4 Catalyst Pretreatment

4.4.1 Pretreatment for In Situ DRIFTS on PdO

The catalyst was calcined (baked out) in dry air at 600 °C.

4.4.2 Pretreatment for Light-off Measurements on PdO

Prior to each run of catalytic light-offs (heating/cooling cycle), the sample was pretreated to preserve a defined state of the catalyst and prevent inconsistent results due to deactivation effects. The pretreatment consisted of reduction with 2 % H_2 in N_2 at 675 °C for 20 min, re-oxidation in 10 % O_2 in N_2 at 675 °C for 40 min and consecutive cooling to 225 °C in 10 % O_2 in N_2. This pretreatment was found to provide reproducible light-off curves.

4.4.3 Pretreatment for Spatial Profiles on Pd

The reaction was first ignited with a mixture of H_2/O_2 of each 100 ml/min in N_2 at a total flow rate of 3.4 SLPM. Once the temperature at the catalyst outlet was stable, the gas-composition at the inlet was switched to the corresponding CH_4/O_2 mixture at 4 SLMP at a constant N_2 balance of 80 %. Measurements were performed at least 1.5 h after the CH_4/O_2-mixture was introduced and a steady-state had been reached.

4.5 Investigated Reaction Conditions

4.5.1 Conditions for In Situ DRIFTS Measurements

The gas composition contained 4000 ppm C_1-compound (methane, methanol or formic acid), 10 % oxygen and helium as balance to one atmosphere. The total flow was 200 mL/min.
The wet reaction gas-mixtures contained additional 2 % water.

4.5.2 Conditions for Light-off Measurements on PdO

Catalytic light-off experiments were performed with three different gas compositions consisting of 1000 ppm CH_4, 10 vol.-% O_2 in balance of N_2 with varying water concentrations (0, 6, 12 vol.-%) at 1 bar and 4 bar, maintaining a constant mass flow and a gas hourly space velocity (GHSV) of 60 000 h^{-1} (15.71 SLPM).

4.5.3 Conditions for Spatial Resolved Measurements on Pd

Experimental concentration and temperature profiles for different carbon-to-oxygen feed ratios as defined for a reactive molar inlet gas ratio C/O-ratio = $x_{CH_4}/(2 \cdot x_{O_2})$, between 0.8 and 1.1, were measured at a constant inlet gas flow rate of 4 standard liters per minute (SLPM) corresponding to standard ambient conditions (SATP) of 298.15 K and 1.013 bar and equivalent to a gas-hourly space velocity of $v_{GHSV} \sim 1.34 \times 10^5\ h^{-1}$ (based on the open volume of the monolith). The hydrodynamic residence time at SATP is equal to 26.8 ms. The reactive methane-oxygen gas-mixtures were diluted for all investigated C/O-ratios with a constant balance of 80 vol.-% of N_2. Experimental data used to test the mechanism in the case of a C/O-ratio = 1.0 has been adapted from reference [5]. The oven temperature was kept constant at 250 °C for all investigated cases. The reactive gas mixture was fed homogeneously premixed into the quartz tube reactor. Gases were preheated to 190 °C.

4.6 Experimental Results and Discussion

4.6.1 Spatially Resolved Profiles at Fuel Rich Conditions

Spatially Resolved Temperature Profiles

Measured wall- and gas-phase temperature profiles along the catalytic channel are shown in Fig. 4.3. The profile shape is similar for all three investigated C/O-ratios but shifts to higher temperatures as the C/O-ratio decreases, approaching the stoichiometric point of the total oxidation. The shape of the pronounced non-uniform temperature profiles are typical for processes where exothermic oxidation reactions (R_{o1}, R_{o2}) at the entrance of the catalyst are coupled with endothermic reforming (R_{o3}, R_{o4}) reactions further downstream [114]. The temperature in the catalyst rises within the first millimeter from the inlet value (989.9 K to 1041.7 K) to its maximum (1007.4 K to 1095.2 K). The reactive gas-mixture enters the catalyst and cools the walls of the catalyst as can be seen from the large temperature difference between gas-phase and wall inlet temperature. Beyond the peak point the temperature of the catalyst wall starts to decrease while the gas-phase temperature has not yet reached its maximum. The temperature drop at the wall is caused by endothermic steam reforming reactions which consume heat and convert CH_4 further into synthesis gas. This can also be inferred from the measured concentration profiles as explained in the next section. The gas-phase temperature rises down the catalyst channel, eventually rising above the temperature level of the wall at ~ 3.2 mm down the catalyst channel, due to the short contact time of the gases and the convective heat transport downstream, when flowing by the temperature hotspot of the catalyst wall near the entrance region of the channel.
The heat dissipation of the rector to the surroundings has been evaluated for all investigated C/O-ratios in terms of the thermal efficiency η_{th} which is given as the ratio of the actual temperature difference between reactor inlet, $T_{\mathrm{exp}}^{\mathrm{in}}$, and outlet, $T_{\mathrm{exp}}^{\mathrm{out}}$, and the maximum possible temperature difference between inlet and adiabatic outlet temperature, $T_{\mathrm{ad}}^{\mathrm{out}}$, assuming adiabatic operation:

$$\eta_{\mathrm{th}} = \frac{T_{\mathrm{exp}}^{\mathrm{out}} - T_{\mathrm{exp}}^{\mathrm{in}}}{T_{\mathrm{ad}}^{\mathrm{out}} - T_{\mathrm{exp}}^{\mathrm{in}}} \tag{4.5}$$

As gases are preheated before entering the reactor, the inlet temperature was taken as $T_{\mathrm{exp}}^{\mathrm{in}} = 190\,^{\circ}\mathrm{C}$. The outlet temperatures were taken at ~ 5 mm downstream of the catalyst. The thermal efficiencies for the investigated C/O-ratios

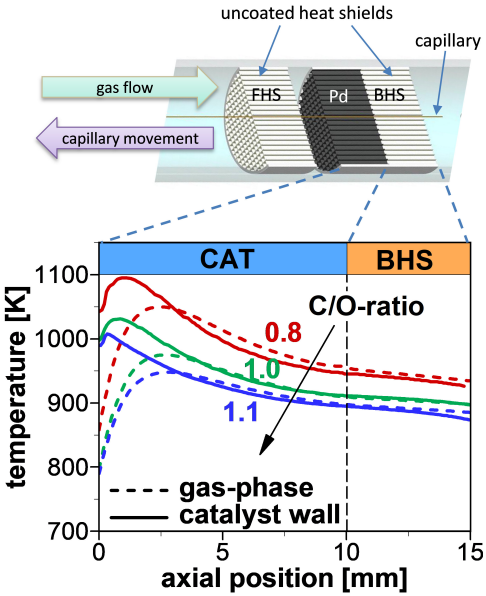

Figure 4.3: Experimental gas-phase temperature and catalyst wall temperature profiles along the channel axis. Profiles for C/O = 1.0 adapted from Diehm and Deutschmann [5]. Figure adapted from Stotz et al. [1].

= {0.8, 1.0, 1.1} are 0.86, 0.96 and 0.95, respectively. The latter two thermal efficiencies at fuel-richer conditions show values close to one, i.e. the flow reactor setup can be considered as quasi-autothermally operated. For the fuel-lean point (C/O-ratio = 0.8), a slightly smaller value is obtained, indicative of the very strong heat release under operating conditions which are closer to the stoichiometric point of the total oxidation. Thus, showing higher heat dissipation to the surroundings.

Spatially Resolved Concentration Profiles

Steady-state species concentration profiles for reactants CH_4 and O_2, partial oxidation products CO and H_2 as well as total oxidation products CO_2 and H_2O, as measured axially along the centered channel of the monolith are comparatively summarized for the investigated C/O-ratios in Fig. 4.4. In all three cases, oxygen is introduced as the stoichiometrically limiting, reactant as complete conversion of oxygen is achieved. Thus, when lowering the available amount of oxygen at the reactor inlet, the conversion of methane decreases over the entire channel length as can be observed from the different concentration profiles. This finding is consistent with the measured wall and gas-phase temperature profiles and their shift towards higher temperatures at fuel-leaner conditions as shown in Fig. 4.3. That is, when more methane is converted at lower C/O-ratios, the wall temperature peak in the catalyst is higher. The experimentally observed consumption of oxygen occurs very fast within ca. the first 2 mm of the catalytic section, when compared to the drop in methane concentration over the channel length. The reaction products CO, H_2 and CO_2 form monotonically over the entire channel axis, while H_2O forms rapidly at the inlet, going through a pronounced maximum near the front part of the catalyst ($z \approx 1.1$ mm to 1.3 mm) and gets then consumed over the remaining catalyst length. CO_2 and H_2O form rapidly at the catalyst inlet (0 mm to 0.25 mm) while no CO and H_2 are found. This observation is in agreement with previous findings [32]. The H_2O concentration peak coincides with the wall temperature peak, within the experimental uncertainty of the measurements, confirming that total oxidation takes place in the inlet region ($0 \leq z < 1.1$ mm to 1.3 mm).

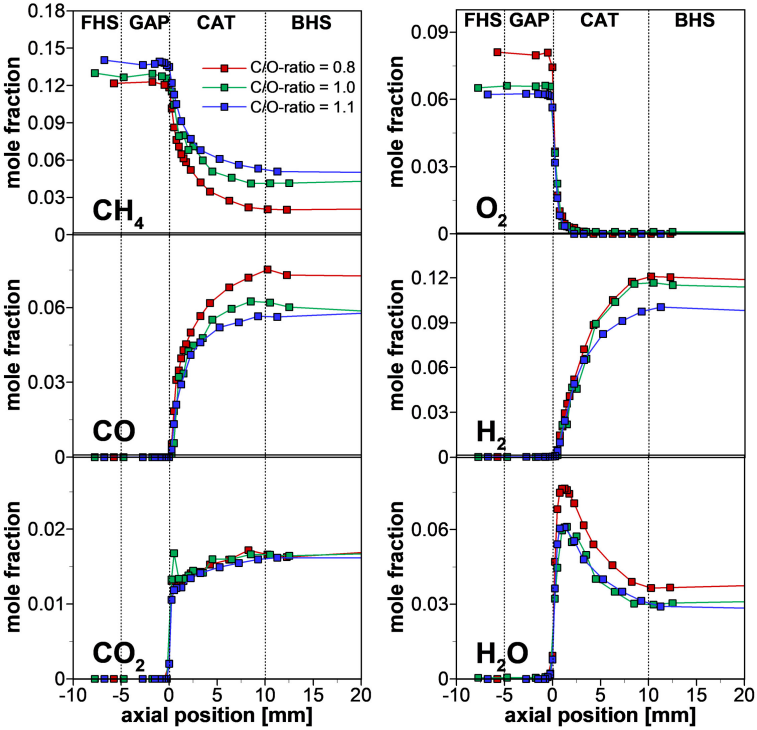

Figure 4.4: Experimentally determined gas-phase species concentration profiles for various feed C/O-ratios = {0.8; 1.0; 1.1}. Profiles for C/O = 1.0 adapted from Diehm and Deutschmann [5]. Figure adapted from Stotz et al. [1].

4.6.2 In Situ DRIFTS Experiments on Powder Catalyst

Using infrared spectroscopy (DRIFTS), adsorbed educts, intermediates and products on the catalyst surface were identified during methane oxidation. The results are shown for representative temperatures of 450 °C and 250 °C corresponding to 70 - 80 % methane conversion and zero-conversion at light-off onset, respectively (cf. Appendix Fig. A.4 on page 181).

The DRIFTS spectra are shown as difference spectra, relative to the baked-out state of the catalyst in 10 % O_2/He at atmospheric pressure i.e. before exposure to the corresponding reaction mixtures. The observed IR bands in Fig. 4.5 and Fig. 4.6 were interpreted by assigning them to surface species as summarized in Tab. 4.5. A summary of the molecular species observed during the in situ DRIFTS experiments under the different reaction conditions is given in Tab. 4.6.

Table 4.5: Assignment of observed IR-bands detected by DRIFTS to gas-phase (g), physisorbed (ps) and chemisorbed (s) species. Table adapted from Stotz et al. [2].

Assignment	ν [cm^{-1}]	Ref.
OH_I(s)	3770	[115]
OH_{II}(s)	3740	[115]
OH_{III}(s)	3690	[115]
H_2O(OH)(s)	3450-3600	-
H_2O(ps)	1570-1700	[116]
HCOO(s)	1370-1400, 1600, 2900, 3000	[117–119]
CH_3OH(ps)	2850, 2950	[120, 121]
HCOOH(ps)	1630, 1660, 1320, 2740	[122]
CH_4(g)	1300, 3000	[123]
CO(s)	2090, 2140	[124, 125]
carbonates	1230, 1350-1650, 1650, 1430, 1470	[126]

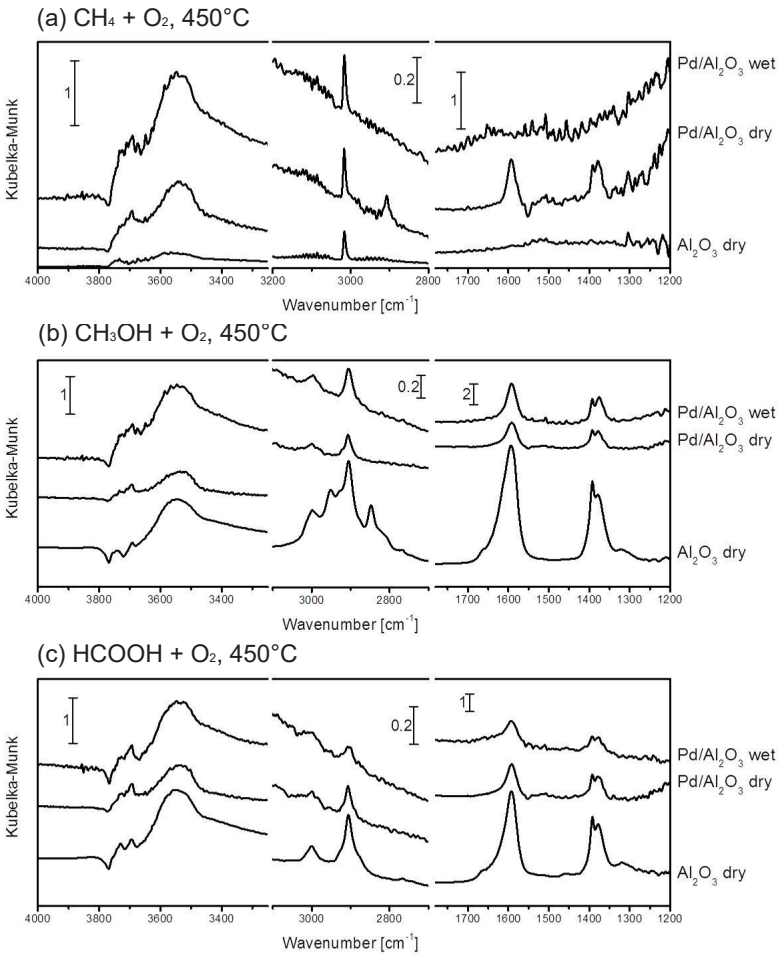

Figure 4.5: In situ DRIFT spectra of 2.4 % Pd/Al_2O_3 and Al_2O_3 exposed to (a) methane + oxygen, (b) methanol + oxygen and (c) formic acid + oxygen at 450 °C. The term "wet" indicates the presence of 2 % H_2O and "dry" the absence of water in the reaction mixture. The gas composition contained 4000 ppm C_1-fuel (methane, methanol or formic acid), 10 % oxygen and balance helium. The total flow was 200 mL min^{-1}. Figure adapted from Stotz et al. [2].

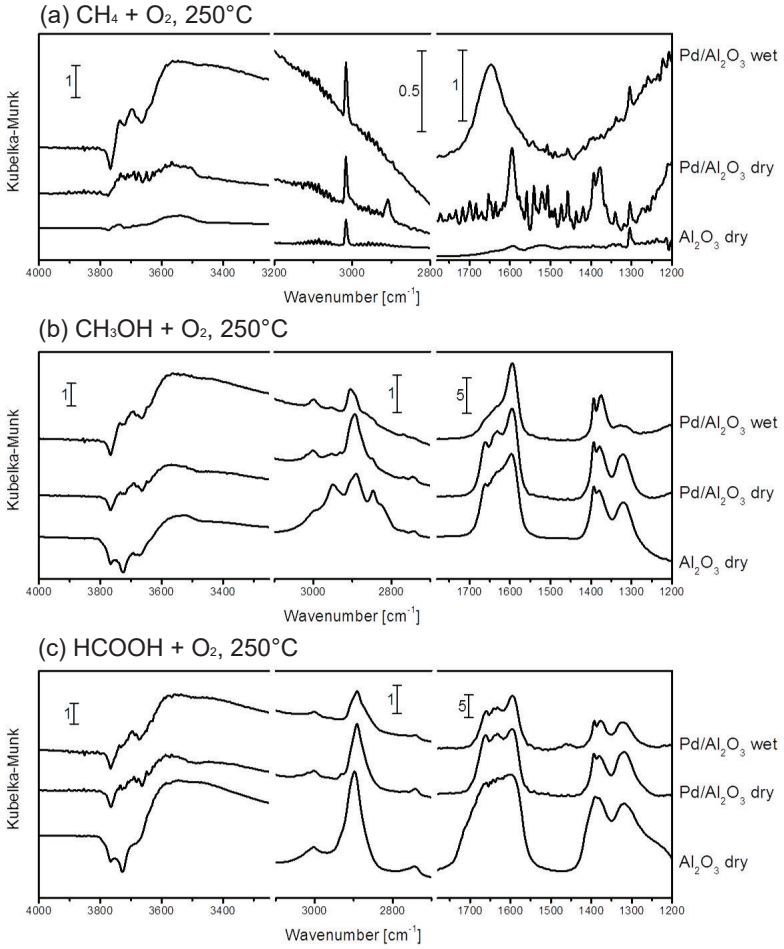

Figure 4.6: In situ DRIFT spectra of 2.4 % Pd/Al_2O_3 and Al_2O_3 exposed to (a) methane + oxygen, (b) methanol + oxygen and (c) formic acid + oxygen at 250 °C. The term "wet" indicates the presence of 2 % H_2O and "dry" the absence of water in the reaction mixture. The gas composition contained 4000 ppm C_1-fuel (methane, methanol or formic acid), 10 % oxygen and balance helium. The total flow was 200 mL min^{-1}. Figure adapted from Stotz et al. [2].

Table 4.6: Observed IR bands during exposure of the Pd/Al_2O_3 catalyst and the Al_2O_3 support to 4000 ppm fuel + 10 % O_2 in balance helium. The label "wet" indicates the inclusion of 2 % H_2O, "dry" conditions were without water. The presence of surface species in accordance with Tab. 4.5 was assigned relative to the baked-out state of the catalyst. Symbols indicating qualitative species abundance: 0, no band; (+), weak band; + or -, positive or negative band; ++ or --, strong positive or negative band. The first and second symbol in each cell corresponds to 450 °C and 250 °C, respectively. Table adapted from Stotz et al. [2].

	C_1-fuel								
	methane			**methanol**			**formic acid**		
Species	Pd/Al_2O_3 (wet)	Pd/Al_2O_3 (dry)	Al_2O_3 (dry)	Pd/Al_2O_3 (wet)	Pd/Al_2O_3 (dry)	Al_2O_3 (dry)	Pd/Al_2O_3 (wet)	Pd/Al_2O_3 (dry)	Al_2O_3 (dry)
OH_I(s)	--|--	-|0	0|0	--|--	0|--	--|--	--|--	-|--	--|--
OH_{II}(s)	++|++	+|+	(+)	+|+	(+)|(+)	-|--	+|(+)	+|0	+|--
OH_{III}(s)	++|++	+|+	0|0	++|++	+|+	(+)|--	+|+	+|+	+|+
$H_2O(OH)$(s)	++|++	++|+	(+)|(+)	++|++	+|+	++|+	++|++	+|+	++|++
H_2O(ps)	(+)|+	0|0	0|0	0|+	0|0	0|0	0|+	0|0	0|0
CH_4(g)	+|+	+|+	+|+						
HCOO(s)	0|0	+|+	0|0	+|+	+|+	++|+	+|+	+|+	++|++
CH_3OH(ps)				(0)|+	0|(+)	+|++			
HCOOH(ps)				0|+	0|++	+|++	0|(+)	0|+	(+)|++

Three different reaction scenarios were investigated:

(1) over a Pd/Al_2O_3 catalyst under dry conditions,

(2) with external 2 % H_2O as inhibitor and

(3) over plain Al_2O_3 support to simulate a situation where methane does not become activated and oxidized.

Also different C_1-compounds were applied: methane, methanol, formic acid, as well as carbon monoxide and carbon dioxide as externally dosed reaction product. The idea was to investigate parts of the reaction paths starting from activated C_1-molecules with higher oxidation state of carbon than methane. This was expected to provide information on the possible mechanism after methane becomes activated, the reaction route and participating reaction intermediates. During methane oxidation at all investigated conditions, gas-phase methane was observed (Fig. 4.5 (a) and Fig. 4.6 (a)).

Dry reaction mixtures over Pd/Al_2O_3

Upon dry reaction conditions, surface formates on the catalyst surface become clearly visible. Exactly the same bands were observed when methanol and formic acid were oxidized. On the contrary, when CO_2 and CO were dosed instead of methane (cf. Appendix Fig. A.8 on page 186) corresponding bands specific for carbonates [126] were formed. This supports that catalytic oxidation of methane over PdO/Al_2O_3 catalysts proceeds via formate intermediates. Since IR-signals of CH_x-metal complexes typically $\sim$1000 cm^{-1} to 1800 cm^{-1} [127, 128] were not observed, it is further concluded that the pyrolytic decomposition route [129] for methane over the PdO surface can be ruled out.
The observed formates were most probably adsorbed on the Al_2O_3 support, as they are expected to rapidly react on the PdO particle, consistent with the MF-MKM modeling results. These observations were made at 250 °C and 450 °C. Hydroxide groups bonded to two or three metal ions (OH_{II} and OH_{III}) were formed as well as H-bond associated water ($H_2O-(OH)$) due to the water formed during reaction [115]. The OH-groups bonded to a single metal ion (OH_I) show negative bands relative to the clean baked-out catalyst, because water molecules most probably adsorb on top of these groups, eliminating their IR-activity [74].

Wet reaction mixtures over Pd/Al_2O_3

The addition of external water inhibits the activation of methane and the formation of formates, hence their absence. Also, the hydroxide-associated water coverage is thereby increased and physisorbed water molecules become highly abundant at lower temperatures.

Dry reaction mixtures over bare Al_2O_3

Considering the non-catalytic scenario, i.e. where no PdO is present on the Al_2O_3 surface, formates are not formed as methane is not activated and oxidized. The hydroxide bands are very similar to the ones observed on the PdO/Al_2O_3 catalyst, indicating that the majority of observed hydroxides are bonded to the Al_2O_3 support.
Oxidation of methanol and formic acid proceeded at or close to full conversion at both 250 °C and 450 °C (Fig. 4.5 (b) and (c) and Fig. 4.6 (b) and (c)) over both the PdO/Al_2O_3 catalyst and Al_2O_3, leading to the appearance of formate and water bands. Additional bands that can be assigned to physisorbed methanol, CH_3OH(ps), can be seen when oxidizing methanol over Al_2O_3 (Fig. 4.5 (b)) and also slightly over PdO/Al_2O_3 at 250 °C (Fig. 4.6 (b)). This means that methanol oxidation is catalyzed by PdO but can nevertheless take place uncatalyzed with a lower efficiency over the bare Al_2O_3 surface. Physisorbed formic acid, HCOOH(ps), was observed when oxidizing methanol or formic acid, respectively. These species were observed in the case of non-catalytic reaction of methanol or formic acid, over Al_2O_3 or at 250 °C over Pd/Al_2O_3 (Fig. 4.5 (b) and Fig. 4.6 (b)), as well as under direct dosage of formic acid (Fig. 4.5 (c) and Fig. 4.6 (c)).

In summary, catalytic methane oxidation proceeds on the PdO site, methane reacts rapidly via formate to CO_2 which is released into the gas phase. A part of the formate intermediates migrate to the Al_2O_3 support, where they are strongly bonded and can be observed spectroscopically. Water inhibits the generation of these formates and/or the migration of formates to the support, as no formate bands are observed when dosing water. Note that water does not inhibit the adsorption of formates on Al_2O_3, as formate bands are observed during oxidation of methanol and formic acid.

4.6.3 Catalytic Light-Off at Lean Conditions

Influence of Water Concentration on Catalytic Light-Off

Catalytic light-off (first heating curve) and subsequent light-out (first cooling curve) measurements for methane oxidation for three different reaction mixtures with varying water concentrations of 0, 6 and 12 vol.% where performed to test the catalytic activity of the Pd/Al_2O_3 catalyst at 1 bar absolute pressure, as depicted in Fig. 4.7 (a). The dry feed case shows the lowest T_{50} light-off temperature of 312 °C at 50 % conversion of all three investigated cases. This high activity is not influenced while cooling the dry reaction mixture, as the preceding heating curve is nearly overlaid by the cooling branch. Thus, no pronounced changes in the catalytic activity for the dry reaction mixture are observed.
However, in case when 6 vol.% water is present in the feed a remarkable increase in T_{50} of 143 K up to 455 °C in comparison to the dry reaction mixture can be seen. This dramatic shift in the light-off activity towards higher temperatures is a direct consequence of the water inhibition effect as has also been shown in the literature [56, 130]. The activity following the light-out branch during cooling deactivates even 50 K earlier at 504 °C (compared to the light-off branch), leading to a visible conversion hysteresis between heating and cooling curves. Note that between each heating/cooling cycle the catalyst was preconditioned in order to obtain a defined initial state as has already been mentioned in section 4.4.2. At even higher amounts of external water in the feed the situation becomes more severe. In the experiment with 12 vol.-% water the activity drop surmounts the preceding two cases for 0 and 6 vol.-% water, while T_{50} increases up to 497 °C for heating and 570 °C during cooling, respectively.

Interestingly, the slope in the light-off curves decreases with increasing amounts of external water. This altered catalyst activity and the appearance of the conversion hysteresis may not be a result of the immediate water inhibition effect but rather due to deactivation phenomena of the catalyst itself during light-off which proceeds at a slower time scale as the inhibition. However, both activity losses are caused by the presence of water. Thus, two different effects contribute to the activity decrease.
While the catalytic activity is influenced by the presence of water, contributions from in situ generated water as reaction by-product and external water need to be distinguished. In the dry feed experiments full conversion is only achieved at 430 °C. Note, at these conditions the maximum stoichiometric amount of only 2000 ppm (0.2 vol.-%) of internally produced water is present as compared to the much higher amounts of 6 and 12 vol.-% in the wet cases. These quantitative

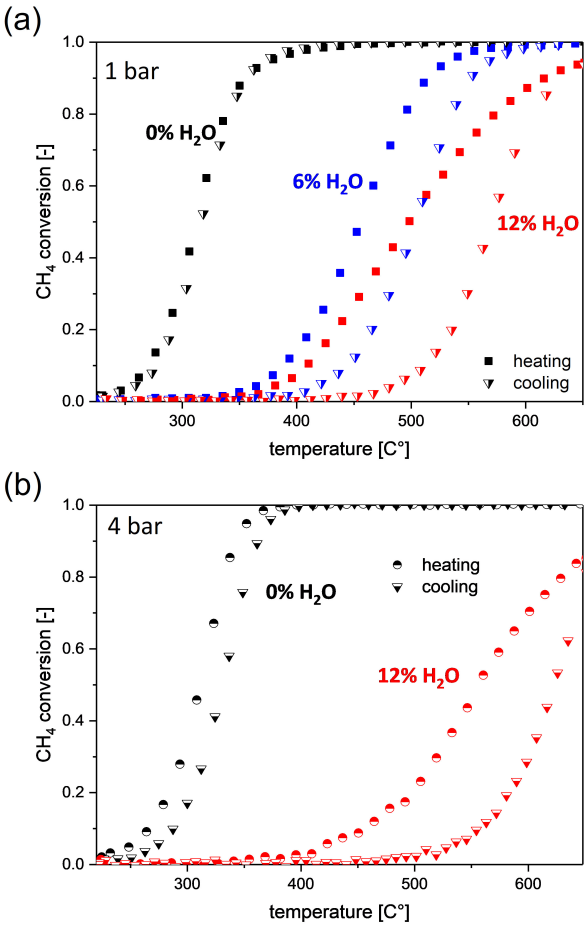

Figure 4.7: Catalytic oxidation of methane at dry and wet feeds on Pd/Al_2O_3 catalyst shown for the 1st heating/cooling cycle at 3 K/min. Reaction conditions: GHSV = 60 000 h^{-1}, 1000 ppm CH_4, 10 vol.% O_2, 0-12 vol.% H_2O, N_2 balance to (a) 1 bar and (b) 4 bar. Figure adapted from Stotz et al. [2].

differences in the water concentrations deteriorate the catalyst's activity towards oxidizing methane to different extents. The mechanistic aspects and implications

on the conversion activity of these latter points will be further discussed in detail in section 6.2.1.

Influence of Pressure on Catalytic Light-Off

To further study the effect of internally formed water on the reaction, experiments at four fold absolute pressure were conducted. The influence of elevated pressure on the ignition and extinction curves is demonstrated in Fig. 4.7 (b) for a dry and wet feed with 12 vol.-% water. Upon increasing the total pressure to 4 bar the cooling branch for the dry experiment shows a minor deactivation of about 9 K. The light-out curve spreads from the nearly unchanged ignition curve with T_{50} shifting towards 330 °C. Since inlet concentrations are kept the same as in the dry low pressure case, the higher pressure induces the onset of forming the conversion hysteresis. Torkashvand et al. have previously reported that higher pressures facilitate an increased conversion activity due to longer residence times τ of the reaction mixture as $\tau \sim \frac{p}{T}$ [56] and thus formation of increased amounts of water. This effect is to a smaller extent counterbalanced by the decreased radial mass transport in the monolith channel gas-phase and washcoat, as diffusivity scales with $D \sim \frac{\sqrt{T}}{p}$. However, activity enhancement due to the residence time effect is not found in the experimental data set for the wet high pressure case, where instead a further shift towards higher light-off temperatures (557 °C for the heating and 623 °C for the cooling branch) and a dramatic activity loss is seen in both heating and cooling curves. Thus, under high pressure wet conditions the by far dominating contribution to the catalyst performance deterioration is rather related to kinetic phenomena at the catalyst particle or support level e.g. due to water induced changes on the structure of the PdO particles itself or the support. The deactivation effect becomes more pronounced at higher pressures [131]. A higher pressure may also facilitate enhanced water adsorption and interactions with PdO particle surface and/or support as compared to the wet low pressure case or at even dry conditions. As water can influence the oxygen exchange from the support to the particle [47, 71, 75], water could also facilitate a destabilizing effect between particle and support leading to a decreased spreading [132].

Metal Oxide Corrected Dispersions for PdO

Pd metal dispersions as function of particle size (calculated using Eq. (4.3)), also expressed in terms of catalytic-to-geometric surface area ratios in a “fresh” state and after the series of light-off experiments (“aged”) was conducted, are presented in Fig. 4.8. The metal dispersions were experimentally determined from

CO-chemisorption measurements and have been evaluated based on Eq. (4.1). The results support the conclusion that the water exposed PdO catalyst (wet cases) undergoes additional structural changes on the particle level during the light-off experiments, in addition to the water inhibition effect. Such particle related changes do typically occur on a slower timescale as the immediate water inhibition effect [133–135] and depend on gas composition, particle support interactions and particle composition [132]. This is also consistent with the progressive flattening out slope of the light-off curves with increasing amounts of water in the feed.

Additionally, metal oxide corrected dispersions for PdO

$$D^{1}_{\mathrm{PdO}} = D_{\mathrm{Pd}} \cdot \frac{\left(\frac{v_{\mathrm{m,PdO}}}{a_{\mathrm{m,PdO}}}\right)}{\left(\frac{v_{\mathrm{m,Pd}}}{a_{\mathrm{m,Pd}}}\right)} \cdot \left(\frac{v_{\mathrm{m,Pd}}}{2 \cdot v_{\mathrm{m,PdO}}}\right)^{1/3} \tag{4.6}$$

$$= 1.20 \cdot D_{\mathrm{Pd}} \tag{4.7}$$

and corresponding calculated particle sizes, d^{1}_{PdO} (using Eq. (5.73)), in the fresh and aged states of the catalyst for the 1st and 2nd TPD measurements are shown in Fig. 4.8, together with the related catalytic-to-geometric surface area ratios for PdO using Eq. (5.67). The $F_{\mathrm{cat/geo}}$ values for the 1st TPD points were used as model input parameters for the simulations in section 6.2.1.

The large deviations observed in the $F_{\mathrm{cat/geo}}$ values between Pd and PdO phase imposes a source of error for the model based kinetic simulations. This effect should not be neglected, instead it is necessary to account for these changes in the kinetic model in order to obtain reasonable simulation results (cf. chapter 5.3.3).

The repeated measurements in the aged catalyst state showed that partial recovery of the Pd metal dispersion with pretreatment in H_2 is possible. These findings are in line with observations that water deactivation is to some extent a reversible phenomenon [51, 53]. On the contrary, repeated measurements in the fresh catalyst state indicate that the high initial dispersion of 49 % is lowered to 38 % after the second measurement. Apparently, fresh and aged catalyst states approach dispersions in between the sampled points, if further TPD measurements were conducted.

Based on a study by Penner et al. [136], using a high resolution transmission electron microscope (HRTEM), showed that reduced PdO on SiO_2 in 10 mbar CO, after initial oxidation of the as prepared Pd/SiO_2 catalyst (reduced state) in 1 bar O_2, can be reversibly formed under these conditions. Therein presented

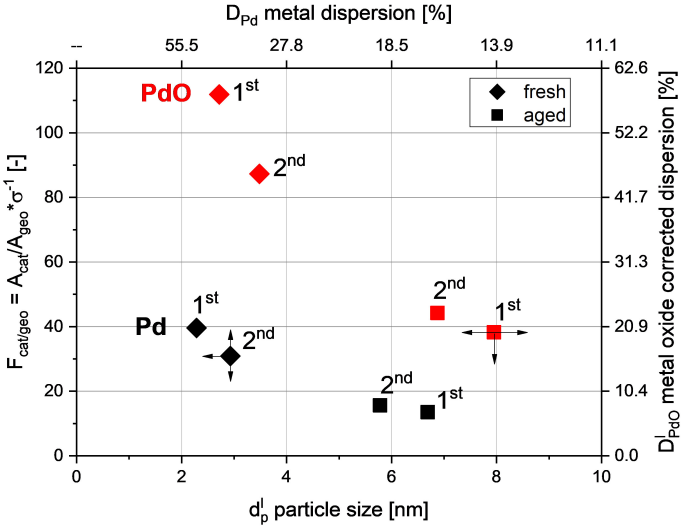

Figure 4.8: Pd metal (black symbols) and PdO metal oxide corrected dispersions (red symbols). TPD measurements for determining the Pd metal dispersions were consecutively repeated (1^{st}, 2^{nd}) for a fresh catalyst state (◆ = fresh) and after the series of light-off experiments was conducted (■ = aged). Also shown, related parametric model input values of $F_{cat/geo}$ according to the definition of Eq. (5.13), as function of the particle size for the corresponding phase (Eq. (4.3) for Pd and Eq. (5.73) for PdO). A_{cat} was determined from Eq. (4.4) for Pd and from Eq. (5.74) for PdO in order to evaluate $F_{cat/geo}$. Figure adapted from Stotz et al. [2].

HRTEM images of the catalyst let infer that Pd to PdO transformation involves formation of fragmented PdO particles consisting of smaller PdO aggregates. Similar effects have also been reported by Ruckenstein et al. [137].

5 Modeling Concept and Chemical Reaction System[1]

5.1 Mathematical Model

5.1.1 Channel Equations

Numerical simulations of the steady-state species concentration profiles in a catalyst channel were performed using DETCHEM$^{\text{CHANNEL}}$ [138]. The model assumes cylindrical symmetry and solves the two-dimensional laminar steady-state flow field using the boundary-layer approximation assuming the axial diffusive transport is negligible as compared to the convective transport. This assumption is valid as long as $Re_{\text{L}} \cdot Sc \gg 1$ or as it is often the case for diluted ideal gas mixtures ($Sc \approx 1$) and $Re_{\text{L}} \gg 1$ [139], i.e. short-contact times in the millisecond range for the given channel dimensions. The contact times at the herein investigated conditions are around 10 ms. Thus, applying the boundary layer approximation is valid.

The channel code integrates the following set of equations according to a marching procedure for the axial coordinate z with an adaptive step size using the LIMEX solver [140].

Total mass conservation:

$$\frac{\partial(\rho u)}{\partial z} = -\frac{1}{r}\frac{\partial(r\rho v)}{\partial r} \tag{5.1}$$

[1] Parts of this chapter have been taken from [1] H. Stotz, L. Maier and O. Deutschmann, Methane oxidation over palladium: on the mechanism in fuel-rich mixtures at high temperatures, *Top. Catal.*, 60 (2017) 83–109 and from [2] H. Stotz, L. Maier, A. Boubnov, A. T. Gremminger, J.-D. Grunwaldt and O. Deutschmann, Surface reaction kinetics of methane oxidation over PdO, *J. Catal.*, 370 (2019) 152–175.

Species mass conservation:

$$\frac{\partial\left(\rho u Y_i\right)}{\partial z} = -\frac{1}{r}\frac{\partial\left(r\rho v Y_i\right)}{\partial r} - \frac{1}{r}\frac{\partial\left(r J_{i,r}\right)}{\partial r} \quad (i = 1, ..., K_{\mathrm{g}}) \tag{5.2}$$

Axial momentum conservation:

$$\frac{\partial\left(\rho u u\right)}{\partial z} = -\frac{1}{r}\frac{\partial\left(r\rho v u\right)}{\partial r} - \frac{\partial p}{\partial z} + \frac{1}{r}\frac{\partial}{\partial r}\left(\mu r\frac{\partial u}{\partial r}\right) \tag{5.3}$$

Radial momentum conservation:

$$\frac{\partial p}{\partial r} = 0 \tag{5.4}$$

Thermal energy balance:

$$\frac{\partial\left(\rho u h\right)}{\partial z} = -\frac{1}{r}\frac{\partial\left(r\rho v h\right)}{\partial r} + u\frac{\partial p}{\partial z} + \frac{1}{r}\frac{\partial}{\partial r}\left(\lambda r\frac{\partial T_{\mathrm{g}}}{\partial r}\right) - \frac{\partial}{\partial r}\left(\sum_{i}^{N_{\mathrm{g}}} r J_{i,r} h_i\right) \tag{5.5}$$

Ideal gas equation of state:

$$\rho = \frac{p\bar{M}}{R T_{\mathrm{g}}} \tag{5.6}$$

In the above equations, z and r are the axial and radial channel coordinates, ρ is the mass density of the mixture, u and v are the axial and radial velocity components, Y_i is the mass fraction of species i, $J_{i,r}$ is the diffusive mass flux in radial direction, p is the pressure, N_{g} is the total number of gas-phase species, T_{g} is the gas-phase temperature, $\bar{M}$ is the mean molecular weight of the gas-mixture, R is the universal gas constant, h_i is the specific enthalpy of species i in the gas-phase.

The fluid properties of the mixture are functions of the gas-phase temperature and the mixture composition and are determined from the kinetic theory of diluted gases based on the Chapman and Enskog theory [141].

Fluid properies:

$$h = h\left(T_{\mathrm{g}}, Y\right) \tag{5.7}$$

$$\mu = \mu\left(T_{\mathrm{g}}, Y\right) \tag{5.8}$$

$$\lambda = \lambda\left(T_{\mathrm{g}}, Y\right) \tag{5.9}$$

Where h, μ and λ are the mixture specific enthalpy, dynamic viscosity and heat conductivity. The radial diffusive mass flux in the channel is described by Fick's law.

Radial Diffusive Flux:

$$J_{i,r} = -D_{i,\mathrm{M}} \cdot \rho \cdot \frac{M_i}{\bar{M}} \cdot \frac{\partial X_i}{\partial r} \tag{5.10}$$

Herein, $D_{i,\mathrm{M}}$ is the mixture averaged diffusion coefficient of species i in mixture M, X_i is the mole fraction of species i, M_i is the molecular weight of species i. The flow velocities at the inlet point of the catalytic channel were determined from the measured inlet gas-phase temperature and its corrected volume flux at the catalytic channel entrance based on the geometric considerations on the dimension of the square channel as given in Tab. 4.1.

$$u_{\mathrm{in}}\left(T,p\right) = \frac{\dot{V}_0}{N_{\mathrm{ch}} \cdot A_{\mathrm{ch,square}}} \cdot \left(\frac{p_0}{p_{\mathrm{in}}}\right) \cdot \left(\frac{T_{\mathrm{in}}}{T_0}\right) \tag{5.11}$$

5.1.2 Washcoat Model and Coupling

Flux Coupling

For the processes in the washcoat several assumptions have been made. The geometric simplifications for deriving the necessary model parameters are shown in Fig. 5.1. In particular, the non-uniform washcoat thickness, which typically results from the dip-coating process during the manufacturing of the catalyst thus, showing thicker parts in corners and thinner parts along the edges of the cordierite square channel carrier, was approximated by a uniform circular washcoat with an effective washcoat thickness $\delta_{\mathrm{wc}}^{\mathrm{eff}}$. For appropriate coupling of the processes in the gas-phase of the channel and the washcoat, the radial diffusive flux at the interface ($r = R$) in direction towards the wall is coupled to the species molar rate of production ($\dot{S}_i > 0$)/consumption ($\dot{S}_i < 0$) as boundary condition.

$$J_{i,r}|_{r=R} = -\dot{S}_i \cdot M_i \cdot F_{\mathrm{cat/geo}} \cdot \eta \tag{5.12}$$

In Eq. (5.13), $F_{\mathrm{cat/geo}}$ represents the ratio of the catalytic-to-geometric surface area. The $F_{\mathrm{cat/geo}}$ parameter is a model specific parameter for the channel flow model and is specific to the present catalyst phase. It is one of the very few model input parameters used herein, which is experimentally based and

determined from CO TPD dispersion measurements. $F_{\mathrm{cat/geo}}$ is responsible for scaling the reaction rates to the actual catalytic surface area.

$$F_{\mathrm{cat/geo}} = \frac{A_{\mathrm{cat}}}{A_{\mathrm{geo}}} \tag{5.13}$$

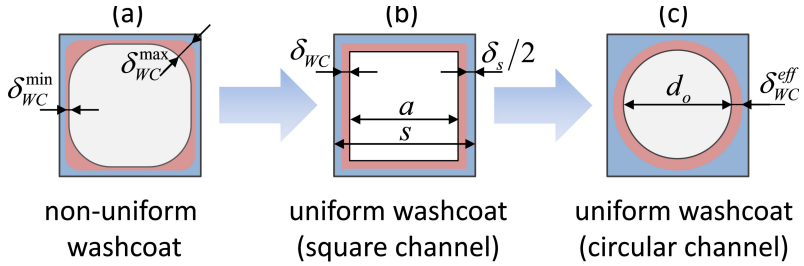

Figure 5.1: Geometric simplifications as used in the assumptions for the derivation of the channel flow model with a circular channel geometry. Figure adapted from Stotz et al. [1].

Catalytic Surface Area

Where A_{cat} was determined based on the manufacturer Pd-loading L_{Pd}, the measured catalyst dispersion D_{Pd} from chemisorption experiments, the surface site density of palladium Γ_{Pd} and/or Γ_{PdO}, and for a monolith catalyst, the volume of a single catalytic channel including wall, washcoat and open space:

$$V_{\mathrm{ch}} = \frac{V_{\mathrm{cat}}}{N_{\mathrm{ch}}} \tag{5.14}$$

$$= s^2 \cdot L \tag{5.15}$$

The monolith cell size, s, in [m] was calculated from

$$s = \sqrt{\frac{1}{N_{\mathrm{cpsi}}}} \cdot 0.0254 \tag{5.16}$$

For the reduced phase of Pd, A_{cat}, is calculated according to Eq. (4.4) on page 20, while for the PdO phase either Eq. (5.74) or Eq. (5.80) was used for A_{cat}, depending on the problem considered.[2]

$$A_{\mathrm{cat}} = \begin{cases} A_{\mathrm{Pd}} = \dfrac{D_{\mathrm{Pd}} L_{\mathrm{Pd}}}{\Gamma_{\mathrm{Pd}} M_{\mathrm{Pd}}} \cdot V_{\mathrm{ch}} & \text{for Pd} \quad (5.17a) \\ \dfrac{A_{\mathrm{PdO}}}{\sigma} & \text{for PdO} \quad (5.17b) \end{cases}$$

Geometric Surface Area

In Eq. (5.13) the geometric surface area A_{geo}, defined as the interfacial channel gas-washcoat surface area, has been determined from the open width of the square channel, a, assuming rectangular geometry.

$$A_{\mathrm{geo}} = 4aL \cdot \sqrt{\frac{\pi}{4}} \tag{5.18}$$

Where a is calculated for the square channel of cell size s and substrate carrier thickness of δ_{s} from

$$a = s - \delta_{\mathrm{s}} - 2 \cdot \delta_{wc} \tag{5.19}$$

The correction factor $\sqrt{\pi/4}$ in Eq. (5.18) accounts for transferring the flow through a square channel problem of dimension a, to one with a circular geometry with an equal cross-sectional area as the square channel. Thus, the diameter of the circular channel used for the simulations is determined from $d_{\mathrm{o}} = a \cdot \sqrt{\frac{4}{\pi}}$.

Assuming constant washcoat loading L_{wc} and density ρ_{wc} between square and circular geometry, the effective washcoat thickness for the circular channel is back-calculated from the given geometry of the square channel configuration as

$$\delta_{\mathrm{wc}}^{\mathrm{eff}} = \left(\frac{L_{\mathrm{wc}}}{\rho_{\mathrm{wc}}} \right) \cdot \frac{s^2}{\pi d_{\mathrm{o}}} \tag{5.20}$$

[2] For the oxidized phase Eq. (5.17a) cannot be used directly, and Eqs. (5.12) and (5.13) need to be corrected as the oxidation process causes morphological changes in the sites and the particle structure, which leads to volume expansion of the bulk phase due to incorporation of oxygen into the lattice structure. The corresponding oxide corrected formulas for the PdO phase are further examined in detail in section 5.3.3 and 5.3.1.

For A_{geo}, the geometric surface area of a single catalyst channels was used, i.e. the interfacial area between channel gas-phase and washcoat, based on the geometric dimensions of the monolith catalyst as given in Tab. 4.1 and Tab. 4.2.

Washcoat Pore Transport

For the description of the transport within the porous washcoat, the effectiveness factor approach has been applied to correct the transport limited free rate $\dot{s}_i$ in Eq. (5.12), accordingly.

The local internal effectiveness factor η for the washcoat is calculated based on the Thiele moduli φ_i of each gas-phase species i and is taken as the minimum out of the set of species effectiveness factors η_i. This procedure guarantees mass conservation upon coupling the washcoat flux with the channel flow and avoids choosing a single representative limiting species.

$$\varphi_i = \delta_{\text{wc}}^{\text{eff}} \cdot \sqrt{\frac{\dot{S}_i F_{\text{cat/geo}}}{c_i^{\text{s}} D_i^{\text{eff}} \delta_{\text{wc}}^{\text{eff}}}} \tag{5.21}$$

$$\eta_i = \frac{\dot{S}_i^{\text{eff}}}{\dot{S}_i} = \frac{\tanh \varphi_i}{\varphi_i} \tag{5.22}$$

$$\eta = \min_i \{\eta_i\} \tag{5.23}$$

In Eq. (5.21), D_i^{eff} is the effective diffusivity of species i based on the random pore model [142] and the Bosanquet approximation assuming no net mass flux through the washcoat [143]. In Eq. (5.22), $\dot{S}_i^{\text{eff}}$ is the pore transport corrected molar rate of production/consumption of species i.

5.1.3 Surface Chemistry

The local variation of the chemical source terms is described through the integration of a set of ordinary differential equations into steady-state,

$$\frac{\partial c_i}{\partial t} = \dot{S}_i\left(c_j\right) \tag{5.24}$$

$$= \sum_{k=1}^{K_\mathrm{s}} \left(\nu_{i,k}^{''} - \nu_{i,k}^{'}\right) \cdot \dot{s}_k(c_j) \tag{5.25}$$

yielding steady-state surface coverages:[3]

$$\theta_i = c_i \cdot \left(\frac{\sigma_i}{\Gamma}\right) \tag{5.26}$$

Herein, θ_i is the site fraction of surface species i on the catalytic surface, σ_i the number of surface sites occupied by species i which is set throughout this study to one for all surface species, Γ is the surface site density of the corresponding catalyst surface, $\dot{s}_i$ is the molar rate of production/consumption of species i through heterogeneous surface reactions, and $\dot{s}_k$ is the rate of reaction in step k. Both the rates are given in units of $[\frac{mol}{cm^2 s}]$.
Reaction rates are modeled within the mean-field approximation by

$$\dot{s}_k = k_{\mathrm{f},k} \prod_{j=1}^{N_\mathrm{g}+N_\mathrm{s}} c_j^{\nu_{j,k}^{'}} - k_{\mathrm{r},k} \prod_{j=1}^{N_\mathrm{g}+N_\mathrm{s}} c_j^{\nu_{j,k}^{''}} \tag{5.27}$$

Herein, $\nu_{i,k}^{'}$ and $\nu_{i,k}^{''}$ are stoichiometric coefficients of reactant ($'$) and product ($''$) species j in step k, respectively, $k_{\mathrm{f},k}$ and $k_{\mathrm{r},k}$ are the forward and reverse rate constants of step k and c_j are species concentrations given in units of $[\frac{mol}{cm^2}]$ for surface species and $[\frac{mol}{cm^3}]$ for gas-phase species. The sum over the indices in Eq. (5.27) are the total number of surface reactions K_s including ad- and desorption, and the number of gas-phase and surface species N_g and N_s, respectively.
A modified Arrhenius expression is used to describe kinetic rate constants for surface reactions.

$$k_k = \underbrace{A_k \cdot \left(\frac{T}{1\,\mathrm{K}}\right)^{\beta_k}}_{\approx A_k(T)} \cdot \exp\left[-\frac{E_{\mathrm{a},k}}{RT}\right] \cdot \prod_{i=1}^{N_\mathrm{s}} \exp\left[\frac{\nu_{k,i}\epsilon_i\theta_i}{RT}\right] \tag{5.28}$$

[3] For palladium an average value over various Pd facets has been reported to $\Gamma_{\mathrm{Pd}} = 2.09 \times 10^{-9}\,\mathrm{mol/cm^2}$ [97].

The product term in Eq. (5.28) accounts for coverage-dependent changes in the heat of formation of surface intermediate i, resulting in additional coverage-dependent contributions to the activation barrier $E_{\mathrm{a},k}$. In order to preserve thermodynamic consistency, the activation energy necessary for the transformation of the reactant state into the transition state in step k is given by

$$E_{\mathrm{af},k} = E_k^{\ddagger} - \sum_j \nu_{k,j}^{'} H_j \tag{5.29}$$

$$= E_k^{\ddagger} - \sum_j \nu_{k,j}^{'} \left(H_j^0 + \sum_i \frac{\partial H_j}{\partial \theta_i} \theta_i \right) \tag{5.30}$$

$$= \left(E_k^{\ddagger} - \sum_j \nu_{k,j}^{'} H_j^0 \right) - \sum_j \nu_{k,j}^{'} \left(\sum_i \epsilon_{j,i} \theta_i \right) \tag{5.31}$$

The differential heat of formation, $\left(\frac{\partial H_j}{\partial \theta_i}\right)$, is herein set equal to the coverage-dependent part of the activation energy, $\epsilon_{j,i}$. However, herein only self interactions of the most abundant surface intermediates are considered, as those contribute the most according to the degree of rate control theory [144–149].

Thus $j = i$, and $\left(\frac{\partial H_i}{\partial \theta_i}\right) = \epsilon_i$, gives

$$E_{\mathrm{af},k} = E_{\mathrm{a},k}^{'0} - \sum_i \nu_{k,i}^{'} \epsilon_i \theta_i \tag{5.32}$$

Where $E_{\mathrm{a},k}^{'0}$ is the activation energy barrier in the zero coverage limit. The coverage dependency onto the activation energy can be incorporated thermodynamically consistent according to the physical behavior observed experimentally. Since, $\epsilon_i > 0$ represents repulsive and $\epsilon_i < 0$ represents attractive self-interactions of species i on the surface. The stoichiometric coefficient $\nu_{i,k}$ in Eq. (5.28) accounts for the molecularity of the considered species i with coverage dependency ϵ_i in step k.

The additional temperature dependence, β_k, on the pre-exponential factor, A_k, leads to a temperature corrected pre-exponential factor, $A_k(T)$, for a surface reaction, as given in Eq. (5.28). Thus, the Arrhenius expression is actually an

empirical approximation of the formula obtained from statistical thermodynamics,

$$A_k(T) = \frac{1}{\Gamma_{\mathrm{Pd}}^{n_{\mathrm{k}}-1}} \cdot \underbrace{\frac{k_{\mathrm{B}}T}{h} \cdot \exp\left[\frac{S_{\mathrm{a},k}(T)}{R}\right]}_{=\tilde{A}_k(T)} \tag{5.33}$$

$$\approx A_k \cdot \left(\frac{T}{1\,\mathrm{K}}\right)^{\beta_k} \tag{5.34}$$

since the activation entropy term, $S_{a,k}$, can actually be calculated from partition functions of the transition state intermediate, $Q_k^{\ddagger}$, and the product/reactant state intermediates, $Q_{\mathrm{R/P}}$, on the surface, respectively:

$$\exp\left[\frac{S_{\mathrm{a},k}(T)}{R}\right] = \frac{Q_k^{\ddagger}(T)}{Q_{\mathrm{R/P}}(T)} \tag{5.35}$$

In Eq. (5.33), $S_{a,k}$ is the activation entropy in going from the reactants to the transition state in step k [150, 151], n_k is the molecularity of step k and $\tilde{A}_k(T)$ is the temperature dependent frequency factor in units of $[\mathrm{s}^{-1}]$.

Ergo, for a bimolecular surface reaction at standard temperature T_0 with zero entropy barrier, the pre-exponential factor approaches the nominal value of $\sim 10^{21}\,\mathrm{cm}^2/(\mathrm{mol\,s})$ which is equivalent to a turn-over frequency of $\sim 10^{13}\,\mathrm{s}^{-1}$.

Based on Eqs. (5.33) and (5.34) it can be shown that

$$\left(\frac{T}{T_{\mathrm{ref}}}\right)^{\beta_k} \approx \left(\frac{T}{T_{\mathrm{ref}}}\right) \cdot \exp\left[\frac{S_{\mathrm{a},k}(T) - S_{\mathrm{a},k}(T_{\mathrm{ref}})}{R}\right] \tag{5.36}$$

$$A_k \approx \frac{1}{\Gamma_{\mathrm{Pd}}^{n_{\mathrm{k}}-1}} \cdot \frac{k_{\mathrm{B}}T_{\mathrm{ref}}}{h} \cdot \exp\left[\frac{S_{\mathrm{a},k}(T_{\mathrm{ref}})}{R}\right] \tag{5.37}$$

with $T_{\mathrm{ref}} = 1\,\mathrm{K}$. Hence, if information on partition functions are available, e.g. from DFT calculations, then the pre-exponential factor at reference condition, A_k, can be determined from Eq. (5.37) and the temperature dependency on the pre-exponential factor, β_k, can be obtained according to Eq. (5.36) by extracting the slope equal to $(\beta_k - 1)$ from a linear fitting:

$$\frac{S_{\mathrm{a}}(T)}{R} = \frac{S_{\mathrm{a}}(T_{\mathrm{ref}})}{R} + (\beta_k - 1) \cdot \ln\left(\frac{T}{T_{\mathrm{ref}}}\right) \tag{5.38}$$

Generalizing Eq. (5.34) for arbitrary reference states, yields a relation to back calculate the pre-exponential factors at $T_{\mathrm{ref}} = 1\,\mathrm{K}$ from an arbitrary reference state pre-exponential factor given β_k is known:

$$A_k = A_k(T_{\mathrm{ref}}) \cdot \left(\frac{1\,\mathrm{K}}{T_{\mathrm{ref}}}\right)^{\beta_k} \tag{5.39}$$

Rate constants for adsorption reactions are modeled through sticking coefficients. Considering the mean molecular speed of the reaction mixture and the initial sticking coefficient s_i^0 of gas-phase species i with respect to the catalyst surface at zero coverage, the pre-exponential factor of an adsorption reaction k involving gas-phase species i is given as:[4]

$$A_k^{\mathrm{ads}} = \frac{s_i^0}{\Gamma_{\mathrm{Pd}}^{n_k}} \cdot \sqrt{\frac{RT}{2\pi M_i}} \tag{5.40}$$

Here, n_k represents the number of participating surface sites in the corresponding adsorption step k, with $n_k = 1$ for molecular adsorption, $n_k = 2$ for dissociative adsorption.

5.1.4 Thermodynamic Consistency

The mechanisms are developed thermodynamically consistent within the mean-field approximation. If, for a given set of $k = 1, ..., K_{\mathrm{s}}$ reversible reactions

$$\sum_i \nu_{i,k}^{'} \cdot \chi_i \overset{k_{\mathrm{f},k}}{\underset{k_{\mathrm{r},k}}{\rightleftharpoons}} \sum_i \nu_{i,k}^{''} \cdot \chi_i \tag{5.41}$$

with reaction rate constant expressions of the form as given in Eq. (5.28)

$$k_k = A_k(T) \cdot \exp\left[-\frac{E_{\mathrm{a},k}}{RT}\right] \tag{5.42}$$

the thermodynamic equilibrium constraints under ideal conditions can be written as:

$$\ln K_k(T) = \left(\frac{-\Delta_{\mathrm{R}} G_k}{RT}\right) \tag{5.43}$$

$$= \ln\left(\frac{k_{\mathrm{f},k}}{k_{\mathrm{r},k}} \cdot \frac{1}{Q_k^0}\right) \tag{5.44}$$

[4] Note: DETCHEM processes the forward rate of an adsorption reaction slightly different to the formulation as given in Eq. (5.27). Instead of surface concentrations the rate is calculated in terms of surface coverages: $\dot{S}_{f,k}^{\mathrm{ads}} = s_i^0 \cdot \sqrt{\frac{RT}{2\pi M_i}} \cdot T^{\beta} \cdot c_i^{(\mathrm{g})} \cdot \prod \theta_j^{\nu}$. This fact is important when transferring data into the DETCHEM fixed-column mechanism format (especially when using the pre-factor notation for adsorption reactions in the mechanism file (.mech) instead of the sticking coefficients notation) by back calculating values from the spatially correlated approach as e.g. given in [10]. Choosing a physically reasonable initial site coverages condition is mandatory to avoid detrimental numerical effects upon calculating the rate of adsorption.

while

(1) kinetics can be described from average values of temperature, pressure and species coverages within each computational cell

(2) the principle of microscopic reversibility holds in form of the well known thermodynamic constraints

$$\Delta_{\mathrm{R}} H_k = E_{\mathrm{af},k} - E_{\mathrm{ar},k} \tag{5.45}$$

$$\Delta_{\mathrm{R}} S_k = S_{\mathrm{af},k} - S_{\mathrm{ar},k} \tag{5.46}$$

$$\approx R \cdot \left[\ln\left(\frac{A_{\mathrm{f},k}}{A_{\mathrm{r},k}} \cdot \frac{1}{Q_k^0} \right) + (\beta_{\mathrm{f},k} - \beta_{\mathrm{r},k}) \cdot \ln\left(\frac{T}{1\,\mathrm{K}} \right) \right] \tag{5.47}$$

and

(3) there exists a unique Gibbs free energy potential for each surface intermediate of the form $G_i = H_i - T \cdot S_i$.

Then, the reaction mechanism herein is called thermodynamically consistent. Where in Eq. (5.43), K_k is the equilibrium constant. In Eq. (5.44), Q_k^0 is the reaction quotient evaluated at a given reference concentration c_i^0:

$$Q_k^0 = \prod_i \left[c_i^0 \right]^{\nu''_{i,k} - \nu'_{i,k}} \tag{5.48}$$

Depending on the type of species considered,

$$c_i^0 = \begin{cases} \dfrac{p_0}{RT} & \text{for gas-phase species} \quad (5.49a) \\ \theta_i^0 \cdot \dfrac{\Gamma_{\mathrm{Pd}}}{\sigma_i} & \text{for surface species} \quad (5.49b) \end{cases}$$

Therein, p_0 is the standard state pressure, θ_i^0 is a reference site fraction set equal to 1 ML. In Eq. (5.48), $\nu'_{i,k}$ and $\nu''_{i,k}$ are stoichiometric coefficients of species i for the forward and reverse reaction in step k.

5.2 Reaction System and Kinetic Model for Reduced Pd

5.2.1 Conceptual Approach and Assumptions

The development of a detailed microkinetic model for the catalytic me-thane oxidation is based on experimental in situ information on spatial resolved concentration and temperature profiles inside a single channel of the Pd/Al_2O_3 coated monolith. With this approach, assumptions regarding uniformity of different channels over the monolith cross-section are not required [152].
In order to circumvent issues related with the complex situation of the location of the capillary within the channel (centered vs. close to wall) and its related influence on the integral nature of the catalytic processes in the channel (i.e. residence time, conversion and concentration flow fields) as has been in detail discussed previously [101, 153–155], the effect of the introduced capillary on the reaction mixture was neglected. More accurate models capturing these effects can be realized with CFD simulations e.g., however, extra assumptions regarding the location of the capillary inside the channel are needed, as well as properly chosen inlet boundary conditions in order to draw accurate quantitative conclusions. Such information is typically not readily available and causes uncertainty even in more elaborated methods such as in CFD simulations.
In situ measured axial wall temperature profiles of the center channel for the corresponding C/O-ratios were applied as boundary condition at the channel wall, and used for the calculation of the 2-dimensional gas-phase temperature field in the channel and the reaction rates within the washcoat. Measured entrance concentrations of the species were set as boundary condition for the species conservation equations in the gas-phase. Tab. 5.1 summarizes the investigated inlet C/O-ratios as fed via mass-flow controllers (MFCs) into the reactor, the average over the C/O-ratios at the sampled points as measured along the catalytic channel, and inlet values of the channel used in the simulation. The deviation between the fed and the average C/O-ratios are within the experimental uncertainty. Gas-phase reactions were not considered since they are not significant [138] for the given conditions of atmospheric pressure and the wall temperature profiles.

5.2.2 Pd Surface Reaction Mechanism

The surface reaction mechanism presented in this work is the first step towards the development of a detailed kinetic scheme. The description of the chemical

Table 5.1: Investigated inlet conditions used for the simulation of the in situ experiments. Values for C/O = 1.0 adapted from Diehm and Deutschmann [5]. Table adapted from Stotz et al. [1].

$\left(\frac{C}{O}\right)_{set}$ (-)	$\left(\frac{C}{O}\right)_{ave}$ (-)	$T_{in,g}$ (K)	u_{in} $\left(\frac{m}{s}\right)$	CH_4 (%)	O_2 (%)	CO (%)	CO_2 (%)	H_2 (%)	H_2O (%)
0.8	0.77	858.3	0.99	11.85	7.45	0.00	0.20	0.05	0.95
1.0	0.96	795.8	0.92	12.05	5.10	0.07	0.66	0.05	1.73
1.1	1.04	794.4	0.92	13.5	6.35	0.00	0.20	0.05	0.78

Species inlet mole fractions and gas-phase temperature as measured at the inlet point of the catalytic channel. $(C/O)_{set}$ are the set-point C/O-ratios as fed to the reactor via MFCs (set-point values) and $(C/O)_{ave}$ is the measured average over sampled points along the length of the catalytic channel for a given feed value.

behavior of the oxidation of methane over the reduced phase of palladium at high temperatures is investigated under quasi-autothermal conditions.
Several global reactions are comprised in the detailed kinetic scheme representing different net reaction paths for the conversion of methane and its products, as listed in Tab. 2.1. These are the total oxidation (R_{o1}), partial oxidation (R_{o2}), steam reforming (R_{o3-4}), and the water-gas shift reaction (R_{o5}).
The reaction mechanism (cf. Tab. 5.2) consists of 7 gas-phase species including the reactants CH_4 and O_2, the partial oxidation products H_2 and CO, the total oxidation products H_2 and CO_2, and the diluent N_2. The processes on the surface are represented by a total of 27 reversible elementary-step reactions comprising 15 surface intermediates

j(s): CH_4(s), CH_3(s), CH_2(s), CH(s), C(s), CO(s), CO_2(s), H_3CO(s), H_2CO(s), HCO(s), COOH(s), O(s), H(s), OH(s), H_2O(s).

Table 5.2: Surface reaction mechanism for CH_4 oxidation over reduced palladium (thermodynamically consistent) [1]. Electronic version available under www.detchem.com.

#	Reaction	forward reaction A_f or S_0 [mol, cm, s]	β_f [-]	$E_{a,f}$ $\left[\frac{kJ}{mol}\right]$	reverse reaction A_r [mol, cm, s]	β_r [-]	$E_{a,r}$ $\left[\frac{kJ}{mol}\right]$
	Adsorption/Desorption						
1	$H_2(g) + 2Pd(s) \rightleftharpoons 2H(s)$	$2.445 \cdot 10^{-01}$	−0.076	0.0	$8.393 \cdot 10^{+19}$	0.303	85.04
2	$O_2(g) + 2Pd(s) \rightleftharpoons 2O(s)$	$5.712 \cdot 10^{-02}$	0.012	1.95	$2.932 \cdot 10^{+22}$	−0.049	$221.82 - 2 \cdot \epsilon_O \theta_O$
3	$CH_4(g) + Pd(s) \rightleftharpoons CH_4(s)$	$8.557 \cdot 10^{-03}$	0.017	0.0	$1.865 \cdot 10^{+13}$	−0.068	29.5
4	$CH_4(g) + 2O(s) \rightleftharpoons H_3CO(s) + OH(s)$	$8.928 \cdot 10^{-03}$	0.007	$159.98 - 2 \cdot \epsilon_O \theta_O$	$2.046 \cdot 10^{+18}$	-0.017	248.69
5	$H_2O(g) + Pd(s) \rightleftharpoons H_2O(s)$	$1.402 \cdot 10^{-01}$	0.033	0.0	$1.244 \cdot 10^{+14}$	−0.134	46.59
6	$CO_2(g) + Pd(s) \rightleftharpoons CO_2(s)$	$8.186 \cdot 10^{-03}$	−0.037	0.0	$1.392 \cdot 10^{+12}$	0.146	23.16
7	$CO(g) + Pd(s) \rightleftharpoons CO(s)$	$6.716 \cdot 10^{-01}$	0.015	0.94	$8.565 \cdot 10^{+13}$	−0.062	$138.56 - \epsilon_{CO} \theta_{CO}$
	Water activation/formation						
8	$O(s) + H(s) \rightleftharpoons OH(s) + Pd(s)$	$3.598 \cdot 10^{+22}$	−0.060	$85.04 - \epsilon_O \theta_O$	$4.169 \cdot 10^{+20}$	0.060	66.46
9	$H(s) + OH(s) \rightleftharpoons H_2O(s) + Pd(s)$	$3.017 \cdot 10^{+20}$	−0.059	0.0	$4.972 \cdot 10^{+22}$	0.059	109.62
10	$OH(s) + OH(s) \rightleftharpoons H_2O(s) + O(s)$	$2.516 \cdot 10^{+19}$	−0.001	54.53	$3.578 \cdot 10^{+23}$	0.000	$183.57 - \epsilon_O \theta_O$
	CO/CO_2 direct oxidation/formation						
11	$C(s) + O(s) \rightleftharpoons CO(s) + Pd(s)$	$5.434 \cdot 10^{+23}$	0.004	$21.1 - \epsilon_O \theta_O$	$2.392 \cdot 10^{+21}$	−0.004	$214.9 - \epsilon_{CO} \theta_{CO}$
12	$CO(s) + O(s) \rightleftharpoons CO_2(s) + Pd(s)$	$6.874 \cdot 10^{+18}$	0.052	$71.25 - \epsilon_O \theta_O - \epsilon_{CO} \theta_{CO}$	$2.400 \cdot 10^{+21}$	−0.052	132.75
	(P1) Pyrolytic CH_4 activation						
13	$CH_4(s) + Pd(s) \rightleftharpoons CH_3(s) + H(s)$	$1.301 \cdot 10^{+22}$	0.064	66.98	$1.052 \cdot 10^{+21}$	−0.064	38.42
14	$CH_3(s) + Pd(s) \rightleftharpoons CH_2(s) + H(s)$	$2.811 \cdot 10^{+24}$	0.064	104.25	$4.870 \cdot 10^{+21}$	−0.064	37.15
15	$CH_2(s) + Pd(s) \rightleftharpoons CH(s) + H(s)$	$8.888 \cdot 10^{+23}$	0.064	100.28	$1.540 \cdot 10^{+25}$	−0.064	63.72
16	$CH(s) + Pd(s) \rightleftharpoons C(s) + H(s)$	$2.811 \cdot 10^{+23}$	0.064	20.75	$4.870 \cdot 10^{+24}$	−0.064	165.85
	(P2) Oxygen-assisted CH_4 activation						
17	$CH_4(s) + O(s) \rightleftharpoons CH_3(s) + OH(s)$	$2.591 \cdot 10^{+24}$	0.004	$96.62\text{-}\epsilon_O \theta_O$	$2.427 \cdot 10^{+21}$	−0.004	49.48
18	$CH_3(s) + O(s) \rightleftharpoons CH_2(s) + OH(s)$	$2.611 \cdot 10^{+25}$	0.004	$97.35\text{-}\epsilon_O \theta_O$	$5.243 \cdot 10^{+20}$	−0.004	11.65
19	$CH_2(s) + O(s) \rightleftharpoons CH_2(s) + OH(s)$	$8.257 \cdot 10^{+21}$	0.004	$88.32\text{-}\epsilon_O \theta_O$	$1.658 \cdot 10^{+21}$	−0.004	33.18
20	$CH(s) + O(s) \rightleftharpoons C(s) + OH(s)$	$2.611 \cdot 10^{+21}$	0.004	$36.45\text{-}\epsilon_O \theta_O$	$5.243 \cdot 10^{+20}$	−0.004	163.35

Table 5.2: continued

#	Reaction	forward reaction A_f [mol, cm, s]	β_f [-]	$E_{a,f}$ $\left[\frac{kJ}{mol}\right]$	reverse reaction A_r [mol, cm, s]	β_r [-]	$E_{a,r}$ $\left[\frac{kJ}{mol}\right]$
	(P3) Methoxy Mediated Pathway						
21	$H_3CO(s) + O(s) \rightleftharpoons H_2CO(s) + OH(s)$	$2.351 \cdot 10^{+24}$	0.017	$65.71 - \epsilon_O \theta_O$	$5.824 \cdot 10^{+21}$	−0.017	56.89
22	$H_2CO(s) + O(s) \rightleftharpoons HCO(s) + OH(s)$	$2.351 \cdot 10^{+24}$	0.017	$31.01 - \epsilon_O \theta_O$	$5.824 \cdot 10^{+21}$	−0.017	14.99
23	$HCO(s) + O(s) \rightleftharpoons CO(s) + OH(s)$	$2.351 \cdot 10^{+24}$	0.017	$12.11 - \epsilon_O \theta_O$	$5.824 \cdot 10^{+21}$	−0.017	$111.19 - \epsilon_{CO} \theta_{CO}$
	Steam Reforming/ WGS						
24	$C(s) + OH(s) \rightleftharpoons H(s) + CO(s)$	$1.898 \cdot 10^{+22}$	0.064	0.0	$7.213 \cdot 10^{+21}$	−0.064	$213.4 - \epsilon_{CO} \theta_{CO}$
25	$CO(s) + OH(s) \rightleftharpoons COOH(s) + Pd(s)$	$4.167 \cdot 10^{+19}$	0.018	$48.4 - \epsilon_{CO} \theta_{CO}$	$3.251 \cdot 10^{+21}$	−0.018	25.9
26	$COOH(s) + Pd(s) \rightleftharpoons CO_2(s) + H(s)$	$1.871 \cdot 10^{+19}$	0.094	0.0	$7.228 \cdot 10^{+21}$	−0.094	92.8
27	$COOH(s) + H(s) \rightleftharpoons CO(s) + H_2O(s)$	$2.532 \cdot 10^{+18}$	0.076	0.0	$5.349 \cdot 10^{+18}$	−0.076	$131.3 - \epsilon_{CO} \theta_{CO}$

Pd(s) denotes a free reduced Pd surface site. The repulsive self-interactions are: $\epsilon_{O(s)}$=11.25 kJ/mol; $\epsilon_{CO(s)}$=31.0 kJ/mol.

The adsorption reactions (R1-R6) of the gas-phase species have been modeled with sticking coefficients based on experimental observations mainly from temperature programmed desorption studies. Pre-exponential factors are derived from transition state theory and are within the reasonable range for uni- and bimolecular surface reactions steps [150, 156, 157]. The enthalpies of formation of all surface intermediates, activation energies, and reaction enthalpies have been initially determined within the unity bond index-quadratic exponential potential (UBI-QEP) framework [158] and afterward adjusted thermodynamically consistent. Selected parameters have been corrected to fit the model predictions with experimental results within a physical meaningful range but always thermodynamically consistent.

For the activation of CH_4 species over the reduced phase of palladium, three different activation paths have been considered. The first path involves the stepwise abstraction of hydrogen from $CH_x(s)$ species with $x = \{4, 3, 2, 1\}$, down to elemental carbon C(s). This path is further on called the "pyrolytic activation" path (P1) and requires unoccupied reduced Pd(s)-Pd(s) site-pairs. The second CH_4 activation path involves pre-adsorbed O(s) via Pd(s)-O(s) site-pairs and leads to the formation of surface methyl $CH_x(s)$ and hydroxyl OH(s) species. The latter path is only active as long as O(s) species are sufficiently present on the surface, and is in the following context called "oxygen-assisted activation" path (P2). A third activation path has been incorporated, additionally capturing experimental observations at fuel-lean conditions and high temperatures [11]. Under these conditions, Pd is still in the reduced state but O(s) species strongly cover the surface and decrease the CH_4 conversion activity significantly, as reduced Pd(s) sites are rarely available. In this path, C-H bond activation of CH_4 proceeds through activated dissociative adsorption of methane and formation of methoxide species $H_3CO(s)$, which can then subsequently undergo further oxygen-assisted dehydrogenation steps ($H_3CO(s) \rightarrow H_2CO(s) \rightarrow HCO(s) \rightarrow CO(s)$). The methoxy mediated activation path is based on the reaction scheme proposed by Chin and Iglesia et al. [36] and incorporates the involvement of site-pairs of O(s)-O(s) and Pd(s)-O(s) over reduced Pd. It has been shown theoretically by means of DFT calculations that these site-pairs provide an additional route to activate the first C-H bond in methane under conditions where the Pd surface is saturated with oxygen. This path will further on be called "dual-oxygen-assisted" path (P3).

For the development of a thermodynamically consistent surface reaction mechanism, an iterative adjustment procedure is applied [1, 159, 160], which corrects the kinetic raw-data (E_a, A and β), to obtain a set of thermodynamic consistent kinetic parameters. Further information on the concept of thermodynamic consistency is presented in Section 5.1.4 and in greater detail the Appendix B.2.

5.2.3 Kinetic Data Base

The kinetic raw input-data used for the construction and development of the mechanism has been developed within the UBI-QEP framework for the reduced catalyst phase of Pd [158, 161–166]. Additional changes on the UBI-QEP raw data set were made where necessary, i.e. when values obtained from experimental results (surface science studies) or elaborated theoretical methods (DFT) can better describe the processes on the catalyst surface than the UBI-QEP values, for comparison with the experimental data. The different raw kinetic data sets need to be distinguished from the thermodynamically consistent data set which is generated by the adjustment procedure[5].

CH_x over reduced Pd

Dissociative initial sticking probabilities of CH_4(s) on clean Pd(111) and Pd(110) surfaces were reported by Valden et al. with $\sim 1.8 \times 10^{-2}$ [167] and $\sim 3.0 \times 10^{-2}$ [168, 169], respectively. Tait et al. [170] found similar values with 2.79×10^{-2} on Pd(111) and 1.03×10^{-2} on Pd nanoparticles. The presented mechanism considers the adsorption of methane through CH_4(s) species as pre-cursor mediated state (R3) on reduced Pd(s) sites, with an initial sticking coefficient of 1.0×10^{-2} (8.6×10^{-3}), which is within the range of the experimentally observed values.
Activation energy barriers for C-H bond activation of methane over different bulk-truncated open and closed-packed Pd facets have been estimated from DFT-calculations by Trinchero et al. [171]. The DFT derived values are reported as 82.98 kJ/mol (0.86 eV), 67.54 kJ/mol (0.7 eV) and 57.89 kJ/mol (0.60 eV) for the Pd(111), Pd(100) and Pd(211) facets, respectively. In our study, the activation energy for the first C-H bond abstraction step (R13) of the pyrolytic path (P1) was calculated from the UBI-QEP method, yielding a barrier of 66.55 kJ/mol (66.98 kJ/mol) which is close to the one reported over Pd(100) by Trinchero et al. [171]. The barriers for the consecutive C-H abstraction steps (R24 - R30) within the CH_x(s) species have been determined from UBI-QEP as well.
The first C-H abstraction barrier (R17) for the oxygen-assisted path (P2) has been chosen to be 101.5 kJ/mol (96.62 kJ/mol), a value which lies between the UBI calculated value of 71.5 kJ/mol and the DFT derived value of 136.9 kJ/mol

[5] Following notation is applied in section 5.2.3: Parameter values presented without brackets corresponds to data which has not been thermodynamically adjusted yet, but correspond to kinetic raw input-data which is used in the adjustment procedure to construct the thermodynamic consistent mechanism; data given in brackets represents adjusted parameters. E.g.: 50.1 kJ/mol vs. (54.9 kJ/mol).

from Chin et al. [36] determined from extrapolation to zero O(s) coverage over Pd(111) surface. The barrier of 158.0 kJ/mol (159.98 kJ/mol) for the dissociative CH_4 activation step (R4) in the dual-oxygen-assisted path (P3) is comparatively high as DFT calculation by Chin et al. [36] showed as well. Taking their value of 141 kJ/mol at 1 ML O(s) as a reference, yields an activation energy barrier of 176 kJ/mol in limit of zero O(s) coverage which is ca. 17 kJ/mol higher than the value listed in the mechanism. The very high barrier of the reverse reaction of 256 kJ/mol (248.69 kJ/mol) was chosen based on comparison of experimental data and model results and indicates that this step is essentially irreversible.

O_2 over reduced Pd

The interaction between oxygen and palladium has been extensively studied in the literature by means of thermal desorption spectra (TDS), low-energy electron diffraction (LEED), high resolution electron energy loss spectroscopy (HREELS), and scanning tunneling microscopy (STM) as comprehensively summarized by Salanov et al. [172]. DFT calculations by Trinchero et al. [171] over Pd(111), Pd(100) and Pd(211) facets at 0.25 ML coverage yielded adsorption energies of −241.22 kJ/mol, −231.57 kJ/mol and −229.64 kJ/mol, respectively. Desorption energies have been determined from temperature programmed desorption (TPD) studies on polycrystalline Pd. Values reported by Milun et al. [173] fall in the in the range of 218 kJ/mol at low and 147 kJ/mol to 166 kJ/mol at high oxygen coverage. In their study they estimate the initial sticking coefficient of oxygen to be in the range of 0.05 to 0.07. Similarly, Conrad et al. [174] finds a value of ca. −230.27 kJ/mol for the adsorption energy over Pd(111) and an initial sticking coefficient of 0.3 for O_2. Salanov et al. [175] determined a desorption energy of 230 kJ/mol at coverages $\leq$ 0.25 ML and $\sim$ 800 K, with TPD data, using a model that took the lateral interaction into account under the assumption of a second-order desorption process (associative desorption) over polycrystalline palladium. The mean pre-exponential factor for desorption was found as 1.2×10^{23} cm^2/(mol s) (0.2 cm^2/(atms s)).
Lateral repulsive interactions of ∼5 kJ/mol to 10 kJ/mol were reported for coverages $\geq$ 0.25 ML. In a later study by Salanov et al. [172], the value of the initial sticking coefficient has been reported to be 0.7.
The initial sticking coefficient used in the presented mechanism (R2) has a value of 0.07 (0.057) which is in line with the experimentally determined value of Milun et al. [173]. The activation energy for associative desorption has been calculated from UBI-QEP method to 229.6 kJ/mol (221.8 kJ/mol), consistent with the reported experimental and DFT derived values [171, 174, 175]. The pre-exponential factor for that step (R8) before thermodynamic adjustment has

been set to $1.3 \times 10^{22}\,\mathrm{cm}^2/(\mathrm{mol\,s})$ ($2.93 \times 10^{22}\,\mathrm{cm}^2/(\mathrm{mol\,s})$), also close to the reported one [175].
A linear O(s) coverage dependency on the heat of formation with a contribution of $\epsilon_{\mathrm{O(s)}} = 11.25\,\mathrm{kJ/mol}$, has been included in order to incorporate lateral repulsive interactions amongst O(s) species and to allow for coverage-dependent changes in the corresponding activation energy barriers for all reactions involving O(s) species as reactants. This value is in close agreement with the experimentally determined value of Salanov et al. [172]. A DFT based value from Chin et al. [36], can be determined from the coverage-dependent C-H bond activation step over Pd(s)-O(s) site pairs which is slightly larger with $\sim 30.8\,\mathrm{kJ/mol}$.

CO over reduced Pd

The interaction of CO with palladium was subject of a number of experimental studies using infrared spectroscopy (IR) [176], work function shift (WS) [177–179], calorimetry [180], and molecular beam techniques (MB) [181]. The adsorption of CO has been studied by Behm et al. [178] over the Pd(100) surface. An initial sticking coefficient of 0.6 was found. Similarly, Engel et al. [181] finds the corresponding value for the Pd(111) surface to be 0.96. Voogt et al. [182] determined the initial isosteric heat of CO adsorption from ellipsometry over the Pd(111) surface to be in the range of $-148 \pm 5\,\mathrm{kJ/mol}$. Furthermore, repulsive CO interactions were found, as observed during the decrease in the initial heat of adsorption with increasing CO coverage. Infrared reflection-absorption spectroscopy (RAIRS) was applied by Szanyi et al. [176] on the Pd(100) and Pd(111) surfaces, yielding values for initial heats of adsorption of $-125.5\,\mathrm{kJ/mol}$ and $-159.1\,\mathrm{kJ/mol}$, respectively. Trinchero et al. [171] determined CO adsorption energies from DFT simulations over different Pd facets. The computed values for the (111), (100) and (211) surfaces are $-188.9\,\mathrm{kJ/mol}$, $-181.2\,\mathrm{kJ/mol}$ and $-184.2\,\mathrm{kJ/mol}$, respectively. Guo et al. [183] determines from TDS the pre-exponential factor for CO desorption to be $\sim 3.16 \times 10^{13}\,\mathrm{s}^{-1}$ at zero coverage. The values used in the present study for the activation energy of CO desorption (R10) of 142.3 kJ/mol (138.56 kJ/mol) as determined from UBI-QEP method, the corresponding pre-exponential factor of $3.5 \times 10^{13}\,\mathrm{s}^{-1}$ ($8.6 \times 10^{13}\,\mathrm{s}^{-1}$) and the CO initial sticking coefficient (R6) of 0.84 (0.67) are in close agreement with the experimentally determined values [176, 178, 181–185]. The activation energy for the CO oxidation step (R21) with a value of 61.0 kJ/mol (71.25 kJ/mol) is comparable with the DFT calculated value by Huang et al. [186] of 77.12 kJ/mol as determined for a Pd(111) surface.

H_2 over reduced Pd

Ad- and desorption properties of H_2 over Pd have been reported in a variety of publications. Initial sticking coefficients of hydrogen from TDS and adsorption energies over Pd(100), (110) and (111) surfaces have been summarized by Christmann [187] and are reported in the range of 0.5 to 0.7 [188–190] and 88 kJ/mol to 102 kJ/mol [188, 191]. Aldag and Schmidt [192] find a slightly lower initial sticking coefficient of 0.13, using flash filament desorption technique over a Pd wire. Activation energies for desorption have been reported by Conrad et al. [191] and are in the range of 75.4 kJ/mol to 100.5 kJ/mol depending on Pd(100) and (111) single crystal surface and extent of coverage. DFT calculations by Greeley and Mavrikakis [193] determine values of 114.7 kJ/mol (PW91) and 76.2 kJ/mol (RPBW) for the closed-packed Pd surfaces. Pre-exponential factors for a second-order desorption of hydrogen have been estimated from TDS experiments for Pd(111) and (100) surfaces as $7.8 \times 10^{22}\,\mathrm{cm}^2/(\mathrm{mol\,s})^{-1}$ [194] and $6.0 \times 10^{22}\,\mathrm{cm}^2/(\mathrm{mol\,s})^{-1}$ [188].
The activation energy for associative desorption of H_2 (R7) of 82.8 kJ/mol (85.0 kJ/mol) used in the mechanism is close to the reported experimental and theoretical values [191, 193]. The used sticking coefficient (R1) of 0.1 (0.24) is comparable to the reported experimental value [192].

H_2O over reduced Pd

Stuve et al. [195] experimentally studied the water interaction with a Pd(100) surface using TPD, LEED and HREELS, suggesting that H_2O adsorbs molecularly on clean Pd surfaces at low temperatures with a desorption energy of $\sim$ 43.12 kJ/mol. DFT adsorption energies for water over the Pd(111) surface have been calculated by Huang et al. [186] to 28.92 kJ/mol. A comparable value of 26.99 kJ/mol is reported by Clay and coworkers [196] for Pd(111) as well. Information in the literature on the sticking probabilities of H_2O on palladium is very scarce. Values reported in the literature list or assume values close to 1.0 [195, 197–199] at low temperatures. Activation energies for water dissociation over Pd(111) surfaces based on DFT calculations were also under the focus of interest. Several groups studied the same reaction but may used different sized unit cells [186, 196, 200]. Values are reported in the range of 80.98 kJ/mol to 119.54 kJ/mol and reaction enthalpies are calculated to be in the range of 31.81 kJ/mol to 62.66 kJ/mol. Moreover, activation energies for further dissociation of hydroxyl intermediates have been stated to be in the range of 84.83 kJ/mol to 130.14 kJ/mol and corresponding reaction enthalpies are stated between 0.0 kJ/mol to 34.7 kJ/mol therein. Clay et al. [196] also report values

for the OH(s) disproportionation reaction with an activation energy barrier of 0.0 kJ/mol and an exothermic reaction enthalpy of −31.81 kJ/mol.
The value used in the present mechanism for the H_2O desorption energy (R9), is based on UBI-QEP calculations, yielding a value of 41.8 kJ/mol (46.59 kJ/mol) which is close to the experimentally determined [195] and the DFT calculated values [186, 196]. The activation energy for the water activation step (R16) determined from UBI-QEP method with a value of 108.8 kJ/mol (109.62 kJ/mol) is similar to the DFT derived one by Phatak et al. [200] with a value of 101.22 kJ/mol. The OH(s) disproportionation reaction barrier (R17) was estimated by comparing of model results with experimental data.

5.2.4 PES of C-H Bond Activation Steps in Methane

Representative potential energy diagrams for the different C-H bond activation paths of CH_4 over reduced palladium (P1-P3), at specific reaction conditions within the single catalytic channel are given in Fig. 5.2. The PESs are derived from the thermodynamic consistent set of enthalpic contributions H_i of the involved species and from the corresponding activation energy barriers of the reaction steps. The initial states (IS) with respect to zero energy, are defined as the clean Pd(s) surface with one CH_4(g) (Fig. 5.2 (a)), one CH_4(g) and one O_2(g) (Fig. 5.2 (b)) and one CH_4(g) and 2.5 O_2(g) (Fig. 5.2 (c)) molecules in the gas-phase, respectively. The distinctive paths illustrate changes in the energetic of the potential energy surface depending on temperature and surface coverage of intermediates O(s) and CO(s). In the case of the oxygen-assisted paths (P2, P3), it can be seen that the activation energy barriers for the C-H bond activation steps in methane and the following steps are lowered upon increasing the oxygen coverage.

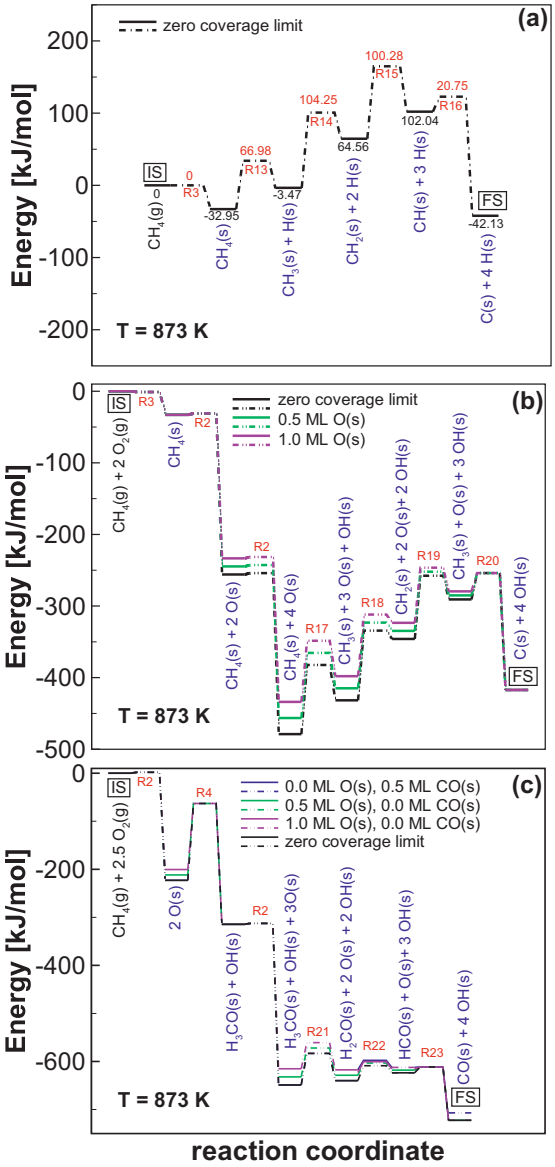

Figure 5.2: Potential energy diagrams for (a) pyrolytic CH_x activation (P1), (b) oxygen-assisted CH_x activation (P2) and (c) dual-oxygen-assisted CH_x activation (P3). Figure adapted from Stotz et al. [1].

5.3 Reaction System and Kinetic Model for PdO

The kinetic model presented in this study is developed based on the DFT derived surface energetics from Grönbeck et al. [10] and comprises two active sites, present in the (101) facet of PdO namely, the coordinatively unsaturated (cus) Pd_{cus} and O_{cus} sites.

One objective of this study is to corroborate whether a mean field extended microkinetic model (MF-MKM) can sufficiently mimic relevant kinetic aspects for methane oxidation when considering two different uncorrelated active sites. Furthermore, we focus on the transferability of available DFT-based kinetic data into a detailed mechanism suitable for technical conditions. The developed MF-MKM comprises a Mars-van-Krevelen (MvK) redox mechanism, consistent with pulse TG experiments [201] and the findings from isotopic labeling studies for CH_4 oxidation over PdO based catalysts [45]. Dual site mechanisms have been previously developed for methane oxidation over PdO, however only in a global kinetic formulation [202] or using the spatially correlated approach [10, 203].

In this context and also for technical exhaust gas applications, it is important to distinguish the reversible water inhibition effect from the water deactivation as the mechanisms behind them seem to be different [22, 50, 71, 74]. Adsorbed H_2O and OH species can provoke changes in the catalytic activity for PdO, towards a decreased conversion [57]. However, the deactivation effect could also be understood based on a loss of catalytic active surface area due to wetting with the support resulting in changes of the particle shape and related factors due to hindered oxygen exchange with the support [132, 137, 204–207]. Nevertheless, water inhibition over PdO catalysts is typically only pronounced under fuel-lean conditions at sufficiently low temperatures ($T < 500\,^{\circ}C$) when water is present in the reaction mixture either in the feed gas, originating from the engine exhaust, or inherently formed as a product during catalytic methane oxidation. The grown interest in the oxidized form of Pd, originates from the fact that the catalytic activity scales with the oxidation state of the Pd-phase as has been shown by several groups [69, 208, 209].

5.3.1 Concept and Assumptions of the MF Extended MKM

In the pair-correlated formalism of the DFT-based MKM of Grönbeck et al. [10], reaction rates are calculated based on joint pair probabilities, i.e. turn-over

frequencies of the elementary reaction rates are based on per site-pair. For example, the reaction rate (turnover frequency) for methane adsorption over empty Pd_{cus}-O_{cus} site-pairs (here denoted as (a)-(b) for simplicity), $CH_4(g)$ + (a)-(b) $\rightleftharpoons$ CH_3(a)-H(b), is expressed according to that formalism as:

$$r_{k,\mathrm{ads}} = k_{k,\mathrm{ads}} \cdot x_{\mathrm{CH_4(g)}} \cdot P_{a-b} = \left[\frac{mol_{\mathrm{ads},k}}{mol_{(a-b)}} \cdot \frac{1}{s} \right] \tag{5.50}$$

$$k_{k,\mathrm{ads}} = \frac{s_i^0}{\Gamma_{\mathrm{site}}} \cdot \frac{1}{\sqrt{2\pi M_i RT}} \cdot \exp\left[-\frac{E_\mathrm{a}}{RT} \right] \tag{5.51}$$

Similarly, rates for surface reactions are expressed analogously on a per site-pair basis and in terms of joint pair probabilities. Obviously, when applying the pairing formalism on spatially correlated sites, the combinatorial number of paired (or correlated) species for a given basis set of unpaired (uncorrelated) surface species is much higher and thus requires more surface species for which the rate equations needs to be solved for. This methodology allows for formulating multiple pathways for essentially the same surface reaction to convert reactant intermediate species into a product intermediate species. For example, reactions where co-adsorbed species or paired species occur may have different energetic parameters as in the undisturbed case. The inclusion of those different 'flavored' reactions may be beneficial for the predictive power of the overall mechanism. However, this benefit is at the cost of a dramatically increased numerical effort, especially in simulations for applications with technical background. Thus, to reduce these overloads of complexity, while still preserving a sufficient degree of mechanistic detailedness, we calculate reaction rates in terms of unpaired species concentrations, c_j, instead of pair probabilities $P_{(\mathrm{x-y})}$. That way, the total number of species and reactions is reduced, while rate constants are evaluated based on standard Arrhenius and kinetic expressions without the need to compute additional subsets of analytical equations for the evaluation of explicit joint pair-probabilities during simulation time (spatial correlation function) [10].

The following assumptions were made for model simplification of the MKM (cf. Fig. 5.3) and to simulate the herein investigated experimental conditions:

(1) Joint pair-probabilities of finding a species x(a) sitting next to a species y(b), $P_{(\mathrm{x-y})}$, can be written as product of the uncorrelated pair-probabilities of species x(a), $P_{(\mathrm{x-*})}$, and species y(b), $P_{(*-\mathrm{y})}$, sitting next to any other, either free or occupied (b) or (a) site (denoted here as *), respectively, and the spatial correlation function $f_{\mathrm{sc}}(P_{(\mathrm{n-m})})$ which in turn is a function of all other explicit joint pair-probabilities: $P_{(\mathrm{x-y})} = P_{(\mathrm{x-*})} \cdot P_{(*-\mathrm{y})} \cdot f_{\mathrm{sc}}(P_{(\mathrm{n-m})})$.

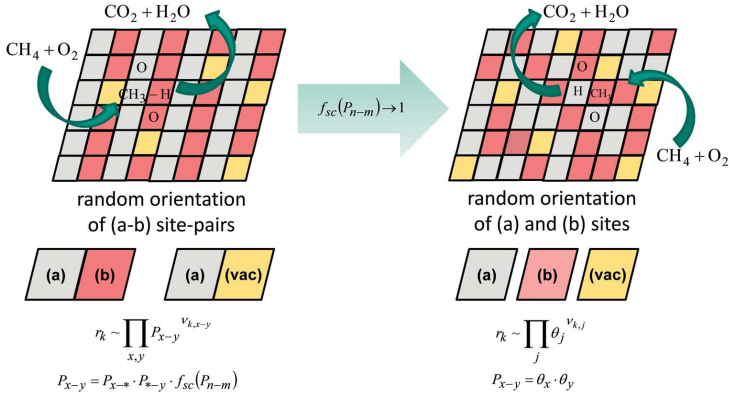

Figure 5.3: Schematic illustration of the simplified PdO(101) model surface and the implications of the mean field extension on pair-wise correlated surface sites/species, (a-b), and rate proportionalities. (a) denotes a Pd_{cus}-site, (b) denotes an O_{cus}-site and vac(b) denotes an oxygen vacancy O^{x}_{cus} within the PdO(101) surface. Figure adapted from Stotz et al. [2].

(2) Intermediates participating in surface reactions on adjacent (a)-(b) site-pairs are treated as unpaired reaction partners, i.e., the Gibbs free energy change and the activation energy of a pairing reaction step is assumed to be zero. Thus, paired and unpaired reaction partners sitting next to each other are indistinguishable. This implies for instance that the reaction $x(\mathrm{a})-y(\mathrm{b}) + (\mathrm{a})-z(\mathrm{b}) \rightleftharpoons (\mathrm{a})-xz(\mathrm{b}) + (\mathrm{a})-y(\mathrm{b})$ is equivalently written as $x(\mathrm{a})|y(\mathrm{b}) + (\mathrm{a})|z(\mathrm{b}) \rightleftharpoons (\mathrm{a})|xz(\mathrm{b}) + (\mathrm{a})|y(\mathrm{b})$, where $x(\mathrm{a})|y(\mathrm{b})$ denotes species $x(\mathrm{a})$ sitting next to $y(\mathrm{b})$ unpaired on an (a-b) site pair. Therefore, the joint probabilities of paired and unpaired species are equivalent: $P_{(\mathrm{x-y})} = P_{(\mathrm{x|y})}$.

(3) The different active surface site pairs are treated as spatially uncorrelated, i.e. active sites occur randomly distributed over the surface according to the mean field approximation and the spatial correlation functions of all other explicit joint probabilities, $f_{sc}(P_{(\mathrm{n-m})})$, approach one in the absence of spatial correlations. This in turn implies that the reaction $x(\mathrm{a})|y(\mathrm{b}) + (\mathrm{a})|z(\mathrm{b}) \rightleftharpoons (\mathrm{a})|xz(\mathrm{b}) + (\mathrm{a})|y(\mathrm{b})$ can be equivalently expressed as $x(\mathrm{a}) + z(\mathrm{b}) \rightleftharpoons xz(\mathrm{b}) + (\mathrm{a})$. Thus, the joint pair probability can be expressed in terms of surface coverages, $\theta_{\mathrm{x(a)}}$ and $\theta_{\mathrm{y(b)}}$: $P_{(\mathrm{x-y})} = P_{(\mathrm{x|y})} = P_{(\mathrm{x-*})} \cdot P_{(\mathrm{*-y})} = \theta_{\mathrm{x(a)}} \cdot \theta_{\mathrm{y(b)}}$.

(4) The PdO catalyst is approximated as fully oxidized PdO(101) facet consisting of equal amounts of sites of the $(Pd)_{cus}$ and $(O)_{cus}$ type (denoted here as (a) and (b) sites). The model surface is representative for the catalytic activity of the oxidation process considered herein.

(5) The surface site density of (a), (b) and (a-b) site-pairs are approximated by a single average value for the PdO(101) surface site density, i.e., $\Gamma_{PdO} = \Gamma_{(a)} = \Gamma_{(b)} = \Gamma_{(a)+(b)} = \sigma \cdot \Gamma_{(a-b)}$, where σ is the (a-b) site-pair to (a)+(b) site conversion factor, with $\sigma = 2$. Thus, it is assumed that (a) and (b) sites require the same space within the PdO(101) surface. Where Γ_{PdO} is the single site density and $\tilde{\Gamma}_{PdO} = \frac{\Gamma_{PdO}}{\sigma}$ is the cus site-pair surface site density.

(6) With the aforementioned assumptions, surface concentrations on a site-pair basis, $\tilde{c}_{(i-*)} = [\frac{mol_i}{cm^2_{(a-b)}}]$, can be expressed on a single site basis, e.g. $c_{i(a)} = \tilde{c}_{(i-*)} \cdot \sigma = [\frac{mol_i}{cm^2_{(a)}}]$. Analogously, reaction rates on a site-pair basis, $\dot{\tilde{s}}_k(\tilde{c}_{(i-j)}) = [\frac{mol_k}{cm^2_{(a-b)} \cdot s}]$, can be equivalently expressed as rate per single site: $\dot{s}_k(c_j) = (\dot{\tilde{s}}_k \cdot \sigma)$.

(7) The standard state enthalpy and entropy of formation for (a) and vac(b) sites are set as reference value to zero.

(8) Support effects, e.g., oxygen exchange between support and PdO particle are not explicitly taken into account as alumina is present as the support.

(9) The catalyst properties such as particle size, catalyst state of oxidation, X_{ox}, and micro-structural parameters of the washcoat do not change during the course of the reaction with time nor vary over the length of the reactor. Those parameters are treated constant during simulation, except when stated explicitly.

(10) The model assumes isothermal conditions over the reactor length. This assumption was legitimate as in the considered experiments gases introduced into the flow-reactor setup were diluted and reactive gas-mixtures were fed under fuel-lean conditions at high space velocities. Gas-phase reactions were not considered since they are not significant [138, 210] for the given conditions of atmospheric pressures, temperatures and inlet concentrations.

The mean field approximation can be applied for the (101) facet since each site (Pd_{cus} or O_{cus}) has equal access to the same amount of anionic or cationic type of sites on the surface and since meanfield averaging will lead to a similar

situation, where on average the same number of anionic or cationic sites sit next to each other.

In the model for the oxidized surface, the species net-reaction rate source terms, $\dot{s}_k$, are given in units of $[\frac{mol_i}{cm^2_{(a)}}\frac{1}{s}]$ or $[\frac{mol_i}{cm^2_{(b)}}\frac{1}{s}]$ and were calculated according to Eq. (5.27). Reaction rate coefficients were calculated according to the Eq. (5.28) with $\epsilon_i = 0$.

Conversion of reaction rates in terms of turnover frequencies, r_k, into area specific rates, $\dot{s}_k$, is given by

$$\dot{s}_k = \left(\dot{\tilde{s}}_k \cdot \sigma\right) \tag{5.52}$$

$$= r_k \cdot \Gamma_{\mathrm{PdO}} \tag{5.53}$$

Uncorrelated pair probabilities, $P_{i(\mathrm{a})-*}$ and $P_{*-i(\mathrm{b})}$ are equivalent to the surface coverage for species occupying (a) or (b) sites, respectively.

$$P_{i(\mathrm{a})-*} = \frac{c_{i(\mathrm{a})}}{\Gamma_{\mathrm{PdO}}} \tag{5.54}$$

$$= \tilde{c}_{i(\mathrm{a})-*} \cdot \left(\frac{\sigma}{\Gamma_{\mathrm{PdO}}}\right) \tag{5.55}$$

$$= \theta_{i(\mathrm{a})} \tag{5.56}$$

$$P_{*-i(\mathrm{b})} = \frac{c_{i(\mathrm{b})}}{\Gamma_{\mathrm{PdO}}} \tag{5.57}$$

$$= \tilde{c}_{*-i(\mathrm{b})} \cdot \left(\frac{\sigma}{\Gamma_{\mathrm{PdO}}}\right) \tag{5.58}$$

$$= \theta_{i(\mathrm{b})} \tag{5.59}$$

Surface coverages are therefore referenced to the total number of $(\mathrm{Pd})_{\mathrm{cus}}$ or $(\mathrm{O})_{\mathrm{cus}}$ sites, equal to one monolayer of cus sites ($\mathrm{ML}_{\mathrm{cus}}$) of each type. Thus, $\theta_{i(\mathrm{a})}, \theta_{i(\mathrm{b})} \in [0,1]$ while $P_{(i-*)} \in [0,1]$ is related to the total number of $(\mathrm{Pd})_{\mathrm{cus}}$-$(\mathrm{O})_{\mathrm{cus}}$ site-pairs equal to one monolayer ($\mathrm{ML}_{(\mathrm{Pd})_{\mathrm{cus}}-(\mathrm{O})_{\mathrm{cus}}}$).

Initially, for a fully oxidized and clean PdO(101) surface $\theta_{(\mathrm{a})} = \theta_{(\mathrm{b})} = 1$, and $\sum \theta_{i(\mathrm{a})} = \sum \theta_{i(\mathrm{b})} = 1$ holds at any condition. Analogously, surface concentrations c_i are referenced to the total number of cus sites of the corresponding type, i.e. either $(\mathrm{Pd})_{\mathrm{cus}}$ or $(\mathrm{O})_{\mathrm{cus}}$, respectively.
The site-balance initial condition is chosen such that a stoichiometric 1:1 ratio of (a):(b)-sites is given.

DFT-data for activation energies and pre-exponential frequency factors for spatially correlated reactions containing paired species were adopted from [10]. The

initial kinetic parameter set was further modified to incorporate the stated assumptions as described above. Pre-exponential frequency factors were converted into units of [cm, mol, s], corrected for the uncorrelated case, and then adjusted to obtain a new set of thermodynamic consistent reaction rate parameters in the temperature range between 300 K to 1073 K. Further explanation regarding the adjustment of reaction rate constants towards thermodynamic consistency is found in section 5.1.4.

Conversion of frequency factors, $\tilde{A}_k$, (units of $\left[s^{-1}\right]$) into pre-exponential factors for surface reactions, A_k, (units in [mol, cm, s]) was obtained according to Eq. (5.39) and Eq. (5.33) assuming $\beta_k = 0$ for simplicity, since a priori information on the temperature dependence of the pre-exponential factors was not provided in [10]. Thus, applying the following conversion formula:

$$A_k \approx \tilde{A}_k^{\text{ref}} \cdot \left(\frac{1}{\Gamma_{\text{PdO}}}\right)^{n_k - 1} \tag{5.60}$$

Where A_k is given in units of $\left[\frac{mol_{\text{transf},k}}{mol_{(\text{a-b})}} \frac{1}{s} \frac{cm^{2(n-1)}}{mol^{(n-1)}}\right]$, and n_k is the number of participating surface species in the corresponding direction of reaction step k. Adsorption steps were converted on the basis of sticking coefficients:

$$s_i^0 = \tilde{A}_{k,\text{ads}}^{\text{ref}} \cdot \tilde{\Gamma}_{\text{PdO}} \cdot \sqrt{2\pi M_i R T_{\text{ref}}} \cdot \left(\frac{100^2}{\sqrt{1000}}\right) \tag{5.61}$$

In Eq. (5.61), s_i^0 is given in units of $\left[\frac{mol_k}{mol_{(\text{a-b})}} \frac{1}{Pa \cdot s} \frac{mol_{(\text{a-b})}}{cm^2_{(\text{a-b})}} \frac{1}{mol_{\text{tot},k}} \frac{kg_i \cdot m}{s}\right]$, i.e. unitless, and $A_{k,\text{ads}}^{\text{ref}}$ is the pre-exponential frequency factor for an adsorption event in $\left[(\text{Pa} \cdot \text{s})^{-1}\right]$ at the thermodynamic reference pressure P_{ref} of 1 bar and at the specified reference temperature, T_{ref}, of 700 K, s_i^0 is the initial sticking coefficient of the adsorbing species i in step k, and M_i is the corresponding molecular weight in [g/mol] and R the universal gas constant in $\left[\text{J mol}^{-1}\,\text{K}^{-1}\right]$. Values for sticking coefficients are adopted from [10] and adjusted to be in a physically reasonable range.

The net turnover frequency for methane consumption through oxidation over PdO was analyzed and calculated from the transport corrected net consumption rate of methane $\dot{s}_{\text{CH}_4}^{\text{eff}}$, the surface site density of PdO(101) and the washcoat effectiveness factor η, according to

$$r_{\text{CH}_4} = \frac{\dot{s}_{\text{CH}_4}^{\text{eff}}}{\Gamma_{\text{PdO}}} \cdot \frac{1}{\eta} \tag{5.62}$$

$$= \frac{\dot{s}_{\text{CH}_4}}{\Gamma_{\text{PdO}}} \tag{5.63}$$

Where r_{CH_4} is the turn over frequency of methane given in units of $\left[\frac{mol_{CH_4}}{mol_{(a-b)} \cdot s}\right]$, and $\dot{S}_{CH_4}$ is the net rate of consumption of methane without effects of internal transport-limitations.

For the PdO phase the species net flux into the gas-phase at the channel-washcoat interface needs to be calculated from the rate on a site-pair basis. Based on Eqs. (5.12), (5.13) and (5.53) we can write:

$$J_{i,r}|_{r=R} = -\dot{\tilde{S}}_i \cdot M_i \cdot \left(\frac{A_{PdO}}{A_{geo}}\right) \cdot \eta \tag{5.64}$$

$$= -\left(\dot{\tilde{S}}_i \cdot \sigma\right) \cdot M_i \cdot \left(\frac{1}{\sigma} \cdot \frac{A_{PdO}}{A_{geo}}\right) \cdot \eta \tag{5.65}$$

$$= -\dot{S}_i \cdot M_i \cdot \tilde{F}_{cat/geo} \cdot \eta \tag{5.66}$$

Eq. (5.65) gives the site-pair corrected catalytic-to-geometric surface area ratio for calculations within DETCHEM^{CHANNEL}:

$$\tilde{F}_{cat/geo} = \frac{1}{\sigma} \cdot \frac{A_{PdO}}{A_{geo}} \tag{5.67}$$

With Eq. (5.65) species rates of formation/consumption can be conveniently calculated with standard kinetic expressions as given in Eqs. (5.27) and (5.28), and as also implemented in established CFD and kinetic reactor model codes such as e.g. DETCHEM or CHEMKIN.

5.3.2 Determination of the PdO(101) Surface Site Density

The surface site density of the PdO phase is determined from the active surface facet, i.e. the stoichiometric PdO(101) surface termination for which equal amounts of palladium and oxygen atoms are located within the surface layer (cf. Fig. 5.4).

The calculations are based on the experimentally determined values of the lattice constants for the tetragonal bulk structure of PdO as reported by Rogers et al. [211] from powder XRD samples and the given rectangular unit cell of the stoichiometric PdO(101) facet [89]. Related parameters for the calculations, e.g. the average unit cell volume per bulk atom $v_{m,PdO}$ and the average unit surface area per surface atom $a_{m,PdO}$ are shown in Tab. 5.3.

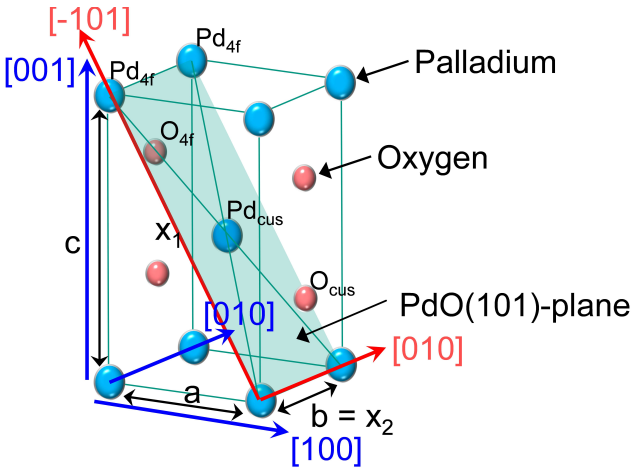

Figure 5.4: Schematic representation of a unit cell cut for the tetragonal crystal lattice of PdO along the (101) plane and therein exposed coordinatively unsaturated (cus) and fourfold (4f) palladium and oxygen atoms. Figure adapted from Stotz et al. [2].

Table 5.3: Lattice constant parameters (a, b and c) of the tetragonal bulk structure of the PdO crystal and associated bulk and surface parameters for the (101)-plane with stoichiometric Pd:O termination. Table adapted from Stotz et al. [2].

Parameter	Value	Unit	Ref.
a, b	3.043	[Å]	[211]
c	5.336	[Å]	[211]
$v_{m,\mathrm{PdO}}$	12.353	[Å^3/atom]	calc.
$a_{m,\mathrm{PdO}}$	4.673	[Å^2/atom]	calc.
$\Gamma_{\mathrm{PdO(101)}}$	$3.553 \cdot 10^{-9}$	[mol/cm^2]	calc.

The surface site density, Γ_{PdO}, was calculated under the assumption that four surface sites per unit cell are available [10, 89]:

$$\Gamma_{\mathrm{PdO}} = \frac{1}{N_{\mathrm{a}}} \cdot \frac{4}{b \cdot (a^2 + c^2)^{0.5}} \tag{5.68}$$

$$= 3.553 \times 10^{-9} \, \frac{\mathrm{mol}}{\mathrm{cm}^2} \tag{5.69}$$

In the work of Grönbeck et al. [10] two bridge and two top-sites of coordinatively unsaturated $(\mathrm{Pd})_{\mathrm{cus}}$ and $(\mathrm{O})_{\mathrm{cus}}$ atoms within the PdO(101) surface were considered for their DFT calculations, respectively. Similarly, combining experimental temperature programmed desorption (TPD) results with DFT calculations, Choi et al. [89] considered two cus-sites ($(\mathrm{Pd})_{\mathrm{cus}}$, $(\mathrm{O})_{\mathrm{cus}}$) and two 4f-sites ($(\mathrm{Pd})_{\mathrm{4f}}$, $(\mathrm{O})_{\mathrm{4f}}$). The important role of coordinatively unsaturated Pd sites and the related stereo-configuration to neighboring sites resulting in different site pairs, (e.g. $(\mathrm{Pd})_{\mathrm{cus}}$-$(\mathrm{O})_{\mathrm{cus}}$, $(\mathrm{Pd})_{\mathrm{cus}}$-$(\mathrm{O})_{\mathrm{Pd(cus)}}$, $(\mathrm{Pd})_{\mathrm{cus}}$-$(\mathrm{O})_{\mathrm{4f}}$) are relevant for methane activation and formation of subsequent intermediates, as has been pointed out previously [36, 45, 84, 115, 212]. $(\mathrm{Pd})_{\mathrm{cus}}$ sites have also been termed "vacancies" [45, 50] due to their unsaturated nature in their oxygen bonds within the stoichiometric PdO(101) facet. However, those sites need to be distinguished from lattice oxygen vacancies of PdO, $(\mathrm{vac})_{\mathrm{O(cus)}}$, stemming from reducible $(\mathrm{O})_{\mathrm{cus}}$ oxide sites ($(*)_{\mathrm{O(cus)}}$). In contrast, within non-stoichiometric PdO terminations, e.g. PdO(100), exposed Pd-atoms are fourfold coordinated to oxygen and barriers for methane activation tend to be higher [36, 80].

As direct accessibility of catalytic active sites through dispersion measurements is difficult to obtain, only an approximate determination of the exposed particle surface area is possible. Additionally, the active site density may also vary during the course of the reaction [22, 45]. Due to the complicated nature of the PdO system, Eq. (5.68) can be considered as a simplification for the applied mean field model, as number and participating active sites may not only be within the (101) facet and site densities may also vary. However, the procedure here gives a value on physical grounds and an estimate on the expected site(-pair) density for the highly active and kinetically relevant (101) facet.

5.3.3 Determination of the Catalytic Surface Area of PdO

In the MKM a number of terms are directly scaled by the catalytic active surface area and the corresponding surface site density. Calculations of the source terms as given in Eq. (5.25), are directly affected through this scaling. Thus

for precise evaluation of the source terms and derived quantities such as TOFs, reaction orders or apparent activation energies, it is essential to know physically reasonable values of the catalytic active surface area and the surface site density of the considered catalytic phase.
This is of particular importance for the comparability and applicability of the mechanism for the purpose of studying kinetic and deactivation effects under technical relevant conditions, as A_{cat} and Γ_{PdO} directly affect the catalytic activity. However, accessibility of these values is demanding. The complex combination of different PdO particle shapes, sizes and exposed facets complicates the assessment and values may even change during the course of the reaction [69, 213]. A principle value, which can be used in typical reactor models with multistep mean field kinetic approach, is thus difficult to obtain. To this extend, the situation for oxidized catalysts is even more complicated as compared to reduced metal catalysts, as direct experimental accessibility of the number of available active PdO-sites from the amount of chemisorbed CO requires the catalyst in the reduced state. However, a reductive pre-treatment of oxidized PdO particles has been shown to alter the catalyst particle properties [136, 137].

Catalytic Surface Area of PdO after Chemical Reductive Pretreatment

As the metal dispersion obtained from CO chemisorption measurements is given for the reduced phase of Pd, it is not equal to bulk oxidized PdO surface area [136, 214]. Nonetheless, PdO is the predominantly present phase under the investigated experimental conditions herein. Therefore, several further assumptions are taken into account in order to correlate the PdO surface area to the exposed metallic Pd surface area (cf. Fig. 5.5). The complete oxidation of Pd particles in the model is rationalized by assuming a 2-step procedure:

(1) Oxidation of the reduced Pd particle under full stoichoimetric oxygen uptake in order to form bulk PdO at a preserved hemispherical particle shape, leading to a larger PdO particle.

(2) Break-up of the larger PdO particles due to stress and strain from the lattice expansion by oxygen incorporation into the initially existing Pd particles. Thus, step two leads to the formation of smaller fragmented and aggregated PdO particles. For the second step a preserved hemispherical particle shape is also assumed.

These assumptions allow to calculate the catalytic active surface area of fully oxidized PdO particles, A^{1}_{PdO}, from the catalytic surface area of reduced Pd

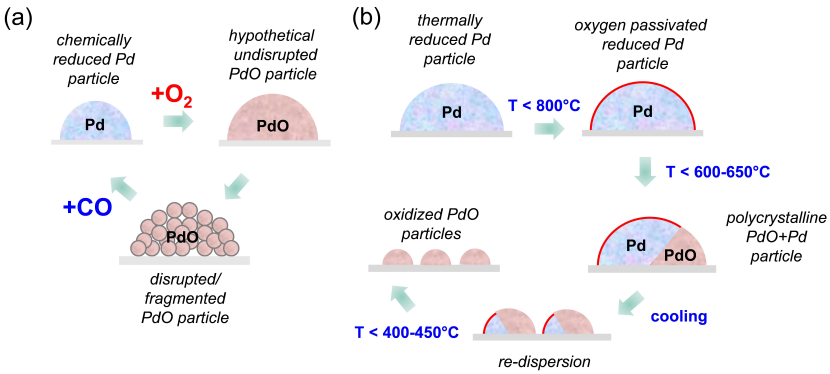

Figure 5.5: Schematic representations of the processes considered for the assumptions used to determine the catalytic active surface area of PdO. (a) When catalytic surface area is determined from experimental metal dispersions of pre-reduced Pd. Fragmentation upon oxidation shown in the schematic is in qualitative agreement with TEM image observations by Penner et al. [136]. (b) For oxidizing Pd during cool down from high temperatures after thermal reduction. Schematic in qualitative agreement with TEM image observations and HT-XRD analysis by Datye et al. [53]. Figure adapted from Stotz et al. [2].

particles, $A^{\mathrm{l}}_{\mathrm{Pd}}$ ($= A_{\mathrm{Pd}}$, using Eq. (4.4)), when no ruptures or break-up during oxidation occurs, according to

$$A^{\mathrm{l}}_{\mathrm{PdO}} = \left(\frac{2 \cdot v_{\mathrm{m,PdO}}}{v_{\mathrm{m,Pd}}} \right)^{2/3} \cdot A^{\mathrm{l}}_{\mathrm{Pd}} \tag{5.70}$$

$$= 1.41 \cdot A^{\mathrm{l}}_{\mathrm{Pd}} \tag{5.71}$$

The un-disrupted PdO particle size is related to the reduced Pd particle size as

$$d^{\mathrm{l}}_{\mathrm{PdO}} = \left(\frac{2 \cdot v_{\mathrm{m,PdO}}}{v_{\mathrm{m,Pd}}} \right)^{1/3} \cdot d^{\mathrm{l}}_{\mathrm{Pd}} \tag{5.72}$$

$$= 1.19 \cdot d^{\mathrm{l}}_{\mathrm{Pd}} \tag{5.73}$$

In Eq. (5.70) and Eq. (5.72), v_m is the average unit cell volume per bulk atom in the respective crystal lattices of either Pd or PdO, while $A^{\mathrm{l}}_{\mathrm{Pd}}$ was initially determined from Eq. (4.4).

Reducing small PdO particles in H_2 leads to small Pd particles [59] and re-dispersion of small Pd particles upon complete oxidation forms aggregates of small PdO particles [136]. As changes upon oxidation leads to a volume increase and additional break-up and surface roughening of the initially reduced Pd particles into smaller aggregates of PdO particles [136], contribution from break-up is accounted for by considering the Pd-to-PdO particle size ratio:

$$A^{\mathrm{s}}_{\mathrm{PdO}} = \left(\frac{d^{\mathrm{l}}_{\mathrm{Pd}}}{d^{\mathrm{s}}_{\mathrm{PdO}}} \right) \cdot 1.19 \cdot A^{\mathrm{l}}_{\mathrm{PdO}} \tag{5.74}$$

Where $A^{\mathrm{s}}_{\mathrm{PdO}}$ is the exposed surface area of the small PdO aggregates assuming preserved hemispherical particle shape, $d^{\mathrm{l}}_{\mathrm{Pd}}$ is the particle size of the reduced (large) Pd particles, $d^{\mathrm{s}}_{\mathrm{PdO}}$ is the diameter of the small PdO aggregates and $A^{\mathrm{l}}_{\mathrm{PdO}}$ is the surface area one would obtain after complete oxidation of the initially reduced Pd particles if their shape would be preserved and no break-up or surface roughening would occur. The Pd-to-PdO particle size ratio was found to be in the range $\frac{d^{\mathrm{l}}_{\mathrm{Pd}}}{d^{\mathrm{s}}_{\mathrm{PdO}}} \sim \{1.7 - 3.5\}$ [136, 214]. The surface area increase upon oxidation has been considered in the model simulations, accounting for the uncertainty in the catalytic surface area. In the model simulations (cf. Section 6.2.1 and 6.2.5) metal oxide corrected dispersions are used to calculate the catalytic active surface area, as determined from CO chemisorption measurements on the metal Pd phase, according to Eqs. (5.74), (5.71) and (4.4). The catalytic active PdO surface area is then approximately given by $A^{\mathrm{s}}_{\mathrm{PdO}} = \{2 - 4\} \cdot A^{\mathrm{l}}_{\mathrm{PdO}}$. This gives

a surface area increase factor, $\frac{A^{\mathrm{s}}_{\mathrm{PdO}}}{A^{\mathrm{l}}_{\mathrm{Pd}}}$, in the range of around $\{2.85 - 5.89\}$ for supported Pd catalysts which falls partly in the range of values reported by Ribeiro et al. [214] as determined for Pd single crystal surfaces, ranging between $\{1.6 - 3.2\}$, when no support effects are present.

Thus, for evaluation of the catalytic surface area of PdO in Eq. (5.67) after a chemical reductive pretreatment (chemisorption measurments), A_{PdO} was calculated with Eq. (5.74), assuming

$$\frac{\left(\frac{d^{\mathrm{l}}_{\mathrm{Pd}}}{d^{\mathrm{s}}_{\mathrm{PdO}}}\right) \cdot 1.19}{\sigma} \approx 1 \tag{5.75}$$

i.e. taking the lower limit value of the particle size ratio from the TEM image observations from [136, 214] as conservative estimate (cf. section 6.2).
Ergo, the term $\frac{A^{\mathrm{s}}_{\mathrm{PdO}}}{\sigma}$ (cf. Eq. (5.17b)), using Eq. (5.74) with the assumption from Eq. (5.75), effectively reduces to Eq. (5.71).[6]

$$A_{\mathrm{cat}} = \frac{A^{\mathrm{s}}_{\mathrm{PdO}}}{\sigma} \tag{5.76}$$

$$\approx 1.41 \cdot A^{\mathrm{l}}_{\mathrm{Pd}} \tag{5.77}$$

Catalytic Surface Area of PdO during Cool Down from High Temperatures after Thermal Reduction

In case of PdO particles obtained from complete oxidation during cool down of large Pd particles, as obtained from thermal reduction at high temperatures (T > 800 °C), when sintering of the reduced Pd particles prior to oxide formation plays a role [11, 69] (cf. Fig. 5.5b and Section 6.3.2), one may rather use experimentally in situ information on the average value for the PdO particle diameter, $\bar{d}_{\mathrm{PdO}}$, and the degree of oxidation of the Pd phase, X_{ox}, as function of temperature during light-out for determining the catalytic active surface area (Eq. (5.78) and Eq. (5.80)):

$$D_{\mathrm{PdO}}(T) = \left(\frac{v_{\mathrm{m,PdO}}}{a_{\mathrm{m,PdO}}}\right) \cdot \frac{6}{\bar{d}_{\mathrm{PdO}}(T)} \cdot f_{\mathrm{ox}}(T) \tag{5.78}$$

$$= 1.59 \cdot \frac{f_{\mathrm{ox}}(T)}{\bar{d}_{\mathrm{PdO}}(T)} \tag{5.79}$$

[6] Note: It is likely that this assumption should actually be further relaxed towards higher particle size ratios, since it is known from the literature that typically not all facets are of the (101) type and particle shape change effects may also lead to deviations in the hemispherical particle assumption.

$$A_{\mathrm{PdO}} = 2 \cdot X_{\mathrm{ox}}(T) \cdot \left(\frac{m_{\mathrm{cat}} w_{\mathrm{Pd}}}{M_{\mathrm{Pd}}}\right) \cdot \frac{D_{\mathrm{PdO}}(T)}{\Gamma_{\mathrm{PdO}}} \tag{5.80}$$

where X_{ox} is the degree of oxidation to convert Pd into PdO with $X_{\mathrm{ox}} \in [0,1]$, and $X_{\mathrm{ox}} \cdot \left(\frac{m_{\mathrm{cat}} w_{\mathrm{Pd}}}{M_{\mathrm{Pd}}}\right)$ is the actual amount of converted Pd atoms into PdO in moles. The factor 2 arises from the fact that not N_{Pd} moles of Pd but $N_{\mathrm{Pd}} + N_{\mathrm{O}} = 2 \cdot N_{\mathrm{Pd}}$ moles of sites in the surface need to be considered. In Eq. (5.79), $\bar{d}_{\mathrm{PdO}}(T)$ is given in [nm] and $\frac{f_{\mathrm{ox}}(T)}{\bar{d}_{\mathrm{PdO}}(T)}$ accounts for temperature dependent changes in the amount of oxidized palladium and particle size. When not explicitly specified, X_{ox} and f_{ox} are set to one, otherwise

$$f_{\mathrm{ox}}(T) = \frac{1}{\left[1 + \left(\frac{\bar{v}_{\mathrm{m,Pd}}}{2 \cdot \bar{v}_{\mathrm{m,PdO}}}\right) \cdot \left(\frac{1 - X_{\mathrm{ox}}(T)}{X_{\mathrm{ox}}(T)}\right)\right]^{1/3}} \tag{5.81}$$

The derivation of Eq. (5.81) can be found in Appendix B.3

5.3.4 PdO Surface Reaction Mechanism

The reaction network with all considered carbonaceous CH_xO_y species (cf. Fig. 5.6) consists in total of 23 surface intermediates, with 15 surface species related to Pd_{cus}-sites:

j(a): (a), O(a), O_2(a), OH(a), H_2O(a), CO(a), HCOO(a), H(a), CO_2(a), CH_3(a), CH_2OH(a), CH_2O(a), CHO(a), CH_2(a), CH(a)

Analogously, 8 surfaces species are associated with O_{cus}-sites:

j(b): (b), vac(b), O(b), H(b), CO(b), CH_2(b), CH_3(b), CHO(b)

Reducible O_{cus}-sites can react to form oxygen vacancies vac(b). The mechanism considers steps for lattice oxygen reduction and formation of oxygen vacancies as well as their regeneration through oxygen incorporation into lattice vacancies, according a Mars-van-Krevelen mechanism. The complete set of 39 reversible reaction steps together with the reaction rate parameters are summarized in Tab. 5.4.

Reacting species participating in the gas-phase are CH_4, O_2, H_2O and CO_2 excluding the diluent N_2 which is only considered as inert component. Since CO and H_2 are neither fed to the reactor nor occurring in the gas-phase during reaction over the PdO phase, ad-/ desorption events were neglected herein. This also improved numerical stability and stiffness of the system.

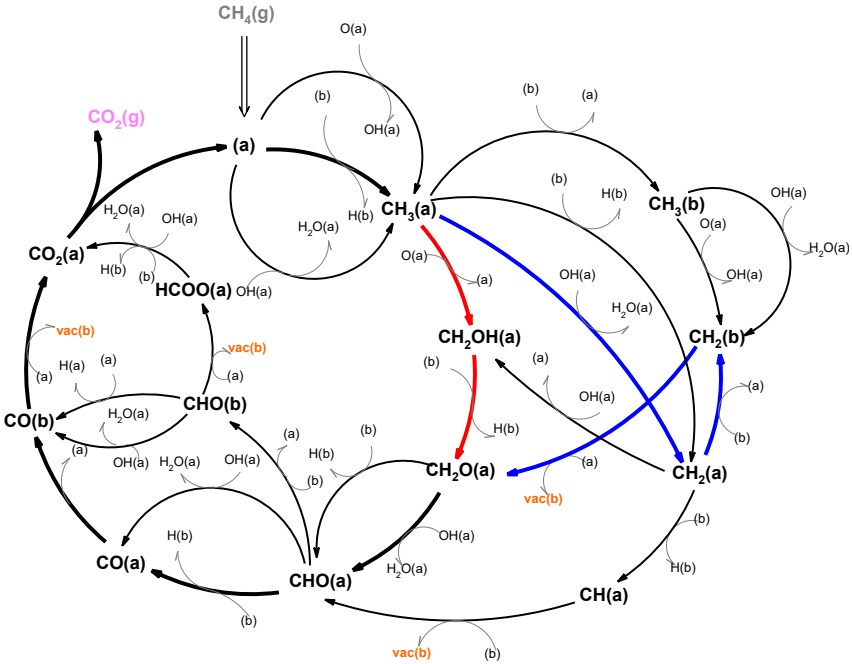

Figure 5.6: Schematic of the considered C_1-pathways containing carbonaceous CH_xO_y intermediates. *Red arrows*: indicate the preferential reaction pathway at dry conditions before light-off (low temperature path). *Blue arrows*: preferential reaction path after light-off at dry and mainly during wet conditions (high temperature path). *Black bold arrows*: common preferential reaction pathway. Figure adapted from Stotz et al. [2].

Table 5.4: Surface reaction mechanism for CH_4 oxidation over oxidized palladium (thermodynamically consistent) [2]. Electronic version available under www.detchem.com.

#	Reaction	forward reaction A_f or s^0 [mol, cm, s]	β_f [-]	$E_{a,f}$ $\left[\frac{kJ}{mol}\right]$	reverse reaction A_r [mol, cm, s]	β_r [-]	$E_{a,r}$ $\left[\frac{kJ}{mol}\right]$
	Adsorption/Desorption						
1	$CH_4(g) + (a) + (b) \rightleftharpoons CH_3(a) + H(b)$	$4.582 \cdot 10^{-02}$	−0.001	33.155	$1.034 \cdot 10^{+21}$	0.003	106.180
2	$CH_4(g) + OH(a) + (a) \rightleftharpoons CH_3(a) + H_2O(a)$	$1.510 \cdot 10^{-02}$	0.001	28.86	$7.071 \cdot 10^{+19}$	−0.004	104.259
3	$CH_4(g) + O(a) + (a) \rightleftharpoons CH_3(a) + OH(a)$	$3.082 \cdot 10^{-02}$	0.007	26.234	$2.695 \cdot 10^{+20}$	−0.029	192.865
4*	$O_2(g) + (a) \rightleftharpoons O_2(a)$	$5.710 \cdot 10^{-02}$	0.0	0.0	$6.702 \cdot 10^{+15}$	−0.031	63.541
5*	$O_2(g) + vac(b) \rightleftharpoons O(b)$	$5.710 \cdot 10^{-02}$	0.0	0.0	$7.024 \cdot 10^{+15}$	−0.027	159.975
6*	$H_2O(g) + O(a) + (a) \rightleftharpoons 2OH(a)$	$1.400 \cdot 10^{-01}$	0.0	0.0	$3.307 \cdot 10^{+20}$	−0.013	191.178
7*	$H_2O(g) + (a) \rightleftharpoons H_2O(a)$	$1.400 \cdot 10^{-01}$	0.0	0.0	$6.293 \cdot 10^{+12}$	−0.045	99.946
8*	$CO_2(g) + (a) \rightleftharpoons CO_2(a)$	$4.910 \cdot 10^{-02}$	0.0	0.0	$4.087 \cdot 10^{+14}$	0.029	65.097
	Surface Reactions						
9	$CH_3(a) + (b) \rightleftharpoons CH_3(b) + (a)$	$1.494 \cdot 10^{+22}$	0.008	131.139	$2.441 \cdot 10^{+23}$	0.008	181.201
10	$CH_3(b) + O(a) \rightleftharpoons CH_2(b) + OH(a)$	$1.250 \cdot 10^{+22}$	0.012	33.366	$1.855 \cdot 10^{+22}$	−0.012	303.074
11	$CH_3(b) + OH(a) \rightleftharpoons CH_2(b) + H_2O(a)$	$1.398 \cdot 10^{+22}$	−0.004	33.193	$1.111 \cdot 10^{+22}$	0.004	221.667
12	$CH_3(b) + O(a) \rightleftharpoons CH_2OH(b) + (a)$	$3.534 \cdot 10^{+21}$	0.016	30.953	$2.466 \cdot 10^{+23}$	−0.016	333.447
13	$CH_3(a) + OH(a) \rightleftharpoons CH_2(a) + H_2O(a)$	$2.014 \cdot 10^{+21}$	−0.004	73.229	$1.175 \cdot 10^{+22}$	−0.004	116.851
14	$CH_2(a) + OH(a) \rightleftharpoons CH_2OH(a) + (a)$	$3.420 \cdot 10^{+21}$	−0.004	12.581	$2.191 \cdot 10^{+22}$	0.004	180.219
15	$CH_2OH(a) + (b) \rightleftharpoons CH_2O(a) + H(b)$	$1.917 \cdot 10^{+22}$	−0.012	12.654	$3.348 \cdot 10^{+20}$	−0.012	57.646
16	$CH_2O(a) + OH(a) \rightleftharpoons CHO(a) + H_2O(a)$	$5.608 \cdot 10^{+21}$	0.012	51.570	$2.119 \cdot 10^{+22}$	−0.012	192.230
17	$CHO(a) + OH(a) \rightleftharpoons CO(a) + H_2O(a)$	$5.921 \cdot 10^{+22}$	0.008	65.968	$8.990 \cdot 10^{+21}$	−0.008	267.530
18	$CH_3(a) + (b) \rightleftharpoons CH_2(a) + H(b)$	$1.827 \cdot 10^{+21}$	0.000	123.976	$5.137 \cdot 10^{+22}$	−0.000	165.224
19	$CH_2(a) + (b) \rightleftharpoons CH_2(b) + (a)$	$1.257 \cdot 10^{+22}$	0.000	13.103	$2.797 \cdot 10^{+22}$	−0.000	198.07
20	$CH_2(a) + (b) \rightleftharpoons CH(a) + H(b)$	$3.793 \cdot 10^{+22}$	0.008	112.541	$2.987 \cdot 10^{+22}$	−0.008	163.159
21	$CH(a) + (b) \rightleftharpoons CHO(a) + vac(b)$	$2.103 \cdot 10^{+21}$	0.008	24.821	$1.218 \cdot 10^{+21}$	−0.008	215.219
22	$CH(b) + (a) \rightleftharpoons CH_2O(a) + vac(b)$	$2.155 \cdot 10^{+22}$	−0.008	91.222	$2.425 \cdot 10^{+20}$	−0.008	9.038
23	$CH_2O(a) + (b) \rightleftharpoons CHO(a) + H(b)$	$3.274 \cdot 10^{+21}$	0.008	69.676	$5.962 \cdot 10^{+22}$	−0.008	207.964

Table 5.4: continued

#	Reaction	forward reaction A_f [mol, cm, s]	β_f [-]	$E_{a,f}$ $\left[\frac{kJ}{mol}\right]$	reverse reaction A_r [mol, cm, s]	β_r [-]	$E_{a,r}$ $\left[\frac{kJ}{mol}\right]$
24	CHO(b) + (b) ⇌ CO(a) + H(b)	$1.088 \cdot 10^{+23}$	0.004	55.610	$7.956 \cdot 10^{+22}$	−0.004	254.800
25	CHO(a) + (b) ⇌ CHO(b) + (a)	$2.746 \cdot 10^{+22}$	0.018	76.549	$6.754 \cdot 10^{+21}$	−0.018	106.611
26†	CHO(b) + (a) ⇌ CO(b) + H(a)	$2.732 \cdot 10^{+21}$	−0.002	141.937	$2.123 \cdot 10^{+21}$	0.002	263.113
27	CO(a) + (b) ⇌ (a) + CO(b)	$1.313 \cdot 10^{+21}$	0.011	33.868	$2.212 \cdot 10^{+21}$	−0.011	16.262
28	CO(b) + (a) ⇌ CO_2(a) + vac(b)	$1.410 \cdot 10^{+21}$	0.010	42.023	$9.554 \cdot 10^{+20}$	−0.010	78.477
29§	H(b) + (a) ⇌ OH(a) + vac(b)	$1.886 \cdot 10^{+22}$	0.000	137.8	$4.222 \cdot 10^{+21}$	0.000	27.9
30	O_2(a) + (a) ⇌ O(a) + O(a)	$3.815 \cdot 10^{+22}$	−0.005	174.961	$1.744 \cdot 10^{+21}$	−0.005	59.139
31	O(b) + (a) ⇌ O(a) + (b)	$2.380 \cdot 10^{+22}$	0.027	116.625	$1.797 \cdot 10^{+21}$	−0.027	107.875
32	O(a) + vac(b) ⇌ (a) + (b)	$8.012 \cdot 10^{+21}$	0.020	48.597	$1.387 \cdot 10^{+22}$	−0.020	252.103
33	O_2(a) + vac(b) ⇌ O(a) + (b)	$1.196 \cdot 10^{+24}$	0.025	81.408	$9.469 \cdot 10^{+22}$	−0.025	169.092
34	H(b) + (a) ⇌ H(a) + (b)	$6.133 \cdot 10^{+22}$	0.002	148.173	$9.505 \cdot 10^{+21}$	−0.002	117.827
35†	CHO(b) + OH(a) ⇌ H_2O(a) + CO(b)	$2.992 \cdot 10^{+22}$	0.001	2.168	$3.113 \cdot 10^{+22}$	−0.001	156.062
36§	CHO(b) + (a) ⇌ HCOO(a) + vac(b)	$3.658 \cdot 10^{+21}$	0.000	11.580	$1.210 \cdot 10^{+21}$	0.000	8.680
37†	HCOO(a) + OH(a) ⇌ CO_2(a) + H_2O(a)	$2.305 \cdot 10^{+23}$	0.011	183.191	$4.912 \cdot 10^{+23}$	−0.011	376.439
38†	HCOO(a) + (b) ⇌ H(b) + CO_2(a)	$1.681 \cdot 10^{+23}$	0.007	177.623	$1.726 \cdot 10^{+24}$	−0.007	368.497
39‡⋆	H_2O(a) + (b) ⇌ OH(a) + H(b)	$3.659 \cdot 10^{+21}$	0.000	12.5	$1.763 \cdot 10^{+22}$	0.008	10.126

‡ After thermodynamic adjustment, the DETCHEM "=" notation was applied for the forward step (instead of ">"). The "=" notation enables calculation of the parameters in reverse direction from the equilibrium constant of that step, i.e. from thermdata information of the involved surface species obtained after adjustment, and from the forward reaction rate constant. The reverse step was therefore commented out after adjustment.

† Kinetic raw data obtained by linear combination of given reaction rate parameters in [10], assuming neither spatial correlation nor pairing.

⋆ Kinetic raw data of forward step was fixed during thermodynamic adjustment procedure, i.e. $w_{f,k} = 0$.

§ Kinetic raw data of forward and reverse step was fixed during thermodynamic adjustment procedure, i.e. $w_{f,k} = w_{r,k} = 0$.

For thermodynamic adjustment, self-interaction coverage dependencies for H(b) and H_2O(a) ($(H(b)) and $(H2O(a))) had been introduced and set to 10 kJ/mol. After adjustment, these values were set to zero, i.e. consistency in the zero coverage limit.

6 Simulation Results[1]

6.1 Simulation Results with Pd Mechanism

6.1.1 Simulated Axial Concentration Profiles

The simulated 2-dimensional contours of concentration flow fields and gas-phase temperature for a feed C/O-ratio = 1.1 are shown in Fig. 6.1. It can be seen from the contours of CH_4 and O_2 that strong external gradients occur at the entrance of the channel. Oxygen is consumed rapidly and is depleted within the first ~ 1.5 mm to 2 mm of the channel. The evolution of the CO_2 contour is representative for a species which is rapidly produced at the entrance region of the catalyst wall and then mixed into the channel. The H_2O contour appears conversely, where a combination of regeneration/mixing at the inlet region and consumption further downstream occurs.
For a better comparison of model predictions and experimental results, the contours are radially averaged over the channel cross-section and further presented as axial concentration profiles. This procedure allows convenient comparison of experimental and simulated concentration profiles as shown in Fig. 6.2. In addition to the cross-sectional average values, the boundary values at the channel wall and centerline have been included. The overlaid shaded areas comprise the profile lines of the averaged values. Shaded areas are confined by the lower and upper concentration bounds which are the axial concentration profiles at the wall ($r = R$) and the channel centerline ($r = 0$) or vice versa, depending on whether the considered species is consumed or produced along the channel axis. The bounds indicate the width of the radial concentration distribution over the channel cross-section at each axial position.

[1] Parts of this chapter have been taken from [1] H. Stotz, L. Maier and O. Deutschmann, Methane oxidation over palladium: on the mechanism in fuel-rich mixtures at high temperatures, *Top. Catal.*, 60 (2017) 83–109 and from [2] H. Stotz, L. Maier, A. Boubnov, A. T. Gremminger, J.-D. Grunwaldt and O. Deutschmann, Surface reaction kinetics of methane oxidation over PdO, *J. Catal.*, 370 (2019) 152–175.

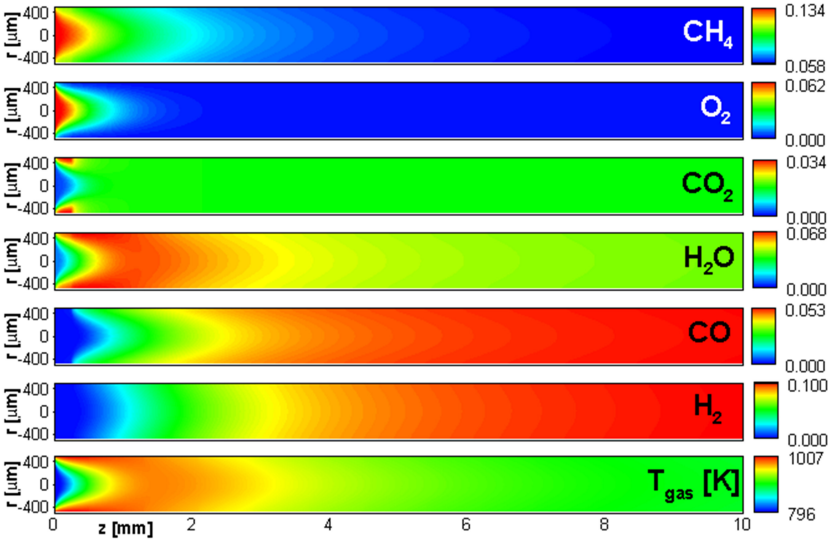

Figure 6.1: Contours of simulated species mole fractions and gas-phase temperature distribution in the catalytic channel. Inlet conditions as fed: C/O-ratio = 1.1, 4 SLPM, N_2-dilution = 80 vol.-%. Figure adapted from Stotz et al. [1].

In the case of a feed C/O-ratio of 1.1, it can be seen from Fig. 6.2. that the model predicts all measured species concentration profiles well. If, to a first approximation, the influence of the presence of the capillary in the channel is neglected, then the concentration distribution over the channel cross-section has a diminishable influence on where the fictive capillary would be radially located within the channel, once the suction rate is properly adjusted. This effect becomes in particularly prominent at the rear part of the catalytic channel where radial concentration gradients disappear. However, at the entrance region of the catalytic channel, larger concentration gradients in radial direction are observed, in particular for O_2, H_2O and CO_2.

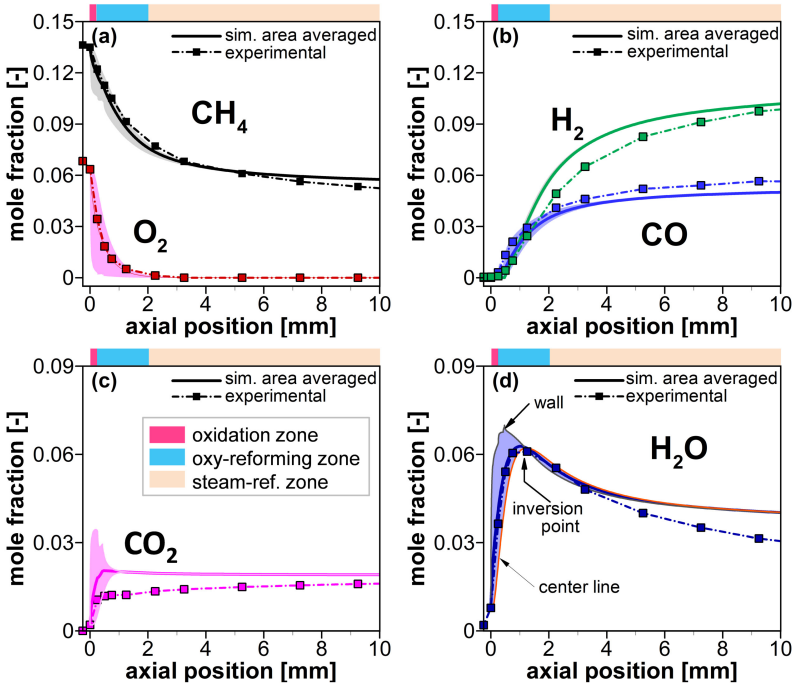

Figure 6.2: Measured and simulated species concentration profiles for (a) reactants CH_4 and O_2, (b) partial oxidation products CO and H_2 and (c) total oxidation products CO_2 and (d) H_2O. Inlet conditions as fed: C/O-ratio = 1.1 at 4 SLPM and N_2-dilution of 80 vol.-%. Simulation parameters: $F_{\mathrm{cat/geo}} = 39.34$, $\delta_{\mathrm{wc}}^{\mathrm{eff}} = 25.6\,\mu\mathrm{m}$ and $d_{\mathrm{o}} = 953.42\,\mu\mathrm{m}$. Figure adapted from Stotz et al. [1].

It should also be noted here that the experimental uncertainty in the measured concentrations falls within the radial concentration distribution of the simulation near the entrance region. Further downstream, this effect becomes increasingly smaller and does not hold at positions of ca. $>1.5\,\mathrm{mm}$ to $2\,\mathrm{mm}$ anymore as elemental balances for O and C close within $\pm 5\,\%$, while the H balance is only within $\pm 10\,\%$ accurate (cf. Fig. 6.3).

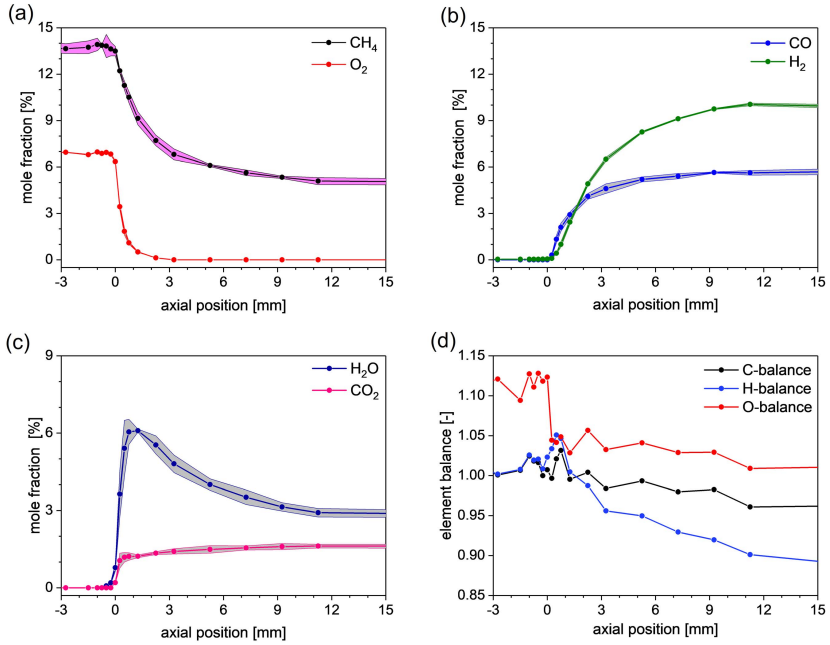

Figure 6.3: (a)-(c) Sample mean of the experimentally determined spatially resolved mole fractions (C/O-ratio = 1.1) and corresponding error bars as given by the confined shaded area, $\bar{x}(z) \pm (\sigma \cdot c)$ with $c = 1$, based on the sample standard deviation, $\sigma = \sqrt{\sum (x_i - \bar{x})^2/(n-1)}$ with $n \geq 3$. (d) Element balances based on the mole fractions' sample mean for C, O and H containing species.

This effect can be seen in the case of the H_2O profile in Fig. 6.2 (d). In this case, lower and upper concentration bounds reverse their role at around 1 mm, and H_2O consuming reactions start to overcompensate the producing ones. The

decrease in H_2O combined with the consumption of CH_4 indicates the onset of a steam reforming (SR) zone, which proceeds from there ($> 1\,\text{mm}$) until the end of the catalytic channel.

In the intermediate section ($0.25 \leq z < 2\,\text{mm}$) an extended oxy-reforming zone is found, where CH_4 is consumed, while combined total and partial oxidation products are formed between 0.25 mm and 1 mm. Slightly further downstream ($1 \leq z < 2\,\text{mm}$) SR and partial oxidation occur together while nearly no further formation of total oxidation products is observed.

Figure A.1 in the appendix, summarizes the experimentally determined concentration and wall temperature profiles together with the simulation results for the other investigated feed C/O-ratios, 1.0 (Fig. A.1 (a)) and 0.8 (Fig. A.1 (b)). For a leaner reaction mixture, the amount of total oxidation products increases within the total oxidation zone as can be inferred from the increase in the H_2O peak. The enhanced H_2O production upstream enables an increase in SR reactions to occur further downstream such that effluent CO and H_2 concentrations increase.

6.1.2 Analysis on Mass Transport Limitations

To quantify the effect of mass-transport limitations within the channel, the external effectiveness factor $\eta_{\text{ext},i}$ has been calculated for the reactant species CH_4 and O_2 as shown in Fig. 6.4, assuming first-order kinetics in component i. The effectiveness profiles show a minimum at around 0.25 mm for both oxygen and methane with oxygen being stronger limited than methane. Beyond this point, the methane effectiveness recovers upon traveling further downstream, whereas the oxygen effectiveness remains at a low level over the rest of the catalytic channel.

The computed washcoat effectiveness is shown in Fig. 6.5 (b). Due to the high temperature conditions, reaction rates are fast and cause strong internal concentration gradients as the axial effectiveness factor profile is small over the entire length of the catalytic channel. A distinct feature is found within the entrance region of the channel ($0 < z < 0.25\,\text{mm}$), as pore transport limitations appear higher than in other parts downstream of the channel, because SR reactions with CH_4 proceeds slower than the oxidation of methane at the front part.

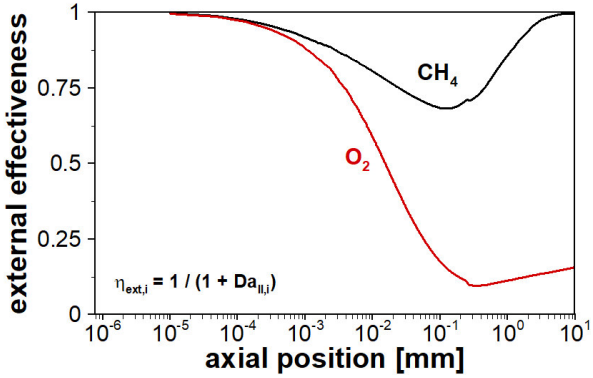

Figure 6.4: Damköhler-number (Da_{II}) based external effectiveness factors as evaluated from simulated reactant species concentrations within the catalytic channel section, assuming first-order kinetics. Inlet conditions as fed: C/O-ratio = 1.1 at 4 SLPM and N_2-dilution of 80 vol.-%. Figure adapted from Stotz et al. [1].

6.1.3 Axial Coverages Profiles

To add to the understanding of the methane oxidation process over reduced palladium under quasi-autothermal operating conditions, Fig. 6.5 (a) shows computed species coverages along the channel axis at the pore mouth of the gas-washcoat interface, for the most abundant surface intermediates: Pd(s), O(s), CO(s), H(s) and C(s). Adsorbed oxygen is rapidly consumed on the surface within the first 0.25 mm of the catalytic channel. In that section, the abundance of H(s) on the surface is suppressed by the presence of O(s). This is possible due to the facile oxidation of H(s). These findings are in agreement with the observation that primarily total oxidation products form at the catalyst inlet section, as has also been found for CH_4 oxidation over a rhodium catalyst [215]. In contrast to H(s), larger amounts of the surface are already covered by CO(s) within this narrow region of high oxygen coverage ($0 \leq z < 0.25$ mm). At this stage of the reaction, CO(s) is not as easily oxidized as H(s). Once the O(s) concentration is sufficiently low enough ($z \geq 0.25$ mm), larger amounts of partial oxidation precursors, CO(s) and H(s), are formed on the surface.

The onset falls together with the inflection point of the rising branch of the H_2O concentration profile in the channel gas-phase, as shown in Fig. 6.2 (d). As the

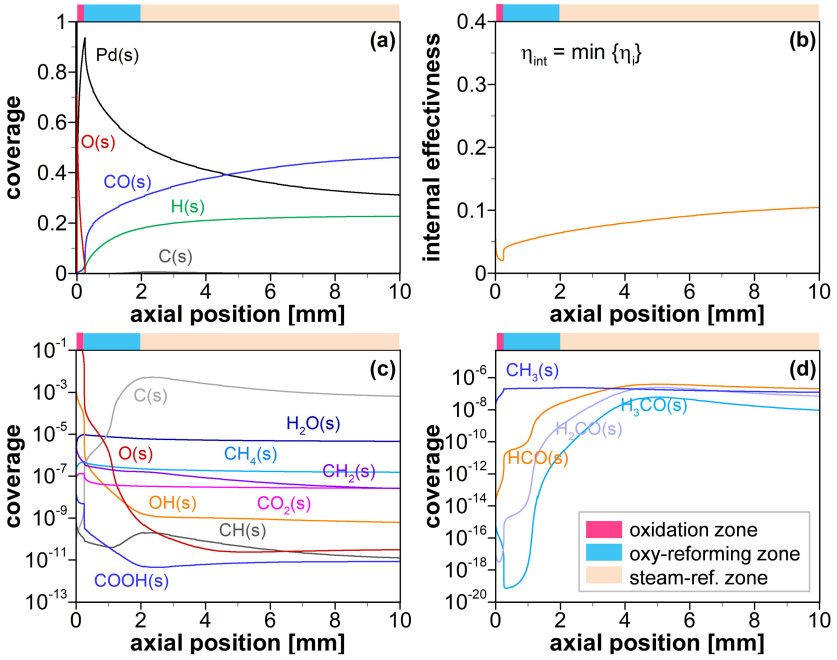

Figure 6.5: Coverage profiles along the channel axis for (a) most abundant surface intermediates, (c), (d) less abundant surface intermediates and (b) internal washcoat effectiveness factor, for specified inlet conditions as fed: C/O-ratio = 1.1 at 4 SLPM and N_2-dilution of 80 vol.-%. Figure adapted from Stotz et al. [1].

water production slows down, the partial oxidation activity increases and H_2 as well as CO production in the channel are enhanced. Coverages of less abundant surface intermediates are shown for completeness in Fig. 6.5 (c) and Fig. 6.5 (d). At around 1 mm, O(s) experiences a second pronounced decrease which coincides with a steep increase in elemental carbon C(s) formation. However, larger amounts of C(s) are not found in the simulation results and have also not been seen by visual inspection of the catalyst after the experiment had been conducted. The steep increase in C(s) coverage at around 1 mm coincides with the H_2O formation peak. At around 2 mm, C(s) reaches a peak value which overlaps with the onset of SR reactions.

Furthermore, as shown in Fig. A.2 (a) and (b) of the appendix, the amount of elemental surface carbon C(s) is lowered under fuel-leaner conditions. Concurrently, with the increase in catalyst peak temperature, the amount of CO(s) on the surface decreases, while available Pd(s) sites slightly increase in the region of the temperature hot-spot ($z \sim 0.5\,\text{mm}$) as shown in Fig. A.2 (b).

6.1.4 Equilibrium Considerations

Taking into account the axial dependence of the equilibrium constant, which can be calculated from the equilibrium concentration profiles as shown in Fig. 6.6, and the reaction quotient depending on the axial gas-phase temperature and species concentrations, allows visualizing the reversibility along the channel axis. In the rear part of the channel, conversion of methane occurs less through total and partial oxidation ($2 \leq z < 10\,\text{mm}$) as oxygen is nearly depleted in the channel. As a result, other sub-processes may become increasingly important in that section. Therefore, the reversibility of SR and WGS were examined. Fig. 6.7 shows the measured and simulation based reversibility profiles for SR (R_{o3}) and WGS (R_{o5}) sub-systems. Both experimental and simulation based reversibility profiles for WGS approach one for $z > 2\,\text{mm}$ within one order of magnitude. Thus, in this range the WGS sub-reaction is more limited by thermodynamics. In contrast, the reversibility of the SR profile in this section ($z \sim 2\,\text{mm}$) is several orders of magnitude smaller ($Z_{\text{SR}} \sim \text{O}(10^{-4})$) than one, and thus kinetically more significant than WGS. This effect diminishes to the end of the channel ($Z_{\text{SR}} \sim \text{O}(10^{-2})$ at $z = 10\,\text{mm}$).

After consumption of nearly all O(s) at axial positions of ca. $> 2\,\text{mm}$, steam reforming of CH_4 is the preferred conversion path, leading to a prolonged consumption of CH_4 and a simultaneous decrease in H_2O concentrations. This observation is supported by the fact that CO and H_2 show a further increase in

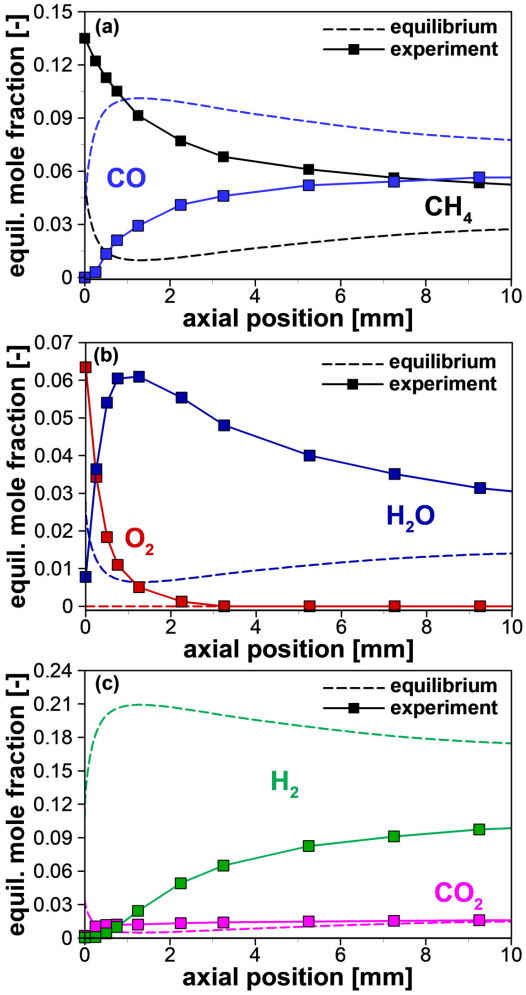

Figure 6.6: Axial equilibrium composition (dashed lines) along the catalytic channel, based on simulated gas-phase temperature and channel concentrations as well as measured concentrations (shown as points, solid lines in between are guide to the eye) for (a) CH_4 and CO, (b) H_2O and O_2 and (c) H_2 and CO_2. Inlet conditions as fed: C/O-ratio = 1.1; 4 SLPM; N_2-dilution = 80 vol.-%. Figure adapted from Stotz et al. [1].

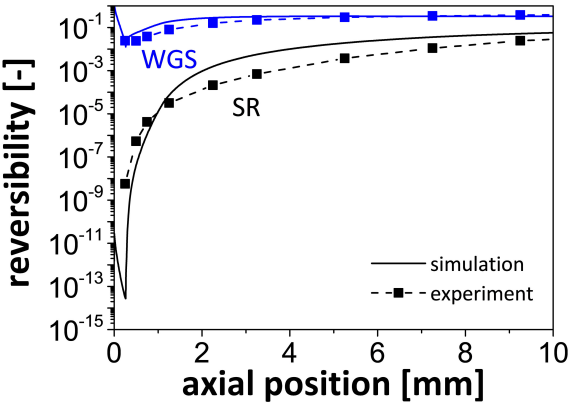

Figure 6.7: Reversibility profiles for SR and WGS evaluated from measured and simulated species concentrations. Inlet conditions as fed: C/O-ratio = 1.1; 4 SLPM; N_2-dilution = 80 vol.-%. Figure adapted from Stotz et al. [1].

concentration, while the CO_2 signal remains nearly constant, as can be seen in Fig. 6.2 (b) and (c).

In order to elucidate whether the catalytically active Pd species are in the reduced state or tend to oxidize for the given conditions within the channel, a further investigation on the thermodynamic behavior of the PdO ⇌ Pd transformation was performed. As the oxygen chemical potential varies significantly over the length of the catalyst, oxidation of the reduced palladium phase is more likely to occur at the inlet section of the catalytic channel. Thermodynamic data based on values for enthalpy and entropy of decomposition for the PdO ⇌ Pd phase transformation has been reported by several groups [6–9, 216, 217]. However, only the data reported by Colussi et al. [6] distinguishes between different PdO decomposition steps, which presumably originate from (i) PdO_x in contact with residual Pd metal, (ii) bulk PdO and (iii) PdO interacting with the support, as shown for a supported Pd on alumina catalyst. Bell et al. [9], Bayer and Wiedemann [8] as well as Peukert [7] have shown data on the thermal decomposition of PdO for unsupported Pd catalysts in form of an oxidized Pd metal sponge, Pd metal powder and oxidized Pd(110) single crystal surface, respectively. Applying the reported data to the linearized version of the Van't Hoff equation for the PdO decomposition, according to the reaction stoichiometry

PdO $\rightleftharpoons \frac{1}{2}O_2$ + Pd, yields information on the necessary O_2 pressure, before the onset of the PdO decomposition becomes thermodynamically favored.

$$\frac{1}{2} \cdot \ln\left(\frac{p_{O_2}}{p_0}\right) = -\frac{\Delta_R H}{RT} + \frac{\Delta_R S}{R} \tag{6.1}$$

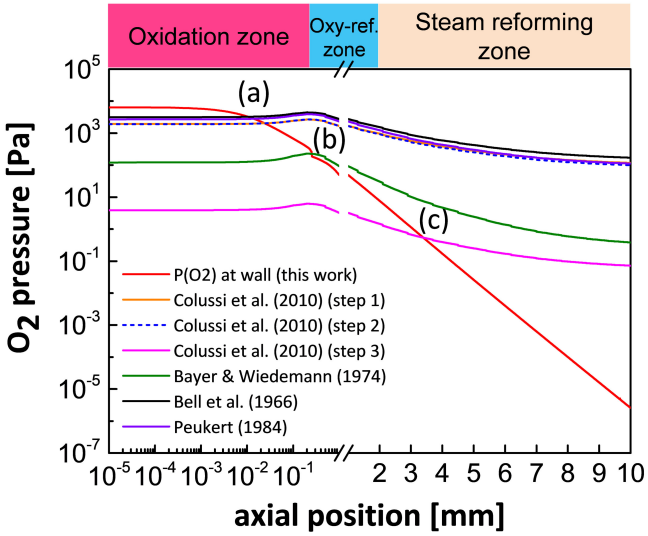

Figure 6.8: Simulated O_2 partial-pressure profile at the gas-washcoat interface (red solid line) for inlet conditions as fed: C/O-ratio = 1.1 at 4 SLPM and N_2-dilution = 80 vol.-%. Equilibrium O_2 pressures (other lines) are calculated based on measured wall temperature profile and according to literature data from Colussi et al. [6], Peukert [7], Bayer and Wiedemann [8] and Bell et al. [9] on PdO decomposition. Figure adapted from Stotz et al. [1].

Figure 6.8 compares the calculated equilibrium O_2 partial pressures from the different reported thermodynamic data sets with our model results, as shown for a feed C/O-ratio of 1.1. The trend of the red line represents the actual O_2 partial pressure profile at the catalyst wall. As the oxygen partial pressure at the channel wall drops below the thermodynamically determined O_2 pressure,

PdO decomposition becomes thermodynamically favored. It can be seen that the data of Peukert, Bell et al. and Colussi et al. (step 1, step 2) are close together and intersect with the O_2 profile in the channel at point (a), around 10 µm beyond the catalytic channel inlet. According to the data of Bayer and Wiedemann a second intersect (b) is found at $z \sim 250$ µm, also close to the inlet. Point (c) represents the decomposition of interfacial PdO in contact with the alumina support as reported by Colussi et al. and is the only decomposition step located significantly further downstream of the channel at $z \sim 3.37$ mm. It should be noted here, that the prediction of PdO decomposition also depends on the type of pretreatment of the catalyst, experimental conditions and whether the catalyst is supported or not.

Table 6.1: Parameters for evaluation of the Van't Hoff Eq. (6.1).

Author	$\Delta_R H$ [cal/mol]	$\Delta_R S$ [cal/mol/K]	Ref.
Colussi et al. (2010), Step1	−24700	20.9†	[6]
Colussi et al. (2010), Step2	−26100	22.3†	[6]
Colussi et al. (2010), Step3	−35300	25.4†	[6]
Bayer & Wiedemann (1974)‡	−25670	28.9	[8]
Peukert (1984)	−28141	24.7	[7]
Bell (1966)	−25800	22.5	[9]

† Author correspondence.
‡ Use T in [°C] for Eq. (6.1).

An important point to note here is the contribution of the total oxidation activity on the reaction kinetics within the catalytic channel due to possible existing PdO at the channel inlet section under the investigated reaction conditions. The total oxidation activity cannot be unequivocally excluded nor attributed to either Pd or PdO. The spatial resolution of the concentration profiles and the accuracy of the in situ sampling technique impose further constraints on the measured inlet point concentrations and make its usage for evaluating the PdO decomposition pressure challenging. Furthermore, also other effects such as upstream diffusion within the entrance region, as recently reported [98, 153], can affect the level of the oxygen chemical potential at the catalyst inlet point. Therefore, a more precise investigation of the Pd state of oxidation under reaction conditions at the channel entrance point is required and makes the usage of in situ characterization methods necessary.

6.1.5 Selectivity, Conversion and Yield

As shown in Fig. 6.9 (a)-(c), additional conversion, selectivity and yield profiles have been evaluated for measured and simulated axial concentration profiles and match well in the case of a feed C/O-ratio of 1.1. Selectivity and yield are based on elemental balances of C and H. As can be inferred from the CO and H_2 selectivity profiles in Fig. 6.9 (c), the CO and H_2 selectivity are low at the catalyst inlet section ($0 \leq z < 0.25\,\text{mm}$), while H_2O and CO_2 selectivity must be high. It is interesting to note here that H_2 selectivity is comparatively lower than the CO selectivity at around 1 mm. This observation becomes even more prominent when plotting directly selectivity vs. conversion as shown in Fig. 6.9 (d). It is important to note here, that the partial oxidation products may not only form through an indirect formation as a result of a combined appearance of total oxidation and steam reforming reactions, but can also form sequentially along the channel axis. First CO, then H_2 at higher conversions is formed.

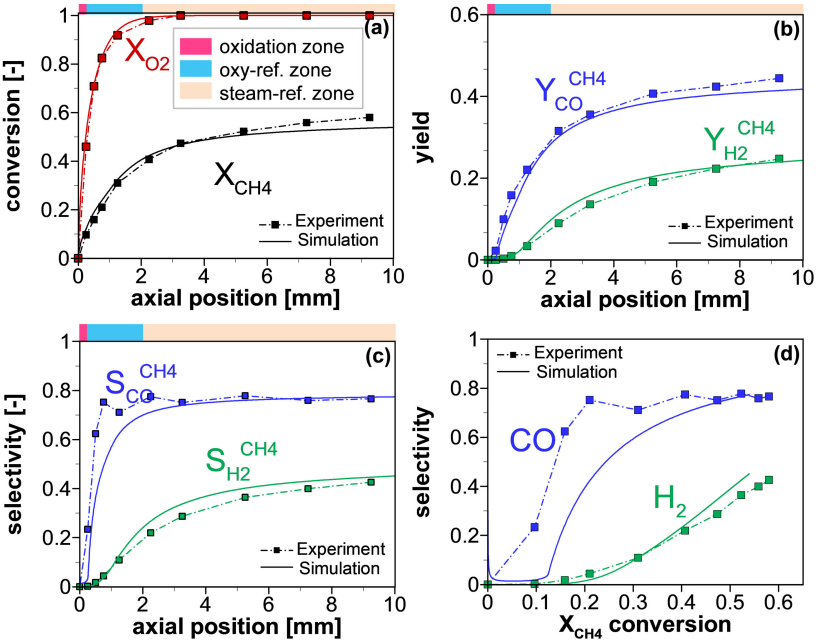

Figure 6.9: Measured and simulated results for (a) conversion, (b) selectivity and (c) yield along the catalytic channel as well as a parity plot of (d) conversion vs. selectivity. Selectivity and Yield are based on elemental balances. Inlet conditions as fed: C/O-ratio = 1.1 at 4 SLPM and N_2-dilution of 80vol.-%. Figure adapted from Stotz et al. [1].

6.1.6 Spatially Resolved Sensitivity Analysis[2]

Figure 6.10 (a)-(b) shows the sensitivity analysis in form of contour plots for selected gas-phase species, namely CH_4, CO, H_2 and H_2O at various axial positions within the channel. It can be inferred from the color contours that different kinetic regimes exist along the length of the catalytic channel. For example, within the narrow oxidation zone in the entrance region at $z \sim 250\,\mu m$, the dehydrogenation step in the reaction (R35), as part of the oxygen-assisted activation path (P2), appears highly sensitive. This result can be seen from the sensitivity coefficients of CH_4, H_2, and H_2O in Fig. 6.10 (a), (c) and (d), respectively. However, further downstream, this step becomes insensitive. Several other steps become quite sensitive once the oxy-reforming zone starts. Between ca. 300 µm to 500 µm, identification of a single rate determining step is not possible, due to the complex chemical behavior of the reaction network and the integrated nature of the reactor setup. As the catalyst temperature rises desorption steps for CO_2 (R11) and CH_4 (R12) become sensitive. Steps for water formation (R13) and activation (R16), CO dissociation (R20), C-H activation steps (R24) and C-H formation steps from C(s) and CO(s) with OH(s) (R38) and (R46) start to become important as well. Slightly further downstream (750 µm to 2 mm), the kinetics have again changed markedly. Now, adsorption and desorption of CO_2 (R5) and (R11) are both sensitive. Additionally, the oxygen-assisted CH_4 activation step (R31) starts to become increasingly sensitive as well as steps (R47), (R45) and (R46) as part of the methoxy mediated path. Towards the end of the catalytic channel, between ca. 3 mm and 9.5 mm, reaction (R31) continues to be quite sensitive for all shown species, whereas step (R38) remains only for CO and CO_2 sensitive (not shown) and reaction (R46) becomes increasingly insensitive for CH_4, H_2O and H_2. Therefore, the various observed zones, as described in the previous sections, appear as consequence of the different kinetic regimes, as found from the spatial resolved sensitivity coefficients.

[2]Numbering of the sensitivity coefficients and reaction steps in this subsection corresponds to the notation given in Stotz et al. [1] for the reduced Pd mechanism.

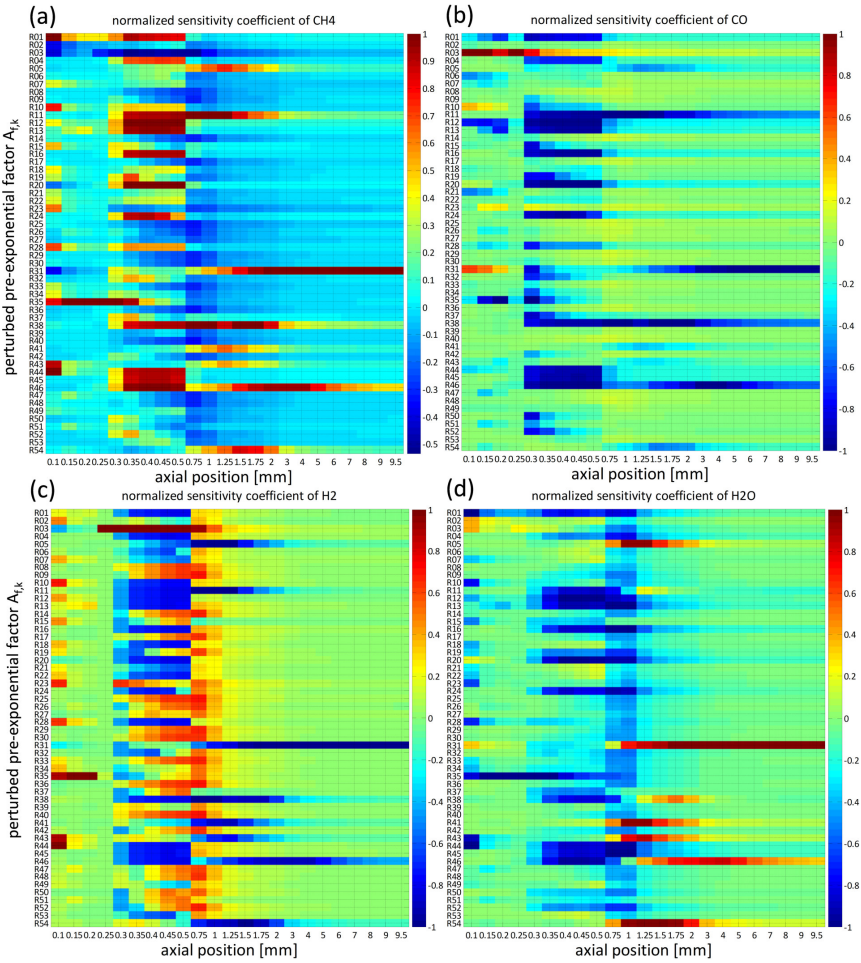

Figure 6.10: Sensitivity analysis for gas-phase mole fractions of (a) CH_4, (b) CO, (c) H_2 and (d) H_2O, normalized to most sensitive reaction rate parameter at various investigated axial positions, respectively. Inlet conditions as fed: C/O-ratio = 1.1 at 4 SLPM and N_2-dilution of 80 vol.-%. Figure adapted from Stotz et al. [1].

6.2 Simulation Results with PdO Mechanism

6.2.1 Influence of Water on Catalytic Light-Off

In order to analyze the water inhibition effect in more detail and hence further consequences for the deactivation mechanism, light-off simulations with the developed MF-MKM where performed and compared against the ignition curves of experimental data sets for dry and wet conditions (cf. Fig. 6.11). Since the MKM considers intrinsic kinetics at the PdO(101) surface, model predictive kinetics allows for comparison with experimental data and the interpretation on deviations from the deactivation process. The influence of deactivated catalyst

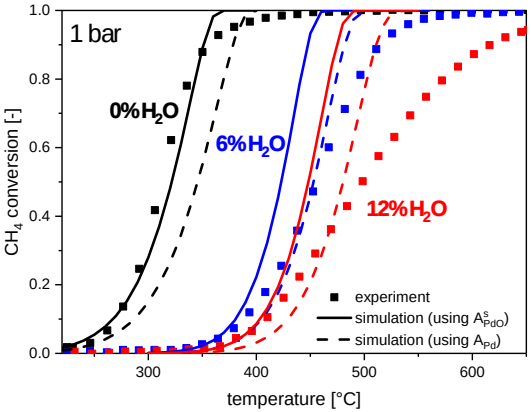

Figure 6.11: Experimental and simulation results during first heating at 1 bar with different feed conditions: 1000 ppm CH_4, 10 vol.-% O_2, 0-12 vol.-% H_2O, N_2 balance to 1 bar. Simulations for 0, 6 and 12 vol.-% H_2O considering changes in dispersion, D^{l}_{PdO} (D_{Pd}): 0 vol.-% H_2O: $D^{l}_{PdO} = 58\,\%$ (48.6 %), 6 vol.-% H_2O: $D^{l}_{PdO} = 28\,\%$ (23 % assumed), 12 vol.-% H_2O: $D^{l}_{PdO} = 20\,\%$ (16.6 %). Figure adapted from Stotz et al. [2].

states on the light-off behavior was simulated with and without the metal oxide corrected dispersions as originally determined from CO-TPD given in Fig. 4.8. After accounting for changes in the metal dispersion, simulation results resemble the experimental curves more closely up to conversions of around 20 %. The exposure times of the catalyst to the different inlet gas-mixtures to reach 50 % conversion at a temperature-ramp of 3 K/min starting at 225 °C heating to

650 °C and cooling afterwards are: 29/253 min (0 % H_2O), 77/190 min (6 % H_2O) and 91/168 min (12 % H_2O) for heating/cooling curves, respectively. With increasing amounts of water in the feed increasing exposure times resemble the rise in T_{50} temperatures. More importantly, the deactivation progresses with duration of exposure to the wet gas mixture. A clear limitation of the applied model is the use of a constant dispersion for simulating the light-off curve. As a result the difference to the experimental data are thus more pronounced at elevated water concentrations and higher temperatures due to the longer exposure time to the water aging environment and more severe conditions for the catalyst as compared at dry conditions. The larger deviations in conversions (>20 %), for the wet cases of the model results, from the experimental light-off curves are likely not entirely caused by losses of sites through sintering and thereby related changes in dispersion during light-off, because the parametric sensitivity of the metal dispersion on the simulated light-off curves would require that the catalyst dispersion assumes abnormally low values, i.e. abnormally large PdO particle sizes would be required in order to achieve conversions similar in size as the ones observed in the wet experiments and such excessive sintering is unlikely at temperatures below the decomposition temperature of PdO (>700 °C) and the applied exposure times to the reaction conditions. Possibly, alternative contributing effects responsible for this behavior could involve shape change effects of the PdO particles in dependence of the gas-phase chemical potentials [213, 218] or changes related to the active facet [83] during light-off, respectively which have not been considered in the model during the light-off simulations.

6.2.2 Influence of Pressure on Catalytic Light-Off

The influence of pressure on the catalytic light-off curves compared with the MKM results is shown in Fig. 6.12. In the dry case both the simulated light-off curves are congruent and increasing pressure has no influence on the light-off position. Contrarily, for the wet (12 % H_2O) feeds, model results show that the conversion increases with pressure. The results for the dry feed are consistent with the experimental data. However, the wet experimental points show the opposite trend on pressure. This suggests that deactivation related changes occur more pronounced at higher pressures for wet conditions while in the dry case the catalyst appears to be more stable.

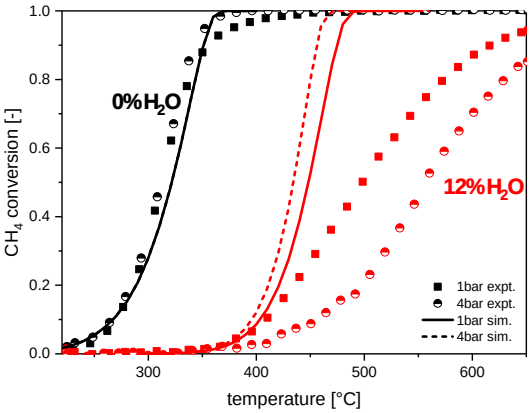

Figure 6.12: Influence of pressure on light-off curves for methane oxidation compared to simulation results at dry (0 vol.-% H_2O; $D^{l}_{Pd} = 58\,\%$) and wet (12 vol.-% H_2O; $D^{l}_{Pd} = 20\,\%$) conditions. Figure adapted from Stotz et al. [2].

6.2.3 Surface Coverage Evolution during Light-Off

For a detailed understanding of the water inhibition effect, most abundant surface intermediates are shown for the dry reaction mixture at ambient pressure in Fig. 6.13. At low temperatures, $(*)_{O(cus)}$ sites are nearly entirely covered as formation of hydroxide species, $(H)_{O(cus)}$ is favored over the complete channel length. These species are primarily formed through hydrogen abstraction reactions as a result of the oxidation process ($CH_3 \rightarrow CH_2OH \rightarrow CH_2O \rightarrow CHO \rightarrow CO$), but mainly and nearly to equal proportions from dissociative adsorption of methane, $CH_4(g) + (*)_{Pd(cus)} + (*)_{O(cus)} \rightleftharpoons (CH_3)_{Pd(cus)} + (H)_{O(cus)}$, and subsequent dehydrogenation steps of $CH_2OH(a)$ and $CHO(a)$ carbonaceous intermediates. The $(H)_{O(cus)}$ species can be considered as precursor state needed to form water as reaction product via interaction with hydroxyls sitting on adjacent Pd(cus) sites.

Significant amounts of $(OH)_{Pd(cus)}$ intermediates are only found at higher temperatures as a result of water activation through oxidative dissociative adsorption from the gas-phase (cf. Fig. 6.19) according to $H_2O(g) + (a) + O(a) \rightleftharpoons OH(a) + (OH)_{Pd(cus)}$, and via vacancy formation through $(H)_{O(cus)}$ according to $(H)_{O(cus)} + (*)_{Pd(cus)} \rightleftharpoons (OH)_{Pd(cus)} + (v)_{O(cus)}$. Before the reaction ignites, at $T < 350\,°C$, internally produced water as a result of the oxidation process forms

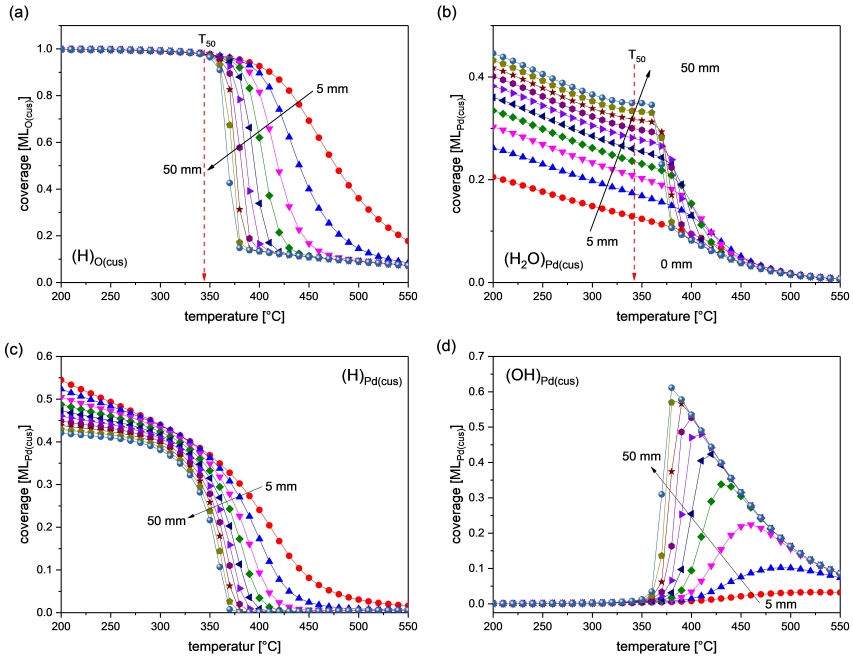

Figure 6.13: Most abundant surface intermediates during simulated light-off at dry conditions: 1000 ppm CH_4, 10 % O_2, 0 % H_2O, N_2 balance to 1 bar. Figure adapted from Stotz et al. [2].

and can re-adsorb out of the gas-phase, accumulating over the length of the catalyst channel. Simultaneously, $(H)_{Pd(cus)}$ species accumulate abundantly, mainly due to formation of $(CO)_{O(cus)}$ from $(CHO)_{O(cus)}$, at the channel entrance. In contrast to the $(H_2O)_{Pd(cus)}$ gradient at low temperatures, $(H)_{Pd(cus)}$ species decrease downstream the channel, as its coverage is coupled to the methane oxidation rate which slows down over the catalyst length with increasing amounts of methane converted. During light-off, above ca. 350 °C, CH_4 conversion increases and larger amounts of $(H_2O)_{Pd(cus)}$ are formed and can now desorb at the higher temperatures more easily. Formation of $(H_2O)_{Pd(cus)}$ proceeds through $(H)_{O(cus)} + (OH)_{Pd(cus)}$ interaction. As a consequence, $(H)_{O(cus)}$ coverage starts to decrease from the channel entrance to the end of the catalyst, enabling $(H)_{Pd(cus)}$ species to shift over onto liberated $(*)_{O(cus)}$ sites. While water concentration in the channel gas-phase rises, higher amounts re-adsorb

through dissociative adsorption, leading to increased amounts of $(OH)_{Pd(cus)}$ over the catalyst length. At even higher temperatures, water adsorption/desorption equilibrium shifts further towards desorption and empty sites become abundantly available. The high amounts of $(H)_{O(cus)}$ species formed for the dry and low temperature conditions suggests that $(H)_{O(cus)}$ are stable and formation is fast. Thus, the gradual deactivation is not a consequence of a gradual build-up of $(H)_{O(cus)}$ species. The results of the MKM instead suggest that $(H)_{O(cus)}$ species play a central role for the water inhibition effect due to internally formed water since $(H)_{O(cus)}$ formation is stable at low temperatures and immediately affects the oxidation process but at a different, much faster time scale as the rather slow water induced deactivation process.

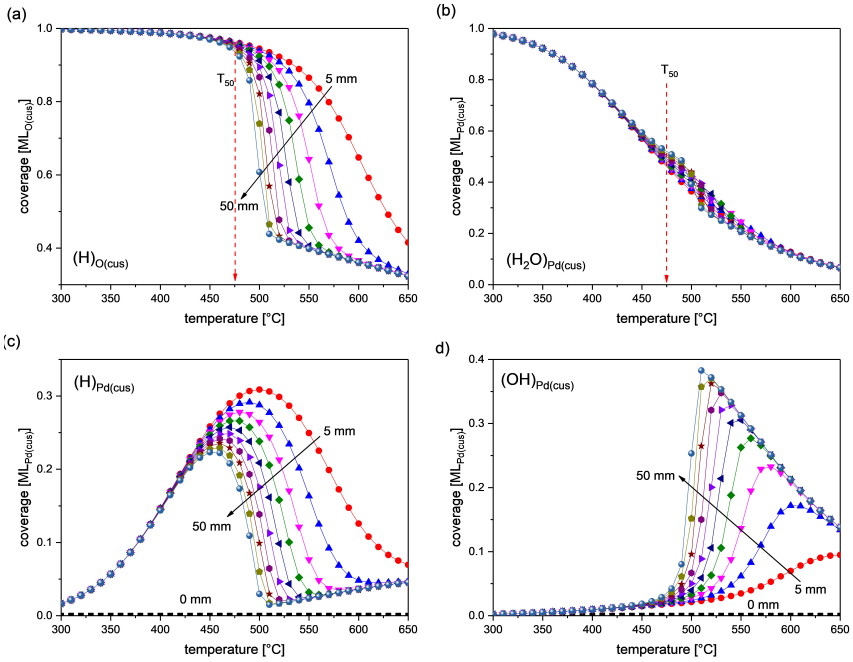

Figure 6.14: Most abundant surface intermediates during simulated light-off at wet conditions: 1000 ppm CH_4, 10 % O_2, 12 % H_2O, N_2 balance to 1 bar. Figure adapted from Stotz et al. [2].

In comparison, Fig. 6.14 shows corresponding $(H_2O)_{Pd(cus)}$ coverages upon feeding 12 vol.-% water to the reactor. The trends are qualitative similar to the

dry case. However, due to larger amounts of water present in the gas-phase from the beginning on, water covers nearly all free $(*)_{Pd(cus)}$ sites, thereby shifting the light-off temperature by more than 100 K, while the axial gradient in $(H_2O)_{Pd(cus)}$ disappears. The extra site-blocking effect of $(H_2O)_{Pd(cus)}$ induces higher $(H)_{O(cus)}$ concentrations towards lower temperatures as compared with the dry case, also pushing $(H)_{Pd(cus)}$ species over to $(*)_{O(cus)}$ sites. These results suggest, that under wet conditions, adsorbed $(H_2O)_{Pd(cus)}$ hinders $(H)_{O(cus)}$ species, primarily at low temperatures, to get further converted into water and therefore preventing the reaction to ignite at lower light-off temperatures.

The interlocking mechanism behind the water inhibition effect, including the most abundant surface intermediates, is summarized in a simplified mechanistic scheme shown in Fig. 6.15.

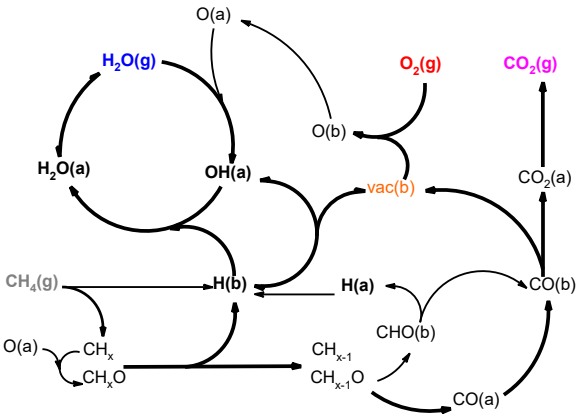

Figure 6.15: Simplified scheme showing the interlocking mechanism behind the water inhibition during methane oxidation over PdO catalyst. Figure adapted from Stotz et al. [2].

The concentration of vacancies in terms of coverage is exemplarily shown in Fig. 6.16 for the dry (a) and wet (b) conditions. It is recognizable that healing of vacancies proceeds fast. The oxygen refill takes place via transfer of adsorbed $(O)_{Pd(cus)}$ species on neighboring Pd(cus) sites and via oxygen adsorption from the gas-phase. Accordingly, major reduction of the catalyst surface, which would lead to an under-stoichiometric PdO surface, may not take place on the PdO(101) facet under the investigated reaction conditions as significant amounts of vacancies are not formed neither in the dry nor the wet cases (not

shown). Hence, it is suggested that the contribution of $(v)_{O(cus)}$ sites plays a minor role for water inhibition or deactivation on PdO(101), respectively. These findings do not exclude the possibility of oxygen exchange from the support to the PdO particle nor its role in influencing the reaction, as e.g. on other facets. The low concentration of vacancies during methane oxidation is consistent with results from in situ XAS spectra under similar reaction conditions, showing no significant bulk reduction during methane oxidation [93].

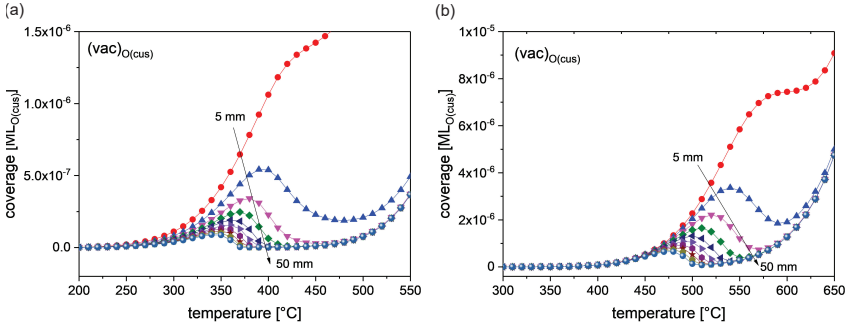

Figure 6.16: Influence of light-off temperature on the local formation of oxygen vacancies via reduction of O(cus) sites during catalytic combustion of methane for a (a) dry and (b) wet (additional 12 % H_2O) feed of 1000 ppm CH_4, 10 % O_2, N_2 balance to 1 bar. Figure adapted from Stotz et al. [2].

Considering the possibility that CH_3–H bond dissociation alternatively takes place over $(O)_{Pd(cus)} - (*)_{Pd(cus)}$ site pairs, the site blocking effect of adsorbed water leads to reduced availability of $(O)_{Pd(cus)}$ species. Anticipating that oxygen also stems from the support, which is not implemented in the MF-MKM model, as observed also experimentally [218], water adsorption on $(*)_{Pd(cus)}$ sites may interrupt transfer of oxygen from the support to $(*)_{Pd(cus)}$ sites, leading to a reduced availability of $(O)_{Pd(cus)} - (*)_{Pd(cus)}$ site pairs.
Alyani et al. [50] argues that vacancy regeneration[3]is hindered by water adsorption through hindered oxygen exchange between support and PdO surface vacancies, causing deactivation. The MKM results herein suggest, that water adsorption could principally inhibit oxygen transfer from the support to PdO particles through a site blocking mechanism of water onto $(*)_{Pd(cus)}$ sites. However, it cannot be univocally concluded that an interrupted oxygen transport

[3]Alyani et al. uses a different notation for vacancies in their work, denoting them as unsaturated Pd sites, i.e. $(*)_{Pd(cus)}$.

from the support to PdO particle is the decisive factor which causes deactivation. The conclusions based on the mechanistic interpretations from the MKM results, without explicitly considering oxygen transport from the support to the PdO surface, are consistent with the experimental observation for water inhibition. Nevertheless, the MF-MKM model can so far not explain the deactivation phenomenon.

6.2.4 Reaction Orders and Apparent Activation Energies

The influence of the reaction conditions onto mechanistic implications for turnover frequencies, reaction orders in water, $n(H_2O)$, and apparent activation energy, E_{app}, in oxidizing methane is demonstrated in Fig. 6.17.
Qualitative differences in the evolution of the reaction orders and apparent activation energies are found when water is present in the reaction mixture and when absent. Even in the presence of only 1000 ppm water in the reaction mixture, the reaction order in water is significantly lowered especially in the low temperature region. In comparison to the dry case, the reaction order in water remains close to zero over the entire investigated temperature range. Higher temperatures result in a lowered absolute magnitude of the reaction order in water, consistent with the diminishing water inhibition effect.

A transition region is found at around 350 °C to 450 °C where $n(H_2O)$ and E_{app} are both less influenced by variations in temperature. In contrast, the curve evolution for the activation energy under dry conditions (Fig. 6.17 (b)) shows a more pronounced decrease with increasing temperature than the corresponding curves for the wet conditions, approaching values of ~ 0.3 eV at 600 °C. The curves for the wet cases between reaction order in water and activation energy seem to have the opposite dependence on temperature and water concentration. The transition region which gives rise to different behaviors at low, intermediate and high temperatures has been explained by Grönbeck et al. [10]. Calculated turnover frequencies tend to be lower than experimentally reported ones by Zhu et al. and Monteiro et al. [24, 46] which were measured over Pd foil catalysts. Additional experimentally reported values [24, 46, 56] on apparent activation energies and reaction orders in water have been included for completeness in Fig. 6.17 (a) and (b) and compared with the model results obtained at the same conditions.

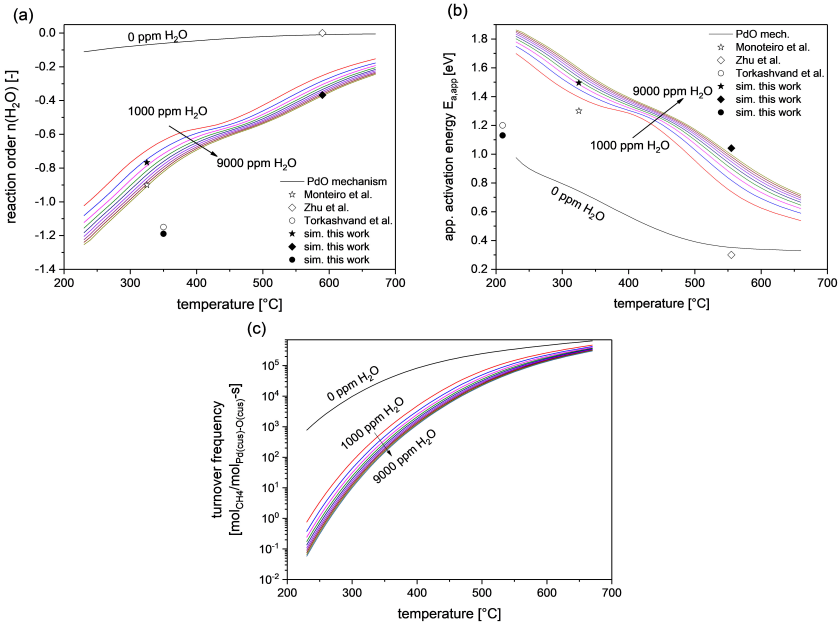

Figure 6.17: Influence of water on (a) reaction order n(H_2O), (b) apparent activation energy $E_{a,app}$ and (c) turnover frequency for methane oxidation over PdO(101) for a mixture of 1000 ppm CH_4, 10 vol.-% O_2, 0 ppm to 9000 ppm H_2O, N_2 balance to 1 bar. Empty symbols (☆,◇,○): experimentally determined values from literature [24, 46, 56]. Filled symbols (★,◆,●): values from simulation according to the experimental conditions from literature. Figure adapted from Stotz et al. [2].

6.2.5 Reaction Path and Sensitivity Analysis

In order to elucidate which reaction channel is preferred under the investigated experimental conditions a detailed reaction path analysis (RPA) has been conducted for the dry and the wet reaction mixture with 12 vol.-% water in the feed at 1 bar. The most important results thereof are presented for different light-off temperatures and at selected axial positions in terms of path preferences. Figure 6.19 on page 114 shows the path preferences of selected species of the dry feed case as calculated form Eq. (C.94) and (C.95). The detailed RPA reveals the strong temperature and position dependence of the surface intermediates' path

preferences. A simple path analysis based on Gibbs free energies at eventually only a single condition evaluated is questionable and needs careful inspection since at different conditions or positions in the reactor the preferential path might change.
Based on the C_1-scheme as shown in Fig. 5.6, the C_1 preferential reaction pathway (PRP) is identified for the temperature range 200 °C to 400 °C according to the following sequence:

$CH_4(g) \rightarrow CH_3(a) \rightarrow CH_2OH(a) \rightarrow CH_2O(a) \rightarrow CHO(a) \rightarrow CO(a) \rightarrow CO(b) \rightarrow CO_2(g)$

About 10 - 30 % of methane is activated through dissociative adsorption over $(*)_{Pd(cus)} - (OH)_{Pd(cus)}$ site pairs. The contribution of $(*)_{Pd(cus)} - (O)_{Pd(cus)}$ sites for activating methane is at the given conditions small (< 5 %) compared to the preferential activation path over $(*)_{Pd(cus)} - (*)_{O(cus)}$ site pairs with about 70-90 %.

The importance of $(*)_{Pd(cus)} - (*)_{O(cus)}$ site pairs for the reaction channel is also confirmed from the degree of rate control (DRC) analysis conducted with the MF-MKM at dry conditions (cf. section C.8 and Fig. 6.18). The DRC analysis shows that dissociative methane adsorption over $(*)_{Pd(cus)} - (*)_{O(cus)}$ site pairs is the major rate controlling step during light-off, in agreement with results reported in the literature [10]. Minor rate controlling contributions become increasingly important towards lower temperatures (< 400 °C) and arise from molecular water adsorption/desorption, vacancy regeneration through oxygen adsorption from the gas-phase and from hydroxide, $(H)_{O(cus)}$, formation/decomposition.

For temperatures higher than 400 °C the PRP of the dry feed mixture switches the reaction channel and follows now the same PRP which is found for the wet feed case (cf. Fig. 6.22 on page 117 and Fig. 6.21).

In the wet feed case the PRP is found as:

$CH_4(g) \rightarrow CH_3(a) \rightarrow CH_2(a) \rightarrow CH_2(b) \rightarrow CH_2O(a) \rightarrow CHO(a) \rightarrow CO(a) \rightarrow CO(b) \rightarrow CO_2(g)$

One major difference in the low and high temperature PRPs is that hydroxylmethyl intermediates, $CH_2OH(a)$, mediate the low temperature PRP, while at higher temperatures methylene, CH_2, groups mediate the reaction sequence. The path preferences for the wet case show less pronounced axial variations in the pre-light-off region as compared to the dry case. This is primarily due to the water inhibition effect which has also been envisioned in the $(H_2O)_{Pd(cus)}$ coverage in Fig. 6.14.

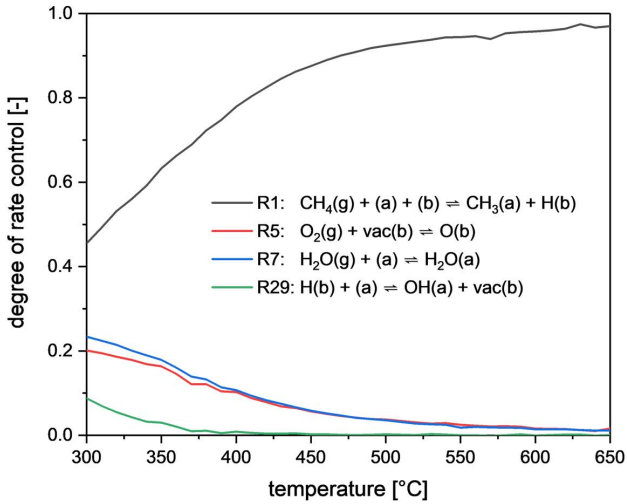

Figure 6.18: Methane degree of rate control at reaction conditions of 1000 ppm CH_4, 10 % O_2, balance to 1 bar in N_2. Figure adapted from Stotz et al. [2].

Based on these findings of the RPA, corresponding catalytic cycles as shown in Fig. 6.20 on page 115 for the low temperatures (dry case, 200 °C to 400 °C) and in Fig. 6.22 on page 117 for high temperatures (wet case, 300 °C to 550 °C) are derived according to a Mars-van-Krevelen mechanism with vacancy regeneration.

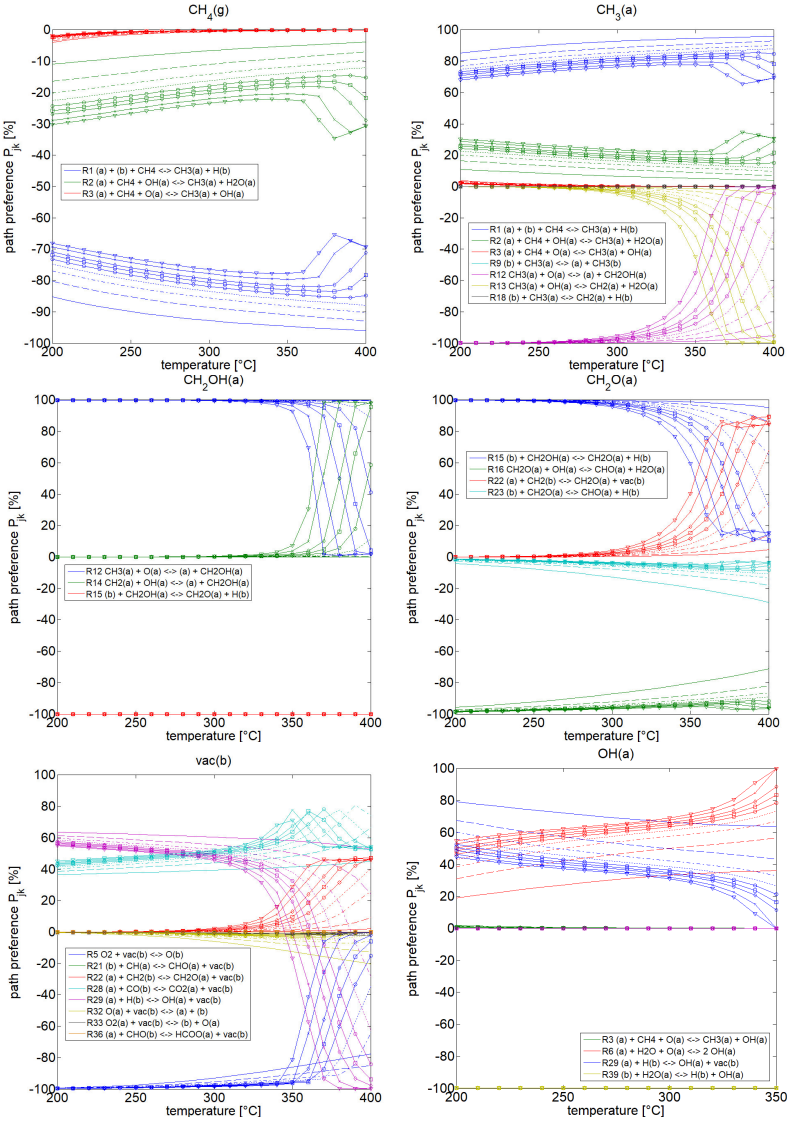

Figure 6.19: Path preferences of selected species for dry feed conditions at 1 mm (–), 5 mm (– –), 10 mm (– · –), 15 mm (- - -), 20 mm (– ○ –), 25 mm (– □ –), 30 mm (– ◇ –), 40 mm (– × –) and 50 mm (– ▽ –). Figure adapted from Stotz et al. [2].

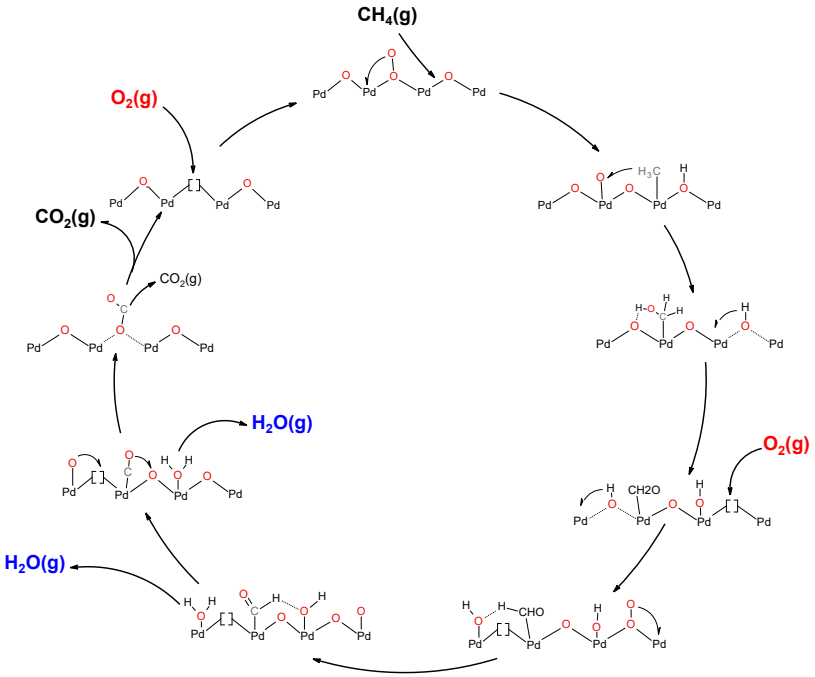

Figure 6.20: Catalytic cycle of the preferential reaction path following a Mars-van-Krevelen redox mechanism for methane oxidation over PdO(101) as found at dry feed conditions (200 °C to 400 °C). Figure adapted from Stotz et al. [2].

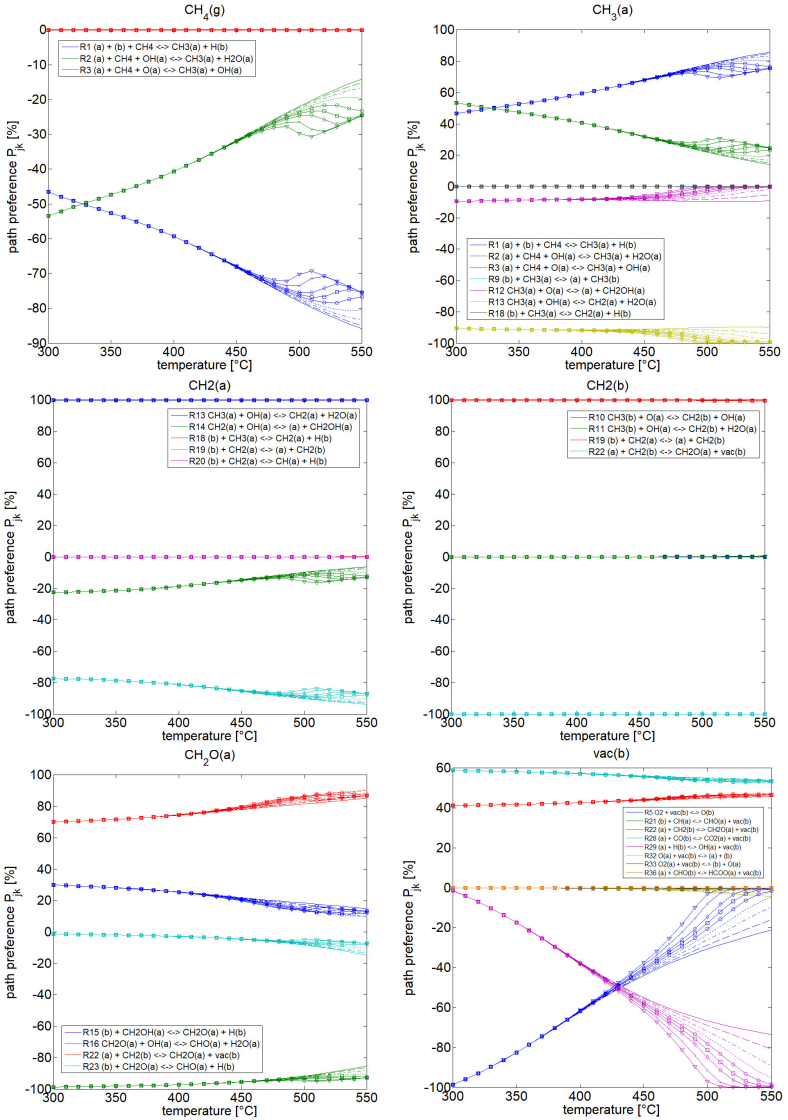

Figure 6.21: Path preferences of selected species for wet feed (12 % H_2O) conditions at 1 mm (–), 5 mm (– –), 10 mm (– · –), 15 mm (- - -), 20 mm (– ○ –), 25 mm (– □ –), 30 mm (– ◇ –), 40 mm (– × –) and 50 mm (– ▽ –). Figure adapted from Stotz et al. [2].

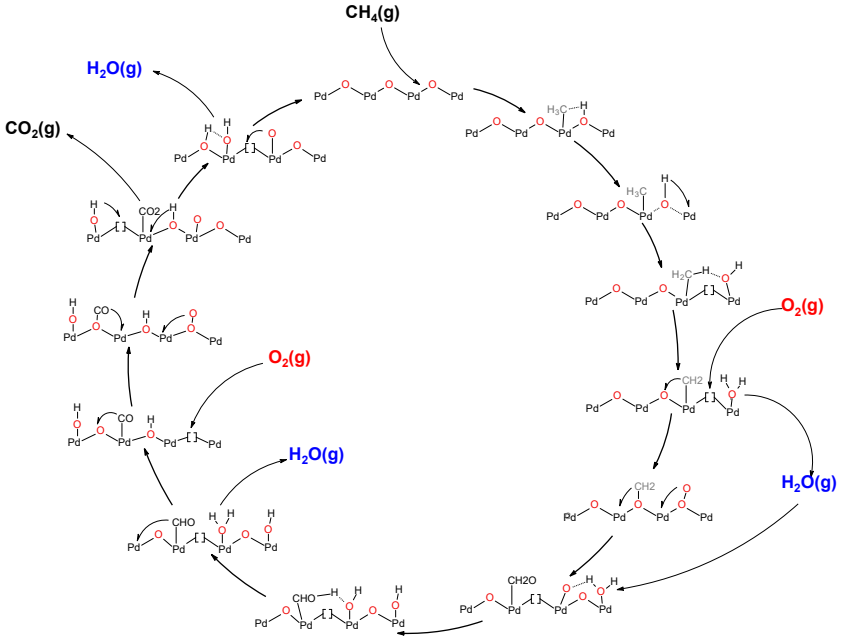

Figure 6.22: Catalytic cycle of the preferential reaction path following a Mars-van-Krevelen redox mechanism for methane oxidation over PdO(101) as found at wet feed conditions (12 % H_2O, 300 °C to 550 °C). Figure adapted from Stotz et al. [2].

6.3 Model Transferability and Validation

Additional simulation studies have been performed for further validation of the predictive capability of the developed mechanisms. Model results are compared with experimental literature data, reported by Groppi et al. [11] and Tarasov et al. [219].

6.3.1 Ex-Situ Experiments with Pd Foil

Tarasov et al. [219] conducted CH_4 oxidation experiments at high temperatures (950 K to 1200 K) and fuel-rich conditions (CH_4/O_2-ratio = 2) over a 2 wt-% Pd deposited on FeCrAl foil. Based on the preparation method of the Pd-foil catalyst, it can be assumed that the experiments were performed under the absence of internal mass-transfer limitations. The reaction was carried out in a flow reactor setup (ID = 10 mm, L_{foil} = 10 mm) at a volumetric inlet flow rate of 70 $\text{cm}^3\,\text{min}^{-1}$ and at SATP. Figure 6.23 shows experimental data and in comparison the simulated results for a chosen $F_{\text{cat/geo}} = 0.35$.

The model results show that the developed mechanism for the reduced phase of Pd can reasonably predict the experimental data points over the entire investigated temperature range.

6.3.2 Conversion Hysteresis in an Annular Reactor Setup

Groppi et al. [11, 43, 55] performed thermal light-off and light-out cycling experiments in an annular reactor configuration. The methane oxidation activity of the catalyst was measured during the thermal cycling process and the size of the Pd and PdO crystallites were determined from XRD sprectra, recorded during operation of the reactor. The calculated crystallite sizes via Rietfeldt analysis ranged between 25 nm to 30 nm for the PdO and 60 nm to 70 nm for the Pd phase. The catalyst was present as a Pd on alumina coated on wahscoat onto the surface of the internal tube.
In analogy to the reported experimental conditions in [11], stationary light-off and light-out simulations have been performed for the annular duct flow configuration (OD = 7 mm, and ID = 6.525 mm of tube without washcoat thickness), applying the boundary layer approximation and the effectiveness factor approach for the washcoat. ($\delta_{\text{wc}} = 25\,\mu\text{m}$, $w_{\text{Pd}} = 10$ wt-%, $\epsilon_{\text{wc}} = 0.5$, $d_{\text{Pd}} = 65$ nm).
Two different sets of simulations were performed under the same fuel-lean conditions (5000 ppm CH_4, 2 vol.-% O_2, balance in He) at atmospheric pressure,

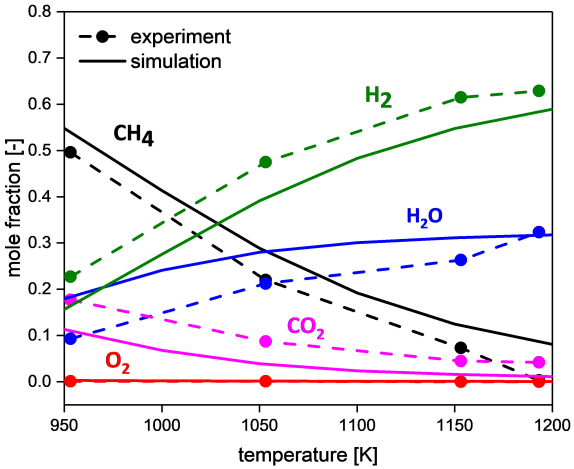

Figure 6.23: Ex-situ concentration measurements during CH_4-oxidation over a Pd-deposited on FeCrAl-foil under fuel-rich conditions (C/O-ratio = 1.0). Experimental data from Tarasov et al. [219]. Dashed lines in between experimental points are guide to the eye. Figure adapted from Stotz et al. [1].

and high flow velocities ($\frac{v_{\mathrm{GHSV}}}{\rho_{\mathrm{cat}}} = 1\,100\,000\ \mathrm{Ncm^3/(g_{wc}h)}$) at a volumetric inlet flow rate, $\dot{V}_{\mathrm{N}}$, of 240 $\mathrm{Ncm^3/min}$ under normal conditions ($T_{\mathrm{N}} = 273.15\,\mathrm{K}$ and $p_{\mathrm{N}} = 1013.25\,\mathrm{mbar}$)).
The first set of simulations was intended to validate the mechanism on the reduced phase of Pd with the experimental conditions in the temperature range of 600 °C $< T <$ 900 °C, since under these conditions palladium is kept presumably in a thermally reduced state [11, 43]. The second set of simulations was performed with the oxide mechanism for the PdO phase in the temperature range of 200 °C $< T <$ 600 °C, where the formation of bulk PdO during cool down becomes thermodynamically favored, when starting the thermal light-out cycling from high temperatures, when Pd is present in its reduced state.

For both sets, the length of the coated zone was back calculated from the data given in Tab. 6.2 for a representative catalyst density, ρ_{cat}, of 1 $\mathrm{g/cm^3}$ to $L_{\mathrm{ctz}} = 25.54\,\mathrm{mm}$ accordingly:

$$L_{\mathrm{ctz}} = \frac{\dot{V}_{\mathrm{N}} \cdot \left(\frac{v_{\mathrm{GHSV}}}{\rho_{\mathrm{cat}}}\right)^{-1}}{\rho_{\mathrm{cat}} \cdot \frac{\pi}{4}\left[(d_{\mathrm{i}} + 2 \cdot \delta_{\mathrm{wc}})^2 - (d_{\mathrm{i}})^2\right]} \tag{6.2}$$

The ratio of catalytic to geometric surface area for the reduced phase was determined for a Pd particle size of 65 nm to $F_{\mathrm{cat/geo}} = 19.12$.

Table 6.2: Catalyst parameters of the Pd/Al_2O_3 catalyst coated-on the surface of the inner tube within the annular duct.

Parameter	Symbol	Value	Unit
Inner diameter of annular duct	d_i	6.5‡	[mm]
Outer diameter of annular duct	d_o	7‡	[mm]
Washcoat thickness	δ_{wc}	25‡	[μm]
Palladium weight fraction	w_{Pd}	10‡	[wt.-%]
Wascoat porosity	ϵ_{wc}	0.5†	[-]
Wascoat pore diameter	d_{p}	20†	[nm]
Tortuosity	τ	3†	[-]
Palladium particle size	$\bar{d}_{\mathrm{Pd}}$	65‡	[nm]
Length of coated-on annulus	L_{ctz}	25.54§	[mm]

‡ Taken from [11].
† Assumption.
§ Calculated value.

Figure 6.25 shows simulated and reported experimental CH_4 conversions at various temperatures. The experimentally observed declining conversion branch

(blue line) between 900 K and 1200 K during the cool down of the catalyst, represents the region where Pd is in the reduced state. In that region the simulated conversion (blue symbols) predicts the experiments well. The low activity which is reflected by the high light-off temperature, primarily results from the fact that oxygen strongly covers the reduced palladium surface. The lower the catalyst temperature during cool down, the higher the oxygen coverage (cf. Fig. 6.24). The tremendeous site blocking effect of O(s) hinders the activation of methane over the reduced catalyst surface, even though the barrier for the first C-H bond activation step is lowered at higher oxygen coverages.

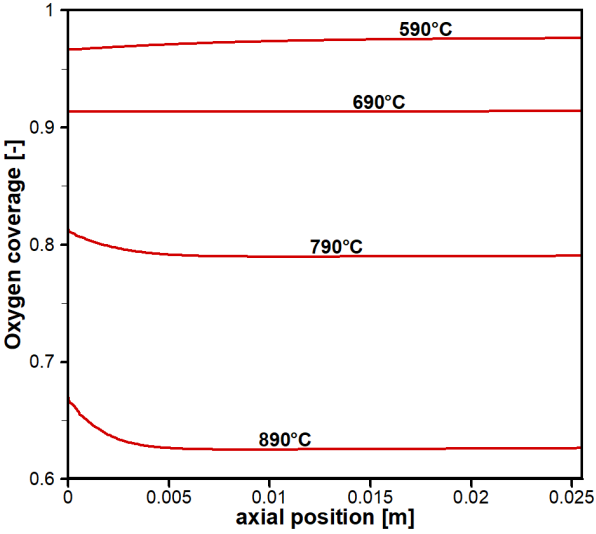

Figure 6.24: Evolution of the simulated axial oxygen coverage over the reduced catalyst surface at selected temperatures during cool down from high temperatures (cf. blue symbols in Fig. 6.25) in analogy to the conditions for the annular reactor experiments [11].

For the further prediction of the conversion at temperatures lower than ca. 900 K an extended mechanism is required which captures the processes over the oxidized phase of Pd and the phase transition between the PdO and Pd.

Based on the TEM observations of Datye et al. [53], which showed for similar experimental reaction conditions, that the formation of the PdO phase starts from

grain boundaries, leading to the formation of metastable aggregated Pd/PdO particles during cool down, a degree of oxidation model (DOM, cf. Appendix B.3) has been developed based on a sectoral PdO particle growth mode according to Eq. (5.78) and Eq. (5.80). Three different scenarios have been investigated (cf. Fig. 6.25).

(i) Constant dispersion, assuming a skin oxide grown on bulk reduced Pd (green symbols), corresponding to a dispersion of 1.71 % PdO at a particle diameter of 65 nm.

(ii) Constant dispersion, at a phase fraction of 100 % PdO (black/red symbols) for two different particle sizes of 25 nm and 5 nm.

(iii) Variable phase fraction and particle size according to the DOM (orange symbols).

Scrutinizing the hypothesis that a surficial oxide (PdO_x) growth mode is responsible for the activity increase during cool down, additional light-out simulations with the MF-MKM for the various scenarios are presented in Fig. 6.25. Starting with a bulk reduced surface oxide model (i), assuming the particle size remains the same as in case of the completely thermally reduced Pd particles ($d_{\mathrm{p,PdO}} = 65\,\mathrm{nm}$, as evaluated from HT-XRD measurments through Rietfeld analysis by Groppi et al. [11]), the MF-MKM results show that the methane oxidation activity is vastly surmounting the experimentally observed one at 600 °C. These results confirm the high activity of the PdO(101) facet [79] and point to the conclusion that formation of a skin oxide is likely not the dominant growth mode, in agreement with TEM observations of Datye et al. [53].

For scenario (ii), two different PdO particle sizes of 25 nm (as experimentally determined by XRD analysis at ca. 450 °C in [11]), and a fictive size of 5 nm which is below the actual detection limit of the XRD analysis [220], have been used to study the sensitivity of particle sizes on the simulated light-out curves, both assumed constant during simulation since no information was given during light-off. In both the cases 100 % Pd is assumed to be present in oxidized form. Simulation results for the 25 nm PdO particle size agrees well with the experimentally observed methane conversion during heating at 450 °C. However, at lower temperatures the simulated conversion curve is less active and shows a delayed light-out in comparison to the experimental curve. In contrast when simulating the light-out with the 5 nm PdO size the low temperature conversion curve of the cooling branch at ca. 300 °C is well captured. Given the fact that the dispersion is treated constant during the simulation and experimental information on particle size through XRD analysis may not resolve particle sizes smaller $\sim$ 5 nm as pointed out by Baylet et al. [220] and also observed

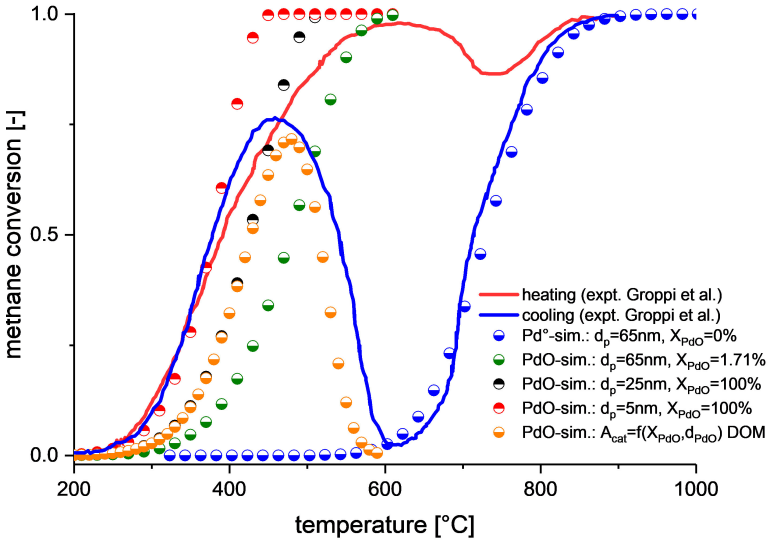

Figure 6.25: Simulated light-off/out curves (steady-state simulations) using the MKM for the PdO(101) surface at different PdO particle sizes and phase fractions (all symbols except blue) for an annular reactor configuration [2]. Experimental conversion hysteresis for heating (red line) and cooling (blue line) at a heating rate of 15 K/min (adapted from Groppi et al. [11]). Simulation results with the reduced Pd mechanism for the cooling branch (blue symbols) for a constant particle size of 65 nm [1]. Reaction conditions: 5000 ppm CH_4, 2 vol% O_2, He in balance to 1 atm at a volumetric inlet flow rate of 240 Ncm^3/min. Figure adapted from Stotz et al. [2].

experimentally by Grunwaldt et al. [69] from in situ XRD and XANES spectra, it seems reasonable to assume that there are additional particle structure related changes occurring during cool down to 350 °C. In principal, such changes could include particle fracturing, roughening of the surface or altered wetting behavior of the Pd particles to the support [136, 137]. Another possibility is given by variations in the active facet with temperature, responsible for the catalytic activity [83].

Lastly, the effect of altered particle size (re-dispersion) was investigated, as e.g. demonstrated in [69], as well as the effect of PdO oxide phase fraction during light-off on the simulated methane activity, by applying the developed DOM taking a sectoral PdO growth mode into consideration. The cool down branch of the conversion hysteresis is qualitatively captured by the simulation results when the DOM is coupled to the microkinetic mechanism. For re-producing these results, the model assumes profiles on the phase fraction and particle size for PdO with temperature which are qualitatively similar to the observed ones by Datye et al. [53] at comparable reaction conditions, determined from in situ XRD measurements during cool down (cf. Appendix Fig. B.2 on page 205). The results are qualitative similar for same supported PdO catalysts but change for other supports [221]. Based on the aforementioned results, it can be concluded that a sectoral PdO growth mode can qualitatively capture the anomalous increase in methane conversion at lower temperatures during cool down when appropriately coupled to the microkinetic model. However, it is likely that additional re-dispersion takes place during cool down in parallel to the actual PdO formation process [136], since the simulated conversions under predict the experimental points for a given limiting particle size of 25 nm. Minor discrepancies between model results and the experimental conversion curve can also arise as consequence of the performed steady-state channel simulations as the effect of the heating/cooling rate on the conversion curve is not considered herein.

7 Conclusions and Future Outlook[1]

This chapter presents the main conclusions of this thesis resulting from the development of the microkinetic mechanisms for the oxide and the reduced phase of palladium for the methane oxidation reaction in conjunction with experimental investigations.

7.1 Conclusions

Methane oxidation on a Pd/Al_2O_3-coated monolith was studied experimentally under quasi-autothermal operating conditions using the in situ sampling technique. Spatially resolved experimental data for temperature and species concentration within a single catalytic channel of the monolith were used to develop a multistep elementary surface reaction mechanism for the partial oxidation of CH_4 at high temperatures for the reduced phase of palladium. Kinetic parameters were calculated using semi-empirical methods such as UBI-QEP.
The mechanism builds up on three different CH_4 activation paths involving different site-pairs: (i) pyrolytic (Pd(s)-Pd(s)), (ii) oxygen-assisted (Pd(s)-O(s)) and (iii) dual-oxygen-assisted (O(s)-O(s) and Pd(s)-O(s))/ methoxy mediated activation. Higher amounts of surface oxygen facilitate easier C-H bond cleavage as coverage-dependent activation energy barriers are lowered.
Under fuel-rich conditions, the indirect formation of synthesis gas is the preferred route for partial oxidation of methane. Three different zones within the catalytic channel can be identified. Methane is first converted via total oxidation within a small, ca. 0.25 mm wide, entrance zone of the catalyst (oxidation zone).

[1] Parts of this chapter have been taken from [1] H. Stotz, L. Maier and O. Deutschmann, Methane oxidation over palladium: on the mechanism in fuel-rich mixtures at high temperatures, *Top. Catal.*, 60 (2017) 83–109 and from [2] H. Stotz, L. Maier, A. Boubnov, A. T. Gremminger, J.-D. Grunwaldt and O. Deutschmann, Surface reaction kinetics of methane oxidation over PdO, *J. Catal.*, 370 (2019) 152–175.

Partial oxidation products, H_2 and CO, are at this stage not observed. Further downstream between ~ 0.25 and 2 mm an extended oxy-reforming zone is found where CH_4 is consumed by combined total oxidation as well as steam reforming. After consumption of nearly all oxygen in the channel at axial positions > 2 mm, steam reforming of CH_4 is the preferred conversion path, leading to a prolonged consumption of CH_4 and a simultaneous decrease in H_2O concentrations (steam reforming zone). The partial oxidation products CO and H_2 form sequentially over the channel length.
The developed multi-step surface reaction kinetics for the reduced phase of palladium predicts all features of the experimental spatially-resolved species profiles. Additional experiments are recommended to clarify the oxidation state of Pd in operando, in particular in the entrance zone of the catalyst.

Secondly, a mean field extended microkinetic model was successfully developed based on available first principles DFT derived kinetic data for the PdO(101) surface, incorporating formate species. The developed kinetic scheme sufficiently captures most important processes over the alumina supported PdO catalyst, once metal oxide corrected dispersions were introduced. In particular, catalytic light-off during methane oxidation, at different water concentrations, was reasonably well reproduced, without explicitly taking into account a pairing formalism or a spatially correlated approach. Such factors have to a large extent no detrimental effect on the predictive power of the developed mechanism regarding methane conversion and transferability of the mechanism is given.

The observed water inhibition proceeded immediately in comparison to the rather slow water deactivation effect with a larger time scale. Water inhibition appears as consequence of a site blocking process due to hydroxide formation, $(H)_{O_{(cus)}}$, and reversible H_2O/OH, adsorption on $(*)_{Pd_{(cus)}}$ sites, leading to a decreased availablablity of $(*)_{O_{(cus)}} - (*)_{Pd_{(cus)}}$-site pairs, relevant for activating methane. The results impede the hypothesis that water deactivation is caused by a gradual process due to adsorption of water or OH species onto the PdO surface from the gas-phase.

Catalyst deactivation for PdO can be captured by considering additional changes in dispersion for the overall kinetic model during light-off, but is not part of the surface reaction mechanism. The exact mechanism behind deactivation remains unclear. Likely, a combination of effects is responsible for the catalyst deactivation, including sintering, structural (roughening/fragmentation) and morphological particle shape change effects or altered appearance of active facets due to the presence of water vapor in the reaction gas mixture, interacting with Pd particles and support, once internally formed or externally introduced.

A comprehensive spatially resolved reaction flow analysis during light-off unrevealed that preferential reaction pathways changed with varying water concentration, at low and high temperatures, as well as along the catalyst channel. Distinctly, $(CH_2)_{Pd_{(cus)}}$ and $(CH_2)_{O_{(cus)}}$ intermediates are specifically participating at higher temperatures, while $(CH_2OH)_{Pd_{(cus)}}$ species are characteristic for the low temperature reaction pathway. The importance of available $(*)_{Pd_{(cus)}}$-$(*)_{O_{(cus)}}$ site pairs was confirmed by the results of the DRC analysis, showing dissociative adsorption of methane over $(*)_{O_{(cus)}}$-$(*)_{Pd_{(cus)}}$ site pairs as the major rate controlling step, as also found participating in the preferred methane activation pathways.

DRIFTS investigations confirm theoretical DFT results from literature that formate (CH_xO_y) species participate in the mechanism for oxidizing methane over PdO. Methane oxidation via a pyrolytic decomposition route over PdO can thus be ruled out. Formation of formate bands are suppressed once water is added to the reaction mixture. The presence of adsorbed water hinders spillover of formates to the support, but not their formation via adsorption of methanol or formic acid onto the support from the gas-phase. Secondly, bands of different forms of hydroxides bonded to a different number of metal ion centers (OH_I, OH_{II}, and OH_{III}) were observed, once water was dosed. Carbonates were not observed when no extra CO_2 was added to the reaction mixture. Clear bands only became visible when extra CO_2 and CO where dosed instead of methane.

Comparison of different oxide growths modes in the simulations with the MKM show that possible PdO formation during cool down of the thermally reduced Pd via skin oxide formation can be ruled out. The methane conversion was best represented by a sectoral growth mode model incorporating PdO phase formation during cool down.

7.2 Outlook

The developed mean field extended MKM in conjunction with the DOM and the previously developed methane oxidation mechanism over the reduced phase of palladium [1] frame the foundation to further build a unified kinetic model for the coupling of the kinetics and phase transformation processes which occur in the anomalous methane conversion hysteresis of the Pd/PdO system. Effects of the support need to be incorporated in order to clarify its influence on the water deactivation.

The development of reliable models for prediction of the methane oxidation kinetics in the palladium system requires not only accurate knowledge on the

actual microkinetics and the mechanisms itself. This work emphasizes that the improvement of these models will require future models to take into account catalyst structure-functional relationships which allow to relate activity in- or decreases of the catalyst due to structural changes with the reaction conditions and chemical potentials of the gas composition, in addition to surface reaction kinetic effects. Therefore, this work frames a basis for the development of future dynamic microkinetic models for methane oxidation over the palladium system. This will allow for prediction of the reaction kinetics under fully transient reaction conditions, by taking into account spatially distributed catalyst phases.

Bibliography

[1] H. Stotz, L. Maier, and O. Deutschmann. Methane oxidation over palladium: On the mechanism in fuel-rich mixtures at high temperatures. *Topics in Catalysis*, 60(1-2):83–109, 2017. ISSN 1022-5528. doi: 10.1007/s11244-016-0717-5.

[2] H. Stotz, L. Maier, A. Boubnov, A. T. Gremminger, J.-D. Grunwaldt, and O. Deutschmann. Surface reaction kinetics of methane oxidation over PdO. *Journal of Catalysis*, 370:152–175, 2019. ISSN 00219517. doi: 10.1016/j.jcat.2018.12.007.

[3] J. N. Armor. Key questions, approaches, and challenges to energy today. *Catalysis Today*, 236:171–181, 2014. ISSN 09205861. doi: 10.1016/j.cattod.2013.12.029.

[4] A. Karion, C. Sweeney, G. Pétron, G. Frost, R. M. Hardesty, J. Kofler, B. R. Miller, T. Newberger, S. Wolter, R. Banta, A. Brewer, E. Dlugokencky, P. Lang, S. A. Montzka, R. Schnell, P. Tans, M. Trainer, R. Zamora, and S. Conley. Methane emissions estimate from airborne measurements over a western united states natural gas field. *Geophysical Research Letters*, 40 (16):4393–4397, 2013. ISSN 00948276. doi: 10.1002/grl.50811.

[5] C. Diehm and O. Deutschmann. Hydrogen production by catalytic partial oxidation of methane over staged Pd/Rh coated monoliths: Spatially resolved concentration and temperature profiles. *International Journal of Hydrogen Energy*, 39(31):17998–18004, 2014. ISSN 03603199. doi: 10.1016/j.ijhydene.2014.06.094.

[6] S. Colussi, A. Trovarelli, E. Vesselli, A. Baraldi, G. Comelli, G. Groppi, and J. Llorca. Structure and morphology of Pd/Al_2O_3 and $Pd/CeO_2/Al_2O_3$ combustion catalysts in Pd-PdO transformation hysteresis. *Applied Catalysis A: General*, 390(1-2):1–10, 2010. ISSN 0926860X. doi: 10.1016/j.apcata.2010.09.033.

[7] M. Peuckert. XPS study on surface and bulk palladium oxide, its thermal stability, and a comparison with other noble metal oxides. *Journal of*

Physical Chemistry, 89(12):2481–2486, 1985. ISSN 0022-3654. doi: 10.1021/j100258a012.

[8] G. Bayer and H. G. Wiedemann. Formation, dissociation and expansion behavior of platinum group metal oxides (PdO, RuO_2, IrO_2). *Thermochimica Acta*, 11(1):79–88, 1975. ISSN 00406031. doi: 10.1016/0040-6031(75)80040-2.

[9] W. E. Bell, R. E. Inyard, and M. Tagami. Dissociation of palladium oxide. *Journal of Physical Chemistry*, 70(11):3735–3736, 1966. ISSN 0022-3654. doi: 10.1021/j100883a502.

[10] M. Van den Bossche and H. Grönbeck. Methane oxidation over PdO(101) revealed by first-principles kinetic modeling. *Journal of the American Chemical Society*, 137(37):12035–12044, 2015. ISSN 0002-7863. doi: 10.1021/jacs.5b06069.

[11] G. Groppi, C. Cristiani, L. Lietti, and P. Forzatti. Study of PdO/Pd transformation over alumina supported catalysts for natural gas combustion. In A. Corma, F. V. Melo, S. Mendioroz, and Fierro, J. L. G., editors, *12th International Congress on Catalysis, Proc of the 12th ICC*, volume 130 of *Studies in Surface Science and Catalysis*, pages 3801–3806. Elsevier, Amsterdam, 2000. ISBN 9780444504807. doi: 10.1016/S0167-2991(00)80615-1.

[12] R. Abbasi, G. Huang, G. M. Istratescu, L. Wu, and R. E. Hayes. Methane oxidation over Pt, Pt:Pd, and Pd based catalysts: Effects of pre-treatment. *The Canadian Journal of Chemical Engineering*, 93(8):1474–1482, 2015. ISSN 00084034. doi: 10.1002/cjce.22229.

[13] T.V Choudhary, S. Banerjee, and V.R Choudhary. Catalysts for combustion of methane and lower alkanes. *Applied Catalysis A: General*, 234(1-2):1–23, 2002. ISSN 0926860X. doi: 10.1016/S0926-860X(02)00231-4.

[14] M. Aryafar and F. Zaera. Kinetic study of the catalytic oxidation of alkanes over nickel, palladium, and platinum foils. *Catalysis Letters*, 48(3/4):173–183, 1997. ISSN 1011372X. doi: 10.1023/A:1019055810760.

[15] T. Maillet, C. Solleau, J. Barbier, and D. Duprez. Oxidation of carbon monoxide, propene, propane and methane over a Pd/Al_2O_3 catalyst. effect of the chemical state of Pd. *Applied Catalysis B: Environmental*, 14(1-2):85–95, 1997. ISSN 09263373. doi: 10.1016/S0926-3373(97)00014-3.

[16] R. Burch, P. K. Loader, and F. J. Urbano. Some aspects of hydrocarbon activation on platinum group metal combustion catalysts. *Catalysis Today*, 27(1-2):243–248, 1996. ISSN 09205861. doi: 10.1016/0920-5861(95)00194-8.

[17] A. T. Gremminger, Pereira de Carvalho, H. W., R. Popescu, J.-D. Grunwaldt, and O. Deutschmann. Influence of gas composition on activity and durability of bimetallic Pd-Pt/Al_2O_3 catalysts for total oxidation of methane. *Catalysis Today*, 258:470–480, 2015. ISSN 09205861. doi: 10.1016/j.cattod.2015.01.034.

[18] H. Dubbe, F. Bühner, G. Eigenberger, and U. Nieken. Hysteresis phenomena on platinum and palladium-based diesel oxidation catalysts (DOCs). *Emission Control Science and Technology*, 2(3):137–144, 2016. ISSN 2199-3629. doi: 10.1007/s40825-016-0038-y.

[19] M. Khosravi, A. Abedi, R. E. Hayes, W. S. Epling, and M. Votsmeier. Kinetic modelling of Pt and Pt:Pd diesel oxidation catalysts. *Applied Catalysis B: Environmental*, 154-155:16–26, 2014. ISSN 09263373. doi: 10.1016/j.apcatb.2014.02.001.

[20] P. Hurtado, S. Ordóñez, H. Sastre, and F. V. Diez. Development of a kinetic model for the oxidation of methane over Pd/Al_2O_3 at dry and wet conditions. *Applied Catalysis B: Environmental*, 51(4):229–238, 2004. ISSN 09263373. doi: 10.1016/j.apcatb.2004.03.006.

[21] T. C. Watling, M. Ahmadinejad, M. Ţuţuianu, Å. Johansson, and M. A.J. Paterson. Development and validation of a Pt-Pd diesel oxidation catalyst model. *SAE International Journal of Engines*, 5(3):1420–1442, 2012. ISSN 1946-3944. doi: 10.4271/2012-01-1286.

[22] N. Sadokhina, F. Ghasempour, X. Auvray, G. Smedler, U. Nylén, M. Olofsson, and L. Olsson. An experimental and kinetic modelling study for methane oxidation over Pd-based catalyst: Inhibition by water. *Catalysis Letters*, 209:301, 2017. ISSN 1011-372X. doi: 10.1007/s10562-017-2133-2.

[23] Ye Lu, Matam Santhosh Kumar, Gian Luca Chiarello, Panayotis Dimopoulos Eggenschwiler, Christian Bach, Martin Weilenmann, Alex Spiteri, Anke Weidenkaff, and Davide Ferri. Operando xanes study of simulated transient cycles on a pd-only three-way catalyst. *Catalysis Communications*, 39: 55–59, 2013. ISSN 15667367. doi: 10.1016/j.catcom.2013.05.006.

[24] G. Zhu, J. Han, D. Y. Zemlyanov, and F. H. Ribeiro. Temperature dependence of the kinetics for the complete oxidation of methane on palladium and palladium oxide. *Journal of Physical Chemistry B*, 109(6): 2331–2337, 2005. ISSN 1520-6106. doi: 10.1021/jp0488665.

[25] P. Forzatti and G. Groppi. Catalytic combustion for the production of energy. *Catalysis Today*, 54(1):165–180, 1999. ISSN 0920-5861. doi: 10.1016/S0920-5861(99)00178-9.

[26] G. W. Graham, D. König, B. D. Poindexter, J. T. Remillard, and W. H. Weber. Ellipsometric study of a palladium catalyst during the oxidation of carbon monoxide and methane. *Topics in Catalysis*, 8(1,2):35–43, 1999. ISSN 1022-5528.

[27] R. Burch. Low nox options in catalytic combustion and emission control. *Catalysis Today*, 35(1-2):27–36, 1997. ISSN 09205861. doi: 10.1016/S0920-5861(96)00131-9.

[28] P. Gélin and M. Primet. Complete oxidation of methane at low temperature over noble metal based catalysts: a review. *Applied Catalysis B: Environmental*, 39(1):1–37, 2002. ISSN 09263373. doi: 10.1016/S0926-3373(02)00076-0.

[29] R. B. Anderson, K. C. Stein, J. J. Feenan, and L. J. E. Hofer. Catalytic oxidation of methane. *Industrial & Engineering Chemistry*, 53(10):809–812, 1961. ISSN 0019-7866. doi: 10.1021/ie50622a024.

[30] G. Centi. Supported palladium catalysts in environmental catalytic technologies for gaseous emissions. *Journal of Molecular Catalysis A: Chemical*, 173(1-2):287–312, 2001. ISSN 13811169. doi: 10.1016/S1381-1169(01)00155-8.

[31] D. Ciuparu, M. R. Lyubovsky, E. Altman, L. D. Pfefferle, and A. Datye. Catalytic combustion of methane over palladium-based catalysts. *Catalysis Reviews*, 44(4):593–649, 2002. ISSN 0161-4940. doi: 10.1081/CR-120015482.

[32] Y.-H. Chin and D. E. Resasco. Catalytic oxidation of methane on supported palladium under lean conditions: kinetics, structure and properties. *Catalysis*, 14:1–39, 1999. ISSN 0140-0568. doi: 10.1039/9781847553263-00001.

[33] Z. Li and G. B. Hoflund. A review on complete oxidation of methane at low temperatures. *Journal of Natural Gas Chemistry*, 12(3):153–160, 2003. ISSN 1003-9953.

[34] L. Wen-Ge, G. De-Yong, and Xin X. Research progress of palladium catalysts for methane combustion. *Journal of China Petroleum Processing & Petrochemical Technology*, 14(3):1–9, 2012.

[35] Y. Xin, H. Wang, and C. K. Law. Kinetics of catalytic oxidation of methane, ethane and propane over palladium oxide. *Combustion and Flame*, 161(4):1048–1054, 2014. ISSN 00102180. doi: 10.1016/j.combustflame.2013.10.023.

[36] Y.-H. C. Chin, C. Buda, M. Neurock, and E. Iglesia. Consequences of metal-oxide interconversion for C-H bond activation during CH_4 reactions on Pd catalysts. *Journal of the American Chemical Society*, 135(41): 15425–15442, 2013. ISSN 0002-7863. doi: 10.1021/ja405004m.

[37] G. Zhu, J. Han, D. Y. Zemlyanov, and F. H. Ribeiro. The turnover rate for the catalytic combustion of methane over palladium is not sensitive to the structure of the catalyst. *Journal of the American Chemical Society*, 126(32):9896–9897, 2004. ISSN 0002-7863. doi: 10.1021/ja049406s.

[38] J. Au-Yeung. Isotopic studies of methane oxidation pathways on PdO catalysts. *Journal of Catalysis*, 188(1):132–139, 1999. ISSN 0021-9517. doi: 10.1006/jcat.1999.2643.

[39] R. J. Farrauto, M. C. Hobson, T. Kennelly, and E. M. Waterman. Catalytic chemistry of supported palladium for combustion of methane. *Applied Catalysis, A: General*, 81(2):227–237, 1992. ISSN 0166-9834. doi: 10.1016/0926-860X(92)80095-T.

[40] R. S. Monteiro, D. Zemlyanov, J. M. Storey, and F. H. Ribeiro. Surface area increase on Pd foils after oxidation in excess methane. *Journal of Catalysis*, 201(1):37–45, 2001. ISSN 0021-9517. doi: 10.1006/jcat.2001.3235.

[41] B. Kimmerle, A. Baiker, and J.-D. Grunwaldt. Oscillatory behaviour of catalytic properties, structure and temperature during the catalytic partial oxidation of methane on Pd/Al_2O_3. *Physical Chemistry Chemical Physics*, 12(10):2288–2291, 2010. ISSN 1463-9076. doi: 10.1039/b924001b.

[42] J. G. McCarty. Kinetics of PdO combustion catalysis. *Catalysis Today*, 26 (3-4):283–293, 1995. ISSN 0920-5861. doi: 10.1016/0920-5861(95)00150-7.

[43] G. Groppi, G. Artioli, C. Cristiani, L. Lietti, and P. Forzatti. Decomposition/reformation processes and CH_4 combustion activity of PdO over Al_2O_3 supported catalysts for gas turbine applications. In *Natural Gas Conversion VI*, volume 136 of *Studies in Surface Science and Catalysis*, pages 345–350. Elsevier, 2001. ISBN 9780444505446. doi: 10.1016/S0167-2991(01)80327-X.

[44] X. Chen, J. W. Schwank, G. B. Fisher, Y. Cheng, M. Jagner, R. W. McCabe, M. B. Katz, G. W. Graham, and X. Pan. Nature of the two-step temperature-programmed decomposition of PdO supported on alumina. *Applied Catalysis A: General*, 475:420–426, 2014. ISSN 0926860X. doi: 10.1016/j.apcata.2014.01.056.

[45] K.-I. Fujimoto, F. H. Ribeiro, M. Avalos-Borja, and E. Iglesia. Structure and reactivity of PdO_x/ZrO_2 catalysts for methane oxidation at low temperatures. *Journal of Catalysis*, 179(2):431–442, 1998. ISSN 0021-9517. doi: 10.1006/jcat.1998.2178.

[46] R. S. Monteiro, D. Zemlyanov, J. M. Storey, and F. H. Ribeiro. Turnover rate and reaction orders for the complete oxidation of methane on a palladium foil in excess dioxygen. *Journal of Catalysis*, 199(2):291–301, 2001. ISSN 0021-9517. doi: 10.1006/jcat.2001.3176.

[47] D. Ciuparu, F. Bozon-Verduraz, and L. Pfefferle. Oxygen exchange between palladium and oxide supports in combustion catalysts. *Journal of Physical Chemistry B*, 106(13):3434–3442, 2002. ISSN 1520-6106. doi: 10.1021/jp013577r.

[48] M. Lyubovsky and L. Pfefferle. Complete methane oxidation over Pd catalyst supported on α-alumina. influence of temperature and oxygen pressure on the catalyst activity. *Catalysis Today*, 47(1-4):29–44, 1999. ISSN 0920-5861. doi: 10.1016/S0920-5861(98)00281-8.

[49] Y.-H. C. Chin, C. Buda, M. Neurock, and E. Iglesia. Reactivity of chemisorbed oxygen atoms and their catalytic consequences during $CH_4 - O_2$ catalysis on supported Pt clusters. *Journal of the American Chemical Society*, 133(40):15958–15978, 2011. ISSN 0002-7863. doi: 10.1021/ja202411v.

[50] M. Alyani and K. J. Smith. Kinetic analysis of the inhibition of CH_4 oxidation by H_2O on PdO/Al_2O_3 and $CeO_2/PdO/Al_2O_3$ catalysts. *Industrial & Engineering Chemistry Research*, 55(30):8309–8318, 2016. ISSN 0888-5885. doi: 10.1021/acs.iecr.6b01881.

[51] K. Persson, L. D. Pfefferle, W. Schwartz, A. Ersson, and S. G. Järås. Stability of palladium-based catalysts during catalytic combustion of methane: The influence of water. *Applied Catalysis B: Environmental*, 74 (3-4):242–250, 2007. ISSN 09263373. doi: 10.1016/j.apcatb.2007.02.015.

[52] C. F. Cullis, T. G. Nevell, and D. L. Trimm. Role of the catalyst support in the oxidation of methane over palladium. *Journal of the Chemical Society, Faraday Transactions 1: Physical Chemistry in Condensed Phases*, 68(0): 1406, 1972. ISSN 0300-9599. doi: 10.1039/f19726801406.

[53] H. Xiong, K. Lester, T. Ressler, R. Schlögl, L. F. Allard, and A. K. Datye. Metastable Pd $\leftrightarrow$ PdO structures during high temperature oxidation. *Catalysis Letters*, 147(5):1095–1103, 2017. ISSN 1011-372X. doi: 10.1007/s10562-017-2023-7.

[54] G. Groppi. Combustion of CH_4 over a PdO/ZrO_2 catalyst: an example of kinetic study under severe conditions. *Catalysis Today*, 77(4):335–346, 2003. ISSN 09205861. doi: 10.1016/S0920-5861(02)00378-4.

[55] G. Groppi, W. Ibashi, M. Valentini, and P. Forzatti. High-temperature combustion of CH_4 over PdO/Al_2O_3: kinetic measurements in a structured annular reactor. *Chemical Engineering Science*, 56(3):831–839, 2001. ISSN 0009-2509. doi: 10.1016/S0009-2509(00)00295-5.

[56] B. Torkashvand, A. Gremminger, S. Valchera, M. Casapu, J.-D. Grunwaldt, and O. Deutschmann. The impact of pre-turbine catalyst placement on methane oxidation in lean-burn gas engines: An experimental and numerical study. *SAE Technical Paper Series*, 2017. doi: 10.4271/2017-01-1019.

[57] N. Sadokhina, G. Smedler, U. Nylén, M. Olofsson, and L. Olsson. The influence of gas composition on Pd-based catalyst activity in methane oxidation – inhibition and promotion by NO. *Applied Catalysis B: Environmental*, 200:351–360, 2017. ISSN 09263373. doi: 10.1016/j.apcatb.2016.07.012.

[58] T. W. Hansen, A. T. Delariva, S. R. Challa, and A. K. Datye. Sintering of catalytic nanoparticles: particle migration or ostwald ripening? *Accounts of chemical research*, 46(8):1720–1730, 2013. ISSN 1520-4898. doi: 10.1021/ar3002427.

[59] T. R. Johns, J. R. Gaudet, E. J. Peterson, J. T. Miller, E. A. Stach, C. H. Kim, M. P. Balogh, and A. K. Datye. Microstructure of bimetallic Pt-Pd catalysts under oxidizing conditions. *ChemCatChem*, 5(9):2636–2645, 2013. ISSN 18673880. doi: 10.1002/cctc.201300181.

[60] X. Chen, Y. Cheng, C. Y. Seo, J. W. Schwank, and R. W. McCabe. Aging, re-dispersion, and catalytic oxidation characteristics of model Pd/Al_2O_3 automotive three-way catalysts. *Applied Catalysis B: Environmental*, 163:499–509, 2015. ISSN 09263373. doi: 10.1016/j.apcatb.2014.08.018.

[61] Y. Deng and T. G. Nevell. Oscillations of methane combustion over alumina-supported palladium catalysts under oxygen-deficient conditions. *Journal of Molecular Catalysis A: Chemical*, 142(1):51–60, 1999. ISSN 13811169. doi: 10.1016/S1381-1169(98)00286-6.

[62] Y. Deng and T. G. Nevell. Oscillatory behaviour of Pd/Al_2O_3, $Pd\text{-}Pt/Al_2O_3$ and $Pd/Al_2O_3 - CeO_2$ in the oxidation of methane. *Faraday Discussions*, 105:33–46, 1996. ISSN 1359-6640. doi: 10.1039/FD9960500033.

[63] X. Zhang, C. S.-M. Lee, D. M. P. Mingos, and D. O. Hayward. Oscillatory behaviour during the oxidation of methane over palladium metal catalysts. *Applied Catalysis A: General*, 240(1-2):183–197, 2003. ISSN 0926860X. doi: 10.1016/S0926-860X(02)00422-2.

[64] V.Yu. Bychkov, Yu.P. Tulenin, M. M. Slinko, A. K. Khudorozhkov, V. I. Bukhtiyarov, S. Sokolov, and V. N. Korchak. Self-oscillations of methane oxidation rate over Pd/Al_2O_3 catalysts: Role of Pd particle size. *Catalysis Communications*, 77:103–107, 2016. ISSN 15667367. doi: 10.1016/j.catcom.2016.01.028.

[65] A. Yu Stakheev, A. M. Batkin, N. S. Teleguina, G. O. Bragina, V. I. Zaikovsky, I. P. Prosvirin, A. K. Khudorozhkov, and V. I. Bukhtiyarov. Particle size effect on CH_4 oxidation over noble metals: Comparison of Pt and Pd catalysts. *Topics in Catalysis*, 56(1-8):306–310, 2013. ISSN 1022-5528. doi: 10.1007/s11244-013-9971-y.

[66] Y.-H. Chin, M. García-Diéguez, and E. Iglesia. Dynamics and thermodynamics of Pd-PdO phase transitions: Effects of Pd cluster size and kinetic implications for catalytic methane combustion. *Journal of Physical Chemistry C*, 120(3):1446–1460, 2016. ISSN 1932-7447. doi: 10.1021/acs.jpcc.5b06677.

[67] R. Gholami and K. J. Smith. Activity of PdO/SiO_2 catalysts for CH_4 oxidation following thermal treatments. *Applied Catalysis B: Environmental*, 168-169:156–163, 2015. ISSN 09263373. doi: 10.1016/j.apcatb.2014.12.037.

[68] R. J. Farrauto, J. K. Lampert, M. C. Hobson, and E. M. Waterman. Thermal decomposition and reformation of PdO catalysts; support effects. *Applied Catalysis B: Environmental*, 6(3):263–270, 1995. ISSN 09263373. doi: 10.1016/0926-3373(95)00015-1.

[69] J.-D. Grunwaldt, N. Van Vegten, and A. Baiker. Insight into the structure of supported palladium catalysts during the total oxidation of methane. *Chemical Communications (Cambridge, United Kingdom)*, (44):4635–4637, 2007. ISSN 1359-7345. doi: 10.1039/b710222d.

[70] D. Gao, C. Zhang, S. eng Wang, Z. Yuan, and S. Wang. Catalytic activity of Pd/Al_2O_3 toward the combustion of methane. *Catalysis Communications*, 9(15):2583–2587, 2008. ISSN 15667367. doi: 10.1016/j.catcom.2008.07.014.

[71] W. R. Schwartz and L. D. Pfefferle. Combustion of methane over palladium-based catalysts: Support interactions. *Journal of Physical Chemistry C*, 116(15):8571–8578, 2012. ISSN 1932-7447. doi: 10.1021/jp2119668.

[72] D. Ciuparu and L. Pfefferle. Support and water effects on palladium based methane combustion catalysts. *Applied Catalysis A: General*, 209(1-2): 415–428, 2001. ISSN 0926860X. doi: 10.1016/S0926-860X(00)00783-3.

[73] L. S. Escandon, S. Ordonez, A. Vega, and F. V. Diez. Oxidation of methane over palladium catalysts: effect of the support. *Chemosphere*, 58(1):9–17, 2004. ISSN 0045-6535. doi: 10.1016/j.chemosphere.2004.09.012.

[74] W. R. Schwartz, D. Ciuparu, and L. D. Pfefferle. Combustion of methane over palladium-based catalysts: Catalytic deactivation and role of the support. *Journal of Physical Chemistry C*, 116(15):8587–8593, 2012. ISSN 1932-7447. doi: 10.1021/jp212236e.

[75] M. Monai, T. Montini, C. Chen, E. Fonda, R. J. Gorte, and P. Fornasiero. Methane catalytic combustion over hierarchical $Pd@CeO_2/Si\text{-}Al_2O_3$: Effect of the presence of water. *ChemCatChem*, 7(14):2038–2046, 2015. ISSN 18673880. doi: 10.1002/cctc.201402717.

[76] D. Martin, P. Kaur, D. Duprez, E. Gaigneaux, P. Ruiz, and B. Delmon. Impact of surface mobility in selective oxidation. isotopic exchange of $^{18}O_2$ with $^{16}O_2$ on various oxides: MoO_3, SnO_2 and Sb_2O_4. effect of a reducer gas. *Catalysis Today*, 32(1-4):329–336, 1996. ISSN 09205861. doi: 10.1016/S0920-5861(96)00092-2.

[77] J. Rogal, K. Reuter, and M. Scheffler. Thermodynamic stability of PdO surfaces. *Physical Review B*, 69(7), 2004. ISSN 1098-0121. doi: 10.1103/PhysRevB.69.075421.

[78] E. Lundgren, J. Gustafson, A. Mikkelsen, J. N. Andersen, A. Stierle, H. Dosch, M. Todorova, J. Rogal, K. Reuter, and M. Scheffler. Kinetic hindrance during the initial oxidation of Pd(100) at ambient pressures. *Physical Review Letters*, 92(4):046101/1–046101/4, 2004. ISSN 0031-9007. doi: 10.1103/PhysRevLett.92.046101.

[79] N. M. Martin, M. Van den Bossche, A. Hellman, H. Grönbeck, C. Hakanoglu, J. Gustafson, S. Blomberg, N. Johansson, Z. Liu, S. Axnanda, J. F. Weaver, and E. Lundgren. Intrinsic ligand effect governing the catalytic activity of Pd oxide thin films. *ACS Catalysis*, pages 3330–3334, 2014. ISSN 2155-5435. doi: 10.1021/cs5010163.

[80] A. Hellman, A. Resta, N. M. Martin, J. Gustafson, A. Trinchero, P.-A Carlsson, O. Balmes, R. Felici, R. Van Rijn, J. W. M. Frenken, J. N. Andersen, E. Lundgren, and H. Grönbeck. The active phase of palladium during methane oxidation. *The Journal of Physical Chemistry Letters*, 3 (6):678–682, 2012. ISSN 1948-7185. doi: 10.1021/jz300069s.

[81] N. Seriani, J. Harl, F. Mittendorfer, and G. Kresse. A first-principles study of bulk oxide formation on Pd(100). *The Journal of chemical physics*, 131 (5):054701, 2009. ISSN 1089-7690. doi: 10.1063/1.3187935.

[82] J. Jelic, K. Reuter, and R. Meyer. The role of surface oxides in NO_x storage reduction catalysts. *ChemCatChem*, 2(6):658–660, 2010. ISSN 18673880. doi: 10.1002/cctc.201000006.

[83] C. Popa, T. Zhu, I. Tranca, P. Kaghazchi, T. Jacob, and E. J. M. Hensen. Structure of palladium nanoparticles under oxidative conditions. *Physical chemistry chemical physics : PCCP*, 17(3):2268–2273, 2015. ISSN 1463-9084. doi: 10.1039/c4cp01761g.

[84] A. Antony, A. Asthagiri, and J. F. Weaver. Pathways and kinetics of methane and ethane C-H bond cleavage on PdO(101). *The Journal of chemical physics*, 139(10):104702, 2013. ISSN 1089-7690. doi: 10.1063/1.4819909.

[85] J. F. Weaver, C. Hakanoglu, A. Antony, and A. Asthagiri. Alkane activation on crystalline metal oxide surfaces. *Chemical Society Reviews*, 43(22):7536–7547, 2014. ISSN 0306-0012. doi: 10.1039/c3cs60420a. URL http://pubs.rsc.org/en/content/articlelanding/2014/cs/c3cs60420a#!divAbstract.

[86] N. M. Kinnunen, J. T. Hirvi, M. Suvanto, and T. A. Pakkanen. Role of the interface between Pd and PdO in methane dissociation. *Journal of Physical Chemistry C*, 115(39):19197–19202, 2011. ISSN 1932-7447. doi: 10.1021/jp204360c.

[87] J. F. Weaver, C. Hakanoglu, J. M. Hawkins, and A. Asthagiri. Molecular adsorption of small alkanes on a PdO(101) thin film: Evidence of σ-complex formation. *The Journal of Chemical Physics*, 132(2):024709, 2010. ISSN 00219606. doi: 10.1063/1.3277672.

[88] H. H. Kan, R. J. Colmyer, A. Asthagiri, and J. F. Weaver. Adsorption of water on a PdO(101) thin film: Evidence of an adsorbed HO−H2O complex. *Journal of Physical Chemistry C*, 113(4):1495–1506, 2009. ISSN 1932-7447. doi: 10.1021/jp808008k.

[89] J. Choi, L. Pan, F. Zhang, J. T. Diulus, A. Asthagiri, and J. F. Weaver. Molecular adsorption of NO on PdO(101). *Surface Science*, 640:150–158, 2015. ISSN 00396028. doi: 10.1016/j.susc.2015.01.010.

[90] N. M. Martin, M. Van den Bossche, H. Grönbeck, C. Hakanoglu, F. Zhang, T. Li, J. Gustafson, J. F. Weaver, and E. Lundgren. CO adsorption on clean and oxidized Pd(111). *Journal of Physical Chemistry C*, 118(2): 1118–1128, 2014. ISSN 1932-7447. doi: 10.1021/jp410895c.

[91] R. Van Rijn, O. Balmes, A. Resta, D. Wermeille, R. Westerström, J. Gustafson, R. Felici, E. Lundgren, and J. W. M. Frenken. Surface structure and reactivity of Pd(100) during CO oxidation near ambient pressures. *Physical chemistry chemical physics : PCCP*, 13(29):13167–13171, 2011. ISSN 1463-9084. doi: 10.1039/c1cp20989b.

[92] J. T. Hirvi, T.-J. J. Kinnunen, M. Suvanto, T. A. Pakkanen, and J. K. Nørskov. CO oxidation on PdO surfaces. *The Journal of chemical physics*, 133(8):084704, 2010. ISSN 1089-7690. doi: 10.1063/1.3464481.

[93] A. Boubnov, M. Casapu, A. Gremminger, B. Torkashvand, and M. Merts. Methan katalytisch ii: Abschlussbericht. Technical report, Forschungsvereinigung Verbrennungskraftmaschinen e.V. (FVV), Vorhaben 1177. URL http://www.itcp.kit.edu/abgaszentrum/downloads/Projekte_FVV_IGF_Methan%20katalytisch%202_Abschlussbericht.pdf.

[94] C. Karakaya and O. Deutschmann. A simple method for CO chemisorption studies under continuous flow: Adsorption and desorption behavior of Pt/Al_2O_3 catalysts. *Applied Catalysis A: General*, 445-446:221–230, 2012. ISSN 0926860X. doi: 10.1016/j.apcata.2012.08.022.

[95] H. Yoshida, T. Nakajima, Y. Yazawa, and T. Hattori. Support effect on methane combustion over palladium catalysts. *Applied Catalysis B: Environmental*, 71(1-2):70–79, 2007. ISSN 09263373. doi: 10.1016/j.apcatb.2006.08.010.

[96] X. Fan, F. Wang, T. Zhu, and H. He. Effects of ce on catalytic combustion of methane over $Pd\text{-}Pt/Al_2O_3$ catalyst. *Journal of Environmental Sciences*, 24(3):507–511, 2012. ISSN 10010742. doi: 10.1016/S1001-0742(11)60798-5.

[97] G. Bergeret and P. Gallezot. 3.1 Particle size and dispersion measurements. In Gerhard Ertl, Helmut Knözinger, Ferdi Schüth, and Jens Weitkamp, editors, *Handbook of Heterogeneous Catalysis*, pages 738–765. Wiley-VCH, Weinheim, 2008. ISBN 3527312412.

[98] D. Livio, C. Diehm, A. Donazzi, A. Beretta, and O. Deutschmann. Catalytic partial oxidation of ethanol over Rh/Al_2O_3: Spatially resolved temperature and concentration profiles. *Applied Catalysis A: General*, 467: 530–541, 2013. ISSN 0926860X. doi: 10.1016/j.apcata.2013.07.054.

[99] G. S. Bugosh, V. G. Easterling, I. A. Rusakova, and M. P. Harold. Anomalous steady-state and spatio-temporal features of methane oxidation on $Pt/Pd/Al_2O_3$ monolith spanning lean and rich conditions. *Applied Catalysis B: Environmental*, 165:68–78, 2015. ISSN 09263373. doi: 10.1016/j.apcatb.2014.09.058.

[100] A. Beretta, A. Donazzi, D. Livio, M. Maestri, G. Groppi, E. Tronconi, and P. Forzatti. Optimal design of a CH_4 CPO-reformer with honeycomb catalyst: Combined effect of catalyst load and channel size on the surface temperature profile. *Catalysis Today*, 171(1):79–83, 2011. ISSN 09205861. doi: 10.1016/j.cattod.2011.03.081.

[101] J. Sá, D. L. A. Fernandes, F. Aiouache, A. Goguet, C. Hardacre, D. Lundie, W. Naeem, W. P. Partridge, and C. Stere. SpaciMS: spatial and temporal operando resolution of reactions within catalytic monoliths. *The Analyst*, 135(9):2260–2272, 2010. ISSN 1364-5528. doi: 10.1039/c0an00303d.

[102] R. Horn, K. Williams, N. Degenstein, and L. Schmidt. Syngas by catalytic partial oxidation of methane on rhodium: Mechanistic conclusions from spatially resolved measurements and numerical simulations. *Journal of Catalysis*, 242(1):92–102, 2006. ISSN 0021-9517. doi: 10.1016/j.jcat.2006.05.008.

[103] H. Schwarz, M. Geske, F. C. Goldsmith, R. Schlögl, and R. Horn. Fuel-rich methane oxidation in a high-pressure flow reactor studied by optical-fiber laser-induced fluorescence, multi-species sampling profile measurements and detailed kinetic simulations. *Combustion and Flame*, 161(7):1688–1700, 2014. ISSN 00102180. doi: 10.1016/j.combustflame.2014.01.007.

[104] J. Touitou, K. Morgan, R. Burch, C. Hardacre, and A. Goguet. An in situ spatially resolved method to probe gas phase reactions through a fixed bed catalyst. *Catalysis Science & Technology*, 2(9):1811–1813, 2012. ISSN 2044-4753. doi: 10.1039/c2cy20141k.

[105] S. Hannemann, J.-D. Grunwaldt, B. Kimmerle, A. Baiker, P. Boye, and C. Schroer. Axial changes of catalyst structure and temperature in a fixed-bed microreactor during noble metal catalysed partial oxidation of methane. *Topics in Catalysis*, 52(10):1360–1370, 2009. ISSN 1022-5528. doi: 10.1007/s11244-009-9315-0.

[106] M. Geske, O. Korup, and R. Horn. Resolving kinetics and dynamics of a catalytic reaction inside a fixed bed reactor by combined kinetic and spectroscopic profiling. *Catalysis Science & Technology*, 3(1):169–175, 2013. ISSN 2044-4753. doi: 10.1039/C2CY20489D.

[107] H. Karadeniz, C. Karakaya, S. Tischer, and O. Deutschmann. Mass transfer effects in stagnation flows on a porous catalyst: Water-gas-shift reaction over Rh/Al_2O_3. *Zeitschrift für Physikalische Chemie*, 229(5): 709–737, 2015. ISSN 0942-9352. doi: 10.1515/zpch-2014-0622.

[108] H. Zhu, R. J. Kee, J. R. Engel, and D. T. Wickham. Catalytic partial oxidation of methane using RhSr- and Ni-substituted hexaaluminates. *Proceedings of the Combustion Institute*, 31(2):1965–1972, 2007. ISSN 15407489. doi: 10.1016/j.proci.2006.07.028.

[109] O. Korup, R. Schlögl, and R. Horn. Carbon formation in catalytic partial oxidation of methane on platinum: Model studies on a polycrystalline Pt foil. *Catalysis Today*, 181(1):177–183, 2012. ISSN 0920-5861. doi: 10.1016/j.cattod.2011.04.051.

[110] S. Blomberg, C. Brackmann, J. Gustafson, M. Aldén, E. Lundgren, and J. Zetterberg. Real-time gas-phase imaging over a Pd(110) catalyst during CO oxidation by means of planar laser-induced fluorescence. *ACS Catalysis*, 5(4):2028–2034, 2015. ISSN 2155-5435. doi: 10.1021/cs502048w.

[111] A. Zellner, R. Suntz, and O. Deutschmann. Two-dimensional spatial resolution of concentration profiles in catalytic reactors by planar laser-induced fluorescence: NO reduction over diesel oxidation catalysts. *Angewandte Chemie (International ed. in English)*, 54(9):2653–2655, 2015. ISSN 1521-3773. doi: 10.1002/anie.201410324.

[112] J. Mantzaras. New directions in advanced modeling and in situ measurements near reacting surfaces. *Flow, Turbulence and Combustion*, 90(4): 681–707, 2013. ISSN 1386-6184. doi: 10.1007/s10494-012-9394-z.

[113] S. Eriksson, A. Schneider, J. Mantzaras, M. Wolf, and S. JärÅs. Experimental and numerical investigation of supported rhodium catalysts for partial oxidation of methane in exhaust gas diluted reaction mixtures. *Chemical Engineering Science*, 62(15):3991–4011, 2007. ISSN 0009-2509. doi: 10.1016/j.ces.2007.04.041.

[114] T. Liu, C. Snyder, and G. Veser. Catalytic partial oxidation of methane: Is a distinction between direct and indirect pathways meaningful? *Industrial & Engineering Chemistry Research*, 46(26):9045–9052, 2007. ISSN 0888-5885. doi: 10.1021/ie070062z.

[115] D. Ciuparu, E. Perkins, and L. Pfefferle. In situ DR-FTIR investigation of surface hydroxyls on γ-al2o3 supported pdo catalysts during methane combustion. *Applied Catalysis A: General*, 263(2):145–153, 2004. ISSN 0926860X. doi: 10.1016/j.apcata.2003.12.006.

[116] B. L. Mojet, S. D. Ebbesen, and L. Lefferts. Light at the interface: the potential of attenuated total reflection infrared spectroscopy for understanding heterogeneous catalysis in water. *Chemical Society reviews*, 39 (12):4643–4655, 2010. ISSN 1460-4744. doi: 10.1039/c0cs00014k.

[117] M. Calatayud, S. E. Collins, M. A. Baltanás, and A. L. Bonivardi. Stability of formate species on beta-Ga_2O_3. *Physical Chemistry Chemical Physics*, 11(9):1397–1405, 2009. ISSN 1463-9076. doi: 10.1039/b800519b.

[118] C. Li, Y. Sakata, T. Arai, K. Domen, K. Maruya, and T. Onishi. Adsorption of carbon monoxide and carbon dioxide on cerium oxide studied by fourier-transform infrared spectroscopy. Part 2. - formation of formate species on partially reduced CeO_2 at room temperature. *Journal of the Chemical Society, Faraday Transactions 1: Physical Chemistry in Condensed Phases*, 85(6):1451, 1989. ISSN 0300-9599. doi: 10.1039/f19898501451.

[119] V. Lochař. FT-IR study of methanol, formaldehyde and methyl formate adsorption on the surface of Mo/Sn oxide catalyst. *Applied Catalysis A: General*, 309(1):33–36, 2006. ISSN 0926860X. doi: 10.1016/j.apcata.2006.04.030.

[120] E. Borello, A. Zecchina, and C. Morterra. Infrared study of methanol adsorption on aerosil. I. Chemisorption at room temperature. *Journal of Physical Chemistry*, 71(9):2938–2945, 1967. ISSN 0022-3654. doi: 10.1021/j100868a026.

[121] R. G. Greenler. Infrared study of the adsorption of methanol and ethanol on aluminum oxide. *Journal of Chemical Physics*, 37(9):2094–2100, 1962. ISSN 0021-9606. doi: 10.1063/1.1733430.

[122] C. Martin, I. Martin, and V. Rives. An FT-IR study of the adsorption of pyridine, formic acid and acetic acid on magnesia and molybdena-magnesia. *Journal of Molecular Catalysis*, 73(1):51–63, 1992. ISSN 03045102. doi: 10.1016/0304-5102(92)80061-K.

[123] C. Li, G. Li, and Q. Xin. FT-IR spectroscopic studies of methane adsorption on magnesium oxide. *Journal of Physical Chemistry*, 98(7):1933–1938, 1994. ISSN 0022-3654. doi: 10.1021/j100058a036.

[124] G. Kadinov, Ch. Bonev, S. Todorova, and A. Palazov. IR spectroscopy study of CO adsorption and of the interaction between CO and hydrogen on alumina-supported cobalt. *Journal of the Chemical Society*, 94(19): 3027–3031, 1998. ISSN 0956-5000. doi: 10.1039/a804315i.

[125] A. Bensalem, J.-C. Muller, D. Tessier, and F. Bozon-Verduraz. Spectroscopic study of CO adsorption on palladium-ceria catalysts. *Journal of the Chemical Society*, 92(17):3233–3237, 1996. ISSN 0956-5000. doi: 10.1039/FT9969203233.

[126] E.-M. Köck, M. Kogler, T. Bielz, B. Klötzer, and S. Penner. In situ FT-IR spectroscopic study of CO_2 and co adsorption on Y_2O_3, ZrO_2, and yttria-stabilized ZrO_2. *Journal of Physical Chemistry C*, 117(34):17666–17673, 2013. ISSN 1932-7447. doi: 10.1021/jp405625x.

[127] H.-G. Cho and L. Andrews. Infrared spectra of CH_3-MH through methane activation by laser-ablated Sn, Pb, Sb, and Bi atoms. *The journal of physical chemistry. A*, 116(33):8500–8506, 2012. ISSN 1520-5215. doi: 10.1021/jp305117d.

[128] V. J. F. Lapoutre, B. Redlich, A. F. G. Van der Meer, J. Oomens, J. M. Bakker, A. Sweeney, A. Mookherjee, and P. B. Armentrout. Structures of the dehydrogenation products of methane activation by 5d transition metal cations. *The journal of physical chemistry. A*, 117(20):4115–4126, 2013. ISSN 1520-5215. doi: 10.1021/jp400305k.

[129] P. Aghalayam, Y. K. Park, N. Fernandes, V. Papavassiliou, A. B. Mhadeshwar, and D. G. Vlachos. A c1 mechanism for methane oxidation on platinum. *Journal of Catalysis*, 213(1):23–38, 2003. ISSN 0021-9517. doi: 10.1016/S0021-9517(02)00045-3.

[130] P. Gélin, L. Urfels, M. Primet, and E. Tena. Complete oxidation of methane at low temperature over Pt and Pd catalysts for the abatement of lean-burn natural gas fuelled vehicles emissions: influence of water and sulphur containing compounds. *Catalysis Today*, 83(1-4):45–57, 2003. ISSN 09205861. doi: 10.1016/S0920-5861(03)00215-3.

[131] K. Persson, A. Ersson, A. Manrique Carrera, J. Jayasuriya, R. Fakhrai, T. Fransson, and S. Järås. Supported palladium-platinum catalyst for methane combustion at high pressure. *Catalysis Today*, 100(3-4):479–483, 2005. ISSN 09205861. doi: 10.1016/j.cattod.2004.08.018.

[132] K. Narui, H. Yata, K. Furuta, A. Nishida, Y. Kohtoku, and T. Matsuzaki. Effects of addition of Pt to PdO/Al_2O_3 catalyst on catalytic activity for methane combustion and TEM observations of supported particles. *Applied Catalysis A: General*, 179(1-2):165–173, 1999. ISSN 0926860X. doi: 10.1016/S0926-860X(98)00306-8.

[133] Q. Xu, K. C. Kharas, B. J. Croley, and A. K. Datye. The sintering of supported Pd automotive catalysts. *ChemCatChem*, 3(6):1004–1014, 2011. ISSN 18673880. doi: 10.1002/cctc.201000392.

[134] R. Schlögl. Heterogene Katalysatoren - Fundamental Betrachtet. *Angewandte Chemie*, 127(11):3531–3589, 2015. ISSN 0044-8249. doi: 10.1002/ange.201410738.

[135] Y. Ozawa, Y. Tochihara, A. Watanabe, M. Nagai, and S. Omi. Deactivation of Pt · PdO/Al_2O_3 in catalytic combustion of methane. *Applied Catalysis A: General*, 259(1):1–7, 2004. ISSN 0926860X. doi: 10.1016/j.apcata.2003.09.029.

[136] S. Penner, Wang D., B. Jenewein, H. Gabasch, B. Klötzer, A. Knop-Gericke, R. Schlögl, and K. Hayek. Growth and decomposition of aligned and ordered PdO nanoparticles. *Journal of Chemical Physics*, 125(9):094703, 2006. ISSN 0021-9606. doi: 10.1063/1.2338028.

[137] E. Ruckenstein and J. J. Chen. Wetting phenomena during alternating heating in O_2 and H_2 of supported metal crystallites. *Journal of Colloid and Interface Science*, 86(1):1–11, 1982. ISSN 00219797. doi: 10.1016/0021-9797(82)90034-0.

[138] O. Deutschmann, S. Tischer, S. Kleditzsch, V. M. Janardhanan, C. Correa, D. Chatterjee, N. Mladenov, H. D. Minh, H. Karadeniz, and M. Hettel. Detchem software package, www.detchem.com, 2014. URL www.detchem.com.

[139] Laxminarayan L. R., R. J. Kee, O. Deutschmann, J. Warnatz, and L. D. Schmidt. A critical evaluation of navier-stokes, boundary-layer, and plug-flow models of the flow and chemistry in a catalytic-combustion monolith. *Catalysis Today*, 59(1-2):47–60, 2000. ISSN 09205861. doi: 10.1016/S0920-5861(00)00271-6.

[140] P. Deuflhard, E. Hairer, and J. Zugck. One-step and extrapolation methods for differential-algebraic systems. *Numerische Mathematik*, 51(5):501–516, 1987. ISSN 0029-599X. doi: 10.1007/BF01400352.

[141] S. Chapman and T. G. Cowling. *The mathematical theory of non-uniform gases: An account of the kinetic theory of viscosity, thermal conduction and diffusion in gases*. Cambridge University Press, Cambridge, 3rd ed. edition, 1970. ISBN 9780521408448.

[142] R. K. Sharma, D. L. Cresswell, and E. J. Newson. Effective diffusion coefficients and tortuosity factors for commercial catalysts. *Industrial & Engineering Chemistry Research*, 30(7):1428–1433, 1991. ISSN 0888-5885. doi: 10.1021/ie00055a004.

[143] R. Dittmeyer and G. Emig. 6.3 Simultaneous heat and mass transfer and chemical reaction. In Gerhard Ertl, Helmut Knözinger, Ferdi Schüth, and Jens Weitkamp, editors, *Handbook of Heterogeneous Catalysis*, pages 1727–1784. Wiley-VCH, Weinheim, 2008. ISBN 3527312412.

[144] C. T. Campbell. The degree of rate control: A powerful tool for catalysis research. *ACS Catalysis*, 7(4):2770–2779, 2017. ISSN 2155-5435. doi: 10.1021/acscatal.7b00115.

[145] S. T. Dix, J. K. Scott, R. B. Getman, and C. T. Campbell. Using degrees of rate control to improve selective n-butane oxidation over model MOF-encapsulated catalysts: sterically-constrained $Ag_3Pd(111)$. *Faraday discussions*, 188:21–38, 2016. ISSN 1359-6640. doi: 10.1039/c5fd00198f.

[146] I. A. W. Filot, R. J. P. Broos, J. P. M. Van Rijn, G. J. H. A. van Heugten, R. A. van Santen, and E. J. M. Hensen. First-principles-based microkinetics simulations of synthesis gas conversion on a stepped rhodium surface. *ACS Catalysis*, 5(9):5453–5467, 2015. ISSN 2155-5435. doi: 10.1021/acscatal.5b01391.

[147] H. Meskine, S. Matera, M. Scheffler, K. Reuter, and H. Metiu. Examination of the concept of degree of rate control by first-principles kinetic monte carlo simulations. *Surface Science*, 603(10-12):1724–1730, 2009. ISSN 00396028. doi: 10.1016/j.susc.2008.08.036.

[148] C. Stegelmann, A. Andreasen, and C. T. Campbell. Degree of rate control: how much the energies of intermediates and transition states control rates. *Journal of the American Chemical Society*, 131(23):8077–8082, 2009. ISSN 0002-7863. doi: 10.1021/ja9000097.

[149] C. A. Wolcott, A. J. Medford, F. Studt, and C. T. Campbell. Degree of rate control approach to computational catalyst screening. *Journal of Catalysis*, 330:197–207, 2015. ISSN 00219517. doi: 10.1016/j.jcat.2015.07.015.

[150] I. Chorkendorff and J. W. Niemantsverdriet. *Concepts of Modern Catalysis and Kinetics*. Wiley-VCH, Weinheim, 2003. ISBN 9783527602650. doi: 10.1002/3527602658.

[151] C. R. F. Lund. Microkinetics of water−gas shift over sulfided Mo/Al_2O_3 catalysts. *Industrial & Engineering Chemistry Research*, 35(8):2531–2538, 1996. ISSN 0888-5885. doi: 10.1021/ie950608u.

[152] M. Hettel, C. Diehm, H. Bonart, and O. Deutschmann. Numerical simulation of a structured catalytic methane reformer by DUO: The new computational interface for OpenFOAM® and DETCHEM™. *Catalysis Today*, 258:230–240, 2015. ISSN 09205861. doi: 10.1016/j.cattod.2015.02.011.

[153] M. Hettel, C. Diehm, B. Torkashvand, and O. Deutschmann. Critical evaluation of in situ probe techniques for catalytic honeycomb monoliths. *Catalysis Today*, 216:2–10, 2013. ISSN 09205861. doi: 10.1016/j.cattod.2013.05.005.

[154] A. Goguet, W. P. Partridge, F. Aiouche, C. Hardacre, K. Morgan, C. Stere, and J. Sá. Comment on "the critical evaluation of in situ probe techniques for catalytic honeycomb monoliths" by hettel et al. *Catalysis Today*, 236: 206–208, 2014. ISSN 09205861. doi: 10.1016/j.cattod.2014.02.034.

[155] M. Hettel, C. Diehm, and O. Deutschmann. Answer to the comment from Goguet et al. to the paper "The critical evaluation of in situ probe techniques for catalytic honeycomb monoliths" by Hettel et al. [1]. *Catalysis Today*, 236:209–213, 2014. ISSN 09205861. doi: 10.1016/j.cattod.2014.02.033.

[156] R. D. Cortright and J. A. Dumesic. Kinetics of heterogeneous catalytic reactions: Analysis of reaction schemes. In *Advances in Catalysis*, volume 46, pages 161–264. Academic Press, 2001. doi: 10.1016/S0360-0564(02)46023-3.

[157] V. P. Zhdanov. Arrhenius parameters for rate processes on solid surfaces. *Surface Science Reports*, 12(5):185–242, 1991. ISSN 01675729. doi: 10.1016/0167-5729(91)90011-L.

[158] E. Shustorovich and H. Sellers. The UBI-QEP method: a practical theoretical approach to understanding chemistry on transition metal surfaces. *Surface Science Reports*, 31(1-3):1–119, 1998. ISSN 01675729. doi: 10.1016/S0167-5729(97)00016-2.

[159] K. Delgado, L. Maier, S. Tischer, A. Zellner, H. Stotz, and O. Deutschmann. Surface reaction kinetics of steam- and CO_2-reforming as well as oxidation of methane over nickel-based catalysts. *Catalysts*, 5(2):871–904, 2015. ISSN 2073-4344. doi: 10.3390/catal5020871.

[160] H. Gossler, L. Maier, S. Angeli, S. Tischer, and O. Deutschmann. CaRMeN: A tool for analysing and deriving kinetics in the real world. *Physical chemistry chemical physics : PCCP*, 20(16):10857–10876, 2018. ISSN 1463-9084. doi: 10.1039/c7cp07777g.

[161] E. Shustorovich and A. T. Bell. An analysis of methanol synthesis from CO and CO_2 on Cu and Pd surfaces by the bond-order-conservation-morse-potential approach. *Surface Science*, 253(1-3):386–394, 1991. ISSN 00396028. doi: 10.1016/0039-6028(91)90609-V.

[162] Evgeny Shustorovich. The bond-order conservation approach to chemisorption and heterogeneous catalysis: Applications and implications. *Advances in Catalysis*, 37(37):101–163, 1990. doi: 10.1016/S0360-0564(08)60364-8.

[163] A. V. Zeigarnik and E. Shustorovich. The UBI-QEP method: Mechanistic and kinetic studies of heterogeneous catalytic reactions. *Russian Journal of Physical Chemistry B*, 1(4):330–356, 2007. ISSN 1990-7931. doi: 10.1134/S1990793107040057.

[164] S. Storsæter, D. Chen, and A. Holmen. Microkinetic modelling of the formation of C1 and C2 products in the fischer-tropsch synthesis over cobalt catalysts. *Surface Science*, 600(10):2051–2063, 2006. ISSN 00396028. doi: 10.1016/j.susc.2006.02.048.

[165] E. Shustorovich and A. V. Zeigarnik. The UBI-QEP treatment of polyatomic molecules without bond-energy partitioning. *Surface Science*, 527 (1-3):137–148, 2003. ISSN 00396028. doi: 10.1016/S0039-6028(03)00013-X.

[166] E. M. Shustorovich and A. V. Zeigarnik. The UBI-QEP method: Basic formalism and applications to chemisorption phenomena on transition metal surfaces. chemisorption energetics. *Russian Journal of Physical Chemistry*, 80(1):4–30, 2006. ISSN 0036-0244. doi: 10.1134/S003602440601002X.

[167] M. Valden, J. Pere, M. Hirsimäki, S. Suhonen, and M. Pessa. Activated adsorption of methane on clean and oxygen-modified Pt111 and Pd110. *Surface Science*, 377-379:605–609, 1997. ISSN 00396028. doi: 10.1016/S0039-6028(96)01462-8.

[168] M. Hirsimäki, S. Paavilainen, J.A Nieminen, and M. Valden. Role of translational and vibrational energy in the dissociative chemisorption of methane on Pd110. *Surface Science*, 482-485:171–176, 2001. ISSN 00396028. doi: 10.1016/S0039-6028(01)00818-4.

[169] M. Hirsimäki and M. Valden. Erratum to: "role of translational and vibrational energy in the dissociative chemisorption of methane on Pd110" [Surf. Sci. 482–485 (2001) 171–176]. *Surface Science*, 562(1-3):284, 2004. ISSN 00396028. doi: 10.1016/j.susc.2004.06.104.

[170] S. L. Tait, Z. Dohnálek, C. T. Campbell, and B. D. Kay. Methane adsorption and dissociation and oxygen adsorption and reaction with CO on Pd nanoparticles on MgO(100) and on Pd(111). *Surface Science*, 591 (1-3):90–107, 2005. ISSN 00396028. doi: 10.1016/j.susc.2005.06.024.

[171] A. Trinchero, A. Hellman, and H. Grönbeck. Methane oxidation over Pd and Pt studied by DFT and kinetic modeling. *Surface Science*, 616: 206–213, 2013. ISSN 00396028. doi: 10.1016/j.susc.2013.06.014.

[172] A. N. Salanov and E. A. Suprun. Interaction between oxygen and polycrystalline palladium at O_2 pressures of 10^{-6}-10 pa. *Kinetics and Catalysis*, 50(1):31–39, 2009. ISSN 0023-1584. doi: 10.1134/S0023158409010054.

[173] M. Milun, P. Pervan, and K. Wandelt. Interaction of oxygen with a polycrystalline palladium surface over a wide temperature range. *Surface Science*, 218(2-3):363–388, 1989. ISSN 00396028. doi: 10.1016/0039-6028(89)90158-1.

[174] H. Conrad, G. Ertl, J. Küppers, and E. E. Latta. Interaction of NO and O_2 with Pd(111) surfaces. II. *Surface Science*, 65(1):245–260, 1977. ISSN 00396028. doi: 10.1016/0039-6028(77)90305-3.

[175] A. N. Salanov, A. I. Titkov, and V. N. Bibin. Mechanisms of oxygen adsorption and desorption on polycrystalline palladium. *Kinetics and Catalysis*, 47(3):430–436, 2006. ISSN 0023-1584. doi: 10.1134/S0023158406030153.

[176] J. Szanyi, W. K. Kuhn, and D. W. Goodman. Co adsorption on Pd(111) and Pd(100): low and high pressure correlations. *Journal of Vacuum Science & Technology A: Vacuum, Surfaces, and Films*, 11(4, Pt. 2): 1969–1974, 1993. ISSN 0734-2101. doi: 10.1116/1.578532.

[177] H. Conrad, G. Ertl, J. Koch, and E. E. Latta. Adsorption of CO on Pd single crystal surfaces. *Surface Science*, 43(2):462–480, 1974. ISSN 00396028. doi: 10.1016/0039-6028(74)90270-2.

[178] R. J. Behm, K. Christmann, G. Ertl, and Van Hove, M. A. Adsorption of CO on Pd(100). *The Journal of Chemical Physics*, 73(6):2984–2995, 1980. ISSN 00219606. doi: 10.1063/1.440430.

[179] J. C. Tracy. Structural influences on adsorbate binding energy. I. Carbon monoxide on (100) palladium. *The Journal of Chemical Physics*, 51(11): 4852–4862, 1969. ISSN 00219606. doi: 10.1063/1.1671876.

[180] Y. Y. Yeo, L. Vattuone, and D. A. King. Calorimetric investigation of NO and CO adsorption on Pd100 and the influence of preadsorbed carbon. *The Journal of Chemical Physics*, 106(5):1990–1996, 1997. ISSN 00219606. doi: 10.1063/1.473306.

[181] T. Engel. A molecular beam investigation of He, CO, and O_2 scattering from Pd(111). *The Journal of Chemical Physics*, 69(1):373–385, 1978. ISSN 00219606. doi: 10.1063/1.436363.

[182] E. H. Voogt, L. Coulier, O. L. J. Gijzeman, and J. W. Geus. Adsorption of carbon monoxide on Pd(111) and palladium model catalysts. *Journal of Catalysis*, 169(1):359–364, 1997. ISSN 0021-9517. doi: 10.1006/jcat.1997.1708.

[183] X. Guo and John T. Yates. Dependence of effective desorption kinetic parameters on surface coverage and adsorption temperature: CO on Pd(111). *The Journal of Chemical Physics*, 90(11):6761–6766, 1989. ISSN 00219606. doi: 10.1063/1.456294.

[184] M. Bowker, P. Stone, R. Bennett, and N. Perkins. CO adsorption on a Pd/TiO_2 model catalyst. *Surface Science*, 497(1-3):155–165, 2002. ISSN 00396028. doi: 10.1016/S0039-6028(01)01640-5.

[185] H. Dropsch and M. Baerns. CO adsorption on supported Pd catalysts studied by adsorption microcalorimetry and temperature programmed desorption. *Applied Catalysis A: General*, 158(1-2):163–183, 1997. ISSN 0926860X. doi: 10.1016/S0926-860X(96)00418-8.

[186] S.-C. Huang, C.-H. Lin, and J.-H. Wang. Trends of water gas shift reaction on close-packed transition metal surfaces. *Journal of Physical Chemistry C*, 114(21):9826–9834, 2010. ISSN 1932-7447. doi: 10.1021/jp1005814.

[187] K. Christmann. Introduction to surface physical chemistry. In H. Baumgärtel, E. U. Franck, and W. Grünbein, editors, *Topics in Physical Chemistry*, Topics in physical chemistry. Steinkopff Verlag and Springer-Verlag, Darmstadt and New York, 1991. ISBN 3662080095.

[188] R. J. Behm, K. Christmann, and G. Ertl. Adsorption of hydrogen on Pd(100). *Surface Science*, 99(2):320–340, 1980. ISSN 00396028. doi: 10.1016/0039-6028(80)90396-9.

[189] M. G. Cattania, V. Penka, R. J. Behm, K. Christmann, and G. Ertl. Interaction of hydrogen with a palladium (110) surface. *Surface Science*, 126 (1-3):382–391, 1983. ISSN 00396028. doi: 10.1016/0039-6028(83)90732-X.

[190] G. E. Gdowski, T. E. Felter, and R. H. Stulen. Effect of surface temperature on the sorption of hydrogen by Pd(111). *Surface Science*, 181(3):L147–L155, 1987. ISSN 00396028. doi: 10.1016/0039-6028(87)90187-7.

[191] H. Conrad, G. Ertl, and E. E. Latta. Adsorption of hydrogen on palladium single crystal surfaces. *Surface Science*, 41(2):435–446, 1974. ISSN 00396028. doi: 10.1016/0039-6028(74)90060-0.

[192] A. Aldag and L. D. Schmidt. Interaction of hydrogen with palladium. *Journal of Catalysis*, 22(2):260–265, 1971. ISSN 0021-9517. doi: 10.1016/0021-9517(71)90193-X.

[193] J. Greeley and M. Mavrikakis. Surface and subsurface hydrogen: adsorption properties on transition metals and near-surface alloys. *Journal of Physical Chemistry B*, 109(8):3460–3471, 2005. ISSN 1520-6106. doi: 10.1021/jp046540q.

[194] H. Conrad. *Wechselwirkung von Gasen mit einer Pd(111)-Oberfläche*. PhD thesis, Universität München, 1976. URL https://opacplus.bib-bvb.de/TouchPoint_touchpoint/start.do?Query=205%3D%22BV002142321%22&Language=De&SearchProfile=.

[195] E. M. Stuve, S. W. Jorgensen, and R. J. Madix. The adsorption of H_2O on clean and oxygen-covered pd(100): Formation and reaction of OH groups. *Surface Science*, 146(1):179–198, 1984. ISSN 00396028. doi: 10.1016/0039-6028(84)90236-X.

[196] J. P. Clay, J. P. Greeley, F. H. Ribeiro, N. W. Delgass, and W. F. Schneider. DFT comparison of intrinsic WGS kinetics over Pd and Pt. *Journal of Catalysis*, 320:106–117, 2014. ISSN 0021-9517. doi: 10.1016/j.jcat.2014.09.026.

[197] P. A. Thiel and T. E. Madey. The interaction of water with solid surfaces: Fundamental aspects. *Surface Science Reports*, 7(6-8):211–385, 1987. ISSN 01675729. doi: 10.1016/0167-5729(87)90001-X.

[198] J. M. Heras, G. Estiú, and L. Viscido. The interaction of water with clean palladium films: A thermal desorption and work function study. *Applied Surface Science*, 108(4):455–464, 1997. ISSN 01694332. doi: 10.1016/S0169-4332(96)00686-1.

[199] A. Hodgson and S. Haq. Water adsorption and the wetting of metal surfaces. *Surface Science Reports*, 64(9):381–451, 2009. ISSN 01675729. doi: 10.1016/j.surfrep.2009.07.001.

[200] A. A. Phatak, W. N. Delgass, F. H. Ribeiro, and W. F. Schneider. Density functional theory comparison of water dissociation steps on Cu, Au, Ni, Pd, and Pt. *Journal of Physical Chemistry C*, 113(17):7269–7276, 2009. ISSN 1932-7447. doi: 10.1021/jp810216b.

[201] C. A. Müller, M. Maciejewski, R. A. Koeppel, R. Tschan, and A. Baiker. Role of lattice oxygen in the combustion of methane over PdO/ZrO_2: Combined pulse TG/DTA and MS study with ^{18}O-labeled catalyst. *Journal of Physical Chemistry*, 100(51):20006–20014, 1996. ISSN 0022-3654. doi: 10.1021/jp961903a.

[202] J. Cortés, E. Valencia, and P. Araya. Two-site mechanism for the oxidation reaction of methane on oxidized palladium. *Journal of Physical Chemistry C*, 114(26):11441–11447, 2010. ISSN 1932-7447. doi: 10.1021/jp909575z.

[203] C.-R. Florén, M. Van den Bossche, D. Creaser, H. Grönbeck, P.-A. Carlsson, H. Korpi, and M. Skoglundh. Modelling complete methane oxidation over palladium oxide in a porous catalyst using first-principles surface kinetics. *Catalysis Science & Technology*, 259:147, 2018. ISSN 2044-4753. doi: 10.1039/C7CY02135F.

[204] H. Lieske and J. Voelter. Palladium redispersion by spreading of palladium(II) oxide in oxygen treated palladium/alumina. *Journal of Physical Chemistry*, 89(10):1841–1842, 1985. ISSN 0022-3654. doi: 10.1021/j100256a001.

[205] M. A. Newton, C. Belver-Coldeira, A. Martínez-Arias, and M. Fernández-García. Dynamic in situ observation of rapid size and shape change of supported Pd nanoparticles during CO/NO cycling. *Nature Materials*, 6 (7):528–532, 2007. ISSN 1476-1122. doi: 10.1038/nmat1924.

[206] K. Nomura, K. Noro, Y. Nakamura, Y. Yazawa, H. Yoshida, A. Satsuma, and T. Hattori. Pd-pt bimetallic catalyst supported on SAPO-5 for catalytic combustion of diluted methane in the presence of water vapor. *Catalysis Letters*, 53(3/4):167–169, 1998. ISSN 1011-372X. doi: 10.1023/A:1019082611978.

[207] J. Chen and E. Ruckenstein. Sintering of palladium on alumina model catalyst in a hydrogen atmosphere. *Journal of Catalysis*, 69(2):254–273, 1981. ISSN 0021-9517. doi: 10.1016/0021-9517(81)90163-9.

[208] J. Nilsson, P.-A. Carlsson, S. Fouladvand, N. M. Martin, J. Gustafson, M. A. Newton, E. Lundgren, H. Grönbeck, and M. Skoglundh. Chemistry of supported palladium nanoparticles during methane oxidation. *ACS Catalysis*, 5(4):2481–2489, 2015. ISSN 2155-5435. doi: 10.1021/cs502036d.

[209] I. Czekaj, K. A. Kacprzak, and J. Mantzaras. Methane catalytic combustion on $Pd_9/\gamma - Al_2O_3$ with different degrees of Pd oxidation. *CHIMIA International Journal for Chemistry*, 67(4):271–274, 2013. ISSN 00094293. doi: 10.2533/chimia.2013.271.

[210] B. Torkashvand, P. Lott, D. Zengel, L. Maier, M. Hettel, J.-D. Grunwaldt, and O. Deutschmann. Homogeneous oxidation of light alkanes in the exhaust of turbocharged lean-burn gas engines. *Chemical Engineering Journal*, 2018. ISSN 13858947. doi: 10.1016/j.cej.2018.08.186.

[211] D. B. Rogers, R. D. Shannon, and J. L. Gillson. Crystal growth and semiconductivity of palladium oxide. *Journal of Solid State Chemistry*, 3 (2):314–316, 1971. ISSN 00224596. doi: 10.1016/0022-4596(71)90045-4.

[212] I. Czekaj, K. A. Kacprzak, and J. Mantzaras. CH_4 combustion cycles at Pd/Al_2O_3 - important role of support and oxygen access. *Physical Chemistry Chemical Physics*, 15(27):11368, 2013. ISSN 1463-9076. doi: 10.1039/c3cp51085a.

[213] C. V. Ovesen, B. S. Clausen, J. Schiotz, P. Stoltze, H. Topsoe, and J. K. Norskov. Kinetic implications of dynamical changes in catalyst morphology during methanol synthesis over Cu/ZnO catalysts. *Journal of Catalysis*, 168(2):133–142, 1997. ISSN 0021-9517. doi: 10.1006/jcat.1997.1629.

[214] J. Han, G. Zhu, D. Y. Zemlyanov, and F. H. Ribeiro. Increase of Pd surface area by treatment in dioxygen. *Journal of Catalysis*, 225(1):7–15, 2004. ISSN 0021-9517. doi: 10.1016/j.jcat.2004.03.035.

[215] M. Maestri. Microkinetic analysis of complex chemical processes at surfaces. In Bruno Pignataro, editor, *New Strategies in Chemical Synthesis and Catalysis*, pages 219–245. Wiley-VCH, Weinheim, 2012. ISBN 9783527645824. doi: 10.1002/9783527645824.ch10.

[216] P. Salomonsson, S. Johansson, and B. Kasemo. Methane oxidation over PdO_x: on the mechanism for the hysteresis in activity and oxygen content. *Catalysis Letters*, 33(1,2):1–13, 1995. ISSN 1011-372X. doi: 10.1007/BF00817041.

[217] J. S. Warner. The free energy of formation of palladium oxide. *Journal of The Electrochemical Society*, 114(1):68–71, 1967. ISSN 00134651. doi: 10.1149/1.2426509.

[218] C. Seidel, A. Jörke, B. Vollbrecht, A. Seidel-Morgenstern, and A. Kienle. Kinetic modeling of methanol synthesis from renewable resources. *Chemical Engineering Science*, 175:130–138, 2018. ISSN 00092509. doi: 10.1016/j.ces.2017.09.043.

[219] A. L. Tarasov and L. M. Kustov. Partial methane oxidation into synthesis gas over catalysts supported on meshed metallic materials. *Catalysis in Industry*, 5(1):14–20, 2013. ISSN 2070-0504. doi: 10.1134/S2070050413010091.

[220] A. Baylet, P. Marecot, D. Duprez, P. Castellazzi, G. Groppi, and P. Forzatti. In situ raman and in situ XRD analysis of PdO reduction and Pd° oxidation supported on γ-Al_2O_3 catalyst under different atmospheres. *Physical Chemistry Chemical Physics*, 13(10):4607–4613, 2011. ISSN 1463-9076. doi: 10.1039/c0cp01331e.

[221] N. Van Vegten, M. Maciejewski, F. Krumeich, and A. Baiker. Structural properties, redox behaviour and methane combustion activity of differently supported flame-made Pd catalysts. *Applied Catalysis B: Environmental*, 93(1-2):38–49, 2009. ISSN 09263373. doi: 10.1016/j.apcatb.2009.09.010.

[222] J. R. McBride, S. Gordon, and Reno M. A. Coefficients for calculating thermodynamic and transport properties of individual species: NASA technical memorandum 4513, 1993. URL https://ntrs.nasa.gov/archive/nasa/casi.ntrs.nasa.gov/19940013151.pdf.

[223] M. Baerns. *Technische Chemie*. Wiley-VCH, Weinheim, 2. edition, 2013. ISBN 3527330720.

[224] G. B. Marin and G. S. Yablonsky. *Kinetics of chemical reactions: Decoding complexity*. Wiley-VCH, Weinheim, Germany, 2011. ISBN 3527317635.

[225] A. Jess and P. Wasserscheid. *Chemical technology: An integral textbook*. CourseSmart. Wiley, Weinheim, 2013. ISBN 3527670610.

[226] P. Linstrom. NIST chemistry webbook, NIST standard reference database 69. URL https://webbook.nist.gov/chemistry/.

[227] R. Sanderson. *Polar Covalence*. Elsevier Science, Oxford, 1983. ISBN 9780126180800.

[228] R. Sanderson. *Chemical Bonds and Bonds Energy*. Elsevier Science, Saint Louis, 2nd ed. edition, 2014. ISBN 0323161952.

[229] W. Reusch. Virtual textbook of organic chemistry: Average bond dissociation energies. URL https://www2.chemistry.msu.edu/faculty/reusch/virttxtjml/react2.htm#rx6.

[230] L. A. Schulz, L. C.S. Kahle, K. H. Delgado, S. A. Schunk, A. Jentys, O. Deutschmann, and J. A. Lercher. On the coke deposition in dry reforming of methane at elevated pressures. *Applied Catalysis A: General*, 504:599–607, 2015. ISSN 0926860X. doi: 10.1016/j.apcata.2015.03.002.

Nomenclature

Latin letters

upper case

Symbol	Description	Unit
$\tilde{A}_k$	temperature dependent frequency factor of step k	s^{-1}
A_{cat}	catalytic active surface area	m^2
$A_{ch,square}$	open cross-sectional area of square channel	m^2
$A_{f,k}$	pre-exponential factor in forward direction of step k at $T_{ref} = 1\,K$	mol,cm,s
A_{geo}	geometric surface area	m^2
$A_{geo,ch}$	geometric surface area of a single monolith channel	mm^2
A_k	pre-exponential factor of reaction step k at reference temperature $T_{ref} = 1\,K$	mol,cm,s
$A_k(T)$	pre-exponential factor of reaction step k at temperature T	mol,cm,s
A_k^0	undisturbed pre-exponential factor of step k	mol,cm,s
A_k^{ads}	pre-exponential factor for an adsorption reaction step k	mol,cm,s
$A_{p,PdO}^s$	surface area of a single small/disrupted PdO particle	m^2
A_{Pd}	catalytic surface area of Pd	mm^2
A_{Pd}^l	catalytic surface area of undisrupted/large reduced Pd particles	mm^2
A_{PdO}	catalytic surface area of PdO	mm^2
A_{PdO}^l	catalytic surface area of undisrupted PdO	mm^2
A_{PdO}^s	catalytic surface area of collective of all small/disrupted PdO particles	mm^2
$A_{r,k}$	pre-exponential factor in reverse direction of step k at $T_{ref} = 1\,K$	mol,cm,s

$\tilde{A}_k$	perturbed pre-exponential factor in step k obtained by a 10% increase of the undisturbed value	mol,cm,s
$A_{k,\mathrm{ads}}^{\mathrm{ref}}$	pre-exponential frequency factor for an adsorption step k at a given reference state temperature and pressure	$(\mathrm{Pa\,s})^{-1}$
A_k^{ref}	pre-exponential frequency factor for surface reaction step k at a given reference state temperature and pressure	s^{-1}
D	diameter, diameter of catalyst (monolith sample)	mm
D	diffusivity	$\frac{\mathrm{m}^2}{\mathrm{s}}$
D_{AB}	total bond dissociation energy in gas-phase of molecule AB	$\frac{\mathrm{J}}{\mathrm{mol}}$
$D_{\mathrm{A\text{-}B}}$	gas-phase bond dissociation energy between partitioning groups A and B	$\frac{\mathrm{J}}{\mathrm{mol}}$
$D_{\mathrm{eff},j}$	effective diffusivity of species i in the washcoat	$\frac{\mathrm{m}^2}{\mathrm{s}}$
$D_{i,\mathrm{M}}$	mixture averaged diffusion coefficient of species i in mixture M	$\frac{\mathrm{m}^2}{\mathrm{s}}$
D_i^{eff}	effective diffusivity of species i in the washcoat	$\frac{\mathrm{m}^2}{\mathrm{s}}$
D_{Pd}	dispersion of Pd phase	-
D_{PdO}	dispersion of PdO phase	-
$D_{\mathrm{PdO}}^{\mathrm{l}}$	dispersion of non-disrupted PdO phase	-
E	Morse potential binary interaction energy	$\frac{\mathrm{J}}{\mathrm{mol}}$
$E_k^{\ddagger}$	binding energy of transition state intermediate in step k	$\frac{\mathrm{J}}{\mathrm{mol}}$
$E_{\mathrm{a},k}$	activation energy barrier in step k	$\frac{\mathrm{J}}{\mathrm{mol}}$
$E_{\mathrm{a},k}^{\prime 0}$	activation energy barrier of forward direction in step k at zero coverage limit	$\frac{\mathrm{J}}{\mathrm{mol}}$
$E_{\mathrm{af},k}$	activation energy barrier in forward direction of step k	$\frac{\mathrm{J}}{\mathrm{mol}}$
E_{app}	apparent activation energy	$\frac{\mathrm{J}}{\mathrm{mol}}$
$E_{\mathrm{ar},k}$	activation energy barrier in reverse direction of step k	$\frac{\mathrm{J}}{\mathrm{mol}}$
E_i	two center i binding energy	$\frac{\mathrm{J}}{\mathrm{mol}}$, eV
E_{int}	Lennard-Jones interaction energy of the transition state intermediate in the corresponding reaction step	$\frac{\mathrm{J}}{\mathrm{mol}}$
$E_k^{\ddagger}$	energy of the transition state intermediate in step k	$\frac{\mathrm{J}}{\mathrm{mol}}$
$\tilde{E}_{\mathrm{f},k}$	coverage dependent activation energy barrier in forward direction of step k	$\frac{\mathrm{J}}{\mathrm{mol}}$

$\tilde{E}_{\mathrm{r},k}$	coverage dependent activation energy barrier in reverse direction of step k	$\frac{\mathrm{J}}{\mathrm{mol}}$
$F_{\mathrm{cat/geo}}$	catalytic to geometric surface area ratio	-
$\tilde{F}_{\mathrm{cat/geo}}$	site-pair corrected catalytic-to-geometric surface area ratio	-
G_i	molar Gibbs free energy of species i	$\frac{\mathrm{J}}{\mathrm{mol}}$
G_i^{ref}	molar Gibbs free energy of species i at references state temperature $T_{\mathrm{ref}} = 298\,\mathrm{K}$	$\frac{\mathrm{J}}{\mathrm{mol}}$
$G_k^{\ddagger}$	Gibbs free energy of the transition state intermediate of step k	$\frac{\mathrm{J}}{\mathrm{mol}}$
H_i	molar enthalpy of species i	$\frac{\mathrm{J}}{\mathrm{mol}}$
H_i^{ref}	molar enthalpy of species i at references state temperature $T_{\mathrm{ref}} = 298\,\mathrm{K}$	$\frac{\mathrm{J}}{\mathrm{mol}}$
H_j	molar specific enthalpy of species j	$\frac{\mathrm{J}}{\mathrm{mol}}$
H_j^0	molar specific enthalpy of species j at zero coverage limit	$\frac{\mathrm{J}}{\mathrm{mol}}$
H_k^{P}	total enthalpy of the product state intermediates P in step k	$\frac{\mathrm{J}}{\mathrm{mol}}$
H_k^{R}	total enthalpy of the reactant state intermediates R in step k	$\frac{\mathrm{J}}{\mathrm{mol}}$
I_0	diffuse reflectance intensity of non-absorbing reference (KBr)	-
I_{r}	diffuse reflectance intensity of sample	-
$J_{i,\mathrm{r}}$	diffusive mass flux of species i in radial direction towards wall	$\frac{\mathrm{kg}_i}{\mathrm{m}^2\,\mathrm{s}}$
$K_{\mathrm{c},k}$	concentration based equilibrium constant of reaction step k	$\mathrm{mol}, \mathrm{cm}$
K_{g}	total number of gas-phase species	-
K_k	activity (pressure) based equilibrium constant	-
K_s	total number of surface reactions	-
L	length of catalyst (monolith sample)	mm
L_{ctz}	length of coated zone	mm
L_{foil}	length of foil	mm
L_{Pd}	catalyst loading of Pd based on monolithic sample volume	$\frac{\mathrm{g}}{\mathrm{L}}$, $\frac{\mathrm{g}}{\mathrm{ft}^3}$
L_{wc}	washcoat thickness	μm

M^{bar}	mean molecular weight of the gas-mixture	$\frac{\mathrm{g}}{\mathrm{mol}}$
M_i	molecular weight of species i	$\frac{\mathrm{g}}{\mathrm{mol}}$
M_{Pd}	molecular weight of Pd	$\frac{\mathrm{g}}{\mathrm{mol}}$
N_a	Avogadro constant	mol^{-1}
N_{ch}	number of channels	-
N_{g}	total number of gas-phase species	-
N_{O}^{0}	total number of moles of oxygen for complete stoichiometric oxidation of Pd as present onto the Al_2O_3 support initially	mol
$N_{\mathrm{O}}^{\mathrm{surf,PdO}}$	amount of oxygen in the surface of the oxidized palladium catalyst phase	mol
N_{Pd}^{0}	total number of moles of Pd introduced onto the Al_2O_3 support initially	mol
$N_{\mathrm{Pd}}^{\mathrm{surf,Pd}}$	amount of palladium in the surface of the reduced palladium catalyst phase	mol
$N_{\mathrm{Pd}}^{\mathrm{surf,PdO}}$	amount of palladium in the surface of the oxidized palladium catalyst phase	mol
N_{s}	total number of surface species	-
$\dot{N}$	molar flow rate	$\frac{\mathrm{mol}}{\mathrm{s}}$
$P_{(*-\mathrm{y})}$	uncorrelated pair-probability of finding species y on a O_{cus} site paired to any other species $*$ sitting next to y on a Pd_{cus} site	-
$P_{(\mathrm{x}-*)}$	uncorrelated pair-probability of finding species x on a Pd_{cus} site paired to any other species $*$ sitting next to x on a O_{cus} site	-
$P_{(\mathrm{x\|y})}$	joint pair-probability of finding species x sitting on a Pd_{cus} site unpaired to species y sitting next to x on a O_{cus} site	-
$P_{(\mathrm{x\text{-}y})}$	joint pair-probability of finding species x sitting on a Pd_{cus} site paired to species y sitting next to x on a O_{cus} site	-
$P_{*-\mathrm{y}}$	pair-probability of finding species y sitting on site (b) next to any other species $(*)$ on site (a)	-
$P_{\mathrm{a\text{-}b}}$	joint pair-probability of finding an empty Pd_{cus} site (a) next to an empty O_{cus} site (b)	-
$P_{i,k}^{-}$	fractional path preference of species i consumed via reaction step k (<0)	-

$P^{+}_{i,k}$	fractional path preference of species i produced via reaction step k (>0)	-
$P_{\mathrm{x}-*}$	pair-probability of finding species x sitting on site (a) next to any other species (*) on site (b)	-
$P_{\mathrm{x\text{-}y}}$	joint probability of finding species x sitting next to species y	-
Q	total bond energy	$\frac{\mathrm{J}}{\mathrm{mol}}$
Q_0	two-center equilibrium bond energy	$\frac{\mathrm{J}}{\mathrm{mol}}$
$Q_{0,\mathrm{A}}$	maximum two-center surface metal atom M-add atom A bond energy at $n = 1$ coordination	$\frac{\mathrm{J}}{\mathrm{mol}}$
$Q_{\mathrm{A(n)}}$	heat of chemisorption of element A adsorbed on surface in coordination with n atom metal cluster	$\frac{\mathrm{J}}{\mathrm{mol}}$
Q_{AB}	heat of chemisorption species AB (total adsorption bond dissociation energy of AB)	$\frac{\mathrm{J}}{\mathrm{mol}}$
Q_i	two-center bond dissociation energy	$\frac{\mathrm{J}}{\mathrm{mol}}$
Q_k	concentration based reaction quotient of reaction step k	mol,cm
$Q^{\ddagger}_k$	partition function of transition state intermediate in step k	-
Q^{0}_k	reference concentration based reaction quotient of step k	mol,cm
$Q_{\mathrm{R/P}}$	total partition function of the reactant or product state in step k	-
R	universal gas constant	$\frac{\mathrm{J}}{\mathrm{mol\,K}}$
R	absolute reflectance	-
R	radius of channel	μm
$\tilde{R}_{\mathrm{CH_4}}$	rate of reaction	$\frac{\mathrm{mol_{CH_4}}}{\mathrm{g_{Pd,surf}\,s}}$
R_{o}	overall reaction	-
$R_{\mathrm{o}k}$	overall (global) reaction step k	-
S	elemental based selectivity	-
S^{cap}	sector cap surface area	m^2
$S_{\mathrm{a},k}$	activation entropy of reaction step k	$\frac{\mathrm{J}}{\mathrm{mol\,K}}$
$S_{\mathrm{af},k}$	activation entropy of forward direction in step k	$\frac{\mathrm{J}}{\mathrm{mol\,K}}$
$S_{\mathrm{ar},k}$	activation entropy of reverse direction in step k	$\frac{\mathrm{J}}{\mathrm{mol\,K}}$
S_{BET}	total porous surface area according Brunnauer Emmet and Teller method	$\frac{\mathrm{m}^2}{\mathrm{g}}$

S_i	molar entropy of species i	$\frac{\mathrm{J}}{\mathrm{mol\,K}}$
$S_{i,k}$	non-normalized integral sensitivity coefficient of species i with respect to step k	-
$S^0_{i,k}$	normalized integral sensitivity coefficient of species i with respect to step k	-
S_i^{ref}	molar entropy of species i at references state temperature $T_{\mathrm{ref}} = 298\,\mathrm{K}$	$\frac{\mathrm{J}}{\mathrm{mol\,K}}$
$S_{\mathrm{PdO}}^{\mathrm{cap}}$	sector cap surface area for PdO phase	m^2
$\dot{S}_i$	rate of production/consumption of species i	$\frac{\mathrm{mol}_i}{\mathrm{cm}^3\,\mathrm{s}}$
$\dot{S}_i$	rate of production/consumption of species i	$\frac{\mathrm{mol}_i}{\mathrm{cm}^2\,\mathrm{s}}$
$\dot{S}_{i,k}$	rate of production/consumption of species i in step k	$\frac{\mathrm{mol}_i}{\mathrm{cm}^2\,\mathrm{s}}$
$\dot{S}^-_{i,k}$	rate of consumption of species i in step k (<0)	$\frac{\mathrm{mol}_i}{\mathrm{cm}^2\,\mathrm{s}}$
$\dot{S}^+_{i,k}$	rate of production of species i in step k (>0)	$\frac{\mathrm{mol}_i}{\mathrm{cm}^2\,\mathrm{s}}$
$\dot{S}^-_i$	net rate of consumption of species i (<0)	$\frac{\mathrm{mol}_i}{\mathrm{cm}^2\,\mathrm{s}}$
$\dot{S}^+_i$	net rate of production of species i (>0)	$\frac{\mathrm{mol}_i}{\mathrm{cm}^2\,\mathrm{s}}$
$\dot{S}_i^{\mathrm{eff}}$	pore transport corrected molar rate of production/consumption of species i	$\frac{\mathrm{mol}_i}{\mathrm{cm}^2\,\mathrm{s}}$
$\dot{S}_j^{\mathrm{eff}}$	transport corrected, site-pair surface area specific, molar rate of production/consumption of species j	$\frac{\mathrm{mol}_j}{\mathrm{cm}^2_{\text{(a-b)}}\,\mathrm{s}}$
$\dot{\tilde{S}}_i$	site-pair surface area specific molar rate of production/consumption of species i	$\frac{\mathrm{mol}_i}{\mathrm{cm}^2_{\text{(a-b)}}\,\mathrm{s}}$
T	temperature	K
T_0	standard state temperature	K
T_{50}	light-off temperature at 50 % conversion	K
$T_{\mathrm{ad}}^{\mathrm{out}}$	temperature at outlet resulting from adiabatic temperature rise of reaction	K
$T_{\mathrm{exp}}^{\mathrm{out}}$	measured temperature at outlet	K
$T_{\mathrm{exp}}^{\mathrm{in}}$	measured temperature at inlet	K
T_{g}	gas-phase temperature	K
T_{in}	channel inlet temperature	K
T_{ref}	reference state temperature	K
V^{sec}	sector volume	m^3
V_{b}	mass specific bulk volume of sample	$\frac{\mathrm{mL}}{\mathrm{g}}$
V_{cat}	volume of monolith catalyst	mm^3
V_{ch}	volume of a single channel	mm^3

V_{mix}	aggregated Pd/PdO spherical particle volume with conical sectoral arrangement of the single phases	m^3
V_{p}	mass specific total pore volume of sample	$\frac{\mathrm{mL}}{\mathrm{g}}$
$V_{\mathrm{p,m}}$	mass specific mesopore volume of sample	$\frac{\mathrm{mL}}{\mathrm{g}}$
$V_{\mathrm{p,M}}$	mass specific macropore volume of sample	$\frac{\mathrm{mL}}{\mathrm{g}}$
$V_{\mathrm{Pd}}^{\mathrm{sec}}$	cocnical sectoral volume of Pd phase	m^3
$V_{\mathrm{PdO}}^{\mathrm{l}}$	spherical volume of a single large/undisrupted PdO particle	nm^3
$V_{\mathrm{PdO}}^{\mathrm{s}}$	spherical volume of a single small/disrupted PdO particle	nm^3
$V_{\mathrm{PdO}}^{\mathrm{sec}}$	conical sectoral volume of PdO phase	m^3
$V_{\mathrm{PdO}}^{\mathrm{tot}}$	total volume of PdO phase	m^3
V_{s}	mass specific scelectal volume of sample	$\frac{\mathrm{mL}}{\mathrm{g}}$
$\dot{V}$	volumetric flow rate	$\frac{\mathrm{m}^3}{\mathrm{s}}$
$\dot{V}_0$	standard state volumetric flow rate	$\frac{\mathrm{m}^3}{\mathrm{s}}$
$\dot{V}_{\mathrm{N}}$	volumetric flow rate at normal conditions (1013.25 mbar and 273.15 K)	$\frac{\mathrm{Ncm}^3}{\mathrm{min}}$
X	total bond order	-
X_i	mole fraction of species i	-
$X_{i,k}^{\mathrm{RC}}$	degree of rate control for the transition state in step k with respect to species i	-
X_{jR}	conversion of reactant species jR	-
X_{ox}	catalyst particle state of oxidation; defined as actual amount of moles PdO divided by amount of moles PdO upon complete stoichiometric oxidation of Pd ($X_{\mathrm{ox}} = 0$ all Pd reduced; $X_{\mathrm{ox}} = 1$ all Pd oxidized)	$\frac{\mathrm{mol}_{(\mathrm{PdO})}}{\mathrm{mol}_{(\mathrm{PdO}),\mathrm{stoic}}}$
$X_{\mathrm{ox}}^{\mathrm{max}}$	maximum degree of oxidation	-
X_{PdO}	degree of oxidation	-
Y	mass fraction	-
$Y_{j_{\mathrm{P}}}^{k,\{j_{\mathrm{R}}\}}$	element k based yield of reactants $\{j_{\mathrm{R}}\}$ into product species j_{P}	-
Y_i	mass fraction of species i	$\frac{\mathrm{kg}_i}{\mathrm{kg}}$
Z	reversibility	-
Z_k	reversibility of reaction step k	-
Z_{SR}	reversibility of steam reforming reaction	-

lower case

Symbol	Description	Unit
a	open width of square channel	μm
a	lattice constant parameter in [100] direction	Å
a_{m}	average unit surface area per surface atom	$\frac{\text{Å}^2}{\text{atom}}$
$a_{\mathrm{m,Pd}}$	average unit surface area per surface atom of the Pd(111) facet	$\frac{\text{Å}^2}{\text{atom}}$
$a_{\mathrm{m,PdO}}$	average unit surface area per surface atom of the PdO(101) facet	$\frac{\text{Å}^2}{\text{atom}}$
b	lattice constant parameter in [010] direction	Å
c	lattice constant parameter in [001] direction	Å
c_i	concentration of species i	$\frac{\text{mol}}{\text{cm}^2}$, $\frac{\text{mol}}{\text{cm}^3}$
$c_{i(a)}$	single-site surface concentration for species i based on surface area of type (a) sites	$\frac{\text{mol}_i}{\text{cm}^2_{(a)}}$
c_i^{s}	concentration of species i at channel-washcoat interface	$\frac{\text{mol}}{\text{cm}^3}$
c_j	concentration of species j	$\frac{\text{mol}}{\text{cm}^2}$, $\frac{\text{mol}}{\text{cm}^3}$
$c_{\mathrm{p},i}$	constant pressure specific heat capacity of species i	$\frac{\text{J}}{\text{mol K}}$
$\tilde{c}_{(i-*)}$	site-pair surface concentration for an uncorrelated species i based on surface area of (a-b) site-pairs	$\frac{\text{mol}_i}{\text{cm}^2_{(\text{a-b})}}$
d_i	inner diameter of annular duct	mm
d_{mix}	spherical diameter an aggregated Pd/PdO spherical particle with conical sectoral arrangements of the single phases	nm
d_{o}	diameter of circular channel	μm
d_{o}	outer diameter of annular duct	mm
d_{p}	washcoat pore diameter	nm
$d_{\mathrm{p,M}}$	macro pore size	μm
$d_{\mathrm{p,m}}$	meso pore size	nm
$d_{\mathrm{p,Pd}}$	particle size of Pd	nm

$d_{\mathrm{p}}^{\mathrm{l}}$	particle diameter	nm
d_{Pd}	equivalent spherical particle diameter of Pd	nm
$d_{\mathrm{Pd}}^{\mathrm{l}}$	particle diameter of non-disrupted reduced Pd	nm
$d_{\mathrm{Pd}}^{\mathrm{max}}$	maximum particle diameter for Pd in reduced state	nm
d_{PdO}	particle diameter of PdO	nm
d_{PdO}	equivalent spherical particle diameter of PdO	nm
$d_{\mathrm{PdO}}^{\mathrm{l}}$	particle diameter of undisrupted PdO	nm
$d_{\mathrm{PdO}}^{\mathrm{max}}$	maximum particle diameter for PdO phase	nm
$d_{\mathrm{PdO}}^{\mathrm{s}}$	particle diameter of disrupted PdO	nm
$\bar{d}_{\mathrm{PdO}}$	experimentally determined average value for the PdO particle diameter	nm
f_{KM}	Kubelka-Munk function	-
f_{ox}	degree of oxidation dependent correction function	-
f_{sc}	spacial correlation function	-
$f_{\mathrm{sc}}(P_{(\mathrm{n\text{-}m})})$	spacial correlation function	-
h	specific enthalpy of the gas-phase mixture	$\frac{\mathrm{J}}{\mathrm{kg}}$
h	Planck's constant	J s
h_i	specific enthalpy of species i in the gas-phase	$\frac{\mathrm{J}}{\mathrm{kg}}$
i	species indices	-
k	reaction indices	-
k_{B}	Boltzmann's constant	$\frac{\mathrm{J}}{\mathrm{K}}$
$k_{\mathrm{CH_4}}^{1^{\mathrm{st}}}$	pseudo first order methane oxidation rate constant	$\frac{\mathrm{mol_{CH_4}}}{\mathrm{kPa\,s\,g_{Pd,surf}}}$
$k_{\mathrm{f},k}$	forward rate constant of step k	mol,cm,s
$k_{\mathrm{f},k}$	reverse rate constant of step k	mol,cm,s
$k_{\mathrm{f},k}$	forward rate constant of step k	mol,cm,s
k_j	pseudo first order surface reaction rate constant for species j	$\frac{\mathrm{mol}_j}{\mathrm{cm^2/,s}}$
k_k	rate constant of step k	mol,cm,s
$k_{k,\mathrm{ads}}$	rate constant for adsorption in step k	s^{-1}
$k_{\mathrm{r},k}$	reverse rate constant of step k	mol,cm,s
$k_{\mathrm{v},j}$	pseudo first order volumetric reaction rate constant for species j	s^{-1}
m_{cat}	catalyst mass	g
n	sample data size	-

n	reaction order	-
n	number of aggreagated Pd/PdO particles	-
n	coordination number	-
n_{CH_4}	reaction order with respect to methane	-
n_{H_2O}	reaction order with respect to water	-
n_k	number of participating surface sites in adsorption step k	-
n_k	number of participating surface sites in the corresponding adsorption step k	-
n_{k,j_P}	atomic number of element k contained in product species j_P	-
n_{k,j_R}	atomic number of element k contained in reactant species j_R	-
n_{O_2}	reaction order with respect to oxygen	-
n_p^s	number of small/disrupted PdO particles	-
n_{Pd}^{max}	maximum number of Pd particles	-
n_{PdO}^{max}	maximum number of PdO particles	-
p	pressure	Pa
p_0	standard state pressure (1013.25mbar)	Pa
p_{CH_4}	partial pressure of methane	kPa
p_{ext}	externally applied pressure	Pa
p_{in}	channel inlet pressure	Pa
p_{O_2}	partial pressure of oxygen	Pa
r	radial coordinate	m
r_j	turnover frequency of species j based on number of moles surface site-pairs	$\frac{\mathrm{mol}_{\mathrm{transf},j}}{\mathrm{mol}_{(\mathrm{a\text{-}b})}\,\mathrm{s}}$
r_k	turnover frequency of reaction k	$\frac{\mathrm{mol}_{\mathrm{transf},k}}{\mathrm{mol}_{\mathrm{sites}}\,\mathrm{s}}$
r_k	turnover frequency of reaction step k based on number of moles surface site-pairs	$\frac{\mathrm{mol}_{\mathrm{transf},k}}{\mathrm{mol}_{(\mathrm{a\text{-}b})}\,\mathrm{s}}$
$r_{k,ads}$	turnover frequency for adsorption in step k	s^{-1}
s	repeat distance of monolith (square) cell	μm
s_i^0	initial sticking coefficient of gas-phase species i with respect to the catalyst surface at zero coverage	-
s_{i^0}	initial sticking coefficient of gas-phase species i with respect to the catalyst surface at zero coverage	-

$\dot{s}_k$	rate of reaction	$\frac{\mathrm{mol}_i}{\mathrm{cm}^2\,\mathrm{s}}$
$\dot{s}_k$	single-site type surface area specific molar rate of reaction based on either type (a) or (b) for surface reaction step k	$\frac{\mathrm{mol}_{\mathrm{transf},k}}{\mathrm{cm}^2_{\text{(single-site)}}\,\mathrm{s}}$
$\dot{s}_k$	rate of reaction in step k	$\frac{\mathrm{mol}_i}{\mathrm{cm}^2\,\mathrm{s}}$
$\dot{\tilde{s}}_k$	site-pair surface area specific molar rate of reaction for surface reaction step k	$\frac{\mathrm{mol}_{\mathrm{transf},k}}{\mathrm{cm}^2_{\text{(a-b)}}\,\mathrm{s}}$
t	time	s
u	axial velocity component	$\frac{\mathrm{m}}{\mathrm{s}}$
u_{in}	channel inlet velocity	$\frac{\mathrm{m}}{\mathrm{s}}$
v	radial velocity component	$\frac{\mathrm{m}}{\mathrm{s}}$
v_{GHSV}	gas hourly space velocity	h^{-1}
v_{m}	average unit cell volume per bulk atom	$\frac{\mathrm{Å}^3}{\mathrm{atom}}$
$v_{\mathrm{m,Pd}}$	average unit cell volume per bulk atom for the fcc bulk crystal structure of Pd	$\frac{\mathrm{Å}^3}{\mathrm{atom}}$
$v_{\mathrm{m,PdO}}$	average unit cell volume per bulk atom for the tetragonal bulk crystal structure of PdO	$\frac{\mathrm{Å}^3}{\mathrm{atom}}$
w	weight fraction	-
$w_{\mathrm{f},k}$	selectable weight for thermodynamic consistency adjustment in forward direction of step k	-
w_k	selectable weight for thermodynamic consistency adjustment for step k	-
w_{Pd}	Pd weight fraction on catalyst mass	-
$w_{\mathrm{r},k}$	selectable weight for thermodynamic consistency adjustment in reverse direction of step k	-
x	mole fraction	-
$\bar{x}(z)$	mean value over sample data at axial channel position z	-
$x_{\mathrm{f},k}$	thermodynamic consistency correction term in forward direction of step k	-
x_i	i^{th} data sample	-
x_i	bond order of the two-center binary interaction i	-
x_i^0	resulting undisturbed mole fraction of species i	-
$x_{\mathrm{r},k}$	thermodynamic consistency correction term in reverse direction of step k	-
$\tilde{x}_i$	resulting perturbed mole fraction of species i	-

z	axial coordinate	m

Greek letters

upper case

Symbol	Description	Unit
$\Gamma_{(a)}$	average single site surface site density of a Pd_{cus} site	$\frac{mol}{cm^2}$
$\Gamma_{(a)+(b)}$	average surface site density of Pd_{cus} and O_{cus} sites for PdO(101)	$\frac{mol}{cm^2}$
$\Gamma_{(a-b)}$	average surface site density of Pd_{cus}-$textO_{cus}$ site-pairs (number of site-pairs per unit surface area)	$\frac{mol}{cm^2}$
$\Gamma_{(b)}$	average single site surface site density of a $textO_{cus}$ site	$\frac{mol}{cm^2}$
Γ_{Pd}	surface site density of Pd defined as number of Pd surface sites per unit surface area	$\frac{mol}{cm^2}$
Γ_{PdO}	average single site surface site density for PdO(101) surface facette	$\frac{mol}{cm^2}$
$\tilde{\Gamma}_{PdO}$	average surface site density of coordinatively unsaturated site-pairs for PdO(101)	$\frac{mol}{cm^2}$
$\Delta_f H_j$	enthalpy of formation of species j from its elements	$\frac{J}{mol}$
$\Delta_R D$	gas-phase reaction energy difference to bond dissociation energies	$\frac{J}{mol}$
$\Delta_R G_k$	Gibbs free energy of reaction in step k	$\frac{J}{mol}$
$\Delta_R H$	enthalpy of reaction	$\frac{J}{mol}$
$\Delta_R H^0_{298\,K}$	enthalpy of reaction in step k at standard state conditions	$\frac{J}{mol}$
$\Delta_R H_k$	enthalpy of reaction in step k	$\frac{J}{mol}$
$\Delta_R Q$	heat of surface reaction difference applied to chemisorption energies	$\frac{J}{mol}$
$\Delta_R S_k$	entropy of reaction in step k	$\frac{J}{mol\,K}$
$\Delta_R S_k$	entropy of reaction	$\frac{J}{mol\,K}$

lower case

Symbol	Description	Unit
β_{Pd}	site occupation number of probe molecule on Pd	-
$\beta_{\mathrm{f},k}$	parameter for temperature dependence on forward pre-exponential factor in step k	-
β_k	parameter for temperature dependence on pre-exponential factor	-
$\beta_{\mathrm{r},k}$	parameter for temperature dependence on reverse pre-exponential factor in step k	-
γ	volume expansion or contraction coefficient of the reaction mixture	-
$\gamma_{\mathrm{l,v}}$	surface tension between liquid-Hg and vapor gas-phase	$\frac{\mathrm{N}}{\mathrm{m}}$
$\gamma_{\mathrm{s,l}}$	surface tension between solid surface and liquid-Hg phase	$\frac{\mathrm{N}}{\mathrm{m}}$
$\gamma_{\mathrm{s,v}}$	surface tension between liquid-Hg and vapor gas-phase	$\frac{\mathrm{N}}{\mathrm{m}}$
δ_{s}	substrate wall thickness of monolith	μm
δ_{wc}	washcoat thickness	μm
$\delta_{\mathrm{wc}}^{\mathrm{eff}}$	effective washcoat thickness	μm
$\delta_{\mathrm{wc}}^{\mathrm{max}}$	maximum washcoat thickness	μm
$\delta_{\mathrm{wc}}^{\mathrm{min}}$	minimum washcoat thickness	μm
ϵ	total porosity of sample	-
ϵ	sensitivity analysis perturbation parameter	-
ϵ_i	parameter for coverage dependent activation energy	$\frac{\mathrm{J}}{\mathrm{mol}}$
$\epsilon_{j,i}$	differential heat of formation of species j upon changing coverage of species i	$\frac{\mathrm{J}}{\mathrm{mol}}$
ϵ_{M}	washcoat macro porosity	-
ϵ_{m}	washcoat meso porosity	-
ϵ_{wc}	washcoat porosity	-
η	washcoat effectiveness factor (internal effectiveness)	-
η_i	washcoat effectiveness factor of species i	-
η_{th}	thermal efficiency ($= (\dot{H}_{\mathrm{out}} - \dot{H}_{\mathrm{in}})/\Delta_{\mathrm{R}}H_{\mathrm{ad}}$)	
θ	contact angle	$^\circ$
$\theta_{i(a)}$	surface coverage / site fraction of species j occupying surface site type (a) ($\theta_{i(\mathrm{a})} \in [0,1]$)	$\frac{\mathrm{mol}_{i(\mathrm{a})}}{\mathrm{mol}_{(\mathrm{a})}}$
θ_j	surface coverage of species j	$\frac{\mathrm{mol}_j}{\mathrm{mol}_{\mathrm{s}}}$

θ_j^0	reference surface coverage of species j (=1ML)	-
θ_{sec}	sector angle	$^\circ$
λ	thermal conductivity of gas-phase mixture	$\frac{\mathrm{W}}{\mathrm{m\,K}}$
λ_k	k^{th} Lagrange multiplier	-
μ	dynamic viscosity	$\mathrm{Pa\,s}$
ν	wave number	cm^{-1}
ν	kinematic viscosity	$\frac{\mathrm{m}^2}{\mathrm{s}}$
$\nu_{k,j}$	stoichiometric coefficient for step k and species j	$\frac{\mathrm{mol}_j}{\mathrm{mol}_{\mathrm{transf,k}}}$
ρ	density of gas-phase mixture based on mass	$\frac{\mathrm{kg}}{\mathrm{m}^3}$
ρ_b	bulk (apparent) density of sample	$\frac{\mathrm{g}}{\mathrm{mL}}$
ρ_{cat}	catalyst density of coated zone	$\frac{\mathrm{g}}{\mathrm{cm}^3}$
ρ_s	skeletal density of sample	$\frac{\mathrm{g}}{\mathrm{mL}}$
ρ_{wc}	washcoat density	$\frac{\mathrm{g}}{\mathrm{L}}$
σ	site-pair correction factor	-
σ_i	number of surface sites occupied by species i	-
τ	residence time	s
τ	washcoat tortuosity	-
φ_i	Thiele modulus of species i	-
χ_i	placeholder for species i	-
ϕ	empirical UBI-QEP transition state location parameter, describing the earliness ($\phi \to 0$) or lateness ($\phi \to 1$) of the transition state	-

Super Indices

Symbol	Description
0	pertaining to zero coverage limit, reference or initial/unperturbed state
$'$	pertaining to reactants
$''$	pertaining to products
$\{j_\mathrm{R}\}$	pertaining to the set of reactant species j_R
$^+$	pertaining to reactor inlet condition

‡	pertaining to transition state intermediate
k	pertaining to element k
P	pertaining to the set of product state species P participating in the corresponding reaction
R	pertaining to the set of reactant state species R participating in the corresponding reaction

Sub Indices

Symbol	Description
0	pertaining to standard state
$\{j_\mathrm{R}\}$	pertaining to the set of reactant species j_R
4f	pertaining a four fold coordinated site
cus	pertaining to a coordinatively unsatureated type of site
f	pertaining to forward direction or formation
i	species indices
I	pertaining to inert component I
j	species indices
j_P	pertaining to product species j_P
j_R	pertaining to reactant species j_R
k	reaction step indices
r	pertaining to reverse direction

Mathematical symbols and special characters

Symbol	Description
$H(.)$	Heavyside function; $H(x) > 0$ for $x > 0$; $H(x) = 0$ for $x \leq 0$
L	Lagrangian function
$\|x\|$	L^2-Norm; $\|x\| = \sqrt{\int_{T_1}^{T_2} x^2 dT}$
$*$	empty surface site or wildcard for surface species

Dimensionless Numbers

Symbol	Description
$Re_{\mathrm{L}} = \frac{u \cdot L}{\nu}$	Reynolds number based on channel length L
$Sc = \frac{\nu}{D}$	Schmidt number
$Da_{II} = \frac{\tau}{\tau_{rxn}}$	Damköhler number of second kind; ratio of residence time to time scale of reaction

Abbreviations

Symbol	Description
$(\frac{\mathrm{C}}{\mathrm{O}})_{stoic}$	stoichiometric atomic carbon-to-oxygen ratio
(g)	gas-phase state
(ps)	physisorbed state
(s)	chemisorbed state
BET	Brunnauer Emmet and Teller
BHS	back heat shield
C/O	atomic carbon-to-oxygen ratio
CFD	computational fluid dynamics
CHEMKIN	chemical Kinetics software for solving complex chemical kinetics problems
CPOX	catalytic partial oxidation
cpsi	cells per squared inch
CTOX	catalytic total oxidation
cus	coordinatively unsaturated
CVT	Institute of Chemical Process Engineering
DETCHEM	Detailed Chemistry (Software Package)
DFT	density functional theory
DRIFTS	diffuse reflectance infrared Fourier transform spectroscopy
EI-MS	electron impact mass spectrometer
fcc	face centered cubic
FHS	front heat shield

FS	final state
FT-IR	fourier-transform infrared spectroscopy
GHSV	gas hourly space velocity
GWP	global warming potential
HC	hydrocarbon
hcp	hexagonal close packed
HPXPS	high pressure X-ray photoelectron spectroscopy
HREELS	high resolution electron energy loss spectroscopy
HRTEM	high resolution transmission electron microscopy
HT-XRD	high-temperature X-ray diffraction
IAM-WET	Institute for Applied Materials - Materials for Electrical and Electronic Engineering
ID	inner diameter
IMR-MS	Ion-molecule reaction mass spectrometer
IR	infrared
IS	initial state
ITCP	Institute for Chemical Technology and Polymer Chemistry
IUPAC	International Union of Pure and Applied Chemistry
KIT	Karlsruhe Institute of Technology
LEED	low energy electron diffraction
LIMEX	extrapolation method based on the semi-implicit Euler discretization for linearly implicit ODEs; mnemotechnically: EXtrapolation integrator for Linearly IMplicit ODEs (DAE-Solver written in FORTRAN code; developed by P. Deuflhard et al., Berlin, Germany)
LM	light microscopy
LMI	light microscopy image
MF	mean field
MFC	mass flow controller
MF-MKM	mean field extended microkinetic model
MKM	microkinetic model
ML	monolayer
MvK	Mars van Krevelen
NDIR	nondispersive infrared sensor
NG	natural gas

OD	outer diameter
P2F	power to fuels
P2G	power to gas
P2L	power to liquids
PM	particulate matter
ppm	parts per million
PRP	preferential reaction path analysis
PTG	power to gas
PW91	Perdew-Wang exchange and correlation functional developed in 1991
RAIRS	reflection Absorption Infra-Red Spectroscopy
RHS	right hand side
RPA	reaction path analysis
RPBE	revised Perdew-Burke-Ernzerhof exchange correlation functional developed in 1999
SATP	standard ambient condition for temperature (298.15 K) and pressure (1013.25 mbar)
SLPM	standard liters per minute
SpaciPro	setup at ITCP for measuring spatial resolved profiles
SR	steam reforming
STM	scanning tunneling microscope
STP	standard condition for temperature (273.15 K) and pressure (1013.25 mbar)
TDS	thermal desorption spectroscopy
TEM	transmission electron microscopy
TG	thermogravimetry
TGA	thermogravimetric analysis
TOF	turn over frequency = number of transfomations per surface site per second
TPD	temperature-programmed desorption
TPO	temperature-programmed oxidation
TPR	temperature-programmed reduction
UBI-QEP	unity bond index-quadratic exponential potential
vol.-%	percentage by volume
w_{Pd}	palladium weight fraction on catalyst

WGS	water-gas shift
wt.-%	percentage by weight
XAS	X-ray absorption spectroscopy
XPS	X-ray photoelectron spectroscopy
XRD	X-ray diffraction

Chemical compounds

Symbol	Description
$(*)_{O(cus)}$	vacant O_{cus} site
$(*)_{Pd(cus)}$	vacant Pd_{cus} site
(a)	vacant Pd_{cus} site
(b)	vacant O_{cus} site
$(O)_{4f}$	oxygen atom adsorbed on a four fold (4f) coordinated surface site
$(Pd)_{4f}$	palladium atom adsorbed on a four fold coordinated (4f) surface site
(s)	vacant reduced Pd site
$(v)_{O(cus)}$	O_{cus} surface lattice oxygen vacancy site
C_1	carbonaceous species containing mono atomic carbon
Ce	cerium
CH(a)	methine (methylidyne) species adsorbed on a Pd_{cus} site
CH_x	C_1 species with x hydrogen
CH_xO_y	formate species
CH_xO_y	generic carbonaceous C_1 species
CH_2(a)	methylene species adsorbed on a Pd_{cus} site
CH_2(b)	methylene species adsorbed on a O_{cus} site
CH_2O(a)	formaldehyde species adsorbed on a Pd_{cus} site
CH_2OH(a)	hydroxymethyl species adsorbed on a Pd_{cus} site
CH_3(a)	methyl species adsorbed on a Pd_{cus} site
CH_3(b)	methyl species adsorbed on a O_{cus} site
CH_4	methane

CHO(a)	formyl species adsorbed on a Pd_{cus} site
CHO(b)	formyl species adsorbed on a O_{cus} site
CO	carbon monoxide
CO(a)	carbon monoxide adsorbed on a Pd_{cus} site
CO(b)	carbon monoxide adsorbed on a O_{cus} site
CO_2	carbon dioxide
CO_2(a)	carbon monoxide adsorbed on a Pd_{cus} site
H(a)	atomic hydrogen adsorbed on a Pd_{cus} site
H(b)	atomic hydrogen adsorbed on a O_{cus} site
H_2	hydrogen
H_2O	water
H_2O(a)	water adsorbed on a Pd_{cus} site
HCOO(a)	formate species adsorbed on a Pd_{cus} site
He	helium
Hg	mercury
j(a)	generic species j adsorbed on a site of type (a) i.e. Pd_{cus} site
j(b)	generic species j adsorbed on a site of type (b) i.e. O_{cus} site
KBr	potassium bromide
N_2	nitrogen
NO	nitrogen (nitric) oxide
NO_x	nitrogen oxides
O(a)	atomic oxygen adsorbed on a Pd_{cus} site
O(b)	atomic oxygen adsorbed on a O_{cus} site
O_{cus}	coordinatively unsaturated oxygen site
O_2	oxygen
O_2(a)	molecular oxygen adsorbed on a Pd_{cus} site
OH(a)	hydroxyl species adsorbed on a Pd_{cus} site
Pd	palladium
Pd(100)	palladium (100) facette
Pd(101)	palladium (101) surface facette
Pd(111)	palladium (111) facette
Pd/Al_2O_3	palladium supported on alumina
Pd_{cus}	coordinatively unsaturated palladium site
Pd_{cus}-O_{cus}	site pair of coordinatively unsaturated palladium and oxygen

PdO	palladium oxide
PdO(100)	palladium oxide (100) facette
PdO_x	PdO with a $1 : x$ stoichiometry of Pd:O
Pt	platinum
Rh	rhodium
SiO_x	silicone oxides
SO_x	sulfur oxides
vac(b)	O_{cus} surface lattice oxygen vacancy site
x(a)	generic species x sitting on a Pd_{cus} = (a) site
x(a)|y(a)	generic species x sitting on a Pd_{cus} site unpaired (not dimerized) next to a species y sitting on a O_{cus} site
x(a)-y(a)	generic species x sitting on a Pd_{cus} site paired to a species y sitting on a O_{cus} site next to x
y(b)	generic species y sitting on a O_{cus}=(b) site
Zr	zirconium

A Appendix: Additional Data[1]

[1] Parts of this chapter have been taken from [1] H. Stotz, L. Maier and O. Deutschmann, Methane oxidation over palladium: on the mechanism in fuel-rich mixtures at high temperatures, *Top. Catal.*, 60 (2017) 83–109 and from [2] H. Stotz, L. Maier, A. Boubnov, A. T. Gremminger, J.-D. Grunwaldt and O. Deutschmann, Surface reaction kinetics of methane oxidation over PdO, *J. Catal.*, 370 (2019) 152–175.

A.1 Complementary Results

A.1.1 Spatial Resolved Results

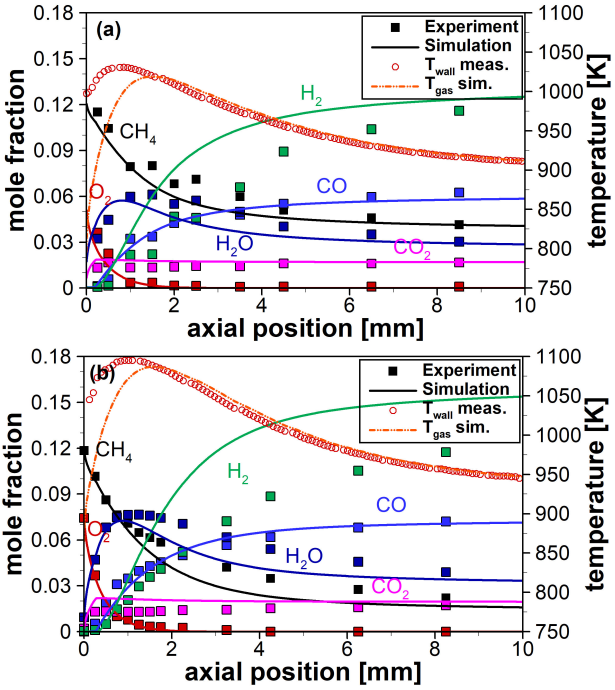

Figure A.1: Experimental and simulated concentration profiles along the channel axis, measured wall temperature and simulated gas-phase temperature profiles. Inlet conditions as fed: C/O-ratio of (a) 1.0 and (b) 0.8 at 4 SLPM and N_2-dilution of 80 vol.-%. Figure adapted from Stotz et al. [1].

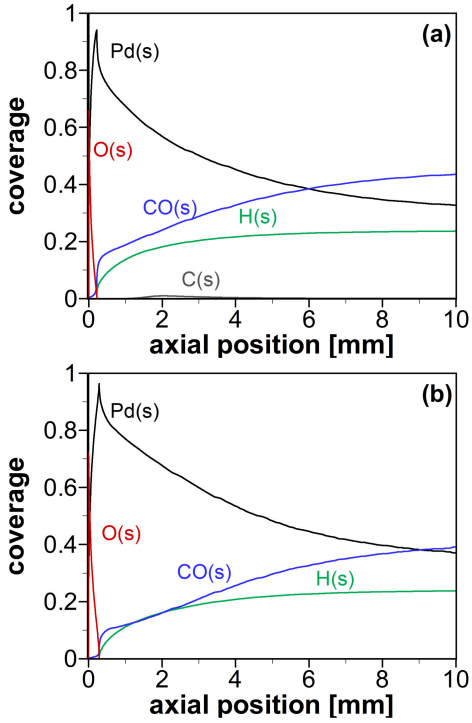

Figure A.2: Simulated coverage profiles along the channel axis for most abundant surface intermediates. Inlet conditions as fed: C/O-ratio of (a) 1.0 and (b) 0.8 at 4 SLPM and N_2-dilution of 80 vol.-%. Figure adapted from Stotz et al. [1].

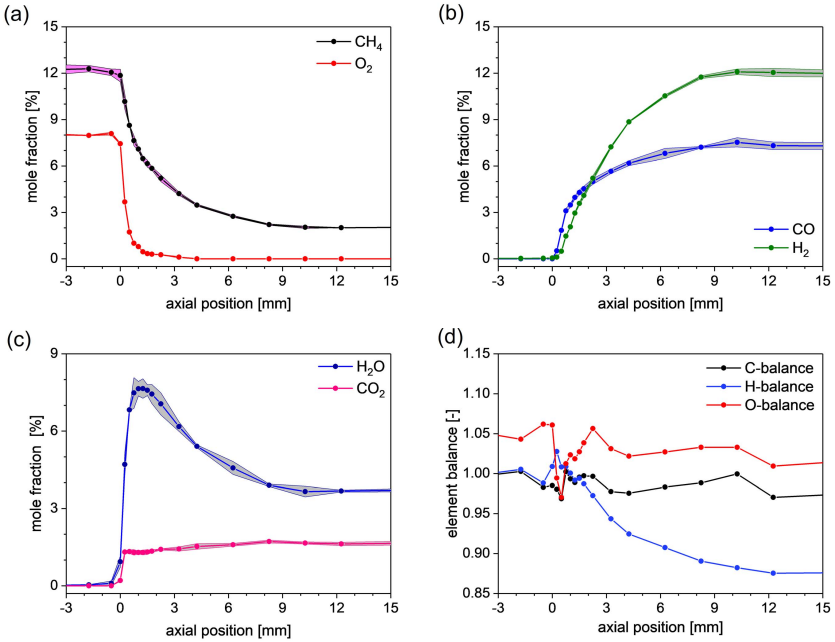

Figure A.3: (a)-(c) Sample mean of the experimentally determined spatially resolved mole fractions (C/O-ratio = 0.8) and corresponding error bars as given by the confined shaded area, $\bar{x}(z) \pm (\sigma \cdot c)$ with $c = 1$, based on the sample standard deviation, $\sigma = \sqrt{\sum (x_i - \bar{x})^2/(n-1)}$. (d) Element balances based on the mole fractions' sample mean for C, O and H containing species.

A.1.2 DRIFTS Results

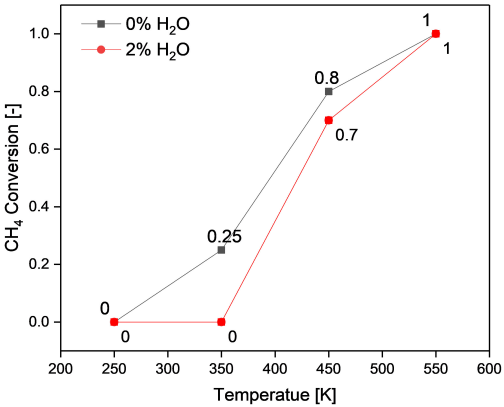

Figure A.4: Catalytic conversion of methane during in situ DRIFTS measurements for dry and wet conditions. Figure adapted from Stotz et al. [2].

DRIFT spectra taken for all investigated temperatures (cf. Fig. A.5, A.6, A.7 and A.8): 250 °C, 350 °C, 450 °C and 550 °C at dry and wet conditions for the prepared Pd/Al_2O_3 catalyst and at dry conditions for the bare Al_2O_3 support only. Spectra at 250 °C and 450 °C are presented in the main text.

Typical vibrational band ranges:
O–H bond stretches: 3400-3800 cm^{-1} (left panels)
C–H bond stretches: 2800-3200 cm^{-1} (middle panels)
C–O bond stretches: 1200-1700 cm^{-1} (right panels)

Assignment of colored bands in Fig. A.5:

Orange bands:
Narrow bands at 3000 and 1300 cm^{-1}: due to gas-phase methane

Green bands:
Broadened bands at 3000, 2900, 1600, 1400 and 1390 cm^{-1} due to surface species formed as a result of adsorption and activation of methane = formates (A parallel study showed that the formation of these species is positively correlated with the methane conversion. These species are stable at low temperatures, also under dry air and vacuum [93].) When oxidizing methanol and formic acid, the same broadened bands marked green in Fig. A.5 (b) and (c) are observed as those

when oxidizing methane. The intermediates common for oxidation of all three fuels thus contains carbon in an oxidation state of at least +2, as in formic acid, and are most probably formates. The pyrolytic decomposition route for methane can thus be ruled out. The oxidized species are not carbonates, since characteristic bands for carbonates formed during dosage of CO_2 (not shown) were not observed.

Water is likewise formed and adsorbed on the surface hydroxyl of the alumina.

Blue bands:
Broad band between 3500-3600 cm^{-1}: O-H stretch of the water molecule, produced in the reaction and adsorbed on the alumina surface hydroxyls
small negative band at 3770 cm^{-1}: O-H stretch of the occupied surface hydroxyl of the alumina

Red bands:
Bands arising at 350 °C and 250 °C (2880, 1640, 1660 and 1315 cm^{-1}): weakly adsorbed formates. These bands are only visible with oxygenated fuels (methanol, formic acid) and appear only at low temperatures. Their bands are correlated with the appearance of the strongly bound formate bands (green bands). The weakly adsorbed formate groups are also likely associated with surface hydroxyls, since the appearance of their bands is correlated to a growth of the negative band at 3770 cm^{-1} (marked red).

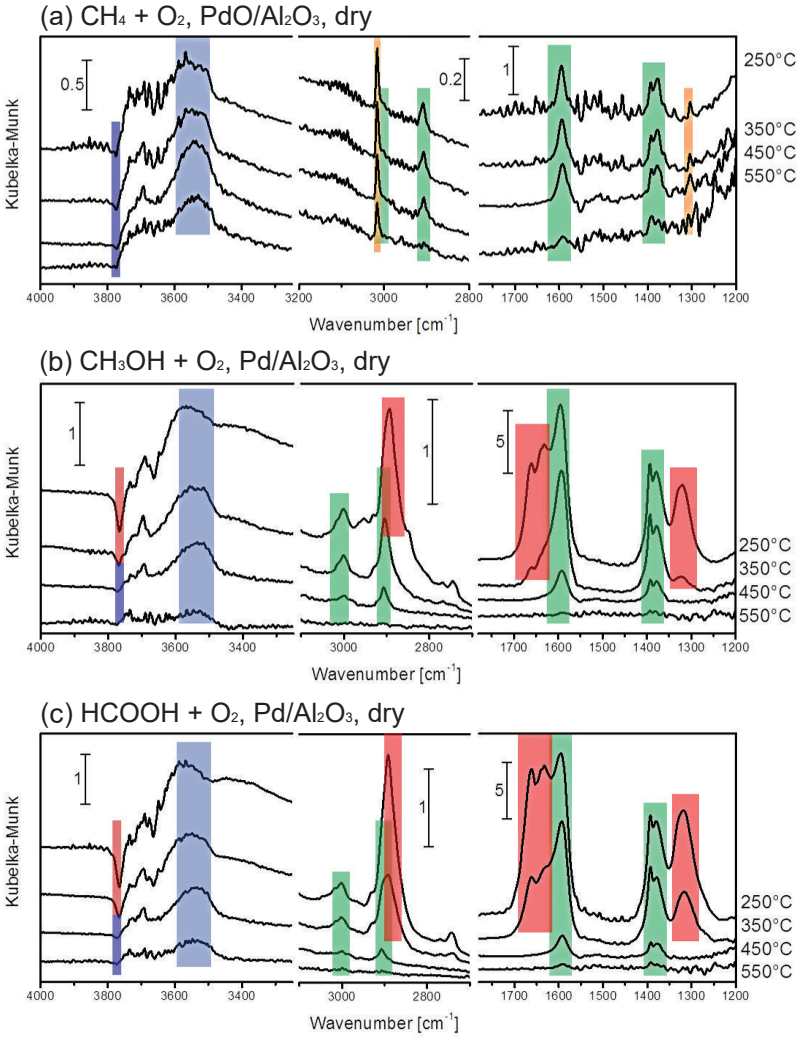

Figure A.5: In situ DRIFT spectra of 2.4 % Pd/Al_2O_3 under dry conditions, exposed to (a) $CH_4 + O_2$, (b) $CH_3OH + O_2$ and (c) $HCOOH + O_2$. The gas composition contained 4000 ppm fuel (methane, methanol or formic acid), 10 % O_2 and in balance helium. The total flow was 200 mL/min. Figure adapted from Stotz et al. [2].

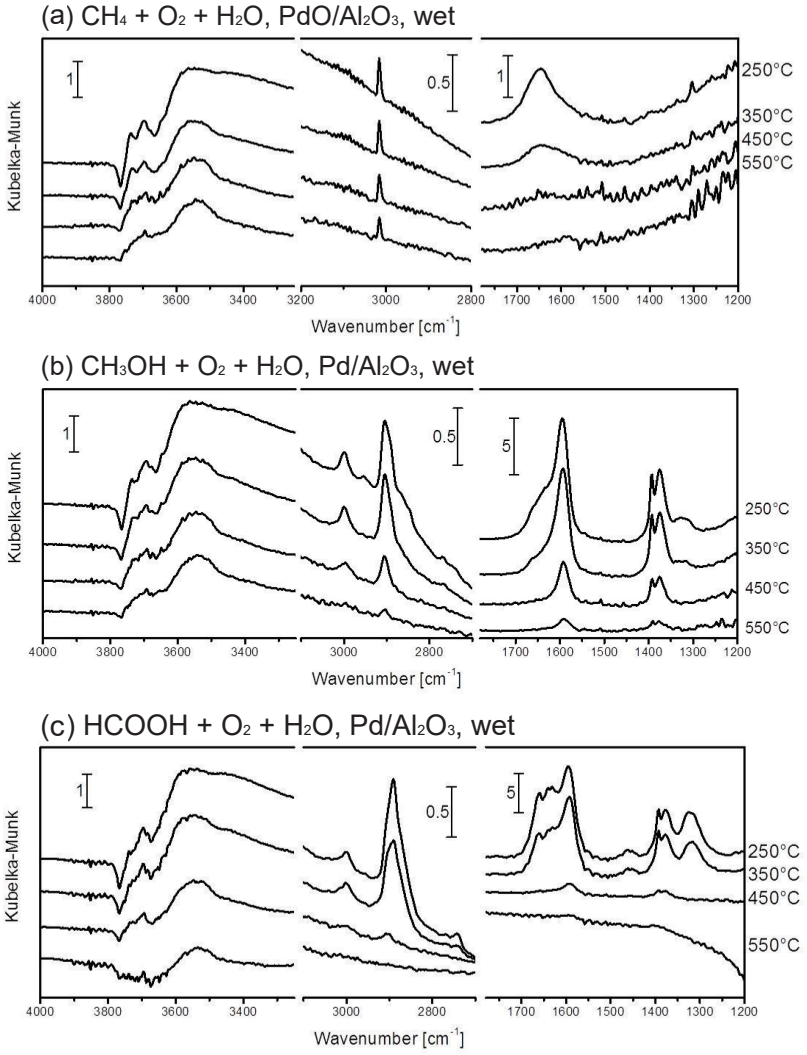

Figure A.6: In situ DRIFT spectra of 2.4 % Pd/Al_2O_3 under wet conditions, exposed to (a) $CH_4 + O_2 + H_2O$, (b) $CH_3OH + O_2 + H_2O$ and (c) $HCOOH + O_2 + H_2O$. The gas composition contained 4000 ppm fuel (methane, methanol or formic acid), 10 % O_2, 2 % H_2O and in balance helium. The total flow was 200 mL/min. Figure adapted from Stotz et al. [2].

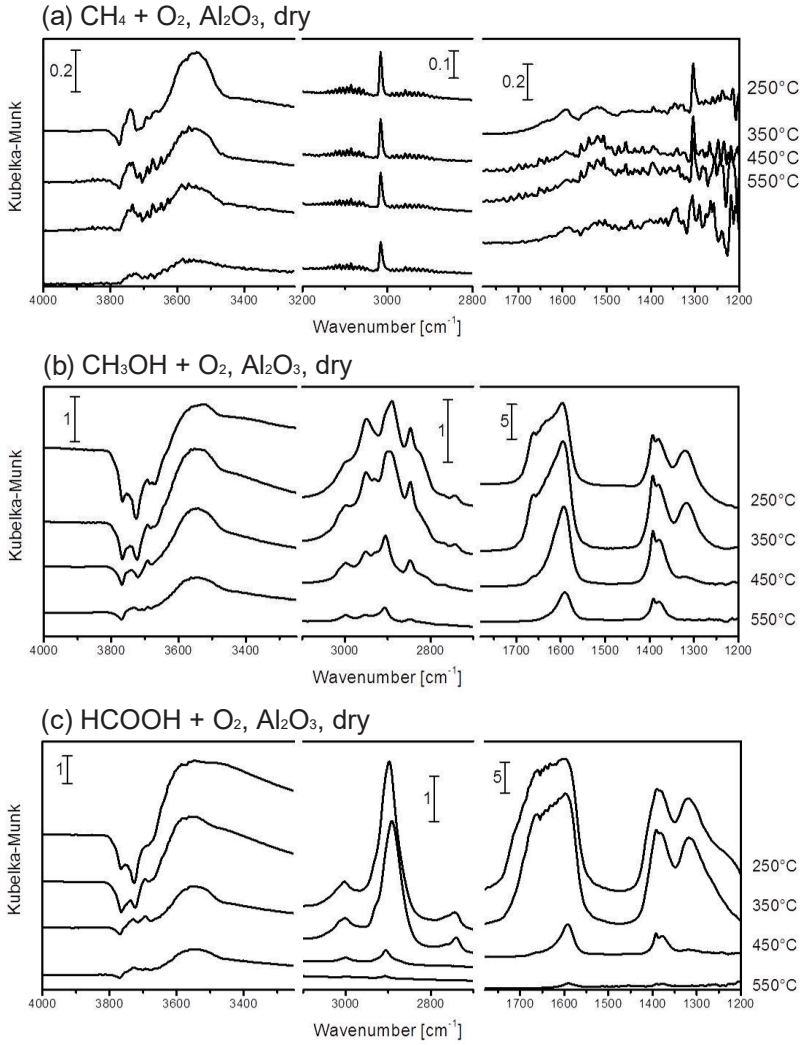

Figure A.7: In situ DRIFT spectra of bare Al_2O_3 under dry conditions, exposed to (a) $CH_4 + O_2$, (b) $CH_3OH + O_2$ and (c) $HCOOH + O_2$. The gas composition contained 4000 ppm fuel (methane, methanol or formic acid), 10 % O_2 and in balance helium. The total flow was 200 mL/min. Figure adapted from Stotz et al. [2].

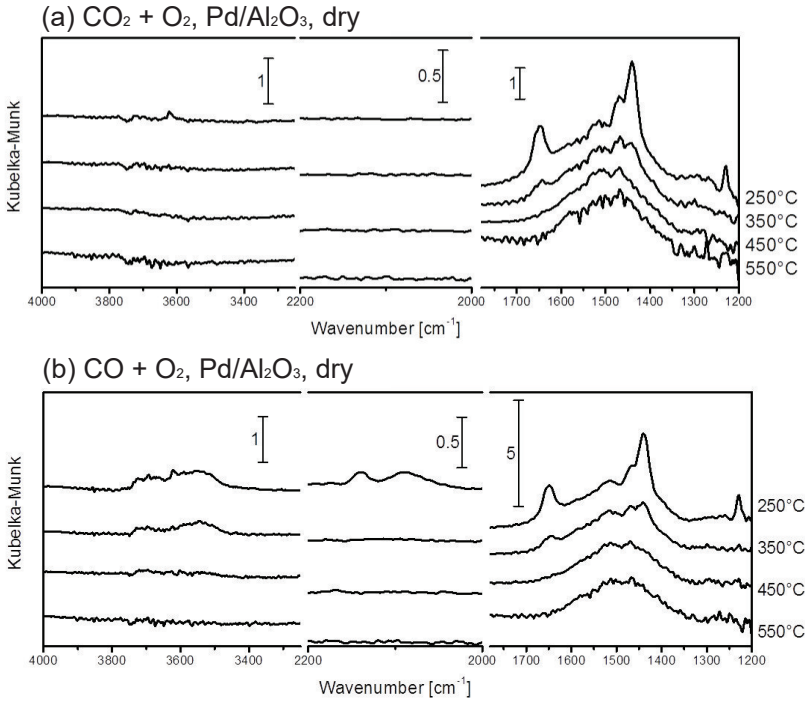

Figure A.8: In situ DRIFT spectra of 2.4 % Pd/Al_2O_3 under dry conditions exposed to (a) 4000 ppm CO_2, 10 % oxygen and balance helium and (b) 4000 ppm CO, 10 % oxygen and balance helium. The total flow was 200 mL/min. Figure adapted from Stotz et al. [2].

A.1.3 Hg Intrusion Porosimetry

The Hg intrusion porosimetry is a method which can determine the apparent density (ρ_b) and the pore size distribution within a porous medium by intruding liquid mercury into the porous media.
According to Fig. A.9, the pore size is related to the applied external pressure through the Washburn equation. This relationship is integrated in the apparatus calibration and output as intrusion curve, the (differential) intruded liquid Hg-volume, V_p, vs. the external applied pressure (or ultimately as pore diameter) on the sample probe, p_{ext}:

$$d_p\,(p_{ext}) = -\frac{4 \cdot \gamma_{l,v} \cdot \cos\theta}{p_{ext}} \tag{A.1}$$

Reading off from the intrusion curve (cf. Fig. 4.1), the pore diameters are given for macro pores, $d_{p,M} = 1.57\,\mu m$, and mesopores, $d_{p,m} = 12.3\,\mu m$.
In Eq. (A.1), θ is the contact angle of the intruded Hg in the pores, γ_{lv} is the surface tension between liquid-Hg and gas-phase and p_{ext} is the external applied pressure on the liquid-Hg phase.
The pore volumes of the total pores is given by, $V_p = 0.3062\,mL/g$, and the macropores is given by, $V_{p,M} = 0.1810\,mL/g$. Both values were read off from the measured intrusion curves (cf. Fig. 4.1) at the peak height of the meso- and macro pore size ranges. Thus, the mesopore volume is given by

$$V_{p,m} = V_p - V_{p,M} \tag{A.2}$$

The total porosity of the sample is calculated from the skeletal density, $\rho_s = 3.339\,g/mL$, and bulk density, $\rho_b = 1.651\,g/mL$, of the sample as obtained from the intrusion measurements and sample weight:

$$\epsilon = \frac{\rho_s - \rho_b}{\rho_s} \tag{A.3}$$

$$= \frac{V_p}{V_b} \tag{A.4}$$

$$= 0.5056 \tag{A.5}$$

The skeletal volume of the catalyst is calculated from V_p and Eq. (A.5) according to

$$V_s = \left(\frac{1-\epsilon}{\epsilon}\right) \cdot V_p \tag{A.6}$$

$$= 0.2995\,mL/g \tag{A.7}$$

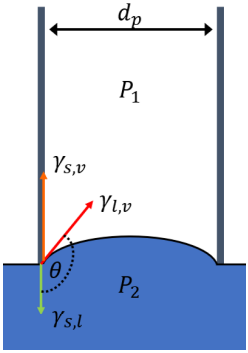

Figure A.9: Hg intrusion into a pore of diamater d_p for an applied external pressure, $p_{\text{ext}} = p_1 - p_2$. A force balance with the surface tensions, $\cos(\theta) = (\gamma_{s,v} - \gamma_{s,l})/\gamma_{l,v}$, relates Young and Laplace's equation with Washburn's equation.

The porosities for the macro- and mesopore range are given by

$$\epsilon_{\text{M}} = \frac{V_{\text{p,M}}}{V_{\text{s}} + V_{\text{p}}} \tag{A.8}$$

$$= 0.2988 \tag{A.9}$$

$$\epsilon_{\text{m}} = \frac{V_{\text{p,m}}}{V_{\text{s}} + V_{\text{p}}} \tag{A.10}$$

$$= 0.2067 \tag{A.11}$$

A.1.4 CO Chemisorption Measurements

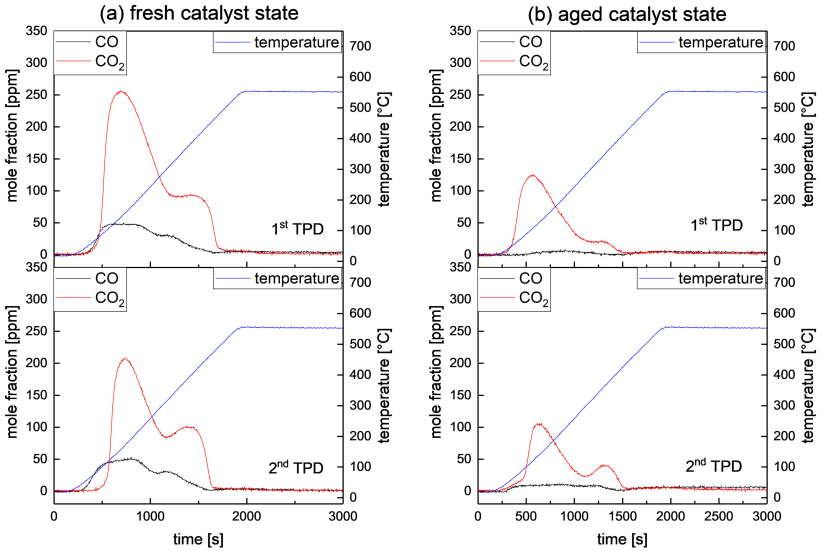

Figure A.10: Time responses during temperature programmed desorption of chemisorbed CO/CO_2 on the Pd/Al_2O_3 catalyst for (a) the fresh state and (b) after light-off experiments. Measurements in fresh and aged states were consecutively repeated twice ($1^{st}/2^{nd}$) TPD.

B Appendix: Complementary Derivations

B.1 Calculation of the Catalytic Active Surface Area

This section shows the derivations on the correlations for $A^{\mathrm{l}}_{\mathrm{PdO}}$. The catalytic surface area of PdO was back calculated from experimental information on the dispersion of the reduced phase of Pd via chemisorption measurements and from experimental information on the PdO particle size. For the correlations also data given in [77, 83, 89, 97, 136, 211] is used.

The catalytic active surface area for the reduced surface of palladium can be expressed in terms of dispersion, surface site-density and total amount of catalytic active material:

$$A^{\mathrm{l}}_{\mathrm{Pd}} = N^{0}_{\mathrm{Pd}} \cdot \frac{D_{\mathrm{Pd}}}{\Gamma_{\mathrm{Pd}}} \tag{B.1}$$

For the oxidized surface of PdO, the catalytic active surface area can be expressed analogously to Eq. (B.1), however the basis for evaluating the amount of sites on the surface from dispersion should be the total sum of the palladium and oxygen atoms loaded on the surface:

$$A^{\mathrm{l}}_{\mathrm{PdO}} = \left(N^{0}_{\mathrm{Pd}} + N^{0}_{\mathrm{O}}\right) \cdot \frac{D_{\mathrm{PdO}}}{\Gamma_{\mathrm{PdO}}} \tag{B.2}$$

The dispersions in Eq. (B.1) and (B.2) are defined as ratio of sites on the surface to the total amount of catalytic active material:

$$D_{\mathrm{Pd}} = \frac{N^{\mathrm{surf,Pd}}_{\mathrm{Pd}}}{N^{0}_{\mathrm{Pd}}} \tag{B.3}$$

$$D_{\mathrm{PdO}} = \frac{N^{\mathrm{surf,PdO}}_{\mathrm{Pd}} + N^{\mathrm{surf,PdO}}_{\mathrm{O}}}{N^{0}_{\mathrm{Pd}} + N^{0}_{\mathrm{O}}} \tag{B.4}$$

Since the bulk lattice structure of the tetragonal PdO unit cell has equal amounts of oxygen and palladium atoms, it follows that $N_{\mathrm{Pd}}^{\mathrm{surf,PdO}} + N_{\mathrm{O}}^{\mathrm{surf,PdO}} = 2 \cdot N_{\mathrm{Pd}}^{\mathrm{surf,Pd}}$ and $N_{\mathrm{Pd}}^{0} + N_{\mathrm{O}}^{0} = 2 \cdot N_{\mathrm{Pd}}^{0}$. Taking the latter result into account and dividing Eq. (B.2) by Eq. (B.1) gives after rearranging:

$$A_{\mathrm{PdO}}^{\mathrm{l}} = 2 \cdot \left(\frac{D_{\mathrm{PdO}}}{D_{\mathrm{Pd}}} \right) \cdot \left(\frac{\Gamma_{\mathrm{Pd}}}{\Gamma_{\mathrm{PdO}}} \right) \cdot A_{\mathrm{Pd}}^{\mathrm{l}} \tag{B.5}$$

Furthermore, the surface site density is related to the unit surface area of the corresponding facet by $\Gamma = \frac{1}{a_{\mathrm{m}} \cdot N_{\mathrm{a}}}$, with $N_{\mathrm{a}} = 6.022 \times 10^{23}\,\mathrm{mol}^{-1}$, the Avogadro constant. The dispersion is expressed under the assumption of hemispherical particles shape, by $D = 6 \cdot \left(\frac{v_{\mathrm{m}}}{a_{\mathrm{m}}} \right) \cdot \frac{1}{d_{\mathrm{p}}}$. Thus, the surface site density and the dispersion ratios can be expressed as:

$$\frac{D_{\mathrm{PdO}}}{D_{\mathrm{Pd}}} = \left(\frac{v_{\mathrm{m,PdO}}}{v_{\mathrm{m,Pd}}} \right) \cdot \left(\frac{a_{\mathrm{m,Pd}}}{a_{\mathrm{m,PdO}}} \right) \cdot \left(\frac{d_{\mathrm{Pd}}^{\mathrm{l}}}{d_{\mathrm{PdO}}^{\mathrm{l}}} \right) \tag{B.6}$$

$$\frac{\Gamma_{\mathrm{Pd}}}{\Gamma_{\mathrm{PdO}}} = \left(\frac{a_{\mathrm{m,PdO}}}{a_{\mathrm{m,Pd}}} \right) \tag{B.7}$$

Replacing terms defined in Eq. (B.6) and (B.7) for Eq. (B.5) gives

$$A_{\mathrm{PdO}}^{\mathrm{l}} = 2 \cdot \left(\frac{v_{\mathrm{m,PdO}}}{v_{\mathrm{m,Pd}}} \right) \cdot \left(\frac{d_{\mathrm{Pd}}^{\mathrm{l}}}{d_{\mathrm{PdO}}^{\mathrm{l}}} \right) \cdot A_{\mathrm{Pd}}^{\mathrm{l}} \tag{B.8}$$

Step (1): Oxidation without fracturing

Assuming hemispherical particles, the particle volume can be expressed as spherical volume, $V_{\mathrm{p}} = \frac{\pi}{6} \cdot d_{\mathrm{p}}^{3}$. Thus, the molar volume ratio in Eq. (B.8) is also given in terms of the particle diameter ratio as

$$\frac{v_{\mathrm{m,PdO}}}{v_{\mathrm{m,Pd}}} = \frac{1}{2} \cdot \left(\frac{d_{\mathrm{PdO}}^{\mathrm{l}}}{d_{\mathrm{Pd}}^{\mathrm{l}}} \right)^{3} \tag{B.9}$$

Alternatively, the particle diameter ratio is given as

$$\frac{d_{\mathrm{Pd}}^{\mathrm{l}}}{d_{\mathrm{PdO}}^{\mathrm{l}}} = \sqrt[3]{\frac{v_{\mathrm{m,Pd}}}{2 \cdot v_{\mathrm{m,PdO}}}} \tag{B.10}$$

$$= 1.19 \tag{B.11}$$

which is equivalent to Eq. (5.73), and Eq. (B.8) can thus be further simplified to

$$A^{\mathrm{l}}_{\mathrm{PdO}} = \left(\frac{d^{\mathrm{l}}_{\mathrm{PdO}}}{d^{\mathrm{l}}_{\mathrm{Pd}}}\right)^{2} \cdot A^{\mathrm{l}}_{\mathrm{Pd}} \tag{B.12}$$

$$= \left(\frac{2 \cdot v_{\mathrm{m,PdO}}}{v_{\mathrm{m,Pd}}}\right)^{2/3} \cdot A^{\mathrm{l}}_{\mathrm{Pd}} \tag{B.13}$$

$$= 1.41 \cdot A^{\mathrm{l}}_{\mathrm{Pd}} \tag{B.14}$$

which is also equivalent to Eq. (5.71) in the main text.
The average molar unit cell volume per bulk atom for bulk PdO was calculated according to the unit cell crystal data given in Tab. 5.3 as $v_{\mathrm{m,PdO}} = \frac{1}{4} \cdot a^2 \cdot c$. Analogously, the average unit surface area per surface atom for the PdO(101) facet was calculated according to $a_{\mathrm{m,PdO}} = \frac{1}{4} \cdot x_1 \cdot x_2$.

Step (2): Fracturing into smaller hemispherical particles

The oxidation process of reduced Pd particles is accompanied by a gradual fracturing into smaller particles which form PdO aggregates. Assuming that the volume and hemispherical shape of the hypothetical non disrupted PdO particle phase is conserved in form of aggregates of smaller PdO particles, gives an additional expression to calculate the catalytic surface area of the disrupted PdO phase (superindex s for small particles) in terms of the particle ratio.
Due to shape conservation, the particle volume ratio of a single large particle and $n^{\mathrm{s}}_{\mathrm{p}}$ small PdO particles is given as

$$n^{\mathrm{s}}_{\mathrm{p}} = \frac{V^{\mathrm{l}}_{\mathrm{PdO}}}{V^{\mathrm{s}}_{\mathrm{PdO}}} \tag{B.15}$$

$$= \left(\frac{d^{\mathrm{l}}_{\mathrm{PdO}}}{d^{\mathrm{s}}_{\mathrm{PdO}}}\right)^{3} \tag{B.16}$$

$$= \left(\frac{d^{\mathrm{l}}_{\mathrm{PdO}}}{d^{\mathrm{s}}_{\mathrm{PdO}}}\right) \cdot \frac{A^{\mathrm{l}}_{\mathrm{PdO}}}{A^{\mathrm{s}}_{\mathrm{p,PdO}}} \tag{B.17}$$

Replacing $d^{\mathrm{l}}_{\mathrm{PdO}}$ in Eq. (B.17) by the expression in Eq. (B.10) and solving for the total surface area of the collective of all small PdO particles, $A^{\mathrm{s}}_{\mathrm{PdO}} = n^{\mathrm{s}}_{\mathrm{p}} \cdot A^{\mathrm{s}}_{\mathrm{p,PdO}}$,

leads to an expression in terms of the particle size ratio, equivalent to Eq. (5.74) of the main text:

$$A^{\mathrm{s}}_{\mathrm{PdO}} = n^{\mathrm{s}}_{\mathrm{p}} \cdot A^{\mathrm{s}}_{\mathrm{p,PdO}} \tag{B.18}$$

$$= \left(\frac{d^{\mathrm{l}}_{\mathrm{Pd}}}{d^{\mathrm{s}}_{\mathrm{PdO}}} \right) \cdot \sqrt[3]{\frac{2 \cdot v_{\mathrm{m,PdO}}}{v_{\mathrm{m,Pd}}}} \cdot A^{\mathrm{l}}_{\mathrm{PdO}} \tag{B.19}$$

$$= \left(\frac{d^{\mathrm{l}}_{\mathrm{Pd}}}{d^{\mathrm{s}}_{\mathrm{PdO}}} \right) \cdot 1.19 \cdot A^{\mathrm{l}}_{\mathrm{PdO}} \tag{B.20}$$

B.2 Thermodynamic Consistency Adjustment

Parts of the thermodynamic adjustment and minimization procedure have been described in [159, 160].

For the case of a rate constant expression of the empirical form of Eq. (5.28), the De Donder relations can be applied to connect kinetic reaction rate parameters $E_{a,k}, \beta_k$ and A_k, with thermodynamics in terms of Gibbs free energy, $\Delta_R G_k$, of the reaction step k and corresponding Gibbs free energies, G_i, of species i, respectively.

For $k = 1, ..., K_s$ reversible reactions, the thermodynamic equilibrium constraints under ideal conditions can be written as:

$$\ln K_k(T) = \left(\frac{-\Delta_R G_k}{RT}\right) \tag{B.21}$$

$$= \ln\left(\frac{k_{f,k}}{k_{r,k}} \cdot \frac{1}{Q_k^0}\right) \tag{B.22}$$

In Eq. (B.21), K_k is the activity (pressure) based equilibrium constant. The Gibbs free energy of reaction step $k, \Delta_R G_k$, is expressed according to the Arrhenius expression Eq. (5.28) and connects kinetics with thermodynamics.

$$\left(\frac{-\Delta_R G_k}{RT}\right) = \ln\left(\frac{A_{f,k}}{A_{r,k}} \cdot \frac{1}{Q_k^0}\right) + (\beta_{f,k} - \beta_{r,k}) \cdot \ln\left(\frac{T}{1\,\mathrm{K}}\right) - \frac{\left(\tilde{E}_{f,k} - \tilde{E}_{r,k}\right)}{RT} \tag{B.23}$$

$$= -\sum_{i=1}^{N_s+N_g} \left(\nu_{i,k}^{''} - \nu_{i,k}^{'}\right) \cdot \left(\frac{G_i(T)}{RT}\right) \tag{B.24}$$

Noting that $\tilde{E}_{f,k}$ and $\tilde{E}_{r,k}$ are coverage dependent activation energies of step k and RHS of Eq. (B.23) has a temperature dependency of the following form

$$\left(\frac{-\Delta_R G_k(T)}{RT}\right) = \underbrace{\tilde{a}_k + \tilde{b}_k \cdot \ln(T) + \tilde{c}_k \cdot \frac{1}{T}}_{=z_k(T)} \tag{B.25}$$

where $\tilde{a}_k$, $\tilde{b}_k$ and $\tilde{c}_k$ are constants equal to

$$\tilde{a}_k = \ln(A_{f,k}) - \ln(A_{r,k}) - \ln\left(Q_k^0\right) \tag{B.26}$$

$$\tilde{b}_k = \beta_{f,k} - \beta_{r,k} \tag{B.27}$$

$$\tilde{c}_k = -\frac{\left(\tilde{E}_{f,k} - \tilde{E}_{r,k}\right)}{R} \tag{B.28}$$

The species specific Gibbs free energies, G_i in Eq. (B.24), can be described in terms of enthalpies H_i and entropies S_i according to

$$G_i = H_i - T \cdot S_i \tag{B.29}$$

A main characteristic of the mean-field approximation is that all surface sites are treated equivalently in order to fulfill uniformity of the surface; each surface intermediate has a well-defined value of its Gibbs free energy on the surface. Thus, the set of reaction rate parameters $(A_k, \beta_k, E_{\mathrm{a},k})$ cannot completely be chosen independently anymore, if the Gibbs free energy, G_i, is described in terms of species specific heat capacities $c_{\mathrm{p},i}$.

$$G_i = G_i^{\mathrm{ref}} + \int_{T_{\mathrm{ref}}}^{T} c_{\mathrm{p},i} dT - T \cdot \int_{T_{\mathrm{ref}}}^{T} \frac{c_{\mathrm{p},i}}{T} dT \tag{B.30}$$

Assuming $c_{\mathrm{p},i}$ is approximately constant over the temperature interval $[T, T_{\mathrm{ref}}]$, $H_i(T)$ and $S_i(T)$ are given as

$$H_i(T) = \left(H_i^{\mathrm{ref}} - \bar{c}_{\mathrm{p},i} \cdot T_{\mathrm{ref}}\right) + \bar{c}_{\mathrm{p},i} \cdot T \tag{B.31}$$

$$S_i(T) = \left(S_i^{\mathrm{ref}} - \bar{c}_{\mathrm{p},i} \cdot \ln(T_{\mathrm{ref}})\right) + \bar{c}_{\mathrm{p},i} \cdot \ln(T) \tag{B.32}$$

Thus, the species specific Gibbs free energies, $G_i(T)$, expressed as a function of temperature, assume the following form:

$$\frac{G_i}{RT} = \frac{G_i^{\mathrm{ref}}}{RT} + \frac{\bar{c}_{\mathrm{p},i}}{R} \cdot \left[\left(1 - \frac{T_{\mathrm{ref}}}{T}\right) - \ln\left(\frac{T}{T_{\mathrm{ref}}}\right)\right] \tag{B.33}$$

$$= \underbrace{a_i + b_i \cdot \ln(T) + c_i \cdot \frac{1}{T}}_{=y_i(T)} \tag{B.34}$$

where a_i, b_i and c_i are constants from which the species specific temperature averaged heat-capacity $\bar{c}_{\mathrm{p},i}$, and the reference state enthalpy H_i^{ref} and entropy S_i^{ref} of the corresponding surface species at $T_{\mathrm{ref}} = 298\,\mathrm{K}$ are determined in order to obtain the temperature dependent values for $H_i(T)$ and $S_i(T)$:

$$a_i = \frac{\bar{c}_{\mathrm{p},i}}{R} \cdot (1 + \ln(T_{\mathrm{ref}})) - \frac{S_i^{\mathrm{ref}}}{R} \tag{B.35}$$

$$b_i = -\frac{\bar{c}_{\mathrm{p},i}}{R} \tag{B.36}$$

$$c_i = \frac{H_i^{\mathrm{ref}}}{R} - \frac{\bar{c}_{\mathrm{p},i}}{R} \cdot T_{\mathrm{ref}} \tag{B.37}$$

Inserting Eq. (B.25) and Eq. (B.34) into Eq. (B.23) and factoring out the known gas-phase potentials yields a system of constraint equations which needs to be fulfilled if the rate constants are thermodynamically consistent formulated, i.e. if the correction terms, $x_k(T)$ (with the same temperature dependent form as $z_k(T)$ and $y_i(T)$), introduced into an initially inconsistent set of rate parameters, are minimized:

$$x_{\mathrm{f},k}(T) - x_{\mathrm{r},k}(T) = \underbrace{\left[-z_k(T) - \sum_{i=1}^{N_\mathrm{g}} \nu_{i,k} \cdot G_i(T)\right]}_{=c_k(T)} - \sum_{i=1}^{N_\mathrm{s}} \nu_{i,k} \cdot y_i(T) \tag{B.38}$$

Assuming $c_k(T)$ has approximately the same temperature dependent form over a sufficient temperature interval $[T_1, T_2]$ as $z_k(T)$, $y_i(T)$ and $x_k(T)$, $c_k(T)$ can be fitted against a function of the same form, since its value is known for each temperature:[1]

$$x_{\mathrm{f},k}(T) - x_{\mathrm{r},k}(T) = \left[a_{\mathrm{c},k} + b_{\mathrm{c},k} \cdot \ln(T) + c_{\mathrm{c},k} \cdot \frac{1}{T}\right] - \sum_{i=1}^{N_\mathrm{s}} \nu_{i,k} \cdot y_i(T) \tag{B.39}$$

With the aforementioned assumptions, Eq. (B.39) can be decomposed into $3 \cdot K_\mathrm{s}$ constraints by comparing coefficients:

$$g_{\mathrm{a},k} = a_{\mathrm{x_r},k} - a_{\mathrm{x_f},k} + a_{\mathrm{c},k} - \sum_{i=1}^{N_\mathrm{s}} \nu_{i,k} \cdot a_i = 0 \tag{B.40}$$

$$g_{\mathrm{b},k} = b_{\mathrm{x_r},k} - b_{\mathrm{x_f},k} + b_{\mathrm{c},k} - \sum_{i=1}^{N_\mathrm{s}} \nu_{i,k} \cdot b_i = 0 \tag{B.41}$$

$$g_{\mathrm{c},k} = c_{\mathrm{x_r},k} - c_{\mathrm{x_f},k} + c_{\mathrm{c},k} - \sum_{i=1}^{N_\mathrm{s}} \nu_{i,k} \cdot c_i = 0 \tag{B.42}$$

In order to solve for the $3{\cdot}(N_\mathrm{s}{+}2{\cdot}K_\mathrm{s})$ unknown coefficients, p, in Eq. (B.40)-(B.42) with

$$p = [(a,b,c)_{\mathrm{x_f},k=1,\ldots,K_s},\ (a,b,c)_{\mathrm{x_r},k=1,\ldots,K_s},\ (a,b,c)_{i=1,\ldots,N_s}] \tag{B.43}$$

an objective function is formulated via a weighted sum of squared residuals

$$\Phi(p) = \sum_{k=1}^{K_\mathrm{s}} \left[w_{\mathrm{f},k} \cdot \|x_{\mathrm{f},k}\|^2 + w_{\mathrm{r},k} \cdot \|x_{\mathrm{r},k}\|^2\right] \tag{B.44}$$

[1] The gas-phase G_i are given in terms of temperature dependent NASA polynomials [222].

which can be solved by the method of Lagrange multipliers. In Eq. (B.44), $\|x_k\|^2$, is defined by the L^2-norm over the temperature interval $[T_1, T_2]$:

$$\|x\|^2 = \int_{T_1}^{T_2} x(T)^2 dT \tag{B.45}$$

$$= \int_{T_1}^{T_2} \left[a + b \cdot \ln(T) + c \cdot \frac{1}{T}\right]^2 dT \tag{B.46}$$

$$= \left[-\frac{c^2}{T} + \left(a^2 - 2ab + 2b^2\right) \cdot T + 2ac \ln(T)\right]_{T_1}^{T_2} \tag{B.47}$$

$$+ \quad \left[2(a-b)bT \ln(T) + b(c+bT) \ln^2(T)\right]_{T_1}^{T_2}$$

Eq. (B.47) can be integrated analytically. The required changes in the correction terms of the rate constants, $x_{\mathrm{f},k}$ and $x_{\mathrm{r},k}$, need to be minimal and fullfill the constraints in order to obtain optimality, i.e.

$$\min_p \ \Phi(p) \tag{B.48}$$

$$\text{s.t. } g_k(p) = 0 \quad k = 1, ..., 3K_\mathrm{s} \tag{B.49}$$

The Lagrangian of the problem formulation is found based on the objective function Eq. (B.44) and the $3 \cdot K_\mathrm{s}$ constraints from Eqs. (B.40)-(B.42) as

$$L(p, \lambda) = \Phi(p) - \sum_{k=1}^{K_\mathrm{s}} \left[\lambda_{\mathrm{a},k} \cdot g_{\mathrm{a},k} + \lambda_{\mathrm{b},k} \cdot g_{\mathrm{b},k} + \lambda_{\mathrm{c},k} \cdot g_{\mathrm{c},k}\right] \tag{B.50}$$

with λ_k, the $3 \cdot K_s$ unknown Lagrange multipliers. To the end, a system of linear equations is found once the Karush-Kuhn-Tucker conditions are derived:

$$\frac{\partial L}{\partial \lambda_k} = g_k \stackrel{!}{=} 0 \quad k = 1, ..., 3K_s \tag{B.51}$$

$$\frac{\partial L}{\partial p_j} = \frac{\partial \Phi}{\partial p_j} - \sum_{k=1}^{K_\mathrm{s}} \left[\lambda_{\mathrm{a},k} \cdot \frac{\partial g_{\mathrm{a},k}}{\partial p_j} + \lambda_{\mathrm{b},k} \cdot \frac{\partial g_{\mathrm{b},k}}{\partial p_j} + \lambda_{\mathrm{c},k} \cdot \frac{\partial g_{\mathrm{c},k}}{\partial p_j}\right] \stackrel{!}{=} 0 \tag{B.52}$$

$$j = 1, ..., 3(2K_s + N_s)$$

The terms $\frac{\partial \Phi}{\partial p_j}$ in Eq. (B.52) require the evaluation of the partial derivatives of the L^2-norms as given in Eq. (B.47) and are given here for completeness:

$$\frac{\partial \|x\|^2}{\partial a} = [a \cdot 2T - b \cdot 2(T + T\ln(T)) + c \cdot 2\ln(T)]_{T_1}^{T2} \tag{B.53}$$

$$\frac{\partial \|x\|^2}{\partial b} = \left[a \cdot 2T(\ln(T) - 1) + b \cdot 4T(1 - \ln(T) + \frac{\ln^2(T)}{2}) + c \cdot \ln^2(T)\right]_{T_1}^{T2} \tag{B.54}$$

$$\frac{\partial \|x\|^2}{\partial c} = \left[a \cdot 2\ln(T) + b \cdot \ln^2(T) - c \cdot \frac{2}{T}\right]_{T_1}^{T2} \tag{B.55}$$

Solving the system of linear Eqs. (B.51)-(B.52) in terms of λ and p, yields the unknown necessary minimal correction factors, p, of the rate constants' parameters $(A_k, \beta_k, E_{\mathrm{a},k})$, as well as the unknown parameters of the thermodynamic potentials of the surface species $(c_{\mathrm{p},i}, H_i^{\mathrm{ref}}, S_i^{\mathrm{ref}})$, being thermodynamically consistent. This is achieved, once the selectable weights w_k in Eq. (B.44) have been chosen. Typically, for a surface reaction mechanism, $K_\mathrm{s} > N_\mathrm{s}$, and a minimum of at least $K_\mathrm{s} - (N_\mathrm{s} - 1)$ weights need to be set unequal to zero, as only $N_\mathrm{s} - 1$ surface species are linearly independent, in order to have the equation system not to be overdetermined (the potential of the free surface site(s) is set as reference value to zero.)[2].

The size of a weight for step k can be chosen accordingly, whether the energetic of the reaction is important (sensitive) to the reaction system or not, in the following way:

$$w_k \begin{cases} = 0 & \text{no changes in rate parameters} \quad \text{(B.56a)} \\ < 1 & \text{small changes in rate parameters} \quad \text{(B.56b)} \\ > 1 & \text{big changes in rate paramters} \quad \text{(B.56c)} \end{cases}$$

That way, the Ahrrenius parameters of important reactions should be determined as accurately as possible, e.g. from DFT calculations, while corresponding weights should be selected such that the energetic parameters are not adjusted too much, vs. parameters of less sensitive reactions can be adjusted to a greater extend by selecting their weights accordingly. The default weights for surface reactions are set to $w_k = 1$, while weights for adsorption steps are set to $w_k = 4$ to 8.

[2] The set of selected weights which can be set to zero cannot be chosen independently, since the system should satisfy linear independence.

B.3 The Degree of Oxidation Model for Phase Transition[3]

Derivation of Eq. (5.76)-(5.81) from the main text:

The volume of an aggregated spherical Pd/PdO particle, V_{mix}, where the single phases are geometrically arranged as conical sectoral aggregates (cf. Fig. B.1) is given by

$$V_{\mathrm{mix}} = V_{\mathrm{PdO}}^{\mathrm{sec}} + V_{\mathrm{Pd}}^{\mathrm{sec}} \tag{B.57}$$

$$= \frac{\pi}{6} \cdot d_{\mathrm{mix}}^3 \tag{B.58}$$

The sectoral volumes of the single phases can be expressed as volume equivalent spheres with equivalent diameters (d_{PdO}, d_{Pd}) for the single phases:

$$V_{\mathrm{PdO}}^{\mathrm{sec}} = V_{\mathrm{PdO}} \tag{B.59}$$

$$= \frac{\pi}{6} \cdot d_{\mathrm{PdO}}^3 \tag{B.60}$$

$$V_{\mathrm{Pd}}^{\mathrm{sec}} = V_{\mathrm{Pd}} \tag{B.61}$$

$$= \frac{\pi}{6} \cdot d_{\mathrm{Pd}}^3 \tag{B.62}$$

The diameter of the integrated Pd/PdO sphere is then given as

$$d_{\mathrm{mix}} = \sqrt[3]{\frac{6}{\pi} \cdot V_{\mathrm{mix}}} \tag{B.63}$$

$$= \left(d_{\mathrm{PdO}}^3 + d_{\mathrm{Pd}}^3\right)^{1/3} \tag{B.64}$$

$$= \begin{cases} d_{\mathrm{Pd}} & \text{for } d_{\mathrm{PdO}} \ll d_{\mathrm{Pd}} \quad \text{(B.65a)} \\ d_{\mathrm{PdO}} & \text{for } d_{\mathrm{Pd}} \ll d_{\mathrm{PdO}} \quad \text{(B.65b)} \end{cases}$$

In Eq. (B.63), d_{mix} is the spherical diameter of the combined Pd/PdO particle and d_{PdO} and d_{Pd} are equivalent diameters of the corresponding Pd and PdO phases, if they would be present as separate spheres.

[3] Parts of this chapter have been taken from [2] H. Stotz, L. Maier, A. Boubnov, A. T. Gremminger, J.-D. Grunwaldt and O. Deutschmann, Surface reaction kinetics of methane oxidation over PdO, *J. Catal.*, 370 (2019) 152-175.

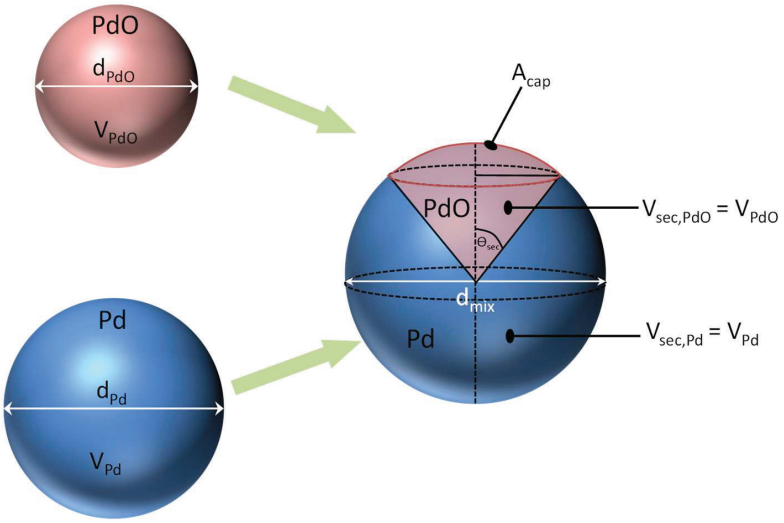

Figure B.1: Schematic showing an aggregated Pd/PdO spherical particle with sectoral arrangement of the single Pd and PdO phases. Figure adapted from Stotz et al. [2].

The sector volume and the outer surface area of the sectoral cap are given in terms of the sector angle, θ_{sec}, as shown in the sketch of Fig. B.1:

$$V^{\mathrm{sec}} = \frac{\pi}{12} \cdot d_{\mathrm{mix}}^3 \cdot (1 - \cos\theta_{\mathrm{sec}}) \tag{B.66}$$

$$S^{\mathrm{cap}} = \frac{\pi}{2} \cdot d_{\mathrm{mix}}^2 \cdot (1 - \cos\theta_{\mathrm{sec}}) \tag{B.67}$$

Using Eq. (B.66) with Eq. (B.64) and Eq. (B.60), and replacing θ_{sec} in Eq. (B.67) yields S^{cap} for the PdO phase in terms of the diameters d_{mix} and d_{PdO}:

$$S_{\mathrm{PdO}}^{\mathrm{cap}} = \pi \cdot \frac{d_{\mathrm{PdO}}^3}{\sqrt[3]{d_{\mathrm{PdO}}^3 + d_{\mathrm{Pd}}^3}} \tag{B.68}$$

For n aggregated Pd/PdO particles present on the catalyst support surface, the total cap surface areas are given by

$$A_{\mathrm{PdO}} = (n \cdot S_{\mathrm{PdO}}^{\mathrm{cap}}) \tag{B.69}$$

$$= \left(\frac{V_{\mathrm{PdO}}^{\mathrm{tot}}}{V_{\mathrm{PdO}}^{\mathrm{sec}}} \cdot S_{\mathrm{PdO}}^{\mathrm{cap}} \right) \tag{B.70}$$

The total volume of the n PdO sector elements is given by

$$(n \cdot V_{\mathrm{PdO}}^{\mathrm{sec}}) = V_{\mathrm{PdO}}^{\mathrm{tot}} \tag{B.71}$$

$$= X_{\mathrm{ox}} \cdot (2 \cdot N_{\mathrm{Pd}}^0) \cdot v_{\mathrm{m,PdO}} \tag{B.72}$$

Analogously, for n Pd sector elements we can write

$$(n \cdot V_{\mathrm{Pd}}^{\mathrm{sec}}) = (1 - X_{\mathrm{ox}}) \cdot N_{\mathrm{Pd}}^0 \cdot v_{\mathrm{m,Pd}} \tag{B.73}$$

With $X_{\mathrm{ox}} = 1$ if all Pd is present as PdO and $X_{\mathrm{ox}} = 0$ if only reduced Pd is present on the surface. Using the definitions in Eq. (B.72), (B.68) and (B.60) for Eq. (B.70) yields the total PdO surface area:

$$A_{\mathrm{PdO}} = X_{\mathrm{ox}} \cdot \left(2 \cdot N_{\mathrm{Pd}}^0\right) \cdot v_{\mathrm{m,PdO}} \frac{6}{\left(d_{\mathrm{PdO}}^3 + d_{\mathrm{Pd}}^3\right)^{1/3}} \tag{B.74}$$

Note: N_{Pd}^0 is the initial number of moles of Pd used on the Al_2O_3 support, i.e. the Pd loading. Assuming the number of Pd and PdO particles is the same, i.e. no partial break-up of aggregated Pd/PdO particles occurs, we can equate Eq. (B.72) with (B.73) for n, and express the sector volumes for Pd and PdO in

terms of the equivalent diameters of the single phase spherical particle volumes, yielding the Pd-to-PdO spherical equivalent particle diameter ratio:

$$\frac{d_{\mathrm{Pd}}}{d_{\mathrm{PdO}}} = \left[\left(\frac{v_{\mathrm{m,Pd}}}{2 \cdot v_{\mathrm{m,PdO}}}\right) \cdot \left(\frac{1 - X_{\mathrm{ox}}}{X_{\mathrm{ox}}}\right)\right]^{1/3} \tag{B.75}$$

Eq. (B.75) is only valid for

$$0 < d_{\mathrm{PdO}} < d_{\mathrm{PdO}}^{\mathrm{max}} \tag{B.76}$$

$$0 < d_{\mathrm{Pd}} < d_{\mathrm{Pd}}^{\mathrm{max}} \tag{B.77}$$

$$0 < X_{\mathrm{ox}} < 1 \tag{B.78}$$

Putting Eq. (B.75) for d_{PdO} into Eq. (B.74) and applying the definition for the surface site density, $a_{\mathrm{m,PdO}} = \frac{1}{\Gamma_{\mathrm{PdO}}}$, we arrive at

$$A_{\mathrm{PdO}} = X_{\mathrm{ox}}(T) \cdot \left(2 \cdot N_{\mathrm{Pd}}^{0}\right) \cdot \left(\frac{v_{\mathrm{m,PdO}}}{a_{\mathrm{m,PdO}}} \cdot \frac{6}{\Gamma_{\mathrm{PdO}}}\right) \cdot \frac{1}{d_{\mathrm{PdO}}(T)} \cdot f_{\mathrm{ox}}(T) \tag{B.79}$$

with

$$f_{\mathrm{ox}}(T) = \frac{1}{\left[1 + \left(\frac{v_{\mathrm{m,Pd}}}{2 \cdot v_{\mathrm{m,PdO}}}\right) \cdot \left(\frac{1 - X_{\mathrm{ox}}(T)}{X_{\mathrm{ox}}(T)}\right)\right]^{1/3}} \tag{B.80}$$

Eq. (B.79) is equivalent to Eq. (5.80) in section 5.3.3.

The derivation is consistent in the sense that no losses in the total amount of Pd during oxidation occurs ($0 < X_{\mathrm{ox}} < 1$). The number of Pd and PdO aggregates remains the same at a given condition during oxidation but the total number of aggregated Pd/PdO particles can change depending on the chosen profiles for $X_{\mathrm{ox}}(T)$ and $d_{\mathrm{PdO}}(T)$, which indirectly accounts for re-dispersion of the aggregated Pd/PdO particles. Additional fragmentation, surface roughening or particle shape change effects for PdO are not considered in the derivations. However, the model does consider changes in particle size due to lattice expansion upon PdO oxide formation for the aggregated Pd/PdO particle diameter, d_{mix}, and hence in the calculations for the catalytic surface area of the PdO phase.

B.3.1 Limiting cases:

Note Eq. (B.75) cannot be used, to directly evaluate the limiting particle sizes in case of $X_{\mathrm{ox}} = 0$ nor $X_{\mathrm{ox}} = 1$.

Case (a): All Pd is present as oxide ($X_{\mathrm{ox}} \to 1$)

Instead of evaluating Eq. (B.75), we can use Eq. (B.72) with Eq. (B.60) and can write for PdO:

$$n_{\mathrm{PdO}}(X_{\mathrm{ox}}) = \frac{X_{\mathrm{ox}} \cdot \left(2 \cdot N^0_{\mathrm{Pd}}\right) \cdot v_{\mathrm{m,PdO}}}{\frac{\pi}{6} \cdot d_{\mathrm{PdO}}(X_{\mathrm{ox}})^3} \tag{B.81}$$

The number of PdO particles when X_{ox} approaches one is then given from the reference PdO particle diameter, $d^{\mathrm{max}}_{\mathrm{PdO}} = d_{\mathrm{PdO}}(X_{\mathrm{ox}} \to 1)$:

$$n^{\mathrm{max}}_{\mathrm{PdO}}(X_{\mathrm{ox}} \to 1) = \frac{\left(2 \cdot N^0_{\mathrm{Pd}}\right) \cdot v_{\mathrm{m,PdO}}}{\frac{\pi}{6} \cdot d^{\mathrm{max}\,3}_{\mathrm{PdO}}} \tag{B.82}$$

Plugging Eq. (B.82) for n_{PdO} into Eq. (B.81) and solving for d_{PdO} gives approximately the PdO particle size in the limiting case when X_{ox} is close to 1:

$$d_{\mathrm{PdO}}(X_{\mathrm{ox}} \to 1) \approx d^{\mathrm{max}}_{\mathrm{PdO}} \cdot \sqrt[3]{X_{\mathrm{ox}}} \tag{B.83}$$

Case (b): All Pd is present as metal ($X_{\mathrm{ox}} \to 0$)

Similarly for Pd, using Eq. (B.73) with (B.62) we arrive at:

$$n_{\mathrm{Pd}}(X_{\mathrm{ox}}) = \frac{(1 - X_{\mathrm{ox}}) \cdot N^0_{\mathrm{Pd}} \cdot v_{\mathrm{m,Pd}}}{\frac{\pi}{6} \cdot d_{\mathrm{Pd}}(X_{\mathrm{ox}})^3} \tag{B.84}$$

and

$$n^{\mathrm{max}}_{\mathrm{Pd}}(X_{\mathrm{ox}} \to 0) = \frac{1 \cdot N^0_{\mathrm{Pd}} \cdot v_{\mathrm{m,Pd}}}{\frac{\pi}{6} \cdot d^{\mathrm{max}3}_{\mathrm{Pd}}} \tag{B.85}$$

The particle size of Pd in the limiting case when nearly all Pd is reduced is then given as:

$$d_{\mathrm{Pd}}(X_{\mathrm{ox}} \to 0) \approx d^{\mathrm{max}}_{\mathrm{Pd}} \cdot \sqrt[3]{1 - X_{\mathrm{ox}}} \tag{B.86}$$

B.3.2 Profiles for simulation of the conversion hysteresis during cool down:

Temperature dependent profiles (cf. Fig. B.2) for crystallite size and amount of PdO have been approximated based on the profile shapes of the experimentally determined values from Datye et al. [53]. The temperature dependent curve shape for $X_{\mathrm{ox}}(T)$ was approximated according a generalized logistic function:

$$X_{\mathrm{ox}}(T) = \frac{X_{\mathrm{ox}}^{\max}}{\left[1 + \exp\left[k \cdot (T - T_{50})\right]\right]^{1/\alpha}} \tag{B.87}$$

Where $X_{\mathrm{ox}}^{\max} = 1.0$, $k = 0.035$, $\alpha = 0.3$ and $T_{50} = 520\,^{\circ}\mathrm{C}$ have been used. For the temperature dependent profile of $d_{\mathrm{PdO}}(T)$, a generalized power function has been used:

$$d_{\mathrm{PdO}}(T) = d_{\mathrm{ox}}^{\max} \cdot \left[b \cdot \frac{T - T_2}{T_1 - T_2}\right]^{1/\beta} \tag{B.88}$$

Therein, $d_{\mathrm{ox}}^{\max} = 25\,\mathrm{nm}$, $b = 1$, $\beta = 3$, $T_1 = 380\,^{\circ}\mathrm{C}$ and $T_2 = 600\,^{\circ}\mathrm{C}$ have been used.

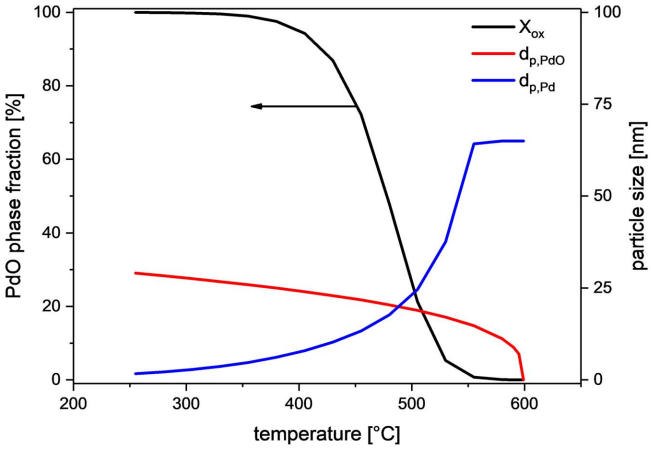

Figure B.2: Profiles for PdO phase fraction, and particle size of PdO and Pd, as assumed for evaluation of the degree of oxidation model. Figure adapted from Stotz et al. [2].

C Appendix: Complementary Methods, Variables and Definitions

C.1 Conversion, Selectivity and Yield

Conversion, selectivity and yield have been used as selected performance parameters to analyze the behavior of the reaction system (cf. Section 6.1.5, 4.6.3, 6.1.1 and 6.2.1).

C.1.1 Conversion

Conversion was defined for reactants, as the ratio of the amount of moles of reactant species, j_R, converted into products, to the amount of moles present at the reactor inlet, and can be expressed either in terms of molar flow rates or corresponding weight fractions:

$$X_{j_\mathrm{R}} = \frac{\dot{N}^{+}_{j_\mathrm{R}} - \dot{N}_{j_\mathrm{R}}(z)}{\dot{N}^{+}_{j_\mathrm{R}}} \tag{C.1}$$

$$= 1 - \frac{w_{j_\mathrm{R}}(z)}{w^{+}_{j_\mathrm{R}}} \tag{C.2}$$

For evaluation in terms of mole fractions, the increase or decrease in the total number of moles due to the reaction (volume expansion or contraction of the reaction mixture), needs to be taken into account.

$$X_{j_\mathrm{R}} = \frac{x^{+}_{j_\mathrm{R}} - x_{j_\mathrm{R}}(z) \cdot \gamma_\mathrm{I}}{x^{+}_{j_\mathrm{R}}} \tag{C.3}$$

$$\gamma_\mathrm{I} = \frac{x^{+}_\mathrm{I}}{x_\mathrm{I}(z)} \tag{C.4}$$

Where γ_{I} is defined as the dilution ratio of an inert component, I, between reactor inlet + and position z. According to the method of internal standard, N_2 is chosen as the internal standard component in this work. If the inert dilution of the reaction mixture is large, then γ_{I} approaches one, and Eq. (C.2) can be written in terms of mole fractions instead.

$$X_{j_{\mathrm{R}}}\left(\gamma_{\mathrm{I}} \to 1\right) \approx 1 - \frac{x_{j_{\mathrm{R}}}(z)}{x^{+}_{j_{\mathrm{R}}}} \tag{C.5}$$

For element wise examinations, conversion can be defined analogously based on a particular element k occurring in all reactants $\{j_{\mathrm{R}}\}$ containing element k:

$$X^{k}_{\{j_{\mathrm{R}}\}} = \frac{\sum_{j_{\mathrm{R}}} n_{k,j_{\mathrm{R}}} \cdot \left(x^{+}_{j_{\mathrm{R}}} - x_{j_{\mathrm{R}}}(z) \cdot \gamma_{\mathrm{I}}\right)}{\sum_{j_{\mathrm{R}}} \left(n_{k,j_{\mathrm{R}}} \cdot x^{+}_{j_{\mathrm{R}}}\right)} \tag{C.6}$$

Where, $n_{k,j_{\mathrm{R}}}$ is the atomic number of element k in reactant species j_{R}.

C.1.2 Selectivity

Selectivity was defined on an elemental basis and taken as the ratio of the amount of element k produced in product(s), j_{P}, to the total amount of element k in reactants $\{j_{\mathrm{R}}\}$, converted.

$$S^{k,\{j_{\mathrm{R}}\}}_{j_{\mathrm{P}}} = \frac{n_{k,j_{\mathrm{P}}} \cdot \left(x_{j_{\mathrm{P}}}(z) \cdot \gamma_{\mathrm{I}} - x^{+}_{j_{\mathrm{P}}}\right)}{\sum_{j_{\mathrm{R}}} n_{k,j_{\mathrm{R}}} \cdot \left(x^{+}_{j_{\mathrm{R}}} - x_{j_{\mathrm{R}}}(z) \cdot \gamma_{\mathrm{I}}\right)} \tag{C.7}$$

C.1.3 Yield

Yield was defined on an elemental basis and taken as the ratio of the amount of element k produced in product species, j_{P}, to the amount of element k present in reactant species, j_{R}, fed to the reactor.

$$Y^{k,\{j_{\mathrm{R}}\}}_{j_{\mathrm{P}}} = \frac{n_{k,j_{\mathrm{P}}} \cdot \left(x_{j_{\mathrm{P}}}(z) \cdot \gamma_{\mathrm{I}} - x^{+}_{j_{\mathrm{P}}}\right)}{\sum_{j_{\mathrm{R}}} \left(n_{k,j_{\mathrm{R}}} \cdot x^{+}_{j_{\mathrm{R}}}\right)} \tag{C.8}$$

It can be seen from the definitions of Eq. (C.6, C.7) and (C.8), that the following relation holds:

$$Y^{k,\{j_{\mathrm{R}}\}}_{j_{\mathrm{P}}} = S^{k,\{j_{\mathrm{R}}\}}_{j_{\mathrm{P}}} \cdot X^{k}_{\{j_{\mathrm{R}}\}} \tag{C.9}$$

C.2 External Transport Limitations - Damköhler Number Calculation

This section serves as supplemental information to section 6.1.2 in calculating the Damköhler number [223–225]. Quantification of the extend of external mass transport limitations can be obtained either experimentally or evaluated based on simulated quantities.

Given a flat catalytic plate under isothermal conditions the external effectiveness factor can be defined as the ratio of the rate of reaction with transport limitations (called observed (obs) rate)

$$r_j^{\text{obs}} = k_j^{\text{obs}} \cdot c_j^{\text{b}} = \left[\frac{mol_j}{m^2 \cdot s}\right] \tag{C.10}$$

to the rate of reaction without any transport limitations (called intrinsic (itc) rate of reaction evaluated at bulk conditions) which is equivalent to the the maximum possible intrinsic rate of consumption, r_j^{itc}, of species j, evaluated at the gas-phase bulk conditions:

$$r_{j,\max}^{\text{itc}} = r_j^{\text{itc}}\left(c_j^{\text{b}}\right) \tag{C.11}$$

$$= k_j^{\text{itc}} \cdot c_j^{\text{b}} = \left[\frac{mol_j}{m^2 \cdot s}\right] \tag{C.12}$$

The ratio of both defines the external effectiveness factor for reactant species j:

$$\eta_{\text{ext},j} = \frac{r_j^{\text{obs}}}{r_{j,\max}^{\text{itc}}} \tag{C.13}$$

$$= \frac{k_j^{\text{obs}}}{k_j^{\text{itc}}} \tag{C.14}$$

The mass-transfer flux of species j at the species boundary layer resulting from external concentration differences between gas bulk c_j^{b} and surface c_j^{s} is related to the mass-transfer coefficient $k_{\text{m},j} = \left[\frac{m}{s}\right]$

$$j_j = k_{\text{m},j} \cdot \left(c_j^{\text{b}} - c_j^{\text{s}}\right) = \left[\frac{mol_j}{m^2 \cdot s}\right] \tag{C.15}$$

At steady-state the mass-transfer flux at the interface between catalytic wall and gas-phase boundary layer should be equal to the intrinsic rate at the surface given a 1$^{\text{st}}$-order reaction in j:

$$r_j^{\text{itc}} = j_j \tag{C.16}$$

$$k_j^{\text{itc}} \cdot c_j^{\text{s}} = k_{\text{m},j} \cdot \left(c_j^{\text{b}} - c_j^{\text{s}}\right) \tag{C.17}$$

The ratio of intrinsic rate constant k_j^{itc} to mass-transfer coefficient $k_{\mathrm{m},j}$ defines the second Damköhler-number for a given 1$^{\mathrm{st}}$-order reaction in reactant species j, which gives the ratio of time scale of external mass transfer to the time scale of the reaction:

$$Da_{\mathrm{II},j} = \frac{k_j^{\mathrm{itc}}}{k_{\mathrm{m},j}} \tag{C.18}$$

$$= \frac{c_j^{\mathrm{b}} - c_j^{\mathrm{s}}}{c_j^{\mathrm{s}}} \tag{C.19}$$

The right-hand side of Eq. (C.19) can be used to evaluate the Damköhler-number based on a given concentration flow field, i.e. from simulations[1].
An alternative expression can be defined from the ratio of the rate without any transport limitations (intrinsic rate evaluated at bulk conditions) to the rate observed at maximum external transport limitations ($c_j^{\mathrm{s}} \to 0$).

$$Da_{\mathrm{II},j} = \frac{k_j^{\mathrm{itc}} \cdot c_j^{\mathrm{b}}}{k_{\mathrm{m},j} \cdot \left(c_j^{\mathrm{b}} - 0\right)} \tag{C.20}$$

$$= \frac{r_{j,\max}^{\mathrm{itc}}}{j_{j,\max}} \tag{C.21}$$

At steady-state, the flux continuity condition also holds between observed rate and intrinsic rate:

$$r_j^{\mathrm{obs}} = r_j^{\mathrm{itc}} \tag{C.22}$$

$$k_j^{\mathrm{obs}} \cdot c_j^{\mathrm{b}} = k_j^{\mathrm{itc}} \cdot c_j^{\mathrm{s}} \tag{C.23}$$

Using Eq. (C.19), the surface concentration can be expressed in terms of the Damköhler-number

$$c_j^{\mathrm{s}} = \frac{c_j^{\mathrm{b}}}{1 + Da_{\mathrm{II},j}} \tag{C.24}$$

Substituting Eq. (C.24) in (C.23) gives an expression for the observed rate constant

$$k_j^{\mathrm{obs}} \cdot c_j^{\mathrm{b}} = \underbrace{\left(\frac{k_j^{\mathrm{itc}}}{1 + Da_{\mathrm{II},j}}\right)}_{=k_j^{\mathrm{obs}}} \cdot c_j^{\mathrm{b}} \tag{C.25}$$

[1] Note that the given definition for the Damköhler-number is only applicable for reactant species, since product species may have zero concentration at the gas-washcoat interface.

Taking the ratio of observed to intrinsic rate constant from Eq. (C.25) we get the definition of the external effectiveness factor in terms of the Damköhler-number which can be further simplified by the definition of $Da_{\mathrm{II},j}$ in Eq. (C.21)

$$\eta_{\mathrm{ext},j} = \frac{1}{1 + Da_{\mathrm{II},j}} \tag{C.26}$$

$$= \frac{c_j^{\mathrm{s}}}{c_j^{\mathrm{b}}} \tag{C.27}$$

Thus, the external effectiveness factor can be conveniently evaluated from the simulated bulk and surface concentrations[2]. Multiplying Eq. (C.26) by $Da_{\mathrm{II},j}$ and using Eq. (C.25) yields an expression which can be evaluated from experimental values:

$$\eta_{\mathrm{ext},j} \cdot Da_{\mathrm{II},j} = \frac{Da_{\mathrm{II},j}}{1 + Da_{\mathrm{II},j}} \tag{C.28}$$

$$= \frac{k_j^{\mathrm{obs}}}{k_{\mathrm{m},j}} \tag{C.29}$$

The observed rate constant k_j^{obs} can be obtained from conversion measurements while one might use mass-transfer correlations to evaluate $k_{\mathrm{m},j}$. Rewriting Eq. (C.28) gives an expression for evaluating the Damköhler-number from experimental data:

$$Da_{\mathrm{II},j} = \frac{\eta_{\mathrm{ext},j} \cdot Da_{\mathrm{II},j}}{1 - \eta_{\mathrm{ext},j} \cdot Da_{\mathrm{II},j}} \tag{C.30}$$

Substituting Eq. (C.30) into Eq. (C.26) gives an expression for $\eta_{\mathrm{ext},j}$ which is experimentally accessible:

$$\eta_{\mathrm{ext},j} = 1 - (\eta_{\mathrm{ext},j} \cdot Da_{\mathrm{II},j}) \tag{C.31}$$

[2] Alternatively, Eq. (C.27) can be expressed in terms of mole fractions using the ideal gas equation of state: $\eta_{\mathrm{ext},j} = \frac{T_j^{\mathrm{s}}}{T_j^{\mathrm{b}}} \cdot \frac{x_j^{\mathrm{b}}}{x_j^{\mathrm{s}}}$

C.3 Internal Diffusion Limitations - Effectiveness Factor Approach

Given a flat plate washcoated surface under isothermal conditions, the Thiele-Modulus for an irreversible reaction with first-order reaction-rate is given for a representative limiting species j as [143]

$$\varphi_j = \delta_{\mathrm{wc}} \cdot \sqrt{\frac{k_{\mathrm{v,j}}}{D_{\mathrm{eff},j}}} \tag{C.32}$$

The effectiveness factor is given as the ratio of average intrinsic rate in the catalyst to the rate evaluated at surface conditions for the limiting species j:

$$\eta_j = \frac{\dot{S}_j^{\mathrm{eff}}}{\dot{S}_j} = \frac{\tanh \varphi_j}{\varphi_j} \tag{C.33}$$

The volumetric first-order reaction rate constant, $k_{\mathrm{v},j}$, in $\left[\frac{1}{\mathrm{s}}\right]$, can be expressed in terms of the surface reaction rate constant, k_j and the catalytic to geometric surface area ratio divided by the washcoat thickness:

$$k_{\mathrm{v},j} = k_j \cdot \left(\frac{F_{\mathrm{cat/geo}}}{\delta_{\mathrm{wc}}}\right) \tag{C.34}$$

Since the reaction is assumed first order, k_j can be expressed in terms of the rate of production/consumption of the limiting species j, $\dot{S}_j$, evaluated at surface conditions c_j^s

$$k_j = \frac{\dot{S}_j}{c_j^s} \tag{C.35}$$

Substituting Eq. (C.34) and (C.35) in Eq. (C.32) yields:

$$\varphi_j = \delta_{\mathrm{wc}} \cdot \sqrt{\frac{\dot{S}_j \cdot F_{\mathrm{cat/geo}}}{c_j^s \cdot D_j^{\mathrm{eff}} \cdot \delta_{\mathrm{wc}}}} \tag{C.36}$$

Using Eq. (C.33) with (C.36), the flux of production/consumption of an arbitrary species i, at the gas-washcoat interface ($r = R$), affected by internal pore transport limitations, is expressed in terms of the effectiveness factor of the limiting species j (cf. Eq. (5.23) on page 52):

$$J_{i,r}|_{r=R} = -\dot{S}_i \cdot \eta_j \cdot M_i \cdot F_{\mathrm{cat/geo}} \tag{C.37}$$

For values of $\varphi_j > 2$ the effectiveness factor is approximately given as $\eta_j \approx 1/\varphi_j$ and Eq. (C.37) reads

$$J_{i,r}|_{r=R} = -\dot{S}_i \cdot \sqrt{\frac{c_j^s \cdot D_j^{\text{eff}}}{\dot{S}_j} \cdot \left(\frac{F_{\text{cat/geo}}}{\delta_{\text{wc}}}\right)} \cdot M_i \tag{C.38}$$

Thus, in the limit when the reactions are fast (internal limitations with $\varphi_j > 2$), the rate of production/consumption affected by internal pore transport limitations, $\dot{S}_i^{\text{eff}}$, shows following dependencies

$$\dot{S}_i^{\text{eff}} \sim \begin{cases} \left(D_j^{\text{eff}}\right)^{1/2} & \text{(C.39a)} \\ F_{\text{cat/geo}}^{1/2} & \text{(C.39b)} \\ \delta_{\text{wc}}^{-1/2} & \text{(C.39c)} \end{cases}$$

Noticing that at $\varphi_j > 2$, only a thin layer of the washcoat is involved for the reactions to take place, i.e. the value of $F_{\text{cat/geo}}$ or the actual shape of the washcoat along the circumference (thickness) is irrelevant for the conversion, because only the ratio of both, $\frac{F_{\text{cat/geo}}}{\delta_{\text{wc}}}$, determines the rate according to Eq. (C.38).

Thus, a decrease of the washcoat thickness by one order of magnitude e.g. should give the same rate of production/consumption as a 10 times higher catalytic-to-geometric surface area ratio.

C.4 Reversibility[3]

The concept of reversibility was applied in Section 7 to analyze to what extent WGS and SR processes play a role as chemical subsystem during the autothermal oxidation of methane over the reduced phase of palladium.
The concept of reversibility can be applied to describe the extent of a chemical reaction system's sub-processes towards their partial equilibrium, i.e. the approach to thermodynamic equilibrium.
Based on the stoichiometry of a reaction as listed e.g. in Tab. 2.1, the reversibility Z_k for the net reaction k is found as the ratio of reaction quo-

[3] Parts of this chapter have been taken from [1] H. Stotz, L. Maier and O. Deutschmann, Methane oxidation over palladium: on the mechanism in fuel-rich mixtures at high temperatures, *Top. Catal.*, 60 (2017) 83-109.

tient $Q_k = \prod_i [c_i]^{\nu''_{i,k} - \nu'_{i,k}}$ and the concentration based equilibrium constant $K_{c,k} = \prod_i [c_i^{eq}]^{\nu''_{i,k} - \nu'_{i,k}}$ according to

$$Z_k = \frac{Q_k}{K_{c,k}} \tag{C.40}$$

For values of $Z_k > 1$ the reverse reaction is favored, whereas for $Z_k < 1$ the forward reaction is preferred. At equilibrium Z_k approaches one.

C.5 Calculations with UBI-QEP Method

The unity bond index-quadratic exponential potential method is a semi-empirical method for the phenomenological modeling of the reaction energetics of adsorption and surface reactions onto (mainly mono-metallic but also possible for poly-metallic) transition metal surfaces [158].
The UBI-QEP method incorporates the heuristic bond order conservation-Morse potential (BOC-MP) method which is based on following assumptions:

1.) Forces are treated as quasi-spherical and depend only on distance in the many-body system.

2.) Each binary interaction, A-B, is described by a Morse potential (MP)

$$\frac{E}{Q_0} = 4 \cdot \left[\left(\frac{x}{2} \right)^2 - \left(\frac{x}{2} \right) \right] \tag{C.41}$$

with x(r) called the two-center bond order (BO), only a function of the bond distance

$$x(r) = \exp\left(-\frac{r - r_0}{b} \right) \tag{C.42}$$

and Q_0 the two-center equilibrium bond energy (e.g. between surface metal, M, and adsorbed atom, A, (M-A), or between two atoms (A-B)) at the equilibrium distance, $r = r_0$, (potential well depth or bond dissociation energy), and b a distance scaling constant for the potential well width.

3.) The total bond order, X, consisting of all, n, binary interactions (bonds), is conserved and normalized to unity in the many-body system along the migration path up to dissociation:

$$X = \sum_{i}^{n} x_i = 1 \tag{C.43}$$

Typically, n is the coordination number (e.g. many-center, $(M)_n$-A, interaction) while only nearest neighbor interactions are considered.

4.) The total bond energy, $Q(x)$, results from the additive contribution of the pairwise interactions, i (two-center interaction, $Q_i = -E_i$, e.g. M-A or

A-B). The enthalpy of formation for a species AB on the surface from its elements A and B out of the gas-phase is then given by:

$$\left(-\Delta_{\mathrm{f}} H_{\mathrm{AB(s)}}\right) = Q_{\mathrm{AB}} + D_{\mathrm{AB}} \tag{C.44}$$

$$= \sum_{i=1}^{n} Q_i(x_i) + D_{\mathrm{AB}} \tag{C.45}$$

$$= -\left(\sum_{i=1}^{n} E_i(x_i) - D_{\mathrm{AB}}\right) \tag{C.46}$$

With the aforementioned assumptions analytical equations for the description of adsorption and activation energies can be derived. The required input parameters for these equations contain:

- experimental values on the atomic heat of adsorption, $Q_{\mathrm{A}(n)}$, of the participating elements on the corresponding catalyst surface and
- thermodynamic information on the total bond dissociation energy of the corresponding molecule, AB, in the gas-phase, D_{AB}, which can be calculated from listed values on standard heats of formation [226] according:

$$D_{\mathrm{AB}} = \Delta_{\mathrm{f}} H^{\circ}_{\mathrm{A(g)}} + \Delta_{\mathrm{f}} H^{\circ}_{\mathrm{B(g)}} - \Delta_{\mathrm{f}} H^{\circ}_{\mathrm{AB(g)}} \tag{C.47}$$

- In some cases, e.g. for specifically bound polyatomic adsorbates, bond partioning becomes necessary, and information on gas-phase bond dissociation energies between the partitioning groups (e.g. between atom A and B, M-A-(B) or any other group(s) X, M-A-(X), respectively), $D_{\mathrm{A\text{-}B}}$, $D_{\mathrm{A\text{-}X}}$, are needed.
  Those parameters can be either calculated from tabulated values on dissociation energies of the molecule and its fragments or, if available directly, taken from the tabulated literature values [227–229].

The UBI-QEP derived equations for specific types of adsorption are summarized below.

C.5.1 Atomic adsorption with on-top coordination: M-A

$$Q_{0,\mathrm{A}} = \frac{Q_{\mathrm{A}}(n)}{2 - \frac{1}{n}} \tag{C.48}$$

$Q_{0,\mathrm{A}}$: Maximum two-center, M-A, bond energy ($n = 1$).

Q_{A}: Experimental heat of chemisorption for element A on the surface with a given $\mathrm{M_n}$-A coordination.

n: Coordination number. Typically for fcc(111) and for hcp(1000) surfaces n equals $n_{\max} = 3$.

C.5.2 Linear molecular adsorption with mono atomic adsorbate surface interaction: $(\mathrm{M})_\mathrm{n}$-A-B

Case (a): Weak adsorption

$$Q_{\mathrm{AB,n}} \approx \frac{Q_{0,\mathrm{A}}^2}{\frac{Q_{0,\mathrm{A}}}{n} + D_{\mathrm{A\text{-}B}}} \tag{C.49}$$

Eq. (C.49) is valid if $D_{\mathrm{A\text{-}B}} > \frac{n-1}{n} \cdot Q_{0,\mathrm{A}}$

Case (b): Strong adsorption

$$Q_{\mathrm{AB}} = \frac{Q_{\mathrm{A}(n)}^2}{Q_{\mathrm{A}(n)} + D_{\mathrm{A\text{-}B}}} \tag{C.50}$$

Case (c): Intermediate adsorption

$$Q_{\mathrm{AB}} = \frac{1}{2} \cdot \left[\frac{Q_{0,\mathrm{A}}^2}{\frac{Q_{0,\mathrm{A}}}{n} + D_{\mathrm{A\text{-}B}}} + \frac{Q_{\mathrm{A}(n)}^2}{Q_{\mathrm{A}(n)} + D_{\mathrm{A\text{-}B}}} \right] \tag{C.51}$$

Note: For diatomic molecules, $D_{\mathrm{A\text{-}B}}$ equals the total bond dissociation energy for molecule AB in the gas-phase, D_{AB}. For polyatomic adsorbates bond partitioning is required. Thus, $D_{\mathrm{A\text{-}B}}$ equals the sum of the bond energies between A and its ligands B in the gas-phase.

For $n = 1$, all three cases Eq. (C.49-C.51) collapse to the same expression, $Q_{\mathrm{AB}(n=1)} = Q_{0,\mathrm{AB}}$, thus

$$Q_{0,\mathrm{AB}} = \frac{Q_{0,\mathrm{A}}^2}{Q_{0,\mathrm{A}} + D_{\mathrm{A\text{-}B}}} \tag{C.52}$$

C.5.3 Bridged molecular adsorption with diatomic adsorbate surface interaction (M-A-B-M)

$$Q_{\mathrm{AB}} = \frac{a \cdot b \cdot (a+b) + D_{\mathrm{A\text{-}B}} \cdot (a-b)^2}{a \cdot b + D_{\mathrm{A\text{-}B}} \cdot (a+b)} \tag{C.53}$$

Depending on the adsorption mode the constants for Eq. (C.53) are given for the different cases below:

Case (a): Diatomic molecule M-A-B-M

$$a = Q_{0,\mathrm{A}}^2 \cdot \frac{(Q_{0,\mathrm{A}} + 2 \cdot Q_{0,\mathrm{B}})}{(Q_{0,\mathrm{A}} + Q_{0,\mathrm{B}})^2} \tag{C.54}$$

$$b = Q_{0,\mathrm{B}}^2 \cdot \frac{(Q_{0,\mathrm{B}} + 2 \cdot Q_{0,\mathrm{A}})}{(Q_{0,\mathrm{A}} + Q_{0,\mathrm{B}})^2} \tag{C.55}$$

For weakly bounded symmetric molecules (CO_2, O_2, etc.), $a = b$, and Eq. (C.53) simplifies to

$$Q_{\mathrm{AB}} = \frac{\frac{9}{2} \cdot Q_{0,\mathrm{A}}^2}{3 \cdot Q_{0,\mathrm{A}} + 8 \cdot D_{\mathrm{A\text{-}B}}} \tag{C.56}$$

Case (b): Polyatomic molecule with multiple ligands X and Y of the same kind $(\mathrm{X})_\mathrm{p}$-A(-M)-B(-M)-$(\mathrm{Y})_\mathrm{q}$

$$a = Q_{0,\mathrm{A}} \cdot \left(1 - \left(\frac{p \cdot Q_{0,\mathrm{X}}}{p \cdot Q_{0,\mathrm{A}} + Q_{0,\mathrm{X}}}\right)^2\right) \tag{C.57}$$

$$b = Q_{0,\mathrm{B}} \cdot \left(1 - \left(\frac{q \cdot Q_{0,\mathrm{Y}}}{q \cdot Q_{0,\mathrm{B}} + Q_{0,\mathrm{Y}}}\right)^2\right) \tag{C.58}$$

Eq. (C.53) with Eq. (C.57-C.58) are valid if $p + q > 0$.

Case (c): Polyatomic molecule with multiple different functional groups (X-)(M-)A-B(-M)(-Y)

$$a = Q_{0,\mathrm{AX}}^2 \cdot \frac{(Q_{0,\mathrm{AX}} + 2 \cdot Q_{0,\mathrm{BY}})}{(Q_{0,\mathrm{AX}} + Q_{0,\mathrm{BY}})^2} \tag{C.59}$$

$$b = Q_{0,\mathrm{BY}}^2 \cdot \frac{(Q_{0,\mathrm{BY}} + 2 \cdot Q_{0,\mathrm{AX}})}{(Q_{0,\mathrm{AX}} + Q_{0,\mathrm{BY}})^2} \tag{C.60}$$

$Q_{0,\mathrm{AX}}$ and $Q_{0,\mathrm{BY}}$ are calculated as sum of the individual bond energy contributions based Eq. (C.52), with the bond partitioned gas-phase dissociation energies $D_{\mathrm{A\text{-}X}}$ and $D_{\mathrm{B\text{-}Y}}$ from the contributions between the atom binding to the surface, A or B, and all other functional groups X or Y bound to A or B, respectively.

$$Q_{0,\mathrm{AX}} = \frac{Q_{0,\mathrm{A}}^2}{Q_{0,\mathrm{A}} + D_{\mathrm{A\text{-}X}}} \tag{C.61}$$

$$Q_{0,\mathrm{BY}} = \frac{Q_{0,\mathrm{B}}^2}{Q_{0,\mathrm{B}} + D_{\mathrm{B\text{-}Y}}} \tag{C.62}$$

Case (d): Chelated bridged molecular adsorption with diatomic adsorbate surface interaction (M-A-X-B-M)

Case (d) is a special case of case (c), when X=Y and $D_{\mathrm{A\text{-}B}} = 0$, while X is considered to be sufficiently far away from the surface, showing no interaction with the surface metal atoms. With these assumptions Eq. (C.53) simplifies to

$$Q_{\mathrm{AB}} = Q_{0,\mathrm{AX}} + Q_{0,\mathrm{BX}} + \frac{Q_{0,\mathrm{AX}} \cdot Q_{0,\mathrm{BX}}}{Q_{0,\mathrm{AX}} + Q_{0,\mathrm{BX}}} \tag{C.63}$$

where $Q_{0,\mathrm{AX}}$ and $Q_{0,\mathrm{BX}}$ are analogously given to Eq. (C.61) and Eq. (C.62). For identical ligands, A=B, Eq. (C.63) simplifies further to

$$Q_{\mathrm{AB}} = \frac{3}{2} \cdot \frac{Q_{0,\mathrm{A}}^2}{Q_{0,\mathrm{A}} + D_{\mathrm{A\text{-}X}}} \tag{C.64}$$

C.5.4 Calculation of activation energies based on the UBI-QEP method

The UBI-QEP based equations for the activation energy are different for different types of reactions. The derivations are applicable with the restriction that a maximum number of four reacting species participate in one elementary reaction, i.e. a maximum of two species can appear on each side of the reaction equation. The used equation for estimating activation energies are given below.

Case (a): Disproportionation reactions ($\sum_j \nu_j = 0$)

In the general case of a given disproportionation reaction when all participating reaction partners are adsorbed on the surface,

$$A(s) + B(s) \rightleftharpoons C(s) + D(s) \tag{C.65}$$

and the UBI-QEP expression for the activation energy is given as

$$E_{\mathrm{a,f}} = \phi \cdot (E_{\mathrm{int}} + \Delta_{\mathrm{R}} H) \tag{C.66}$$

$$E_{\mathrm{a,r}} = \phi \cdot (E_{\mathrm{int}} - \Delta_{\mathrm{R}} H) \tag{C.67}$$

with $\phi = 0.5$, and E_{int} the Lennard-Jones interaction energy for the transition state intermediate, defined depending on the value of $\Delta_{\mathrm{R}} H^{\mathrm{gas}}$, i.e. in dependence on the formulated direction of the reaction Eq. (C.65):

$$E_{\mathrm{int}} = \begin{cases} E_{\mathrm{int}}^{\mathrm{P}} = \dfrac{Q_{\mathrm{C}} \cdot Q_{\mathrm{D}}}{Q_{\mathrm{C}} + Q_{\mathrm{D}}} & \text{if } \Delta_{\mathrm{R}} H^{\mathrm{gas}} > 0 \quad \text{(C.68a)} \\ E_{\mathrm{int}}^{\mathrm{R}} = \dfrac{Q_{\mathrm{A}} \cdot Q_{\mathrm{B}}}{Q_{\mathrm{A}} + Q_{\mathrm{B}}} & \text{if } \Delta_{\mathrm{R}} H^{\mathrm{gas}} \leq 0 \quad \text{(C.68b)} \end{cases}$$

with P and R denoting that E_{int} is either evaluated with the corresponding adsorption energies, Q_j, of the product or reactant species.

The reaction enthalpy, $\Delta_{\mathrm{R}} H$, and the reaction enthalpy of the hypothetical reaction in the gas-phase, $\Delta_{\mathrm{R}} H^{\mathrm{gas}}$, are also defined in forward direction according to reaction Eq. (C.65):

$$\Delta_{\mathrm{R}} H = -\left(\Delta_{\mathrm{R}} D + \Delta_{\mathrm{R}} Q\right) \tag{C.69}$$

$$\Delta_{\mathrm{R}} H^{\mathrm{gas}} = \left(-\Delta_{\mathrm{R}} D\right) \tag{C.70}$$

Note: Eq. (C.66) and (C.67) fulfill sufficiently the thermodynamic consistency constraint of Eq. (5.45).

Nonetheless, the necessary condition for both equations to be valid is that the energy of the transition state intermediate, is given as

$$E^{\ddagger} = E_{\mathrm{a,f}} + H^{R} \tag{C.71}$$
$$= E_{\mathrm{a,r}} + H^{P} \tag{C.72}$$
$$= \phi \cdot \left(E_{\mathrm{int}} + H^{\mathrm{P}} + H^{\mathrm{R}}\right) \tag{C.73}$$

(using $\phi = 0.5$) and needs to fulfill the minimization condition:

$$E^{\ddagger} \overset{!}{<} min\left\{H^{\mathrm{P}}, H^{\mathrm{R}}\right\} = \begin{cases} H^{\mathrm{P}} & \text{if } \Delta_{\mathrm{R}} H > 0 \quad \text{(C.74a)} \\ H^{\mathrm{R}} & \text{if } \Delta_{\mathrm{R}} H \leq 0 \quad \text{(C.74b)} \end{cases}$$

Where, H^{P} and H^{R} are the total enthalpy of the product or reactant state intermediates defined as:

$$H_k^{\mathrm{P}} = \sum_j \nu_{k,j}^{''} H_j \tag{C.75}$$

$$H_k^{\mathrm{R}} = \sum_j \nu_{k,j}^{'} H_j \tag{C.76}$$

Thus, the reaction enthalpy is given to $\Delta_{\mathrm{R}} H_k = H_k^{\mathrm{P}} - H_k^{\mathrm{R}}$ and $\Delta_{\mathrm{R}} D$ and $\Delta_{\mathrm{R}} Q$ can be calculated analogously with the latter definitions.
If the UBI-QEP based equations for the activation energy calculations fail in fulfilling this condition, due to the many assumptions and approximations made during the derivation, then the transition state energy is instead adjusted to be equal to the minimum of the two values in order to be thermodynamically consistent. In terms of activation energies this means nothing else than

$$E_{\mathrm{a,f}} = E^{\ddagger} - H^{\mathrm{R}} = \begin{cases} H^{\mathrm{P}} - H^{\mathrm{R}} = \Delta_{\mathrm{R}} H \text{ if } \Delta_{\mathrm{R}} H > 0 \quad \text{(C.77a)} \\ H^{\mathrm{R}} - H^{\mathrm{R}} = 0 \quad \text{if } \Delta_{\mathrm{R}} H \leq 0 \quad \text{(C.77b)} \end{cases}$$

and for the reverse barrier:

$$E_{\mathrm{a,r}} = E^{\ddagger} - H^{\mathrm{P}} = \begin{cases} H^{\mathrm{P}} - H^{\mathrm{P}} = 0 \quad \text{if } \Delta_{\mathrm{R}} H > 0 \quad \text{(C.78a)} \\ H^{\mathrm{P}} - H^{\mathrm{R}} = -\Delta_{\mathrm{R}} H \text{ if } \Delta_{\mathrm{R}} H \leq 0 \quad \text{(C.78b)} \end{cases}$$

Case (b): Dissociation and recombination reactions on the surface $(\sum_j \nu_j \neq 0)$

The same equations for calculating the activation energy as for disproportionation reactions apply for dissociation reactions on the surface (cf. Eq. (C.66) and Eq. (C.67)):

$$AB(s) \rightleftharpoons A(s) + B(s) \tag{C.79}$$

and for recombination reactions on the surface:

$$A(s) + B(s) \rightleftharpoons AB(s) \tag{C.80}$$

However, the only exception is that the interaction energy is now calculated depending on the formulated forward direction, i.e. if $\sum_j \nu_j > 0$ for dissociation and if $\sum_j \nu_j < 0$ for recombination.

$$E_{\mathrm{int}} = \begin{cases} E_{\mathrm{int}}^{\mathrm{P}} = \dfrac{Q_{\mathrm{A}} \cdot Q_{\mathrm{B}}}{Q_{\mathrm{A}} + Q_{\mathrm{B}}} & \text{if } \displaystyle\sum_j \left(\nu_{j,k}^{''} - \nu_{j,k}^{'}\right) > 0 \qquad \text{(C.81a)} \\ E_{\mathrm{int}}^{\mathrm{R}} = \dfrac{Q_{\mathrm{A}} \cdot Q_{\mathrm{B}}}{Q_{\mathrm{A}} + Q_{\mathrm{B}}} & \text{if } \displaystyle\sum_j \left(\nu_{j,k}^{''} - \nu_{j,k}^{'}\right) < 0 \qquad \text{(C.81b)} \end{cases}$$

Analogously to the previous case (a), Eq. (C.74a) and Eq. (C.74b) have to be fulfilled otherwise, Eq. (C.77a-C.78b) are enforced instead.

Case (c): Dissociative adsorption and associative desorption reactions ($\sum_j \nu_j \neq 0$)

The class of reactions is described by

$$AB(g) \rightleftharpoons A(s) + B(s) \tag{C.82}$$

The activation energy is calculated accordingly with the UBI-QEP approach:

$$E_{\mathrm{a,f}} = \phi \cdot (E_{\mathrm{int}} + \Delta_{\mathrm{R}} H) - Q \tag{C.83}$$

$$E_{\mathrm{a,r}} = \phi \cdot (E_{\mathrm{int}} - \Delta_{\mathrm{R}} H) - Q \tag{C.84}$$

where

$$Q = \begin{cases} Q^{\mathrm{P}} = Q_{\mathrm{AB}} & \text{if } \displaystyle\sum_j \left(\nu_{j,k}^{''} - \nu_{j,k}^{'}\right) > 0 \qquad \text{(C.85a)} \\ Q^{\mathrm{R}} = Q_{\mathrm{AB}} & \text{if } \displaystyle\sum_j \left(\nu_{j,k}^{''} - \nu_{j,k}^{'}\right) < 0 \qquad \text{(C.85b)} \end{cases}$$

and E_{int} is calculated according Eq. (C.81a) and Eq. (C.81b).

Analogously to the previous case (a) and (b), Eq. (C.74a) and Eq. (C.74b) have to be fulfilled otherwise, Eq. (C.77a-C.78b) are enforced instead.

Case (d): Molecular Ad- and Desorption ($\sum_j \nu_j = 0$)

The class of reactions is described by

$$AB(g) \rightleftharpoons AB(s) \tag{C.86}$$

The activation energy for the adsorption step is set to zero, i.e.:

$$E_{\mathrm{a,ads}} = 0 \tag{C.87}$$

$$E_{\mathrm{a,des}} = -\Delta_{\mathrm{R}} H \tag{C.88}$$

C.6 Reaction Path Analysis[4]

The kinetic model considers various paths for the catalytic conversion of methane over the PdO surface. To study which paths are preferred under specific reaction conditions, it is advisable to conduct a reaction paths analysis [230]. The reaction path analysis is post-processed from the calculated reaction rates at specific reaction conditions. The net reaction rate for reaction step k is given as

$$\dot{s}_k = k_{\mathrm{f},k} \cdot \prod_{j=1}^{N_\mathrm{g}+N_\mathrm{s}} c_j^{\nu'_{j,k}} - k_{\mathrm{r},k} \cdot \prod_{j=1}^{N_\mathrm{g}+N_\mathrm{s}} c_j^{\nu''_{j,k}} \tag{C.89}$$

It is convenient to decompose the species net rate $\dot{S}_i$ into individual contributions for production $\dot{S}_i^+$ and consumption $\dot{S}_i^-$ regarding species i, i.e.

$$\dot{S}_i = \sum_k \left(\nu''_{i,k} - \nu'_{i,k}\right) \cdot \dot{s}_k \tag{C.90a}$$

$$= \sum_k \dot{S}_{i,k} \tag{C.90b}$$

$$= \dot{S}_i^+ + \dot{S}_i^- \tag{C.90c}$$

The net rate of a step k contributing to species i, is either a producing or consuming rate according to the definition

$$\dot{S}_{i,k} = \begin{cases} \dot{S}_{i,k}^+ & \text{if } \dot{S}_{i,k} > 0 \quad \text{(C.91a)} \\ \dot{S}_{i,k}^- & \text{if } \dot{S}_{i,k} < 0 \quad \text{(C.91b)} \end{cases}$$

In Eq. (C.90c) the species net rates of production and consumption are expressed as

$$\dot{S}_i^+ = \sum_k H\left(\dot{S}_{i,k}\right) \cdot \dot{S}_{i,k} \tag{C.92}$$

$$\dot{S}_i^- = \sum_k H\left(-\dot{S}_{i,k}\right) \cdot \dot{S}_{i,k} \tag{C.93}$$

$H(\cdot)$ denotes the Heaviside-function.

[4] Parts of this chapter have been taken from [2] H. Stotz, L. Maier, A. Boubnov, A. T. Gremminger, J.-D. Grunwaldt and O. Deutschmann, Surface reaction kinetics of methane oxidation over PdO, *J. Catal.*, 370 (2019) 152-175.

To the end, the fractional contributions to formation or consumption of species i through path k, $P_{i,k}$ is then calculated by normalizing each individual contribution by the net rate of formation or consumption, respectively.

$$\dot{P}^{+}_{i,k} = \frac{\dot{S}^{+}_{i,k}}{\dot{S}^{+}_{i}} \tag{C.94}$$

$$\dot{P}^{-}_{i,k} = \frac{\dot{S}^{-}_{i,k}}{\dot{S}^{-}_{i}} \tag{C.95}$$

This procedure guarantees that the sum over all net producing or consuming contributions normalizes to 1, respectively. The sequence of the preferred reaction steps, the so-called preferential reaction path, can thus be evaluated by post-processing calculated fractional contributions through identifying the maximum contribution for each species i regarding formation and consumption.

C.7 Integral Sensitivity Analysis[5]

In order to analyze which reaction steps are most sensitive or even rate limiting at various axial positions of the channel, calculations of integrated normalized sensitivity coefficients $S^{0}_{i,k}$ have been performed. The $S^{0}_{i,k}$ are calculated by consecutively multiplying the initial pre-exponential factor A^{0}_{k} by $\epsilon = 1.1$, yielding a perturbed prefactor of $\tilde{A}_k = A^{0}_{k} \cdot \epsilon$, which is then used to compute a new solution in terms of mole fractions.

$$S^{0}_{i,k} = \frac{S_{i,k}}{\max_k |S_{i,k}|} \tag{C.96}$$

In Eq. C.97, $S_{i,k}$ is the non-normalized sensitivity coefficient of reaction k with respect to gas-phase species i and is calculated from

$$S_{i,k} = \left(\frac{\partial x_i(z)}{\partial \ln(A_k)} \right)_{A_{j \neq k}} \approx \frac{\tilde{x}_i\left(z; \tilde{A}_k\right) - x^{0}_{i}\left(z; \tilde{A}^{0}_{k}\right)}{\ln(\epsilon)} \tag{C.97}$$

Where $\tilde{x}_i\left(z; \tilde{A}_k\right) - x^{0}_{i}\left(z; \tilde{A}^{0}_{k}\right)$ is the change in the calculated mole fractions of species i at the given channel position z upon increasing the pre-exponential factor of step k by 10 % from the initial value.

[5] Parts of this chapter have been taken from [1] H. Stotz, L. Maier and O. Deutschmann, Methane oxidation over palladium: on the mechanism in fuel-rich mixtures at high temperatures, *Top. Catal.*, 60 (2017) 83-109.

C.8 Degree of Rate Control Sensitivity Analysis[6]

For evaluation of the most sensitive reaction rate parameters on the simulation results, the degree of rate control (DRC) method for transition states according to Campbell [148] was applied. The method allows analyzing which steps are most rate controlling with respect to the net rate of production or consumption, $\dot{S}_i$, of species i, while it maintains thermodynamic consistency during perturbation of the reaction rate parameters. For a set of reversible reactions as given in Eq. (5.41), the degree of rate control is defined as

$$X_{i,k}^{\mathrm{RC}} = \frac{\partial \ln\left(\dot{S}_i\right)}{\partial\left(-\frac{G_k^{\ddagger}}{RT}\right)} \tag{C.98}$$

The numerical evaluation of X_k^{RC} is computed based on a finite difference approximation by evaluating the rate of methane consumption while perturbing the Gibbs free energy of the transition state in step k, $G_k^{\ddagger}$, by adding a small amount of $dG_k = 0.01\,\mathrm{kJ/mol}$ to the activation energy.

$$X_{i,k}^{\mathrm{RC}} \approx -\frac{RT}{dG_k} \cdot \ln\left(\frac{\dot{S}_i(G_k^{\ddagger} + dG_k)}{\dot{S}_i(G_k^{\ddagger})}\right) \tag{C.99}$$

In Eq. (C.99), $\dot{S}_i^{'}$ and $\dot{S}_i^{''}$ are the rates of methane consumption as obtained from the set of original reaction rate constants and in case when the transition state energy in step k is perturbed, respectively.

[6] Parts of this chapter have been taken from [2] H. Stotz, L. Maier, A. Boubnov, A. T. Gremminger, J.-D. Grunwaldt and O. Deutschmann, Surface reaction kinetics of methane oxidation over PdO, *J. Catal.*, 370 (2019) 152-175.

List of Publications

This thesis has been created during the period from May 1st 2013 to August 31st 2018 at the Institute for Chemical Technology and Polymer Chemistry of the Karlsruhe Institute of Technology under the lead of Prof. Dr. rer. nat. Olaf Deutschmann.

Parts of this work have been published in following international peer reviewed scientific journals and conference contributions:

- H.Stotz, S. Schwarz, K. Keller, P. Lott, B. Torkashvand, H. Gossler, S. Tischer, L. Maier, O. Deutschmann. „Exhaust treatment of natural gas engines: Some modelling aspects.“(International Symposium on Modeling of Exhaust-Gas After-Treatment / MODEGAT VI, Bad Herrenalb, Germany), 08.09.-10.09.19 (Oral).
- H. Stotz, L. Maier, A. Boubnov, A. Gremminger, J.-D. Grunwaldt, O. Deutschmann. „Surface Reaction Kinetics of Methane oxidation over PdO.“ *Journal of Catalysis*, 370 152-175 (2019)
- H. Stotz, L. Maier, A. Boubnov, A. Gremminger, S. Valchera, J.-D. Grunwaldt, O. Deutschmann. „Methane oxidation over Palladium Oxide: Surface Reaction Kinetics at Fuel Lean Conditions.“(European Summer School on Multi-Scale Modeling in Chemical Reaction Engineering/ MultiMod Summer School, Halkidiki, Greece), 18.09.-22.09.17 (Poster).
- H. Stotz, L. Maier, A. Boubnov, A. Gremminger, S. Valchera, J.-D. Grunwaldt, O. Deutschmann. „Methane oxidation over Palladium Oxide: Surface Reaction Kinetics at Fuel Lean Conditions.“(International Symposium on Modeling of Exhaust-Gas After-Treatment / MODEGAT V, Bad Herrenalb, Germany), 03.09.-05.09.17 (Poster).
- H. Stotz, L. Maier, A. Boubnov, A. Gremminger, S. Valchera, J.-D. Grunwaldt, O. Deutschmann. „Surface Reaction Kinetics of Methane Oxidation over Palladium Oxide.“, (North American Catalysis Society Meeting / NAM25, Denver/Colorado, USA), 04.06.-09.06.2017, (Oral).

- H. Stotz, L. Maier, A. Boubnov, A. Gremminger, S. Valchera, J.-D. Grunwaldt, O. Deutschmann. „Methane oxidation over Palladium Oxide: Surface Reaction Kinetics at Fuel Lean Conditions.“(10. Jahrestreffen Reaktionstechnik, Würzburg, Germany), 22.04.-24.04.17 (Poster).
- H. Stotz, L. Maier, O. Deutschmann. „Methane oxidation over Palladium - On the mechanism in fuel-rich mixtures at high temperatures.“ *Topics in Catalysis*, 60(1-2) (2017) 83-109.
- H. Stotz, J. Schütz, L. Maier, O. Deutschmann. „An experimental and microkinetic modeling study for the total oxidation of CO over a Pd/Al_2O_3 monolith based DOC“, (International Symposium on Modeling of Exhaust-Gas After-Treatment / MODEGAT IV, Bad Herrenalb, Germany), 13.09.-15.09.15 (Poster).
- H. Stotz, L. Maier, O. Deutschmann. „Methane oxidation over palladium: On the mechanism in rich methane-oxygen mixtures at high temperatures“, (European Catalysis Conference / EUROPACAT XII, Kazan, Russia), 30.08.-04.09.2015 (Oral).
- H. Stotz, C. Diehm, L. Maier, Olaf Deutschmann. „Detailed kinetics of the catalytic partial oxidation of CH_4 over a Pd/Al_2O_3 Coated Monolith“, (North American Catalysis Society Meeting / NAM24, Pittsburgh/Pennsylvania, USA), 14.06.-19.06.2015, (Oral).
- H. Stotz, L. Maier, O. Deutschmann. „Methane oxidation over Palladium: On the mechanism in rich methane-oxygen mixtures at high temperatures.“(48. Jahrestreffen Deutscher Katalytiker, Weimar, Germany), 16.03.-18.03.15 (Poster).

Further publications by the author related to other topics are:

- L. T. Espinoza, H. Stotz, O. Deubzer, R. B. Garcia, G. R. Lepe, K. Bilewska, M. Osadnik, J. Mazur, L. S. Ökvist, J. Eriksson, X. Hu. „SCREEN Solutions for Critical Raw materials - a European Expert Network: Critical Raw Material Substitution Profiles.“, *EU Project*, (2018).
- K. Delgado, L. Maier, S. Tischer, A. Zellner, H. Stotz, O. Deutschmann. „Surface Reaction Kinetics of Steam- and CO_2-Reforming as Well as Oxidation of Methane over Nickel-Based Catalysts.“ *Catalyts*, 5 (2) (2015) 871-904.
- H. Stotz, U. Sauter. „Electrode For An Electrochemical Energy Store.“, *US Patent Application*, Pub.-Nr. 20160372738, (2014)

Danksagung

All denjenigen sei mein herzlichster Dank ausgesprochen, die zum erfolgreichen Gelingen dieser Arbeit mit beigetragen haben. Mein Dank gilt insbesondere

Herrn Prof. Dr. Olaf Deutschmann für die fachliche Betreuung und die Möglichkeit zur Promotion,

Herrn Prof. Dr. Roland Dittmeyer, für die Übernahme der Co-Betreuung dieser Arbeit seitens der Chemie-Ingenieurs Fakultät, für seine Hilfsbereitschaft zu fachlichen Aspekten und den vielen nützlichen Anmerkungen,

Dr. Luba Maier, für die Übernahme der fachlichen Betreuung, die Ratschläge sowie wissenschaftlichen Diskussionen und für Ihre Expertise zur Entwicklung von Oberflächenreaktionsmechanismen,

Prof. Dr. Jan-Dierk Grunwaldt, für die Möglichkeiten zur Durchführung von in-situ DRIFTS Messungen am ITCP,

Prof. Dr. Gianpiero Groppi von der Politechnico di Milano, Italien, für die fachkundigen Hinweise und sachdienliche Kritik, sowie für die Bereitstellung experimenteller Daten zur Konversions Hysterese für die Mechanismus Validierung,

Dr. Alexey Boubnov, Dr. Andreas Gremminger, Dr. Claudia Antinori, Azize Ünal und Kathrin Schäfer für die Unterstützung bei den Experimenten,

Ursula Schwald, Yvonne Dedecek und Martin Spoo für die Unterstützung bei organisatorischen und infrastrukturellen Fragen jeglicher Art,

den Dres. Steffen Tischer, Matthias Hettel, Martin Wörner, Maria Casapu und Dimitri Doronkin für die Hilfe bei Problemen mit DETCHEM, bei numerischen oder experimentellen Fragen jeglicher Art,

meinen Arbeitskolleginnen und Kollegen Dr. Karla Herrera Delgado, Dr. Sofia Angeli, Dr. Hoda Torkashvand, Anna Bertótiné Abai, Dr. Sivaram Kannepalli, Dr. Aayan Bannerjee und Dr. Vikram Menon für die unzähligen gemeinsam verbrachten Stunden, die wissenschaftlichen Diskussionen und die gute Zeit miteinander.

Ebenso möchte ich mich bei all denjenigen Menschen bedanken, denen ich während dieser Zeit abseits meiner Wissenschaftlichen Laufbahn begegnet bin und die mich stets dabei unterstützt und ermutigt haben diesen Weg bis zum Schluss zu gehen und so zum Erfolg dieser Arbeit wesentlich mit beigetragen haben.

Danke den Leuten von der KHG Karlsruhe, insbesondere Hans-Jörg Krieg, Friederike Maier, Martin Kühlmann, Ulrich Beer-Bercher, Andrea Legge, Ilka Hammer, Hanna und Alex Schuhmacher, Aleksandra und Matthias Gotsch, Tobias Schodrok, Annett Kaufhold und Anika Bludau, Inga Melkowá, Susanne Cernak, und Pascal Hagenah. Mein Dank geht an Dr. Luis A. Tercero Espinoza für die Übergangszeit am Fraunhofer ISI; meinen ehemaligen Mitbewohnern Jessica Hobusch, Tobias Schmidt und Frederik Nägele, danke für die herzliche Aufnahme bei euch in die WG, sowie meinen Freunden Jan Bujk und Bernhard Wieland aus der Heimat, danke für die anhaltende Freundschaft in dieser Zeit.

Schließlich möchte ich von Herzen meiner Familie danken, meinen Eltern Erika und Gebhard, sowie meiner Schwester Britta mit Stephan für eure Unterstützung und Geduld in dieser Zeit.

Leinfelden-Echterdingen, im Sommer 2020 Henning Stotz